Title
Laser Wakefield Acceleration of Multi-GeV Electron Bunches with Petawatt-Scale Laser Pulses Guided in a Laser-Heated Capillary Discharge

Author
Pieronek, Christopher Valentine

Publication Date
2021

Peer reviewed|Thesis/dissertation

Laser Wakefield Acceleration of Multi-GeV Electron Bunches with Petawatt-Scale Laser Pulses Guided in a Laser-Heated Capillary Discharge

by

Christopher Valentine Pieronek

A dissertation submitted in partial satisfaction of the

requirements for the degree of

Doctor of Philosophy

in

Engineering - Nuclear Engineering

in the

Graduate Division

of the

University of California, Berkeley

Committee in charge:

Professor Ka-Ngo Leung, Co-chair
Dr. Anthony Gonsalves, Co-chair
Professor Karl Van Bibber
Professor Jonathan Wurtele

Fall 2021

Laser Wakefield Acceleration of Multi-GeV Electron Bunches
with Petawatt-Scale Laser Pulses Guided in a Laser-Heated Capillary Discharge

Abstract

Laser Wakefield Acceleration of Multi-GeV Electron Bunches
with Petawatt-Scale Laser Pulses Guided in a Laser-Heated Capillary Discharge

by

Christopher Valentine Pieronek

Doctor of Philosophy in Engineering - Nuclear Engineering

University of California, Berkeley

Professor Ka-Ngo Leung, Co-chair

Dr. Anthony Gonsalves, Co-chair

Laser wakefield accelerators (LWFAs), which accelerate electrons in the fields of a plasma wave driven by the ponderomotive force of an intense laser pulse, have attracted intense research interest in recent years due to the high gradients they can support. These devices hold promise as a new class of compact accelerators for applications including free-electron lasers, particle colliders, and Thomson-scattered gamma ray sources. To date, the highest energy gains for a given laser power in LWFAs have been achieved by guiding the driving laser pulse in a pre-formed plasma channel. This dissertation covers the development and demonstration of a novel guiding structure: the laser-heated gas-filled capillary discharge waveguide. These structures are capable of guiding intense laser pulses over many diffraction lengths at low plasma densities required to mitigate bunch dephasing and accelerate electrons to high energies. In the work presented here were used to accelerate electrons to 7.8 GeV in 20 cm using 850 TW of power from the BELLA laser at Lawrence Berkeley National Laboratory (LBNL). Low power guiding experiments demonstrating the feasibility of the technique are described. Plasma heating was demonstrated through visible light plasma spectroscopic measurements, which through coincidence with improved guiding of a sub-ns probe beam indicated formation of a waveguide by plasma expansion driven by inverse-bremsstrahlung heating. The density and matched spot size of the plasma channel formed by laser-heating were diagnosed using measurements of the group velocity and spot-size oscillation of a guided probe beam. Two spectral interferometers were constructed for the group velocity measurements: a fiber-based Mach-Zehnder interferometer installed on a target prototyping vacuum chamber, and a two-color common path interferometer on the main BELLA beam line. The design of these setups as well as the algorithms used for analyzing the interferograms are described. These diagnostic measurements revealed strategies for optimizing waveguide performance through tuning of plasma and laser parameters, and were found to be in excellent agreement

with magnetohydrodynamic simulations using the MARPLE code. Guiding of petawatt pulses and acceleration of electrons to multi-GeV energies in laser-heated capillary discharges is demonstrated, showing good agreement between low power guiding measurements, particle-in-cell simulations with the INF&RNO code, and the results of high power laser experiments. Additionally, electron beams were produced using ionization injection in a localized region of high-Z gas in the capillary entrance with channel and laser parameters tuned to suppress self-trapping. Finally, a numerical model of third harmonic generation for femtosecond laser pulses is presented, which is used to simulate a possible design for an ultraviolet beamline for a future demonstration of laser-triggered bunch injection. The work described in this dissertation constitutes a foundation for future LWFA experiments aimed at the production of low energy spread electron beams and staged acceleration at the multi-GeV level through demonstration of controlled bunch injection with multi-GeV energy gain and development of a nonlinear optical modeling tool useful for the design of laser sources required for triggered bunch injection schemes.

"Remember kids:
the only difference between screwing around and science,
is writing it down."
–Adam Savage

To my Dad, who taught me to screw around,
and my Mom, who told me to write it down.

(And my older brother who was always there
to keep me from feeling too clever.)

Contents

List of Figures

List of Tables

List of Symbols

$\mathbf{a}$	Normalized vector potential	7
$\mathbf{A}$	Vector potential	7
$\mathbf{B}$	Magnetic field	7
β_g	Normalized group velocity	34
$\beta_{g,geo}$	Normalized group velocity component from channel matched spot size	44
$\overline{\beta}_{g,geo}$	Normalized group velocity component from channel matched spot size, longitudinally averaged	44
$\Delta\overline{\beta}_{g,geo}$	Longitudinally averaged normalized group velocity difference between fundamental and second harmonic probe pulses from plasma channel matched spot size	88
β_{g,n_e}	Normalized group velocity component from channel on-axis plasma density	44
$\Delta\overline{\beta}_{g,n_{e0}}$	Longitudinally averaged normalized group velocity difference between fundamental and second harmonic probe pulses from plasma channel on-axis density	88
$\overline{\beta}_{g,n_e}$	Normalized group velocity component from channel on-axis plasma density, longitudinally averaged	44
β_p	Normalized plasma wave phase velocity	6
$\boldsymbol{\beta}$	Relativistic normalized velocity	7
c	Vacuum speed of light	5
c_s	Ion acoustic speed	41
E	Kinetic energy	10
E_0	Plasma wave breaking field, cold nonrelativistic case	6
E_{WB}	Plasma wave breaking field, cold relativistic case	6
E_p	Electron ponderomotive energy in the low-power limit	40
$\mathbf{E}$	Electric field	7
η	Plasma refractive index	33
η_r	Relativistically modified plasma refractive index	21
γ	Relativistic factor	7
γ_d	Dephasing limited energy	27
γ_p	Plasma wave phase velocity relativistic factor	6
γ_{pd}	Pump depletion limited energy	27

r_m	Plasma channel matched spot size	31
$\overline{r}_m$	Plasma channel matched spot size, longitudinally averaged	62
r_s	e^{-2} Gaussian beam radius	20
ρ	Normalized proper electron density	12
$\tilde{\rho}$	Charge density	11
t	Delay from peak heater power, Chapter 4 onward	59
t_d	Delay from peak of discharge current	59
ΔT	Laser pulse delay induced by plasma channel	44
T_e	Electron temperature	40
T_i	Ion temperature	40
ΔT_{rb}	Delay between fundament and second-harmonic probe pulses induced by plasma channel	88
τ	Normalized time $\tau = ct$. In Chapters 4 and 5, refers to interferogram Fourier transform variable	12
θ_i	Laser propagation angle at plasma channel entrance plane	33
$\mathbf{u}$	Normalized relativistic mechanical momentum	7
$\mathbf{u}_\perp$	Normalized transverse relativistic mechanical momentum	12
v_p	Plasma wave phase velocity	6
$\boldsymbol{v}$	Velocity	7
x_c	Transverse laser centroid displacement from plasma channel axis	33
x_{ci}	Transverse laser centroid displacement from plasma channel axis at entrance plane	33
x_i	Centroid oscillation amplitude	33
ξ	Plasma wave phase velocity comoving variable, $\xi = z - v_p t$	12
Z	Ionization degree	40
Z_R	Rayleigh length	20
ζ	Light-speed comoving variable, $\zeta = z - ct$	12

Acknowledgments

I must first thank Wim Leemans, who gave me the opportunity to do this research in the first place. He originated the laser-heated capillary discharge concept and its implementation on the BELLA laser, and his scientific leadership was crucial to its success. I am grateful for his mentorship and encouragement as I embarked on this project.

I was fortunate to work closely with Tony Gonsalves during my time at BELLA center. His guidance was essential to the success of the experiments described in this dissertation, directing my efforts in the most productive directions and steering the heater project through numerous technical challenges. Every aspect of my work was improved by his involvement.

I salute the rest of the GVD boys—Joost Daniels and Jeroen van Tilborg. Joost, for leading the way on the Plasma 2 heater and teaching me how to work with big scary lasers. Jeroen, for always being excited about my fringe patterns and being available for emergency meetings at the BELLA Auxiliary Conference Center.

Experiments on a laser system like BELLA involve a lot of people, all of whom I owe gratitude for their hard work and long hours: Kei Nakamura, Lieselotte Obst-Huebl, Marlene Turner, Jianhui Bin, Kelly Swanson, and Csaba Toth. Special thanks to the intrepid interns who joined us for our high power laser campaigns: Tim de Raadt, Franco Rabec, and Rick van den Berg.

I thank my fellow graduate students, Brian Shaw, Danny Mittelberger, Joost Daniels, Kelly Swanson, Blagoje Djordjevic, Fumika Isono, and Liona Fan-Chiang for their consistent attendance at happy hours and for keeping me sane. Danny in particular has my thanks for being my indispensable student-mentor and perennial source of tasteful banter. And Kelly, for her ever-tactful words of encouragement and making those last few runs on the Plasma 2 setup feel like a party.

I wish to acknowledge Carlo Benedetti, who performed the particle-in-cell simulations with the INF&RNO code described in this dissertation. Thanks goes as well to Gennadiy Bagdasarov, Nadezhda Bobrova, Vladimir Gasilov, and their colleagues at the Keldysh Institute of Applied Mathematics RAS and elsewhere who performed the simulations with the MARPLE magnetohydrodynamics code. Special thanks goes to Stepan Bulanov for coordinating with our collaborators at the Keldysh Institute.

This work would not have been possible without the technical and moral support of the BELLA Center laser engineers, and mechanical and electrical technicians. I thank Art Magana and Joe Riley for helping me get good focal spots out of old pump lasers, and for sharing so much practical laser engineering knowledge. Special thanks to Zachary Eisentraut, Tyler Sipla, and Greg Mannino, who answered whenever I lit the beacons for emergency support on mechanical or electrical setups.

Finally, I wish to acknowledge that my graduate studies and research activities have been financially supported by the Director, Office of Science, Office of High Energy Physics, of the U.S. Department of Energy under Contract No. DE-AC02-05CH11231 as well as by the National Science Foundation, most recently under Grant No. PHY-1415596. This research

used the resources of the National Energy Research Scientific Computing Center, a DOE Office of Science User Facility.

Chapter 1

Introduction

1.1 Particle accelerators

Particle physics seeks to describe the universe in terms of the interactions of a few types of fundamental objects, continuing an enterprise that arguably began with Democritus and reached maturity when Mendeleev organized the then-known chemical elements into the periodic table. Probing structure beneath the scale of atoms, however, has relied extensively upon the strategy of colliding energetic particles with the object to be investigated. Indeed, science owes in large part the modern picture of the atom to the scattering experiments of Rutherford, in which the deflection of 5 MeV alpha particles from ^{222}Rn impinging on a gold foil revealed the concentration of positive charge in the nucleus.

Beginning with Cockcroft and Walton's demonstration of the reaction $^{7}\mathrm{Li}(p,\alpha)^{4}\mathrm{He}$ with a DC accelerator in 1932 and Ernest Lawrence's experiments with a series of cyclotrons, to which Lawrence Berkeley National Laboratory owes its existence, particle accelerators have since probed matter at the nuclear level and beyond. Throughout the twentieth century, the Standard Model of particle physics was verified by a succession of particle collider experiments, the most recent result being the discovery of the Higgs boson on 2012 at the Large Hadron Collider, a synchrotron with beam energy 6.5 tera-electronvolts (TeV) [1]. Concurrent with the progress of particle physics, accelerators have also emerged as drivers for radiation sources important in other scientific disciplines: chemistry, biology, materials science. These systems include synchrotron light sources and more recently, X-Ray free-electron lasers (FELs).

For particle physics, new measurements typically require particle beams of higher energy for two reasons. The first is that the mass energy of particles created in a collision is converted from the kinetic energy of the colliding particles, hence the discovery of new massive particles requires more energetic collisions. The second is that the de Broglie wavelength $\lambda = h/p$ of a particle, with h Planck's constant and p the particle momentum, sets the minimum length scale of structures to which the particle will be sensitive.

To reach the higher energies required to observe new physics, however, conventional RF accelerators must increase in size and therefore cost. This is because the maximum practical

energy gain per unit length or "gradient" for an RF accelerator is limited to ~ 100 MV m^{-1} by electrical breakdown [2]. For this reason, progress towards higher energies has slowed in recent decades [3, 4], and plans for future conventional particle colliders have drawn public criticism from within the physics community [5].

Accelerator-based particle physics would therefore benefit from technologies that can increase accelerating gradients, and reduce system size and cost. A promising means of generating larger accelerating gradients is to use a plasma as an accelerating medium. Specifically, if electrons are made to "surf" on a plasma wave with phase velocity $\sim c$, they may be accelerated to very high energies in short distances. This is in large part because plasma waves can support very high electric fields, which are limited only by wave breaking. In the cold nonrelativistic limit, the maximum field is

$$E_0 \ (\mathrm{GV\,m^{-1}}) \simeq 96\sqrt{n_0 \ (10^{18}\mathrm{cm^{-3}})} \ , \tag{1.1}$$

which for a plasma density of 10^{18} cm^{-3} yields a gradient 96 GV m^{-1}, three orders of magnitude greater than currently achievable in conventional accelerators. Such plasma waves can be excited by intense relativistic charged particle beams [6] or the ponderomotive force of intense laser pulses [7].

This dissertation is concerned with "laser-wakefield acceleration" (LWFA), which employs a resonant, high-intensity laser pulse to excite a plasma wave with relativistic phase velocity. LWFA requires femtosecond-scale laser pulse durations to achieve resonance with the plasma, and thus only became practical with the advent of energetic femtosecond laser sources based on chirped-pulse amplification (CPA) in the 1990s [8, 9]. Quasi-monoenergetic electron beams from LWFAs were first demonstrated at the 100 MeV level using millimeter-scale plasmas and terawatt-scale (TW) laser powers in a series of publications in 2004 [10–12]. Energies at the GeV level were attained by the end of that decade [13, 14], with the first results from petawatt (PW) lasers in 2013 yielding electron energies in the 2-3 GeV range [15, 16].

LWFA employing a waveguiding structure or "plasma channel" can provide increased energy gain by increasing the acceleration length. A plasma channel consists of a plasma with a radial density gradient that refractively confines the energy of the driver near the axis, suppressing diffraction in the same manner as a graded-index fiber optic. Research at Lawrence Berkeley National Laboratory (LBNL) has extensively pursued this approach, beginning with the production of 80 MeV electron beams in a laser-formed channel in a supersonic gas jet in 2004 [10]. Subsequent experiments at LBNL have relied on gas-filled capillary discharges, where the plasma gradient is provided by ohmic heating within a wall-stabilized arc discharge formed in a capillary tube [17]. This approach yielded 1 GeV electron beams from a 3-cm-long capillary with 50 TW of laser power in 2006 [13], and 4 GeV electron beams from a 9-cm-long capillary with 300 TW of laser power using the BELLA ("BErkeley Lab Laser Accelerator") laser.

This dissertation reports the development and demonstration of a new type of plasma channel, the laser-heated gas-filled capillary discharge. This device is a further development of the gas-filled capillary discharge where the radial plasma gradient is further enhanced

by inverse-bremsstrahlung heating by a collinear, Joule-level, nanosecond-scale laser pulse [18, 19]. The diagnostic measurements described in this thesis show that the additional control of the plasma profile via laser heating makes this structure more tunable than a conventional capillary discharge [20], and allows it to effectively guide high energy laser pulses without sustaining damage. Furthermore, acceleration of electrons to 7.8 GeV in a 20-cm-long laser-heated capillary discharge is demonstrated [21, 22]. Electron acceleration experiments relevant to staged acceleration, including demonstration of triggered injection with suppressed self-trapping are also presented [23].

1.2 Outline

The physics of laser plasma acceleration as it applies to the work in this dissertation is reviewed in Chapter 2. This includes physical principles that motivate the need for an accelerating stage providing energy gain at the 10 GeV level, as well as physics relevant to the diagnostics used in the experiments reported here. Laser guiding in plasma channels is reviewed in Chapter 3, including the rationale for development of the laser-heated gas-filled capillary discharge as a guiding structure for LWFA, and the principles governing the formation of plasma channels by laser heating.

In Chapter 4, a laser-heated capillary discharge waveguide is characterized using a spectral interferometer setup. The setup design and analysis techniques are described in detail. Variation of the plasma density and matched spot size of the waveguide with heater laser and discharge parameters is measured. Text and figures for Chapter 4 are adapted from the author's publication

[20] C. V. Pieronek et al., "Laser-heated capillary discharge waveguides as tunable structures for laser-plasma acceleration", Physics of Plasmas 27, 093101 (2020)

Chapter 5 describes in-situ diagnostic measurements of laser-heated capillary discharges on the BELLA main beamline using a two-color common path interferometer. The setup design is described, as are analysis methods where they depart from Chapter 4.

In Chapters 6 and 7, the results of LWFA experiments on the BELLA laser system are reported. In Chapter 6, guiding of 850 terawatt (TW) laser pulses in a 20-cm-long laser-heated capillary discharge is demonstrated, generating broad spectrum electron beams with quasi-monoenergetic peaks up to 7.8 GeV. This result represents a record for single-stage energy gain in a laser-wakefield accelerator. Diagnostic measurements of the plasma channel employing high power laser pulses are presented as well. The BELLA laser system and diagnostics are outlined as relevant to this chapter and Chapter 7 Figures for Chapter 6 are adapted from the author's coauthored publications

[21] A. J. Gonsalves et al., "Petawatt Laser Guiding and Electron Beam Acceleration to 8 GeV in a Laser-Heated Capillary Discharge Waveguide", Physical Review Letters 122, 084801 (2019)

[22] A. J. Gonsalves et al., "Laser-heated capillary discharge plasma waveguides for electron acceleration to 8 GeV", Physics of Plasmas 27, 053102 (2020)

In Chapter 7, trapping of electron bunches through field ionization by the driver pulse is demonstrated in a laser-heated capillary discharge. Suppression of self-trapping is demonstrated as well. These experiments were performed at 16 J laser pulse energy, less than half the maximum pulse energy of the BELLA laser system, and are thus relevant for future two-beam experiments that include demonstration of staged acceleration in two 5 GeV stages[24] and tests of strong field quantum electrodynamics [25]. Figures and text are taken from the author's working paper

[23] C. V. Pieronek et al., "Ionization injection and dark-current suppression in a 20-cm-long channel-guided laser-plasma accelerator" (in preparation)

Finally, results are summarized in Chapter 8, with potential directions for future research.

Chapter 2

Laser wakefield acceleration

2.1 Introduction

The purpose of this chapter is to outline the theoretical considerations that inform the work of this dissertation. Laser wakefield acceleration is a large and rapidly growing field of research, and a comprehensive review is neither possible nor desirable here. As such, only those results most directly relevant to the work described later are considered. Most of this material is derived from Ref. [2], which reviews laser-driven plasma electron accelerators in detail.

Lasers are an attractive source of high fields for charged particle acceleration. The main difficulty encountered in developing high fields in accelerators is mitigating interaction of the fields with the materials of which the accelerating structures are constituted, specifically, suppressing various forms of electrical breakdown. The short wavelength of optical radiation, however, allows electromagnetic energy to be focused to high densities far from material surfaces where breakdown occurs. Imparting a net energy to charged particles with laser radiation in free space is difficult, due to the rapid oscillation period of optical radiation, as well as the vacuum phase velocity c. In fact, the Lawson-Woodward theorem [26, 27] states in certain conditions that phase-slippage of particles interacting with an electromagnetic wave renders net energy gain impossible. The Lawson-Woodward theorem assumes the following conditions, one or more of which must be violated in order for particles to gain energy from an electromagnetic wave:

1. The interaction region is infinite
2. The laser fields are in vacuum with no boundaries
3. Particle velocity is highly relativistic, i.e. $v \sim c$
4. No static electric or magnetic fields are present
5. Nonlinear effects, e.g. the ponderomotive force, are negligible

One means of overcoming the Lawson-Woodward theorem is to violate condition 2, and introduce a plasma as an interaction medium. The plasma acts to "rectify" the rapidly oscillating transverse field of the laser into a more slowly oscillating longitudinal field useful for accelerating particles, as was first recognized by Tajima and Dawson in 1979 [7].

Plasma waves are an appealing means of accelerating particles. First, they are longitudinal waves, and capable of accelerating appropriately-phased particles continuously along their direction of propagation. Second, plasma waves can support extremely high electric fields. A cold, unmagnetized plasma supports a longitudinal electrostatic wave mode with dispersion relation

$$\omega_p = \left(\frac{4\pi n_0 q_e^2}{m_e} \right)^{1/2} , \tag{2.1}$$

with n_0 the unperturbed plasma density, q_e the electron charge, and m_e the electron mass. This is the well-known plasma or Langmuir oscillation. One physical interpretation of the plasma oscillation is that if the electrons within a "slab" of plasma are displaced, they will oscillate about an equilibrium position with a characteristic frequency ω_p.

As stated previously, the plasma oscillation dispersion relation [Eqn. 2.1] lacks any dependence on wavenumber k. This is a peculiar feature for a dispersion relation, and implies that the wavenumber and phase velocity can take on any value. This is indeed the case, with the plasma wave phase velocity $v_p = \omega_p/k$ set by the characteristic velocity of the excitation mechanism. For accelerator applications, this mechanism is either an intense laser pulse or ultrarelativistic charged particle beam with velocity $\sim c$, in which case $v_p \sim c$. Because of this, the plasma wavenumber k_p is defined $k_p = \omega_p/c$. The corresponding plasma wavelength $\lambda_p = 2\pi/k_p$ is a convenient quantity for characterizing plasma properties, and is expressed in terms of practical units

$$\lambda_p(\mu\mathrm{m}) = 33\sqrt{1 \times 10^{18}/n_0(\mathrm{cm}^{-3})} . \tag{2.2}$$

The principle limit on the electric field of a plasma wave is wave breaking, which occurs when the plasma fluid velocity associated with the wave matches the phase velocity of the wave. In the cold, nonrelativistic case, wave breaking occurs for a maximum electric field [28]

$$E_0 = \frac{c m_e \omega_p}{q_e} \text{ or } E_0(\mathrm{V\,m}^{-1}) \simeq 96\sqrt{n_0(\mathrm{cm}^{-3})} . \tag{2.3}$$

Relativistic effects suppress wave breaking, with the cold relativistic [29, 30] wave breaking field given by

$$E_{\mathrm{WB}} = \sqrt{2}(\gamma_p - 1)^{1/2} E_0 , \tag{2.4}$$

with $\gamma_p = (1 - {\beta_p}^2)^{-1/2}$ the relativistic factor associated with the plasma wave phase velocity, and $\beta_p = v_p/c$.

The laser ponderomotive force is the mechanism by which laser-driven plasma waves are excited. The ponderomotive force is an ambipolar force exerted by oscillating fields on charges in the direction opposite the gradient in electromagnetic energy density. The fundamental mechanism at work is the small, but nonzero distance sampled by a particle during its leading

order motion, the "quiver" at the field oscillation frequency ω. One half-cycle of the quiver motion will move a particle against the gradient in field amplitude, and the following half-cycle will not return the particle to its initial position. Rather it, will be slightly displaced in the direction opposite the gradient in the field energy density, since on the "return" half-cycle it experiences a lower average force. For weak fields, the time-averaged force associated with this process can be derived from the nonrelativistic Lorentz force equation assuming a weak gradient in the field to obtain [31]

$$\mathbf{F}_P = \frac{-q^2}{m\omega^2}\nabla(|\mathbf{E}|^2/2) \ , \tag{2.5}$$

with q the charge, m the mass, and ω the frequency of the field. An important feature of the ponderomotive force is the m^{-1} scaling. Electrons in a hydrogen plasma experience a ponderomotive force greater than the ions by a factor of the mass ratio $m_p/m_e \sim 2 \times 10^3$, with m_p the proton mass and m_e the electron mass. Thus, ion motion can in many cases of interest be neglected in a LWFA, and the ions regarded as constituting a stationary neutralizing background.

Because it is a component of the canonical momentum of a charged particle in an electromagnetic field, it is convenient to express the ponderomotive force in terms of the vector potential $\mathbf{A}$, which is related to the electric and magnetic fields according to $\mathbf{E} = -c^{-1}\partial\mathbf{A}/\partial t$ and $\mathbf{B} = \nabla \times \mathbf{A}$. Eqn. 2.5 can then be rewritten

$$\mathbf{F}_p = -m_e c^2 \nabla(a^2/2) \ , \tag{2.6}$$

with $\mathbf{a} = q_e\mathbf{A}/m_e c^2$ the normalized vector potential or "laser strength parameter," and q_e the elementary charge.

The linear expression for the ponderomotive force Eqn. 2.6 is only valid for $a \ll 1$. However, $a \sim 1$ in typical laser wakefield accelerators, corresponding to a peak intensity $\sim 10^{18}$ W/cm^2. Such laser intensities are referred to as "relativistically intense," because the electron quiver velocity approaches the speed of light. This is evident from the canonical momentum of a charged particle in an electromagnetic field [32]

$$\mathbf{P} = \mathbf{u} - \mathbf{a} = 0 \ , \tag{2.7}$$

with $\mathbf{u} = \gamma\boldsymbol{\beta}$ the normalized relativistic mechanical momentum, $\gamma = (1-\beta^2)^{-1/2}$ the relativistic factor, $\boldsymbol{\beta} = \boldsymbol{v}/c$ the normalized velocity. $\mathbf{P} = 0$ in all cases of interest, which in involve the interaction of laser pulse of finite duration interacting with an electron initially at rest. Eqn. 2.7 is a consequence of assuming a laser field that is uniform in the transverse directions and follows directly from the Euler-Lagrange equations: $\partial L/\partial x_{\perp,i} = 0 \Rightarrow \partial L/\partial \dot{x}_{\perp,i} =$ constant, with L the Lagrangian for a charged particle in an electromagnetic field [32]. This is approximately true for a laser pulse of finite size as long as the quiver motion samples only small portion of the laser spot. Due to the finite speed of light, the characteristic size of the electron quiver motion is limited to $< \lambda/2$ and hence Eqn. 2.7 holds for $\lambda/2 \ll r_0$ with r_0 the laser spot size.

It is clear from Eqn. 2.7 that the motion becomes relativistic for $a \sim 1$, and effects neglected in the derivation of Eqns. 2.5 and 2.6 become important, such as the v $\times$ B force and the relativistic mass. In this situation, the nonlinear or relativistic ponderomotive force then becomes [2, 33]

$$\mathbf{F}_{pN} = -m_e c^2 \nabla \gamma \ . \tag{2.8}$$

The most straightforward method of exciting plasma waves for acceleration is through the use of a single resonant, relativistically intense laser pulse with duration $\sim \lambda_p/2c$. This is the so-called "standard" LWFA, and is the approach used in the research presented in this dissertation. For typical plasma densities 10^{17}-10^{19} cm^3, this requires laser pulse lengths of order 50-150 fs. Producing energetic laser pulses with this duration is technically demanding for a number of reasons, including the requirement for large gain bandwidths and mitigation of deleterious nonlinear optical phenomena arising from the required intensities, and only became practical with the development of Ti:Sapphire chirped-pulse amplification (CPA) laser sources in the late 20$^{\text{th}}$ century [8, 9, 34, 35]. Indeed, progress on standard LWFA has closely tracked with the technical development of (CPA) laser systems. At the time of writing, commercially available Ti:Sapphire CPA systems can produce Joule-level pulses with < 30 fs duration at repetition rates of 10 Hz.

Other schemes exist for exciting plasma waves for acceleration with intense laser beams. Plasma-beat-wave acceleration (PBWA) relies on a long laser pulse containing two copropagating frequencies separated by a ω_p. This introduces a modulation in the laser pulse envelope at the beat frequency ω_p, which will resonantly excite a plasma wave on a timescale many times larger than the plasma period. PBWA was primarily pursued before femtosecond laser sources were widely available, however the concept continues to be implemented in the form of resonant trains of femtosecond pulses, each with duration $\sim \lambda_p/2c$ and separated by intervals of λ_p/c. Self-modulated laser wakefield acceleration (SMLWFA) operates similarly to PBWA, however the resonant modulation of the laser pulse is supplied by nonlinear interaction with the plasma itself via forward Raman scattering.

2.2 A simple kinematic picture of laser wakefield acceleration

It is instructive to consider the operation of a laser-plasma accelerator from a purely kinematic perspective. Here, it is assumed that the plasma wave is transversely infinite in extent and non-evolving. Hence, accelerated electrons interacting with the plasma wave are subjected to a conservative field associated with the electrostatic potential of the plasma wave. The maximum energy of the accelerated electrons can be estimated using relativistic velocity addition. In the rest frame of a plasma wave with phase velocity v_p, an electron at rest in the lab frame approaches at velocity $-v_p$. By definition, a trapped electron will be slowed to zero velocity by the wave potential, and will eventually rebound with final velocity v_p according to the conservation of energy if it is allowed to completely outrun the plasma wave. Thus,

in the lab frame the final velocity of v of such an electron is given by adding the lab frame plasma wave velocity v_p and wave frame electron velocity v_p relativistically:

$$v = \frac{2v_p}{1 + v_p^2/c^2} \ . \tag{2.9}$$

With $\beta \equiv v/c$ and $\gamma \equiv (1-\beta^2)^{-1/2}$, squaring both sides of Eqn. 2.9 yields an equation for the final electron energy

$$1 - \gamma^{-2} = \frac{4(1-\gamma_p^{-2})}{(2-\gamma_p^{-2})^2} \tag{2.10}$$

with solution

$$\gamma = 2\gamma_p^2 - 1 \ . \tag{2.11}$$

From Eqn. 2.11, it is clear that the relativistic energy γ of an electron after interacting with a plasma wave is much greater than the relativistic factor γ_p associated with the phase velocity of the plasma wave itself. For laser-driven plasma waves in the linear limit, the wave phase velocity is simply the laser group velocity $v_g = c(1-\omega_p^2/\omega^2)^{1/2}$, for which the associated relativistic factor γ_p is

$$\gamma_p = \left(1 - \frac{v_g^2}{c^2}\right)^{-1/2} = \frac{\omega}{\omega_p} \ . \tag{2.12}$$

For commonly used laser drivers with $\lambda \simeq 1$ µm and typical plasma densities for LWFA $10^{17} - 10^{19}$ cm^{-3}, $\gamma_p \sim 10 - 100$. Hence, one might expect electron energy gains to be limited to the 50 MeV level based on γ_p alone. However, accounting for the fact that acceleration proceeds similarly to a *collision* with an object having γ_p as in the derivation of Eqn. 2.11, it is clear that electrons can be accelerated to ultrarelativistic energies by interacting with a plasma wave with a "modest" γ_p.

The preceding discussion, though suggestive, is a considerable oversimplification. Specifically, one will note the absence of any field or potential amplitudes in Eqn. 2.11. This is because that equation was derived with the assumption that electrons are allowed to fully outrun the wake after interaction. In practice, LWFAs are designed such that accelerated electrons are extracted at the maximum of the wake potential. This both maximizes the kinetic energy of the accelerated electrons and ensures that they are focused by the transverse fields of the wake for the duration of the interaction. The maximum energy gain in this situation can be derived through a straightforward use of special relativity, again assuming non-evolving plasma wave fields as in the derivation of Eqn. 2.11. Adopting the convention that the plasma wave propagates in the positive x direction (denoted index 1) and using the Coulomb gauge, the lab-frame four-potential

$$A^\alpha \equiv (\Phi, \boldsymbol{A}) \ , \tag{2.13}$$

with $\mathbf{A}$ and Φ the vector and scalar potentials respectively, transforms into the rest frame of the wake according to

$$A'^\alpha = \Lambda^\alpha_\beta A^\beta \tag{2.14}$$

with the Lorentz transformation

$$\Lambda^{\alpha}_{\beta} = \begin{pmatrix} \gamma_p & -\beta_p\gamma_p & 0 & 0 \\ -\beta_p\gamma_p & \gamma_p & 0 & 0 \\ 0 & 0 & 1 & 0 \\ 0 & 0 & 0 & 1 \end{pmatrix}. \tag{2.15}$$

The final lab-frame four-momentum $(E/c, \tilde{\mathbf{p}})$ of an electron trapped in the plasma wave can be calculated in terms of the transformed potential, $\Phi' = \gamma_p\Phi - \beta_p\gamma_p A_1$. Neglecting the rotational currents associated with the plasma wave and taking $A_1 = 0$ (equivalent to assuming that the driving laser beam waist is large compared to λ_p) for the sake of simplicity, this reduces to $\Phi' = \gamma_p\Phi$. In the wake frame, the final energy and momentum of an electron at the maximum of the wake potential is then given by,

$$E' = q_e\gamma_p\Phi_{\max} + \gamma_p mc^2 \tag{2.16}$$

$$\tilde{p}'_1 = mc[(E'/mc^2)^2 - 1]^{1/2}, \tag{2.17}$$

with the second term of Eqn. 2.16 accounting for the fact that electrons at rest in the lab frame approach the wake with velocity $-v_p$ at zero potential ($\Phi' = 0$) in the wake frame. The lab-frame energy E is found by Lorentz-transforming the wake-frame four-momentum $(E'/c, \tilde{\mathbf{p}}')$

$$E/c = \gamma_p E'/c + \beta_p\gamma_p\tilde{p}'_1$$

$$E = \gamma_p(\gamma_p q_e\Phi_{\max} + \gamma_p mc^2) + \beta_p\gamma_p mc^2\left[\left(\frac{\gamma_p q_e\Phi_{\max} + \gamma_p mc^2}{mc^2}\right)^2 - 1\right]^{1/2}. \tag{2.18}$$

In the ultrarelativistic limit $\gamma_p \to \infty$, $\beta_p \to 1$, Eqn. 2.18 can be rearranged to obtain the lab-frame relativistic factor for the accelerated electrons

$$\gamma = 2\gamma_p^2(\phi_{\max} + 1), \tag{2.19}$$

with $\phi \equiv q_e\Phi/mc^2$ the normalized potential. As will be discussed later in this chapter, the normalized potential ϕ is a function of laser power and pulse length and is typically $\lesssim 10$, and in the experiments considered in this thesis $\phi \simeq 1 - 3$.

This is an interesting result, which illustrates some important features of electron acceleration in plasma waves with no analysis of plasma waves themselves. Clearly, the wake phase velocity is the most sensitive parameter for maximum energy gain, through the γ_p^2 dependence of Eqn. 2.19. Wake phase velocity is in turn a function of plasma density, and in the linear limit obeys $\gamma_p = \omega/\omega_p$, causing the energy gain [Eqn. 2.19] to scale roughly as n_0^{-1}. Therefore, achieving high single stage energy gain in a laser wakefield accelerator is in large part a matter of operating at the lowest plasma density permitted by other constraints of the accelerator design.

What has been derived here in Eqn. 2.19 is an expression for the "dephasing-limited" energy gain, that is, the maximum energy attainable before a particle outruns the accelerating phase of the plasma wave. In the interest of clarifying the fundamental physics involved in accelerating electrons in a plasma wave, other important physical processes have been neglected or simplified. Specifically, it was assumed that the laser pulse is non-evolving during acceleration, and it was assumed that the laser pulse propagates as in a linear medium. Moreover, the mechanism by which electrons initially at rest are trapped and accelerated to the phase velocity of the plasma wave was not discussed. These other processes will be addressed in the following sections of this chapter.

2.3 Excitation of large-amplitude plasma waves by intense, ultrashort laser pulses

In this section, the fundamental equations of electrodynamics with which laser-plasma interactions are analyzed are introduced. The basic theory of 1D, nonlinear plasma waves derived from these fundamental equations will be presented, following the treatment in Ref. [2]. Although LWFA is a fully 3D process in all regimes of interest, useful insight into the relationship between laser and plasma parameters and accelerator performance can be gained from the analytically tractable model presented here.

The fields of both the laser and plasma wave are governed by Maxwell's equations. For the present analysis, these are most usefully expressed in terms of the potentials $\mathbf{E} = -\nabla\Phi - c^{-1}\partial\mathbf{A}/\partial t$ and $\mathbf{B} = \nabla\times\mathbf{A}$ as the inhomogeneous wave equation and Poisson equation in the Coulomb or transverse gauge such that $\nabla\cdot\mathbf{A} = 0$:

$$\nabla^2\mathbf{A} - \frac{1}{c^2}\frac{\partial^2\mathbf{A}}{\partial t^2} - \nabla\left(\frac{1}{c^2}\frac{\partial\Phi}{\partial t}\right) = -\frac{4\pi}{c}\mathbf{J} \tag{2.20}$$

$$\nabla^2\Phi = -4\pi\tilde{\rho} \tag{2.21}$$

with $\mathbf{J}$ the current density and $\tilde{\rho}$ the charge density. Fluid motion is governed by the cold plasma fluid equations, since the electron temperature $T_e \sim 10$ eV typical of the field-ionized plasmas encountered in LWFA [36, 37] is much less than the quiver energy and fluid pressure can be neglected:

$$\frac{\partial\tilde{\mathbf{p}}}{\partial t} + (\mathbf{v}\cdot\nabla)\tilde{\mathbf{p}} = -q_e\left(\mathbf{E} + \frac{\mathbf{v}}{c}\times\mathbf{B}\right) \tag{2.22}$$

$$\frac{\partial n}{\partial t} + \nabla\cdot(n\mathbf{v}) = 0\ , \tag{2.23}$$

with $\mathbf{v}$ the electron fluid velocity, n the electron density, and $\tilde{\mathbf{p}} = \gamma m_e\mathbf{v}$ the relativistic fluid momentum. Two useful simplifications can be applied to the wave equation Eqn. 2.20. First, the potential term $\nabla(c^{-2}\partial\Phi/\partial t)$, which contains the fast $\Phi \sim e^{i\omega t}$ part of the electrostatic potential, is typically negligible compared to other sources of the fast part of the plasma

current [2]. Second, the current $\mathbf{J}$ is well approximated by the leading-order quiver motion of the electrons in the typical case $\lambda/2 \ll r_0$, such that $\mathbf{J} = -q_e n c \mathbf{a}/\gamma$ by momentum conservation [Eqn. 2.7] and hence the wave equation becomes

$$\nabla^2 \mathbf{A} - \frac{1}{c^2}\frac{\partial^2 \mathbf{A}}{\partial t^2} = k_p^2 \rho \mathbf{A} \ , \tag{2.24}$$

with n_0 the unperturbed plasma density and $\rho = \gamma^{-1}(n/n_0)$ the normalized proper electron density.

The set of equations Eqns. 2.20-2.24 are difficult to solve analytically, and fully self-consistent treatment of a relativistic laser pulse propagating in a plasma is typically approached computationally. However, useful physical insight can be gained through analysis of these equations if simplifications are applied, the most straightforward of which is to restrict the problem to one dimension, effectively assuming a transversely infinite plane wave driver pulse.

In 1D, symmetries of the plasma fluid equations in the quasi-static approximation impose the relations [2]

$$\mathbf{u}_\perp - \mathbf{a}_\perp = 0 \ , \tag{2.25}$$

$$\gamma - \beta_p u_z - \phi = 1 \ , \tag{2.26}$$

$$n(\beta_p - \beta_z) = \beta_p n_0 \ , \tag{2.27}$$

with $\mathbf{u}_\perp = \tilde{\mathbf{p}}_\perp / m_e c = \gamma \boldsymbol{\beta}_\perp$ the normalized transverse momentum and n_0 the initial unperturbed plasma density. Using Eqns. 2.25-2.27 and taking the limit $\gamma_p \gg 1$ which applies to nearly all situations of interest for LWFA, the wave equation and Poisson equation can be written [38, 39]

$$k_p^{-2}\left(2\frac{\partial}{\partial \zeta} - \frac{\partial}{\partial \tau}\right)\frac{\partial \mathbf{a}}{\partial \tau} = \rho \mathbf{a} \tag{2.28}$$

$$k_p^{-2}\frac{\partial^2 \phi}{\partial \xi^2} = \frac{(1+a^2)}{2(1+\phi)^2} - \frac{1}{2} \ , \tag{2.29}$$

The evolution of the driving laser pulse is described by Eqn. 2.28 and the evolution of the plasma wave is described by Eqn. 2.29, with the respective algebraic transformations $\zeta = z - ct$, $\tau = ct$ and $\xi = z - v_p t$ applied. The differing comoving velocities are required by the structure of the Coulomb-gauge potential equations, as c is fundamental to the wave equation and subluminal group velocities enter through the evolution terms $\partial/\partial\tau$. These equations can be regarded as decoupled from each other, as the laser driver evolves on a much larger timescale than a plasma period: $T_{ev} \sim 2\gamma |n_0/n| (\omega/\omega_p)/\omega_p \ll \omega_p^{-1}$ [38]. Hence, Eqn. 2.29 will be the subject of this chapter. Eqn. 2.28 will be addressed in Section 2.4 in the context of driver pulse energy depletion and spectral shifting.

Using Eqns. 2.25-2.27, the plasma fluid quantities below can be obtained

$$n/n_0 = \frac{\gamma_\perp^2 + (1+\phi)^2}{2(1+\phi)^2} \ , \tag{2.30}$$

$$u_z = \frac{\gamma_\perp^2 - (1+\phi)^2}{2(1+\phi)} \ , \tag{2.31}$$

$$\gamma = \frac{\gamma_\perp^2 + (1+\phi)^2}{2(1+\phi)} \ , \tag{2.32}$$

with $\gamma_\perp \equiv 1 + \mathbf{u}_\perp^2 = 1 + a^2$.

As a nonlinear, second-order differential equation, Eqn. 2.29 is difficult to solve analytically for general forms of $a(\xi)$. It can be solved readily with a numerical integrator, as has been done in Fig. 2.1. For high laser driver intensities with $a \sim 1$, the resulting plasma waves are visibly nonlinear, departing from the sinusoidal structure assumed in the derivation of the plasma frequency in Section 2.1 and acquiring the sawtooth profile characteristic of nonlinear wave steepening.

Electrons can only be accelerated in regions of the wake where not only $-q_e\partial\phi/\partial\xi < 0$, but also where the transverse forces in the wake are focusing. Focusing forces are inherently 3D, and arise from the finite transverse extent of the wake potential and the longitudinal current, which produce a radial electric field and azimuthal magnetic field that can focus appropriately phased particles. Analysis of plasma waves in the linear limit using the Panofsky-Wentzel theorem shows that trapping and focusing occurs in a region of length $k_p\xi = \pi/4$ such that $-q_e\partial\phi/\partial\xi < 0$ and $-q_e\phi < 0$ [2]. A simple analytical treatment is not possible for the nonlinear case, but the focusing region still roughly corresponds to $-q_e\partial\phi/\partial\xi < 0$ and $-q_e\phi < 0$. Conversely, for positrons, the accelerating and focusing region is defined by the condition $q_e\partial\phi/\partial\xi < 0$ and $q_e\phi < 0$. This is problematic for positron acceleration in highly nonlinear plasma waves, because these focusing regions become increasingly narrow as the wave amplitude increases due to nonlinear steepening. It is for this reason that weakly nonlinear plasma waves driven with peak laser fields $a \sim$ 1-2 are favored for electron-positron collider applications [40].

A number of useful analytical results have nevertheless been obtained from Eqn. 2.29 for square laser pulse profiles, in which case Eqn. 2.29 can be solved in terms of elliptic integrals [38, 39, 41, 42]. These are useful for understanding scalings of laser wakefield accelerator performance with respect to driver laser and plasma parameters, and qualitative aspects of plasma wave excitation. Of particular concern are the dependence of the wake field amplitudes ϕ and E on a, as well as the nonlinear plasma wavelength λ_{Np}. For a resonant, square laser pulse of length $L \simeq \lambda_{Np}$, the maximum wake electric field is

$$\hat{E}_{\max} = \frac{a_0^2/2}{(1 + a_0^2/2)^{1/2}} \tag{2.33}$$

and the minimum and maximum electrical potential in the wake are given by [30]

$$\phi_m = \hat{E}_{\max}^2/2 \pm \beta_p[(1 + \hat{E}_{\max}^2/2)^2 - 1]^{1/2} \ , \tag{2.34}$$

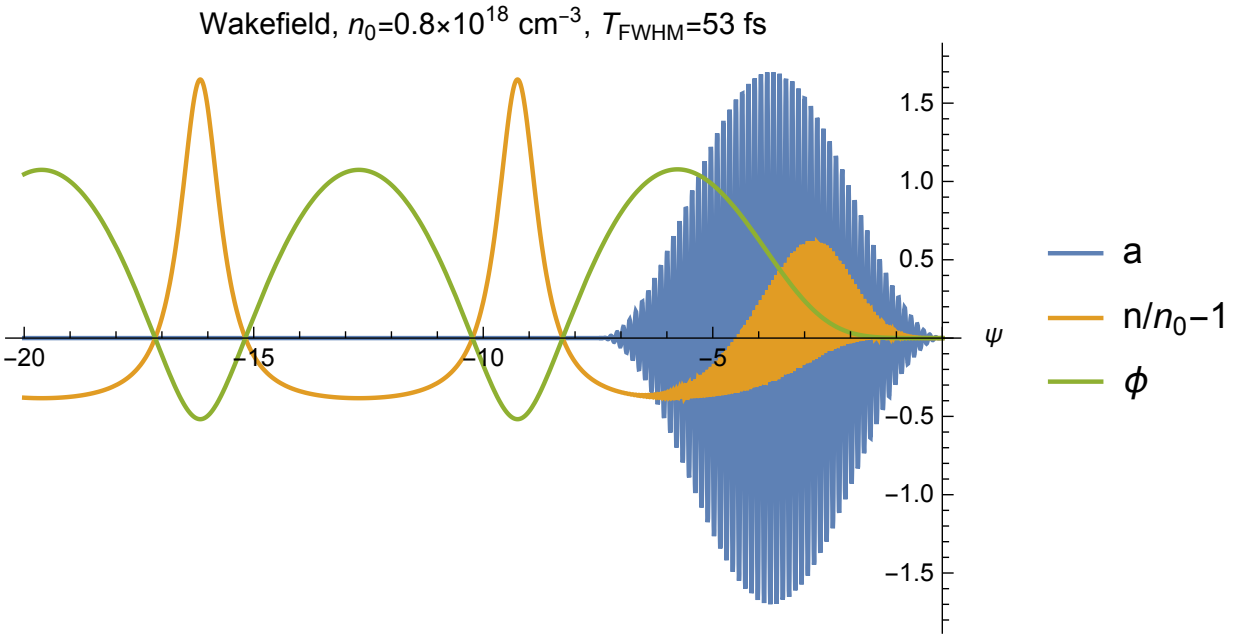

Figure 2.1: Solution of Eqn. 2.29 for a laser pulse with $a_0 = 1.7$, plotted with respect to the comoving wake phase $\psi = k_p\xi$. Normalized residual electron density $n/n_0 - 1$ calculated from Eqns. 2.30-2.32.

with $\hat{E} \equiv E/E_0$. The nonlinear plasma wavelength can be expressed in terms of Elliptic integrals[38, 39, 41, 42] by solving Eqn. 2.29 in quadrature for $a = 0$:

$$\lambda_{Np} = (2/\pi)\lambda_p(1+\phi_{\max})^{1/2}E_2(\varrho)\ , \tag{2.35}$$

with

$$E_2(\varrho) = \int_0^{\pi/2} \mathrm{d}\theta(1-\varrho^2\sin^2\theta)^{1/2} \tag{2.36}$$

the complete elliptic integral of the second kind and $\varrho^2 = 1-(1+\phi_{\max})^{-2}$. Eqn. 2.35 has the limiting values

$$\lambda_{Np} = \lambda_p \begin{cases} 1+3\hat{E}_{\max}^2/16 & \text{for } \hat{E}_{\max} \ll 1 \\ (2/\pi)(\hat{E}_{\max}+\hat{E}_{\max}^{-1}) & \text{for } \hat{E}_{\max} \gg 1 \end{cases}\ . \tag{2.37}$$

Lengthening of the nonlinear plasma wavelength is an important process in a LWFA. Through the nonlinear dependence of the plasma wavelength on a, evolution of the driving laser pulse can shift the phase of a trapped bunch in the wake. This can result in loss of the bunch if it is moved into the defocusing region of the wake, roughly corresponding to the density spikes in Fig. 2.1. Alternatively, lengthening of the plasma period can increase the acceleration length and hence the final bunch energy by increasing the length of the accelerating region of the wake, in which case a trapped electron bunch will take longer to outrun the wake.

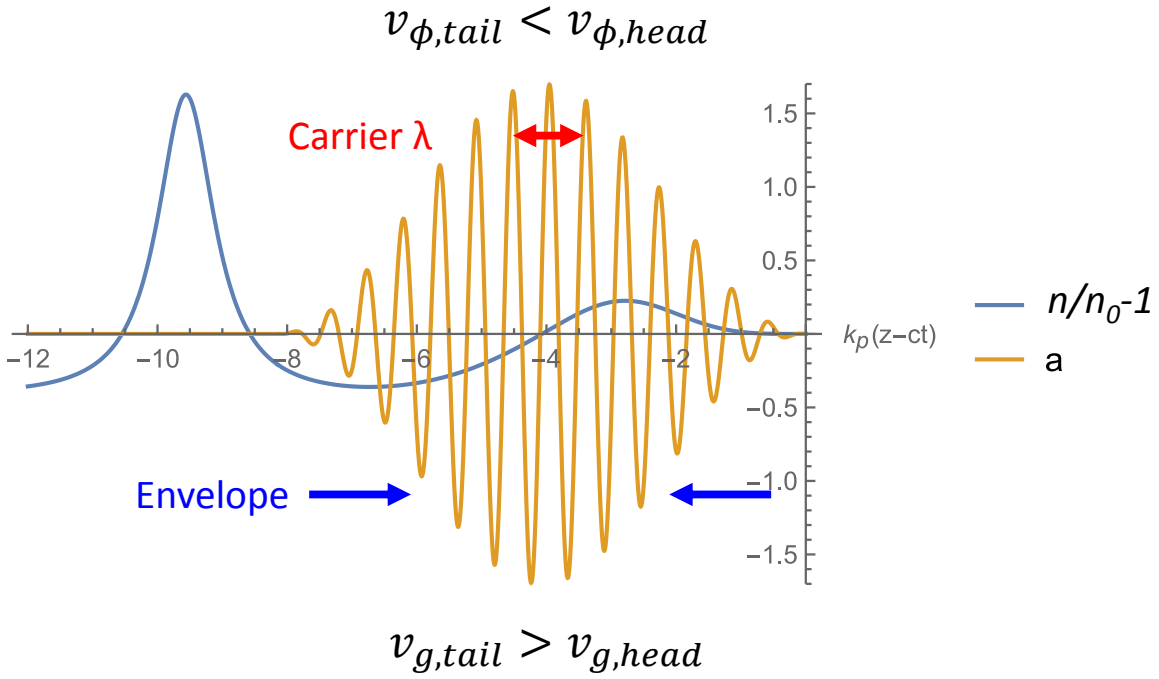

Figure 2.2: Density gradient within a relativistically intense laser pulse exciting a plasma wave. The resulting gradients in local phase velocity and group velocity result in redshifting of the carrier frequency and self-steepening of the pulse envelope.

2.4 Spectral shifts, self-steepening, and pump depletion

Excitation of a plasma wave depletes the energy of the driving laser pulse, as energy is transferred to the plasma wave. However, both the frequency and shape of the pulse are modified as well, due to the local gradient of the plasma density within the driver pulse. This process is shown schematically in Fig. 2.2. For most locations within the pulse, $\partial n/\partial(k_p\zeta) > 0$. This creates a positive gradient in the local phase velocity, and a negative gradient in the local group velocity. Respectively, this in turn results in "stretching" of the laser cycles, "redshifting," and compression of the pulse envelope, "self-steepening." All of these processes are correlated with depletion of the pulse energy and the structure of the driven plasma wave, and hence laser redshifting is an important diagnostic for LWFA [2, 43].

The frequency shift induced by the ponderomotively-driven plasma gradient within an intense laser pulse can be derived from Eqn. 2.28. The proper density ρ is taken as a known function, obtained from the solution of Eqn. 2.29 and evolving on a timescale $\gg \omega_p^{-1}$. Note that with this approximation, Eqn. 2.28 effectively becomes a linear homogeneous equation in $\mathbf{a}$. The driver pulse is represented as a slowly varying envelope with phase factor: $a(\zeta,\tau) = \hat{a}(\zeta)\exp[i\Psi(\zeta,\tau)]$, with $a(\zeta,\tau)$ slowly varying compared to the laser period.

Substituting this representation of $a(\zeta,\tau)$ into Eqn. 2.28 and taking the approximation of a smooth, slowly evolving envelope such that $|\partial\hat{a}/\partial\tau| \ll |\partial\Psi/\partial\tau|$ and $|\partial\hat{a}/\partial\zeta| \ll |\partial\Psi/\partial\zeta|$, the following equation for the evolution of the local temporal phase $\Psi(\zeta,\tau)$ within the pulse is obtained [44]:

$$-\left(\frac{\partial\Psi}{\partial\zeta}\right)\left(\frac{\partial\Psi}{\partial\tau}\right)+i\frac{\partial^2\Psi}{\partial\zeta\partial\tau}=\frac{1}{2}k_p^2\rho(\zeta)\ . \tag{2.38}$$

This equation can be solved analytically assuming a solution of the form

$$\Psi(\zeta,\tau)=k(\tau)\zeta+\Theta(\tau)\ , \tag{2.39}$$

which is equivalent to restricting the problem to the local phase in a neighborhood of few wavelengths about an arbitrary point ζ in the pulse. Substituting Eqn. 2.39 into Eqn. 2.38 yields

$$-k(\tau)k'(\tau)\zeta-k(\tau)\Theta'(\tau)+ik'(\tau)=(1/2)k_p^2\rho(\zeta)\ , \tag{2.40}$$

with primes denoting derivatives with respect to τ. The above can be reduced to an ordinary differential equation for a single function $k(\tau)$ by taking the partial derivative $\partial/\partial\zeta$ of both sides. The equation for the evolution of the local wavenumber is then

$$[k^2(\tau)]'=-k_p^2\frac{\partial\rho}{\partial\zeta}\ , \tag{2.41}$$

which has the solution

$$\frac{k(\tau)}{k(0)}=\left(1-\frac{k_p^2}{k(0)^2}\int_0^\tau \mathrm{d}\tau\frac{\partial\rho}{\partial\zeta}\right)^{1/2}\ . \tag{2.42}$$

Using the identities Eqns. 2.30-2.32, this can be rewritten in terms of the potential ϕ

$$\frac{k(\tau)}{k(0)}=\left(1-\frac{k_p^2}{k(0)^2}\int_0^\tau \mathrm{d}\tau\frac{\partial}{\partial\zeta}[(1+\phi)^{-1}]\right)^{1/2}\ . \tag{2.43}$$

From Eqns. 2.42 and 2.43, it is clear that the density gradients of a plasma wave induce frequency shifts in laser pulses. Depending on the wake phase, this can either result in an increase in frequency, "blueshift," or decrease in frequency, "redshift." Laser pulses driving plasma waves will be redshifted according to plasma density, wake amplitude, and propagation distance. Moreover, the local frequency shift within a laser pulse depends on which part of the wake is sampled, with the most redshifted frequencies corresponding to the laser energy in the tail of the pulse that sampled the deepest parts of the wake.

Excitation of a plasma wave depletes the energy of the driver pulse. This "pump depletion" process is one of the two primary limits on acceleration length and thus energy gain in a LWFA. The rate of energy depletion can be derived from energy conservation, with the energy extracted from the pulse given by the work done by the fields on the plasma [32]:

$$\frac{\mathrm{d}U}{\mathrm{d}t}=\int \mathbf{E}\cdot\mathbf{J}\ \mathrm{d}\zeta \tag{2.44}$$

In terms of the vector potential and plasma current per Section 2.3

$$\mathbf{E}\cdot\mathbf{J} = \frac{k_p^2}{4\pi}\rho\mathbf{A}\cdot\frac{\partial\mathbf{A}}{\partial t} = \frac{k_p^2}{8\pi}\rho\frac{\partial|\mathbf{A}|^2}{\partial t} \tag{2.45}$$

Once again representing the laser pulse as a complex envelope with a phase factor

$$\mathbf{a} = \frac{1}{2}\hat{a}(\zeta,\tau)\exp(ik_0\zeta)\hat{\mathbf{e}}_\perp + \text{c.c.}\ , \tag{2.46}$$

with k_0 the initial center wavenumber. As in the discussion of frequency shifts, slow variation of the laser pulse envelope is assumed such that $|\partial\hat{a}/\partial\tau| \ll |\partial\hat{a}/\partial\zeta|$. With the preceding relations, transforming to the comoving variables ζ,τ, and transforming to the envelope averaged normalized vector potential [Eqn. 2.46], the evolution of the laser pulse energy can be written

$$\frac{\mathrm{d}U}{\mathrm{d}\tau} = \frac{E_0^2}{16\pi}\int\rho\frac{\partial|\hat{a}|^2}{\partial\zeta}\mathrm{d}\zeta = -\frac{E_0^2}{16\pi}\int|\hat{a}|^2\frac{\partial\rho}{\partial\zeta}\mathrm{d}\zeta \tag{2.47}$$

Within the laser pulse, $\partial\rho/\partial\zeta > 0$, and the pulse energy depletes. Eqn. 2.29 can be used to express Eqn. 2.47 in terms of plasma wave amplitude. Eqn. 2.29 can solved for $|\hat{a}|$, and it possesses a first integral for $\hat{a} = 0$ (outside the laser pulse). These are written, respectively [2, 45, 46]:

$$|\hat{a}|^2\frac{\partial\rho}{\partial\zeta} = -2\frac{\partial}{\partial\zeta}\left[1+\phi+(1+\phi)^{-1}+k_p^{-2}\left(\frac{\partial\phi}{\partial\zeta}\right)^2\right] \tag{2.48}$$

$$k_p^{-2}\left(\frac{\partial\phi}{\partial\zeta}\right)^2 = \left(\frac{E_{\max}}{E_0}\right)^2 + 1 - \phi + (1+\phi)^{-1}\ , \tag{2.49}$$

with $E_{\max}$ the peak electric field of the plasma wave. Using Eqns. 2.48-2.49, the integral over the laser pulse in Eqn. 2.47 can be evaluated to obtain

$$\frac{\mathrm{d}U}{\mathrm{d}\tau} = \frac{-E_{\max}^2}{8\pi}\ . \tag{2.50}$$

Normalizing the pulse energy to $(k_0^2/k_p^3)(E_0^2/8\pi)$, the above can be expressed [45]

$$\frac{\partial\mathcal{E}}{\partial\tau} = -\frac{k_p^3}{k_0^2}\left(\frac{E_{\max}}{E_0}\right)^2 \tag{2.51}$$

with E_m the peak field of the plasma wave. Defining the characteristic length over which laser energy is deposited into the driven plasma wave

$$\frac{\partial\mathcal{E}}{\partial\tau} \equiv -\frac{\mathcal{E}}{L_{pd}}\ , \tag{2.52}$$

the pump depletion length L_{pd} is given by

$$L_{pd} = \frac{k_0^2}{k_p^3}\left(\frac{E_{\max}}{E_0}\right)^2 . \tag{2.53}$$

Depletion of the driver pulse energy limits the distance over which particles can be accelerated. However, self-evolution of the pulse, which was not addressed by the simple model used here, causes plasma wave excitation to cease before L_{pd}. The principle mechanism at work is lengthening of the depleted laser pulse: as the increased bandwidth from self-steepening eventually allows dispersion to overwhelm self-steepening, causing the pulse to lengthen and lose resonance with the plasma. Simulations show that this occurs at $\sim L_{pd}/2$ in the nonlinear regime $a_0 \gtrsim 1$ [45].

A general relationship between frequency redshifting and energy depletion of laser pulses during excitation of plasma waves can be derived through conservation of the "wave action," an adiabatic invariant that exists for $k_0 \gg k_p$. Importantly, this relationship holds in 3D, and so is of great practical importance as a diagnostic tool for experiments. The wave equation for the laser envelope in 3D is

$$\left[\nabla_\perp^2 + 2\left(ik_0 + \frac{\partial}{\partial\zeta}\right)\frac{\partial}{\partial\tau} - \frac{\partial^2}{\partial\tau^2}\right]\hat{a} = k_p^2\rho\hat{a} . \tag{2.54}$$

Associated with Eqn. 2.54 is an adiabatic invariant, the wave action [46, 47]

$$\mathcal{A} = \int \mathrm{d}^2\mathbf{x}_\perp \int \mathrm{d}\zeta k_p \hat{a}^*[1 - ik_0^{-1}(\partial_\zeta - \partial_\tau)]\hat{a} , \tag{2.55}$$

and the normalized energy

$$\mathcal{E} = \int \mathrm{d}^2\mathbf{x}_\perp \int \mathrm{d}\zeta k_p \left|[1 - ik_0^{-1}(\partial_\zeta - \partial_\tau)]\hat{a}\right|^2 . \tag{2.56}$$

Adopting the slowly varying envelope approximation such that $|\partial_\tau\hat{a}| \ll |\partial_\zeta\hat{a}|$, these quantities can be expressed in the frequency domain as

$$\mathcal{A} = \int \mathrm{d}^2\mathbf{x}_\perp \int \mathrm{d}k k_p \left(\frac{k}{k_0}\right)|\hat{a}(k)|^2 \tag{2.57}$$

$$\mathcal{E} = \int \mathrm{d}^2\mathbf{x}_\perp \int \mathrm{d}k k_p \left(\frac{k}{k_0}\right)^2|\hat{a}(k)|^2 . \tag{2.58}$$

From action conservation follows a useful general relationship between laser energy depletion and the mean wavenumber of the laser pulse. Motivated by the form of Eqns. 2.57 and 2.58, the mean wavenumber is defined

$$\langle k/k_0\rangle \equiv \mathcal{E}/\mathcal{A} = \frac{\int \mathrm{d}^2\mathbf{x}_\perp \int \mathrm{d}k \left(\frac{k}{k_0}\right)^2|\hat{a}(k)|^2}{\int \mathrm{d}^2\mathbf{x}_\perp \int \mathrm{d}k \left(\frac{k}{k_0}\right)|\hat{a}(k)|^2} . \tag{2.59}$$

Because the wave action is adiabatically invariant such that $\partial_\tau \mathcal{A} = 0$, the laser energy depletion is related to the mean wavenumber by the simple expression [48]

$$\mathcal{A}\langle k/k_0\rangle = \partial_\tau \mathcal{E} \tag{2.60}$$

The preceding result is completely general and applies in three dimensions, and states that as energy from a laser pulse is transferred into a trailing plasma wave, the laser spectrum becomes redshifted. Furthermore, if the geometry is restricted to the 1-D case (i.e. the plane wave or large beam waist limit), energy depletion and redshifting can be further related to peak electric field within the driven plasma wave via the nonlinear wake equations of Section 2.3 [48]

$$\mathcal{A}\langle k/k_0\rangle = \partial_\tau \mathcal{E} = -\partial_\tau \mathcal{Q} = \frac{k_p^3}{k_0^2 E_0^2} E_m^2 \tag{2.61}$$

with E_m the peak electric field and

$$\mathcal{Q} = \int \mathrm{d}\zeta k_p |a|^2 \tag{2.62}$$

which is a measure of the steepening of the laser pulse.

Because of the simple relationship between spectral redshifting, laser energy depletion, and self-steepening, spectral redshifting has become an important diagnostic for laser-plasma accelerators [2, 43]. Strictly speaking, the three-dimensional nature of the laser-plasma interaction in a real laser-plasma accelerator invalidates the 1-D geometry in which Eqn. 2.61 is derived and thus a simple relationship between driver depletion and the accelerating field E_m does not exist. This is due to the varying partition of energy between the transverse and longitudinal fields of the wake as the spot size of the driver evolves [43]. Simple calculations using the 1-D theory predict the accelerating field to within a factor $\lesssim 3$ in the 3-D case, and greater accuracy requires the use of PIC simulations. However, as it requires little more than an optical spectrometer, spectral redshifting measurement is a common and readily implemented diagnostic for plasma wave amplitude.

For this reason, it is useful for the experimentalist to express the quantities of Eqns. 2.57 and 2.58 in terms of the electric field and ordinary energy spectral density of the laser pulse. This can be done by via the relation $\hat{a}(k) = i(k_p/k)(\hat{E}(k)/E_0)$ to obtain

$$\mathcal{A} = \frac{k_p^3}{k_0^2 E_0^2} \int \mathrm{d}^2\mathbf{x}_\perp \int \mathrm{d}k \left(\frac{k_0}{k}\right) \left|\hat{E}(k)\right|^2 \tag{2.63}$$

$$\mathcal{E} = \frac{k_p^3}{k_0^2 E_0^2} \int \mathrm{d}^2\mathbf{x}_\perp \int \mathrm{d}k \left|\hat{E}(k)\right|^2 . \tag{2.64}$$

In turn, these definitions can be used to rewrite the mean wavenumber in terms of the laser energy spectral density

$$\langle k/k_0\rangle \equiv \mathcal{E}/\mathcal{A} = \frac{\int \mathrm{d}^2\mathbf{x}_\perp \int \mathrm{d}k \left|\hat{E}(k)\right|^2}{\int \mathrm{d}^2\mathbf{x}_\perp \int \mathrm{d}k \left(\frac{k_0}{k}\right) \left|\hat{E}(k)\right|^2} . \tag{2.65}$$

2.5 Focusing and propagation of intense lasers in plasmas

The discussion so far has focused on the longitudinal aspects of LWFA. However, transverse evolution of the driver pulse is just as important to accelerator performance. To begin with, all LWFA systems rely on focusing optics to concentrate laser energy to a small spot to reach the intensities required for plasma wave excitation. In a vacuum, a laser pulse with a Gaussian transverse profile at focus such that $a = a_0 \exp(-r^2/r_0^2)$ propagates according to

$$r_s = r_0(1 + z^2/Z_R^2)^{1/2} \tag{2.66}$$

$$I = I_0(r_0^2/r_s^2)\exp\left(-2r^2/r_s^2\right) , \tag{2.67}$$

with the Rayleigh length defined

$$Z_R = kr_0^2/2 . \tag{2.68}$$

Z_R roughly corresponds to the distance over which a laser pulse will remain focused to high intensity, and hence the distance over which plasma waves can be excited and particles accelerated. However, this neglects important plasma processes that can modify the evolution of the driver spot size. These include effects that cause laser pulses to focus and defocus, some of which can be used to extend the acceleration length beyond Z_R. It might be expected that a pre-formed radial plasma gradient could suppress diffraction of the driver and extend the acceleration length. This is indeed the case, and in fact a chief concern of this dissertation. However, discussion of pre-formed plasma waveguides or "plasma channels" is left for Chapter 3. This section, rather, is focused on nonlinear processes that affect laser propagation in homogeneous media.

Intense laser pulses can ionize gas non-resonantly through a number of nonlinear processes [36, 49]. This allows the use of neutral gas as an accelerating medium for LWFA, as the very leading edge of relativistically intense driver pulse will ionize the gas into a plasma. However, ionization can also result in the defocusing of intense laser beams. Ionization will create a defocusing "plasma lens" that is strongest on-axis, which causes the beam to diverge. This "ionization defocusing" can prevent a laser pulse from focusing to the maximum intensity permitted by diffraction.

Ionization defocusing can be suppressed if the half-space upstream of the laser focus can be kept at vacuum. Thus, nearly all LWFA systems employ target configurations that allow for the gas or plasma to be localized. These include pulsed supersonic gas jets that create a gas density profile with a sharp boundary onto which the driving laser pulse can be focused, or gas cells with pinholes for laser coupling that restrict flow into the target chamber [37].

Intense laser pulses propagating in plasmas undergo nonlinear self-focusing effects arising from modification of the electron mass by relativistic quiver motion and modification of the plasma density within the laser pulse by the laser ponderomotive force. These effects can be useful, serving to suppress the diffraction of LPA drive pulses, increasing peak intensities in the plasma and the propagation distances over which those intensities are maintained.

Relativistic self-focusing occurs due to a third-order nonlinearity in the laser field arising from the relativistic mass associated with the electron quiver motion. From the nonlinear current of Eqn. 2.24 $J = k_p(n/n_0)\mathbf{a}/\gamma$ in the weakly relativistic limit, the effective refractive index within an intense laser beam can be derived [50, 51]

$$\eta_r \simeq 1 - \frac{\omega_p^2}{2\omega^2}\left(1 - \frac{a_0^2}{2}\right) \ . \tag{2.69}$$

The normalized spot size $R = r_s/r_0$ of a Gaussian laser pulse $|\hat{a}|^2 = (a_0 r_0/r_s)^2 \exp(-2r^2/r_s^2)$, with r_0 the minimum spot size in vacuum, evolves according to [50, 51]

$$\frac{\mathrm{d}^2 R}{\mathrm{d}z^2} = \frac{1}{Z_R R^3}\left(1 - \frac{P}{P_c}\right) \ , \tag{2.70}$$

with $Z_R = k_0 r_0^2/2$ the vacuum Rayleigh length, and $P/P_c = k_p^2 a_0^2 r_0^2/32$ the normalized power for linear polarization (for circular polarization $a_0^2 \to 2a_0^2$). The critical power, P_c, is an important parameter in high-intensity laser plasma interactions, and worth expressing in practical units:

$$P_c(\mathrm{GW}) \simeq 17.4(\omega/\omega_p)^2 \ . \tag{2.71}$$

If the laser power P exceeds P_c, the modified refractive index [Eqn. 2.69] will cause the laser to self-focus, as is evident from the second factor on the RHS of Eqn. 2.70. However, as the intensity of the self-focusing laser beam grows, other processes prevent it from collapsing to zero size [51, 52]. One such process is the ponderomotive force: as the laser intensity grows and the spot size shrinks, the ponderomotive force becomes sufficient to expel plasma electrons from the beam, suppressing the nonlinear current responsible for relativistic self-focusing.

Though illustrative, the preceding discussion of relativistic self-focusing does not strictly apply to short pulses $L < \lambda_p$. Modification of the plasma density by the laser ponderomotive force, i.e. plasma wave excitation, will in fact suppress the relativistic self-focusing process just described [33, 38, 39].

Accounting for the plasma density response to the laser ponderomotive force using a perturbative calculation with the Poisson equation of Section 2.3, the refractive index becomes[39]

$$\eta_r \simeq 1 - \frac{\omega_{p0}}{2\omega^2}\left(1 - \frac{a^2\zeta^2}{4}\right) \ , \tag{2.72}$$

with $\zeta = k_p(z - ct)$. The intensity required for self-focusing at the head of a short laser pulse is seen to then be infinite. The mechanism responsible for cancelling of the relativistic self-focusing for short pulses is the ponderomotively-driven density rise at the head of the pulse, which can be seen in the solution to the Poisson equation in Fig. 2.1. This creates a defocusing plasma lens on axis that cancels the effect of the gradient in the relativistic quiver motion.

Self-focusing of short $L \sim \lambda_p$ laser pulses arises from a combination of relativistic and ponderomotive effects. The ponderomotive force can support density gradients that suppress

laser diffraction [2]. There exists a very important regime for LWFA wherein electrons are completely expelled from the driving laser pulse, forming a roughly spherical ion cavity with dimensions $\sim \lambda_p$. This is the so-called "bubble", "blow-out", or "cavitation" regime, and allows for the suppression of laser diffraction over many Z_R [2, 53, 54].

The bubble regime is highly nonlinear, and a complete analytic theory does not exist. However, the condition for bubble formation can be estimated by balancing the ponderomotive force with the space charge of the ion cavity such that $F_{pN} \sim -q_e E_r$. Taking the limit $a_0^2 \gg 1$ and with the bubble radius $R \simeq r_0$ the characteristic length scale of the interaction, $-m_e c^2 a_0/R \sim -(4\pi/3) q_e^2 n_0 R \Rightarrow k_p R \simeq k_p r_0 \sim (3a_0)^{1/2}$. Simulations of bubble propagation yielded a slightly different semi-empirical formula for "matched" bubble propagation, where evolution of the laser spot size is minimized [54]:

$$k_p R \simeq k_p r_0 = 2a_0^{1/2} \ . \tag{2.73}$$

Formation of a spherical ion cavity (the eponymous "bubble") is subject to the additional condition $a_0 \gtrsim 4$ [55, 56]. The bubble regime has some useful properties. Because the charge density inside the ion cavity is uniform, the focusing forces on the electron bunch are linear, which preserves the transverse RMS emittance [2, 40]. However, bubble propagation can only be used to accelerate electrons, as nonlinear wave steepening restricts the region with negative potential in which positively charged particles can be focused to very small regions between bubbles [40].

Extension of the acceleration length beyond Z_R through nonlinear self-focusing processes, particularly bubble regime propagation, is the subject of active research [16, 54, 57]. However, the approach has a number of limitations. The head of a laser pulse, which by necessity has a much lower intensity than the body of the pulse, is subject to weaker focusing forces and will diffract. This causes the pulse pulse to "etch" away from the front as it propagates [2, 54, 58]. Moreover, the high laser intensities required for $a_0 \simeq 4$ [54–56] at focus raise the cost and technical requirements of the laser driver.

As a nonlinear process, self-focusing is difficult to control with precision and the high laser intensities and plasma wave amplitudes involved constrain other aspects of the acceleration, particularly the trapping of electrons in the wake which is discussed in the next section. Finally, the small accelerating and focusing regions for positively charged particles in nonlinear plasma waves is a severe limitation for collider applications, most of which are aimed at producing electron-positron collisions [24, 40]. For these reasons, this dissertation is concerned with the investigation of pre-formed plasma guiding structures in which weakly nonlinear plasma waves can be driven over many Rayleigh lengths with laser intensities $a_0 \sim$ 1-2.

2.6 Bunch injection

The discussion so far has focused on the excitation of large-amplitude plasma waves by a relativistically-intense driving laser pulse, with no consideration of the process by which electrons initially at rest become trapped and accelerated by the wave. Injection of an electron

bunch into a wave is not straightforward: for particles to "catch" a plasma wave and become trapped, they must have a velocity comparable to the phase velocity of the plasma wave. This requires particles be accelerated to relativistic velocities on a timescale $\sim \omega_p^{-1}$. Moreover, injection must be precisely controlled to minimize the energy spread of an accelerated bunch. If the final energy of an accelerated electron is $W = q_e E(L_{\rm inj} + L_{\rm acc})$, minimizing the spread in final electron energies requires minimizing the length $L_{\rm inj}$ over which particles are injected relative to the total length of the accelerator.

Many mechanisms have been implemented for injecting electron bunches into laser-driven plasma waves [2], including ponderomotive injection by colliding laser pulses and plasma density transitions[59]. However, this section will focus on the two mechanisms at play in the experiments of this dissertation, namely, self-injection and ionization injection.

Self-Injection

Sufficiently high plasma wave amplitudes, typically $a_0 \gtrsim 3$, can cause background electrons to become spontaneously trapped and accelerated in the wake. Criteria have been derived [60] for this "self-trapping" or "self-injection" process for 1D plasma waves, however in most situations of interest for LWFA self-trapping occurs due to combination of transverse focusing and longitudinal acceleration. As such, self-trapping is effectively a form of 3D wave breaking, with the electron fluid velocity becoming multiply-valued where particle orbits cross. Various criteria have been derived analytically for self-trapping in bubble wakes [53, 54, 61, 62], however, these treatments all rely on approximations to cope with the complex field structure at the rear of a bubble where $n/n_0 \gg 1$. As such, numerical calculations with particle-in-cell (PIC) codes are essential tools for studying self-trapping [57, 63, 64] A comprehensive numerical investigation of self-trapping in the bubble regime performed with the INF&RNO particle-in-cell (PIC) code produced the trapping criterion [64]

$$a_0 \gtrsim 2.75[1 + (\gamma_p/22)^2]^{1/2} \ , \tag{2.74}$$

for matched bubble propagation.

Self-trapping is a convenient means of injecting an electron bunch into a plasma wave, requiring no special arrangements beyond sufficiently high laser intensity and plasma density. However, because self-trapping is a complex and highly nonlinear process, precise control of the resulting electron bunch properties is difficult. Moreover, self-trapping can occur continuously throughout an accelerating structure, leading to large energy spreads. Therefore, self-trapping is frequently regarded as a process to be suppressed in acceleration schemes designed for high quality bunch production [23], and thus for many prospective laser wakefield accelerator designs Eqn. 2.74 suggests the constraint $a_0 \lesssim 3$.

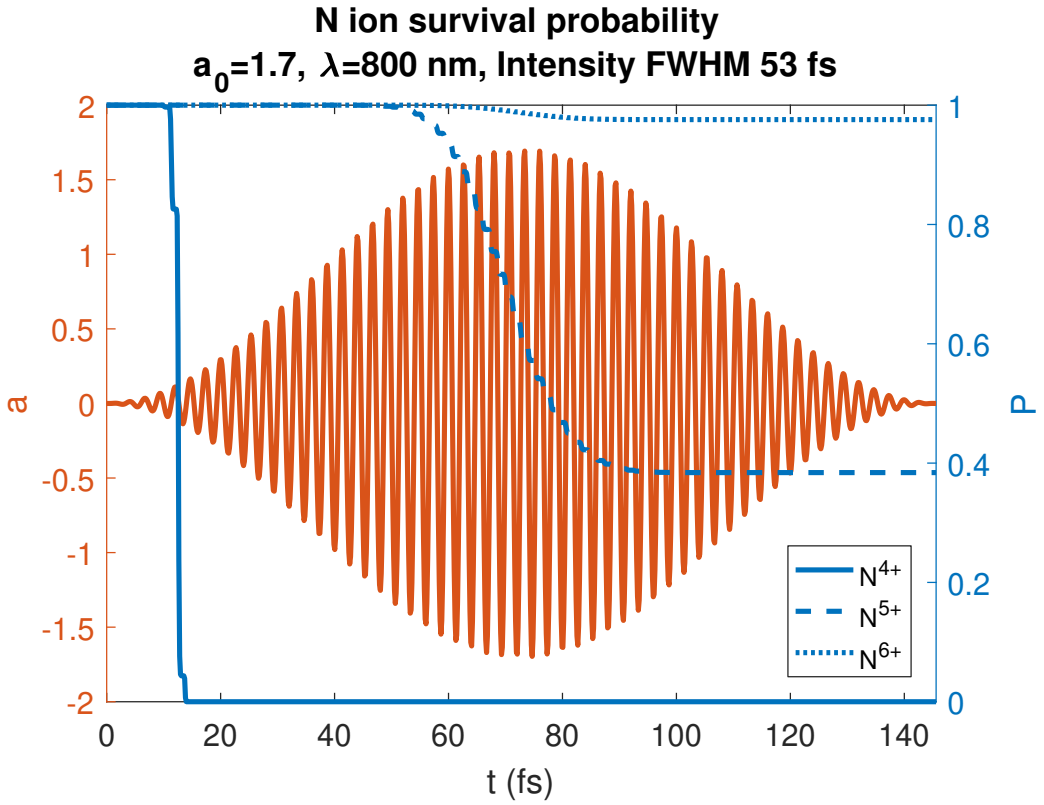

Figure 2.3: Survival probability calculated from Eqn. 2.75 of some high-Z ions of nitrogen. Laser pulse is the same as that used for Figs. 2.1 and 2.4.

Ionization Injection

Intense laser pulses will ionize atoms via quantum tunneling. The rate of ionization in the tunneling regime is given by [49]

$$D = 4\omega_a C \frac{(U_I/U_H)^{(6n^*-3|m|-1)/2}}{|E/E_a|^{2n^*-|m|-1}} \exp\left[-\frac{2(U_I/U_H)^{3/2}}{3|E/E_a|}\right] , \tag{2.75}$$

with $\omega_a = \alpha^3 c/r_e$, U_I the ionization potential, $U_H = 13.6\text{eV}$ the ionization potential of hydrogen, E the laser electric field, $E_a = q_e/r_B^2 \simeq 0.5\text{TV m}^{-1}$, r_B the Bohr radius, $r_e = q_e^2/m_e c^2$ the classical electron radius, and α the fine structure constant. m is the magnetic quantum number associated with the angular momentum quantum number l, and the effective principal and angular momentum quantum numbers are defined $n^* = Z(U_H/U_I)^{1/2}$ and $l^* = n_0^* - 1$, with Z the ion charge after ionization and n_0^* the effective principal quantum number of the ground state. The constant C is defined

$$C = \frac{2^{4n^*-4-2|m|}}{n^*\Gamma(n^*+l^*+1)\Gamma(n^*-l^*)} \frac{(2l+1)(l+|m|)!}{|m|!(l-|m|)!} . \tag{2.76}$$

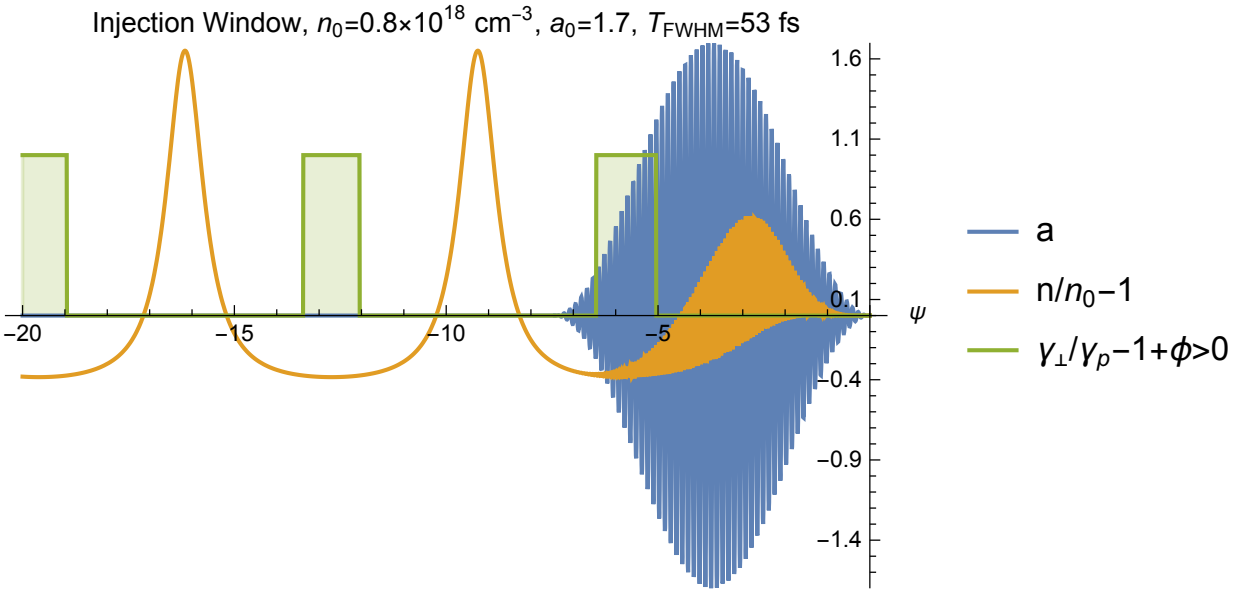

Figure 2.4: Locations where electrons ionized at rest will be trapped and focused in the plasma wave of Fig. 2.1 (green trace, = 1), calculated according to the condition Eqn. 2.80.

The probability P that an ion of a given species will survive can be calculated from Eqn. 2.75 according to $P = \exp\left[-\int_{-\infty}^{\infty} D(t)\mathrm{d}t\right]$. This expression has been evaluated numerically in Fig. 2.3 for three high-charge ions of nitrogen.

Electrons ionized from high-Z background ions at the correct phase in a plasma wave with sufficiently high amplitude will be trapped and accelerated. This can be exploited to inject electron bunches for laser wakefield acceleration: electrons ionized from high-Z background ions by the driving laser pulse will be trapped if the laser and plasma parameters are chosen correctly [65, 66].

Ionization injection provides for a straightforward means to localize injection of an electron bunch and reduce energy spread, requiring only that a target be designed in such a way that a high-Z gas can be localized to a small fraction of the acceleration length [66]. Moreover, because electrons are ionized near the peak of the laser field where $|\mathbf{a}| \ll 1$, transverse momentum conservation [Eqn. 2.7] dictates that electron bunches trapped in this way may possess very small transverse momentum spread. Schemes have been proposed to take advantage of this fact to produce very low emittance bunches by using a trailing high frequency injection pulse with $a \ll 1$ to inject a bunch into a wake generated by a low frequency driver pulse [67, 68].

The trapping condition for ionized electrons can be derived from the Hamiltonian of an electron in a plasma wave [30]:

$$H(u,\psi) = (\gamma_\perp^2 + u^2)^{1/2} - \beta_p u - \phi(\psi) \ , \tag{2.77}$$

with $\psi = k_p\xi$. Defining $\phi(\psi_{\min}) \equiv \phi_{\min}$, the value of the Hamiltonian on the separatrix is

$$H_s = \gamma_\perp(\psi_{\min})/\gamma_p - \phi_{\min} \ , \tag{2.78}$$

i.e. the Hamiltonian of a particle with kinetic energy γ_p at the minimum wake potential. With $H(0, \psi_i)$ the value for electrons ionized from atoms at rest at wake phase ψ_i, the trapping condition follows from $H(0, \psi_i) < H_s$

$$\gamma_\perp/\gamma_p - 1 + \phi_i > \phi_{\min} \ . \tag{2.79}$$

Note that for electrons ionized at the peak of the laser electric field, $\mathbf{a}_\perp(\psi)$ and hence $\gamma_\perp = 1$. However, this trapping condition is not generally applicable to the three-dimensional case, as $\phi_{\min} < 0$ and the wake is defocusing in regions where $\phi < 0$. Such electrons that enter the defocusing phase of the wake will be lost from the wake and not accelerated.

A more restrictive and generally applicable condition that requires electrons to be trapped without entering the defocusing region of the wake can be obtained by making the replacement $\phi_{\min} \to 0$

$$\gamma_\perp/\gamma_p - 1 + \phi_i > 0 \ . \tag{2.80}$$

The "injection window" defined by Eqn. 2.80 for the plasma wake of Fig. 2.1 has been plotted in Fig. 2.4. Electrons ionized in the green shaded regions will be trapped and accelerated in the wake.

The plasma wave phase velocity is a crucial parameter for trapping, as is evident from the γ_p dependence of Eqns. 2.79 and 2.80. In Section 2.2 the linear laser group velocity was used, i.e. $\gamma_p = \omega/\omega_p$, however this is only valid in the linear limit. In much the same way it does transverse evolution of a laser pulse, the nonlinear transverse current induced by a relativistically intense laser pulse modifies the group velocity. Additionally, evolution of the laser pulse will modify γ_p through the nonlinear plasma wavelength [69]. Various analytical corrections to the group velocity to account for the nonlinear current have been proposed [2]. For the calculation shown in Fig. 2.4, the 1D intensity transport velocity of the driving laser pulse was used, such that $\gamma_p = \gamma_g \simeq (\omega/\omega_p)(1 + 3a^2/8)$ [70]. Nonlinear period lengthening has been neglected, essentially equivalent to assuming a nonevolving driver pulse.

Limits to injected charge: beam loading

Bunch charge is limited by shielding of the plasma wave electric field by the bunch space charge field. When the bunch charge becomes large enough, injection into the wake becomes impossible, a phenomenon referred to as "beam loading." The beam loading limit scales roughly as the bunch charge required to cancel the charge contained in the ion cavity of a plasma wave. An order of magnitude estimate of this charge can be obtained assuming an ion cavity with dimensions $\lambda_p/2$: $Q \lesssim -q_e n_0 \lambda_p^3/8 \propto n_0^{-1/2}$. This is a crude estimate, however it captures the $n_0^{-1/2}$ scaling with density obtained in more quantitative treatments of beam loading in the bubble regime [2] and illustrates the essential physics involved, including the

counterintuitive fact that injected charge decreases with plasma density due to the dependence of the wake size on the plasma density.

However, beam loading is complex process that does not lend itself to a single, simple analytical model. The point at which the space charge of an electron bunch suppresses injection is dependent on the field structure and particle trajectories through the wake, and hence the injection mechanism and evolution of the wake.

2.7 Scaling laws

In the absence of diffraction, energy gain in a LWFA is limited by two primary mechanisms. The first is bunch dephasing, wherein in the accelerated electron bunch outruns the accelerating phase of the wake. The second is pump depletion, wherein the driver pulse amplitude decays as electromagnetic energy is transferred into the driven plasma wave. Scaling laws with respect to density (through the plasma wavelength λ_p), a_0, and laser wavelength λ have been derived using the linear group velocity for the driver pulse $\gamma_p = \omega/\omega_p = \lambda_p/\lambda$ and the field amplitudes for a resonant flat-top pulse given in Section 2.3. The dephasing[71] and pump depletion[45] lengths, respectively, are

$$L_d \simeq \frac{\lambda_p^3}{2\lambda^2}\begin{cases}1 & \text{for } a_0^2 \ll 1 \\ (\sqrt{2}/\pi)a_0/N_p & \text{for } a_0^2 \gg 1\end{cases}, \tag{2.81}$$

$$L_{pd} \simeq \frac{\lambda_p^3}{\lambda^2}\begin{cases}2/a_0^2 & \text{for } a_0^2 \ll 1 \\ (\sqrt{2}/\pi)a_0 & \text{for } a_0^2 \gg 1\end{cases}, \tag{2.82}$$

where N_p is the number of periods behind the laser driver pulse. The ideal energy gain $\Delta W = q_e E_z L_{acc}$ can be obtained from these scalings with the expression for the maximum accelerating field for an optimal, flat-top, linearly polarized laser pulse [Eqn. 2.33]. If acceleration is limited by dephasing, $L_{acc} \simeq L_d$, and the energy gain is

$$\gamma_d \simeq \pi\frac{\lambda_p^2}{2\lambda^2}\begin{cases}a_0^2/2 & \text{for } a_0^2 \ll 1 \\ a_0^2/\pi N_p & \text{for } a_0^2 \gg 1\end{cases}. \tag{2.83}$$

As an aside, the $a_0^2 \gg 1$ case of Eqn. 2.83 agrees with the expression for dephasing limited energy gain [Eqn. 2.19] derived in Section 2.2, $\gamma = 2\gamma_p^2(\phi_{\max} + 1)$, with $\gamma_p = \lambda_p/\lambda$ and Eqns. 2.33 and 2.34. The $a_0^2 \ll 1$ case differs by a factor $\pi/2$.

Alternatively, if acceleration is limited by pump depletion, $L_{acc} \simeq L_{pd}/2$ and

$$\gamma_{pd} \simeq \pi\frac{\lambda_p^2}{2\lambda^2}\begin{cases}1 & \text{for } a_0^2 \ll 1 \\ a_0^2/\pi & \text{for } a_0^2 \gg 1\end{cases}. \tag{2.84}$$

2.8 Design of LWFAs and the central problem of this dissertation

Some important conclusions can be drawn from Eqns. 2.81-2.84. In the linear regime, dephasing is the principal limit on energy gain as can be seen from the fact $L_d < L_{pd}$ for $a_0^2 \ll 1$. However, in the nonlinear regime where $a_0^2 \gg 1$, $L_d = L_{pd}$ and dephasing and pump depletion occur on the same length scale. The latter regime is preferred for accelerator operation, as laser energy and wake bucket phase space are simultaneously exhausted.

Additionally, energy gain scales as n^{-1}, motivating the use of low density plasmas as accelerating media. However, the $n^{-3/2}$ scaling of acceleration length dictates that accelerating structures must be made longer as density is decreased. The n^{-1} scaling of the energy gain suggests that increasing accelerator performance entails the pursuit of ever-lower plasma densities. After all, a plasma density of $n = 4 \times 10^{12}$ cm^{-3} yields a single stage energy gain of 30 TeV. However, the accelerating gradient in this case is ~ 100 MV m^{-1}. This offers no performance advantage over conventional RF accelerators, which is to say nothing of the difficulties attendant to the creation of the required 300-km-long plasma structure. Rather, consideration must also be given not only to energy gain but also to the accelerating gradient $\sim \gamma m_e c^2 / L_{acc}$, which can be deduced to scale as $n^{1/2}$.

The conflicting dependence of energy gain and accelerating gradient on plasma density thus necessitates a staged acceleration approach, wherein electron bunches are transported through a series of discrete plasma accelerating structures [40]. At each stage, fresh driver pulses can be injected and the electron bunch can be re-phased to the wake, enabling operation at higher densities where the accelerating gradient is higher but the single-stage energy gain is lower. The inter-stage "coupling length" required to accommodate the laser and electron beam optics to transport bunches between stages is thus an important consideration for staged acceleration schemes. Conventional optics would require several meters between accelerating stages, however the use of plasma mirrors [72–74] and plasma-based electron beam lenses [74, 75] can reduce the required coupling length to the meter scale.

It is straightforward to derive an optimum plasma density that minimizes the total length of a multi-stage laser wakefield accelerator system. For an accelerator composed of a series of identical stages, the total system length is minimized when the average effective accelerating gradient of a single stage is maximized. The "stage-averaged" gradient can be defined $\langle W' \rangle_{\text{stage}} \equiv W_{\text{stage}}/(L_{\text{acc}} + L_c)$, with $W_{\text{stage}} = \gamma_{pd} m_e c^2$, $L_{\text{acc}} = L_{pd}/2$, and $L_c = 0.5$-2 m the inter-stage coupling length. Given the need to suppress self-trapping and allow for the acceleration of positrons, it is assumed that the accelerator is driven in the weakly nonlinear regime such that $a_0 \sim$1-2. $a_0 = 1.5$ for this analysis, which also implies the use of a guiding structure to suppress diffraction as this laser intensity is below the threshold for bubble propagation. Assuming the nonlinear pump depletion length and energy gain of Eqns. 2.82 and 2.84, the stage-averaged gradient is given by

$$\langle W' \rangle = m_e c^2 a_0^2 \frac{\lambda_p^2}{2\lambda^2} \left(\frac{1}{\pi\sqrt{2}} a_0 \frac{\lambda_p^3}{\lambda^2} + L_c \right)^{-1} . \tag{2.85}$$

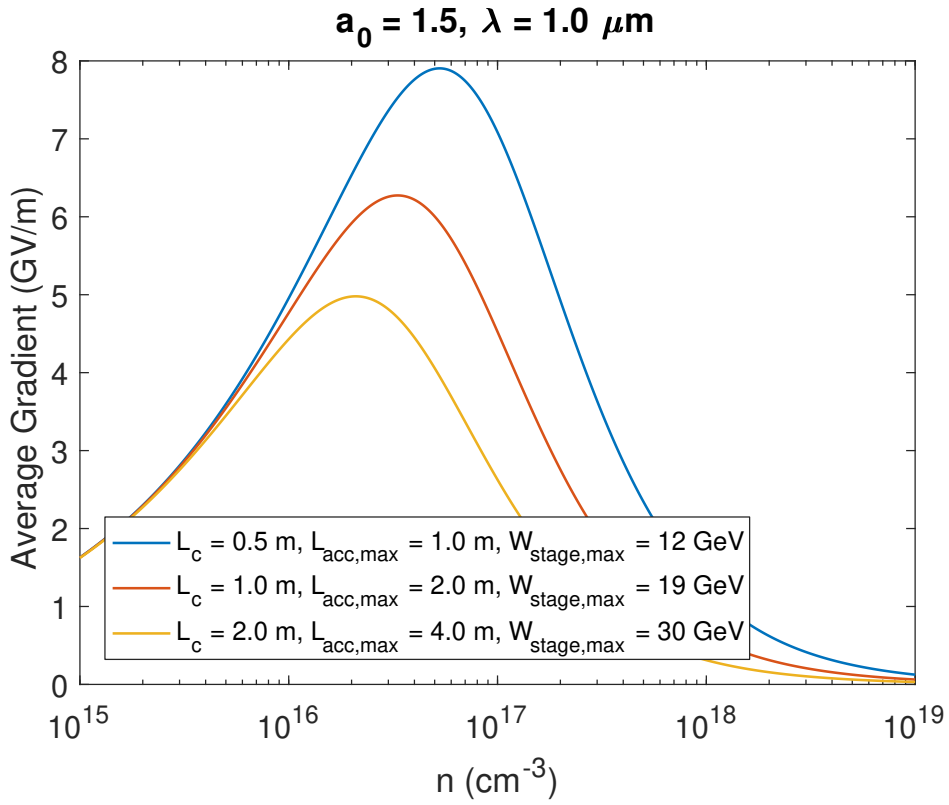

Figure 2.5: Stage-averaged gradient of a staged LWFA system [Eqn. 2.85] plotted as a function of plasma density, for three values of the coupling length L_c occupied by laser and electron beam optics for transfer of bunches between acceleration stages. A broad maximum exists in the range

Eqn. 2.85 has been plotted as a function of plasma density n for three values of the coupling length L_c in Fig. 2.5. A broad maximum is present in the range 0.5-1 $\times$ 10^{17} cm^{-3}, with single stage energy gains of 10-30 GeV in meter-scale accelerating structures.

It should be stated that Eqn. 2.85 constitutes a fairly crude model. The limiting expressions for nonlinear energy gain and acceleration length are not strictly applicable to the weakly nonlinear $a_0 = 1.5$ case. However, the results derived here approximately reproduce the maximum gradient obtained a similar analysis using plasma fluid simulations to compute the accelerating fields and depletion lengths[40]

This analysis indicates a clear approach to the development of laser wakefield acceleration for high energy collider applications. Specifically, demonstration of $\sim$ 10 GeV energy gain in a meter-scale waveguiding structure with density $\sim 1 \times 10^{17}$ cm^{-3} is a requirement for development of a compact, high-energy staged laser wakefield accelerator [24]. This is a higher single stage energy gain and lower operating density than achieved in a LWFA prior to the work of this dissertation, the closest example being the experiments of Refs. [76, 77], in which electrons were accelerated to 4.2 GeV in a 9-cm-long capillary discharge waveguide

at density 6-8 $\times 10^{17}$ cm^{-3}. Development and demonstration of a guiding structure capable of 7.8 GeV single-stage energy gain, a laser-heated capillary discharge waveguide, is the principal outcome of the research in this dissertation. Laser propagation in plasma channels, as well as the specific considerations that led to the development of a laser-heated capillary discharge, are the subject of the next chapter.

Chapter 3

Pre-formed plasma channels

3.1 Introduction

As was introduced in the previous chapter, a structured plasma with a positive radial density gradient can be used to suppress diffraction of a driving laser pulse in a LWFA. Such a waveguide or "plasma channel" confines the driver energy near the axis via refraction, analogously to a graded-index optical fiber [78], allowing plasma waves to be driven at large amplitude over much larger distances than allowed by laser diffraction [2].

When guiding structures are used to mitigate diffraction, beam energies are limited by depletion of the driver energy and dephasing of the electron bunch from the plasma wave accelerating field. In the quasi-linear regime, energy gain scales as $\sim a_0 n_e^{-1}$, with a_0 the laser strength parameter [2], and so the production of higher energy beams requires both increasing driver energy and reducing plasma density.

A useful model that is applicable to many plasma guiding structures is that of the parabolic plasma channel, which has a plasma profile of the form

$$n_e(r) = n_{e0} + r^2/\pi r_e {r_m}^4 \ , \tag{3.1}$$

with r_e the classical electron radius, n_{e0} the on-axis density, and r_m the matched spot size. This represents the lowest-order expansion of a radially symmetric plasma profile around the axis. The on-axis density n_{e0} sets the limit on energy gain due to dephasing and pump depletion, and the matched spot size r_m characterizes the strength of the guide. If a low power Gaussian beam is coupled into a channel at focus with r_m equal to its beam waist r_0, the guided beam will maintain a constant size while it propagates in the channel. If the beam waist and matched spot size are not equal, however, the guided beam will undergo oscillations in spot size as it propagates, degrading accelerator performance and possibly destroying the guiding structure. In the quasi-linear regime, self-focusing helps confine laser energy near the axis and relaxes the condition for matched propagation, but this amounts to a modest increase in the required matched spot size and does not eliminate the need for a pre-formed plasma channel to guide over long distances [69].

Many methods have been implemented for the creation of plasma channels capable of guiding high-intensity laser pulses. These include discharge ablated capillaries [79, 80], hydrodynamically expanded field-ionized plasmas in gas jets and gas cells [10, 81–83], and gas-filled capillary discharge waveguides [17, 84]. Gas-filled capillary discharge waveguides have been an especially successful implementation of the plasma channel concept, having been used to set records for single-stage LWFA energy gain on two separate occasions at LBNL: 1 GeV with 40 TW of laser power in 2006 [13] and 4 GeV with 300 TW in 2014 [76]. However, these structures are not particularly tunable. For a fixed plasma density (which controls energy gain per Chapter 2), the only way to adjust the matched spot size is to change the capillary radius. Hence the addition of laser heating for additional control of the plasma profile.

The chapter is organized as follows. Linear theory of laser propagation in parabolic channels essential to the diagnostic measurements of Chapters 4 and 5 is reviewed in Section 3.2. Guiding in general, i.e. non-parabolic, density profiles, as well as guiding in the nonlinear regime, is addressed in Section 3.3. The operation of capillary discharge waveguides is reviewed in Section 3.4, and the limitations of these devices that necessitated the development of laser-heated capillary discharges for acceleration to energies approaching 10 GeV are described in Section 3.5. Finally, the physics of laser plasma heating in the inverse bremsstrahlung regime as applied to modification of the plasma profile within a capillary discharge is described in Section 3.6.

3.2 Linear propagation in parabolic channels

In this section, key elements of the linear theory of guiding in parabolic plasma channels are reviewed. Fundamental aspects of Gaussian laser beam propagation in parabolic channels useful for diagnosing plasma profiles are described. An analysis of a parabolic channel as waveguiding structure in terms of normal modes is used to derive the group velocity of guided laser pulses, which is essential for the plasma density measurements of Chapter 4 and Chapter 5.

In Ref. [85], the paraxial wave equation in a parabolic plasma channel was solved to obtain simple analytical equations for the envelope evolution for a guided gaussian laser pulse (i.e. u_{00} of Eqn. 3.10), including the pulse centroid trajectory and spot size evolution. As is described in Ref. [86], these analytical results are useful for diagnosing plasma channel properties and are used extensively in the work described in this dissertation.

The spot size of a Gaussian beam focused at the entrance of a parabolic channel evolves as it propagates in the channel according to

$$r_s^2 = \frac{r_i^2}{2}\left[1 + \frac{r_m^4}{r_i^4} + \left(1 - \frac{r_m^4}{r_i^4}\right)\cos(2k_{\beta c}z)\right], \tag{3.2}$$

with r_s the laser spot size at longitudinal position z, r_0 the laser spot at the channel entrance, and $k_{\beta c} = 2/kr_m^2$. From Eqns. 3.1 and 3.2 follows the condition for matched guiding $r_0 = r_m$,

in which case the laser beam will propagate through the channel with constant size. For $r_0 \neq r_m$ the spot size will oscillate, which as previously stated will degrade accelerator performance and possibly damage the guiding structure if it involves a structural component such as a capillary tube.

Similarly, if a laser pulse is injected into a plasma channel off-axis or at an angle with respect to the axis, the centroid of the pulse will oscillate in the channel as it propagates. Within a parabolic channel, the centroid trajectory is given by [86]

$$x_c = x_i \cos[k_{\beta c} z - \tilde{\phi}_c], \tag{3.3}$$

with x_c the displacement of the centroid from the channel axis at longitudinal position z, $x_i = [x_{ci}^2 + \theta_i^2 k_{\beta c}^{-2}]^{1/2}$ the oscillation amplitude, x_{ci} the injection displacement, θ_i the injection angle, and $\cos\tilde{\phi}_c = x_{ci}/x_i$. This behavior of guided laser pulses is quite useful, and can be used to measure the matched spot size [86].

Laguerre-Gaussian eigenmode propagation

Propagation of an arbitrary laser pulse in a parabolic plasma channel can be completely described using a decomposition into the eigenmodes of the channel. This is equivalent the standard eigenmode analysis of graded-index optical fibers. The eigenmode dispersion relation, from which the pulse group velocity can be obtained, will now be derived.

Using the scalar wave approximation and taking the electric field to be of the form $E(\mathbf{r}, t) = \hat{E}(\mathbf{r})e^{i\omega_0 t}$, the electromagnetic wave equation reduces to the Helmholtz equation:

$$\nabla^2 \hat{E} + k_0^2 \eta(\mathbf{r}, \omega)^2 \hat{E} = 0 \ , \tag{3.4}$$

with $\mathbf{r} = x\hat{\mathbf{i}} + y\hat{\mathbf{j}} + z\hat{\mathbf{k}}$, $k_0 = \omega_0/c$, and $\eta(\mathbf{r}, \omega)$ the spatially inhomogeneous refractive index. Using cylindrical coordinates (r, φ, z) and restricting to the refractive index to radial variation only, separation of variables can be applied to Eqn. 3.4 according to $\hat{E} = R(r)F(\varphi)Z(z)$:

$$\frac{1}{r}\frac{\mathrm{d}}{\mathrm{d}r}\left(r\frac{\mathrm{d}R}{\mathrm{d}r}\right) + \left[k_0^2\eta(r,\omega)^2 - k^2 - \frac{p^2}{r^2}\right]R = 0 \tag{3.5}$$

$$\frac{\mathrm{d}^2 F}{\mathrm{d}\varphi^2} + p^2 F = 0 \tag{3.6}$$

$$\frac{\mathrm{d}^2 Z}{\mathrm{d}z^2} + k^2 Z = 0 \tag{3.7}$$

Eqns. 3.6 and 3.7 admit solutions $F \propto e^{\pm ip\varphi}$ and $Z \propto e^{\pm ikz}$, respectively. The periodic boundary condition in azimuth restricts p to integer values. The dispersion equation for the waveguide is obtained through the solution of Eqn. 3.5. Note that this derivation has thus far been agnostic to the form of the index $\eta(r, \omega)$, and hence Eqns. 3.5-3.7 are applicable to arbitrary radial index profiles.

Assuming a parabolic plasma density profile of the form

$$n_e = n_{e0} + \Delta n_e \frac{r^2}{r_m^2} \ , \tag{3.8}$$

$\eta(r,\omega)^2$ becomes

$$\eta^2 = 1 - \frac{\omega_p^2}{\omega^2} - \frac{\Delta\omega_p^2}{\omega^2}\frac{r^2}{r_m^2} \tag{3.9}$$

with $\Delta{\omega_p}^2 = 4\pi q_e^2 \Delta n_e/m_e$. In this case, Eqn. 3.4 admits the Laguerre-Gaussian functions

$$u_{mp}(r,\varphi,z) = \sqrt{\frac{2m!}{\pi(m+|p|)!}}\left(\frac{\sqrt{2}r}{r_m}\right)^{|p|} L_m^{|p|}\left(\frac{2r^2}{r_m^2}\right)\exp\left[-\frac{r^2}{r_m^2} + i(p\varphi + \beta z)\right] \tag{3.10}$$

as solutions, with $L_m^{|p|}$ the generalized Laguerre polynomials, $m \geq 0$ the radial mode number, p the azimuthal mode number, and m, p both integers. The modes [Eqn. 3.10] are orthonormal according to the inner product

$$\langle u_{mp}|u_{m\prime p\prime}\rangle \equiv \int_0^{2\pi}\int_0^{\infty} r u_{mp} u_{m\prime p\prime} \mathrm{d}r\mathrm{d}z = \delta_{mm\prime}\delta_{pp\prime}. \tag{3.11}$$

Substituting the radially varying factors of Eqn. 3.10 into Eqn. 3.5, the condition for matched guiding

$$\Delta n_e = \frac{1}{\pi r_e r_m^2} \implies n_e = n_{e0} + \frac{1}{\pi r_e r_m^4} r^2 \tag{3.12}$$

is recovered, with r_e the classical electron radius, and the dispersion relation

$$k^2 = \frac{\omega^2}{c^2} - \frac{\omega_p^2}{c^2} - \frac{4(2m+|p|+1)}{r_m^2} \tag{3.13}$$

is obtained. Given the matched spot size r_m and the field at the entrance of the waveguide, pulse propagation can be modeled entirely using Eqns. 3.10, 3.11, and 3.13.

The quantity of greatest interest is the normalized group velocity in the waveguide $\beta_g \equiv c^{-1}\mathrm{d}\omega/\mathrm{d}k$, which can be obtained by differentiating both sides of Eqn. 3.13 with respect to k:

$$\beta_g^2 = c\frac{k^2}{\omega^2} = 1 - \frac{k_p^2}{k_0^2} - \frac{4(2m+|p|+1)}{k_0^2 r_m^2} \tag{3.14}$$

$$\beta_g \simeq 1 - \frac{k_p^2}{2k_0^2} - \frac{2(2m+|p|+1)}{k_0^2 r_m^2} \tag{3.15}$$

Laguerre-Gaussian envelope propagation

A nonparaxial treatment of higher-order Laguerre-Gaussian mode propagation in parabolic channels is presented in Ref. [48], the results of which are used extensively in the analysis of group-velocity-based plasma density measurements reported here. The simple analytical formulas obtained in Ref. [48] are often more convenient for modeling the group velocity of multimode or mismatched beams in parabolic channels than decomposition into normal modes of the channel as outlined in Section 3.2. The laser pulse normalized vector potential is expressed in terms of the envelope $\hat{a}$ and comoving variable $\xi = z - \beta_g ct$ as $a(\boldsymbol{r}, t) = \hat{a}(\mathbf{r}_\perp, \xi, z)\exp(ik_0 z - i\omega t)$, with The global group velocity is defined

$$\beta_G = \beta_g + \frac{\mathrm{d}\langle\xi\rangle}{\mathrm{d}z} \ , \tag{3.16}$$

with β_g per Eqn. 3.14 and the pulse centroid

$$\langle\xi\rangle(z) = \frac{\int_0^\infty \mathrm{d}\mathbf{r}_\perp \int_{-\infty}^\infty \xi|\hat{a}(\mathbf{r}_\perp,\xi,z)|^2\mathrm{d}\xi}{\int_0^\infty \mathrm{d}\mathbf{r}_\perp \int_{-\infty}^\infty |\hat{a}(\mathbf{r}_\perp,\xi,z)|^2\mathrm{d}\xi} \ . \tag{3.17}$$

For a transverse beam profile given by a Laguerre-Gaussian mode [Eqn. 3.10] such that $\hat{a} = a_0 f(\xi, z) u_{m,p}(\mathbf{r}_\perp)$, the global group velocity is constant [48]

$$\beta_G = 1 - \frac{k_p^2}{2k_0^2} - \frac{(2m + |p| + 1)}{k_0^2 r_m^2}\left(1 + \frac{r_i^4}{r_m^4}\right) \ . \tag{3.18}$$

Alternatively, the "centroid group velocity," defined analogously to Eqn. 3.16 but in terms of the transverse centroid of the pulse, i.e.

$$\langle\xi\rangle_c(z) = \frac{\int_{-\infty}^\infty \xi|\hat{a}(0,\xi,z)|^2\mathrm{d}\xi}{\int_{-\infty}^\infty |\hat{a}(0,\xi,z)|^2\mathrm{d}\xi} \ , \tag{3.19}$$

is given by [48]

$$\begin{aligned}\beta_{G,c}(z) = 1 - \frac{k_p^2}{2k_0^2} - \frac{2(2m + |p| + 1)}{k^2 r_m^2}\Bigg\{ &\frac{r_0^2 r_m^2 \sec^2(k_{\beta c} z)}{r_0^4 + r_m^4 \tan^2(k_{\beta c} z)} \\ &+ \frac{2r_0^2 r_m^2 (r_m^4 - r_0^4)(k_{\beta c} z)\tan(k_{\beta c} z)\sec^2(k_{\beta c} z)}{[r_0^4 + r_m^4 \tan^2(k_{\beta c} z)]^2}\Bigg\} \ .\end{aligned} \tag{3.20}$$

Note that unlike the global group velocity [Eqn. 3.18], the centroid group velocity [Eqn. 4.26] varies longitudinally. For density measurements, the longitudinally-averaged group velocity $\overline{\beta}_{G,c} \equiv L^{-1}\int_0^L \beta_{G,c}(z)\mathrm{d}z$ is the measurable quantity of interest, which can be obtained by integrating Eqn. 3.20:

$$\begin{aligned}\overline{\beta}_{G,c}(L) = 1 - \frac{k_p^2}{2k_0^2} \\ - \frac{2(2m + |p| + 1)}{k^2 r_m^2}\frac{r_0^2}{r_m^2}\left\{\frac{2\tan^{-1}[\frac{r_m^2}{r_0^2}\tan(k_{\beta c} L)]}{r_0^2 r_m^2 k_{\beta c} L} + \frac{2}{r_0^4 + r_m^4 + (r_0^4 - r_m^4)\cos(2k_{\beta c} L)}\right\} \ .\end{aligned} \tag{3.21}$$

3.3 Guiding of high-intensity laser pulses in plasma channels, guiding in general density profiles

Treatment of high power laser propagation in plasma channels must included nonlinear effects arising from relativistic electron motion and modification of the plasma density by the laser ponderomotive force, as described in Section 2.5. Self-consistent treatment of the laser propagation including these effects is described by the nonlinear paraxial wave equation [87]

$$\left(\nabla_\perp^2 + 2ik\frac{\partial}{\partial z}\right)\hat{a} = k_p^2\rho\hat{a} \tag{3.22}$$

with $\rho \equiv n_e(\zeta, r)/n_{e0}\gamma(\zeta, r)$ the normalized proper density and k_p the on-axis plasma wavenumber.

As a Gaussian pulse will only maintain a fixed spot size in a plasma channel in the linear regime, a more general definition of the matched spot size in the nonlinear regime is needed. Additionally, this dissertation is concerned primarily with guiding laser-heated capillary discharges, which have density profiles that often are often significantly nonparabolic. In this dissertation, the general matching condition derived in Ref. [87] is used to define a matched spot size in these circumstances. For a given radial plasma profile, the matched spot size is defined as the laser spot size w_0 such that the laser's second-order transverse moment

$$\sigma_\zeta^2(z) = \frac{\int_0^\infty r\mathrm{d}r r^2|\hat{a}(\zeta, r, z)|^2}{\int_0^\infty r\mathrm{d}r|\hat{a}(\zeta, r, z)|^2} \tag{3.23}$$

remains constant. The quasi-matched laser pulse is assumed to have a Gaussian envelope with flat phase fronts:

$$\hat{a}_{qm} = a_0\frac{w_0}{w(\zeta)}f(\zeta)e^{-r^2/w^2(\zeta)} \ , \tag{3.24}$$

with $w(\zeta)$ the slice-dependent spot size, $f(\zeta)$ the temporal profile of the laser pulse ($0 \leq f(\zeta) \leq 1$). Using Eqn. 3.22 the following quasi-matched guiding condition is obtained [87]:

$$k_p^2\int_0^\infty \mathrm{d}r r\rho(\zeta, r)\left(\frac{2r^2}{w^2(\zeta)} - 1\right)\exp\left(-\frac{2r^2}{w^2(\zeta)}\right) = \frac{1}{2} \implies \frac{\mathrm{d}\sigma_\zeta^2}{\mathrm{d}z} = 0 \ . \tag{3.25}$$

One consequence of the plasma response to the laser ponderomotive force is that, at high intensity, a quasi-matched laser pulse no longer has a single spot size. Rather, the spot size $w(\zeta)$ tapers, decreasing towards the back of the pulse due to the stronger plasma gradient present in the driven plasma wave.

In general, Eqn. 3.25 cannot be solved analytically, due to the need to self-consistently model the proper density $\rho(\zeta, r)$ with the plasma fluid equations. However, for the case of very low intensity laser pulses $a_0 \to 0$, Eqn. 3.25 becomes

$$4\pi r_e\int_0^\infty \mathrm{d}r r n_e(r)\left(\frac{2r^2}{r_m^2} - 1\right)\exp\left(-\frac{2r^2}{r_m^2}\right) = \frac{1}{2} \ , \tag{3.26}$$

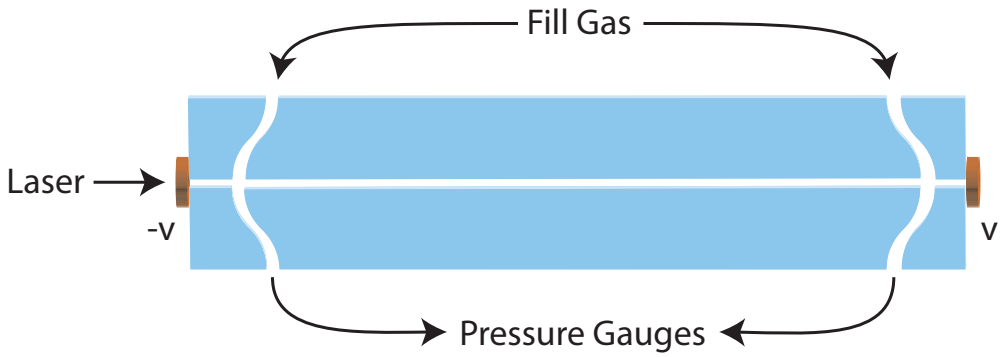

Figure 3.1: Schematic of a gas-filled capillary discharge waveguide. The center channel, the "capillary" is filled with neutral gas, which breaks down and forms an arc discharge when high voltage is applied to the electrodes at the ends. The ends of the capillary and the electrodes are open to allow passage of the laser and electron beam.

with the laser pulse once more characterized by a single matched spot r_m in the absence of a plasma wave. This is the definition of matched spot size used for non-parabolic plasma profiles in this dissertation, as is discussed in Chapter 4 and Chapter 5.

3.4 Gas-filled capillary discharge waveguides

A capillary discharge waveguide, pictured schematically in Fig. 3.1, consists of a cylindrical capillary tube filled with neutral gas in which a wall-stabilized arc discharge is driven. A pulsed high-voltage power supply connected to electrodes on both ends of the capillary drives the arc discharge, with duration $\sim$ 1 µs and peak current 100-1000 A, to form the plasma channel [17, 88]. Characteristic plasma densities and temperatures are 10^{17}-10^{19} cm^{-3} and a few eV, respectively [20, 22, 84, 89–91]. The ends of the structure, including the electrodes, are open to vacuum to allow for laser and electron beam coupling.

To survive the thermal loading of both repeated discharges and laser shots, discharge capillaries are typically fabricated from refractory materials [17], The capillaries used in the work of this dissertation were fabricated from synthetic monocrystalline sapphire (Al_2O_3), with transversely symmetrical halves of the capillary tube and gas slots laser-machined into sapphire plates that were subsequently bonded and clamped together [19, 88]. Such capillaries have been shown to survive millions of discharges with micron-scale wall erosion [92]. In the LWFA experiments of this dissertation, typical operational lifetimes of capillaries are thousands of laser shots.

The plasma formed in a capillary discharge is dominated by thermal pressure and ohmic heating. After a the arc establishes itself following a $\sim$ 100ns breakdown and initiation phase, the plasma reaches the so-called "quasi-static" condition, where the plasma density profile becomes independent of the discharge current and ceases evolving. However, the plasma

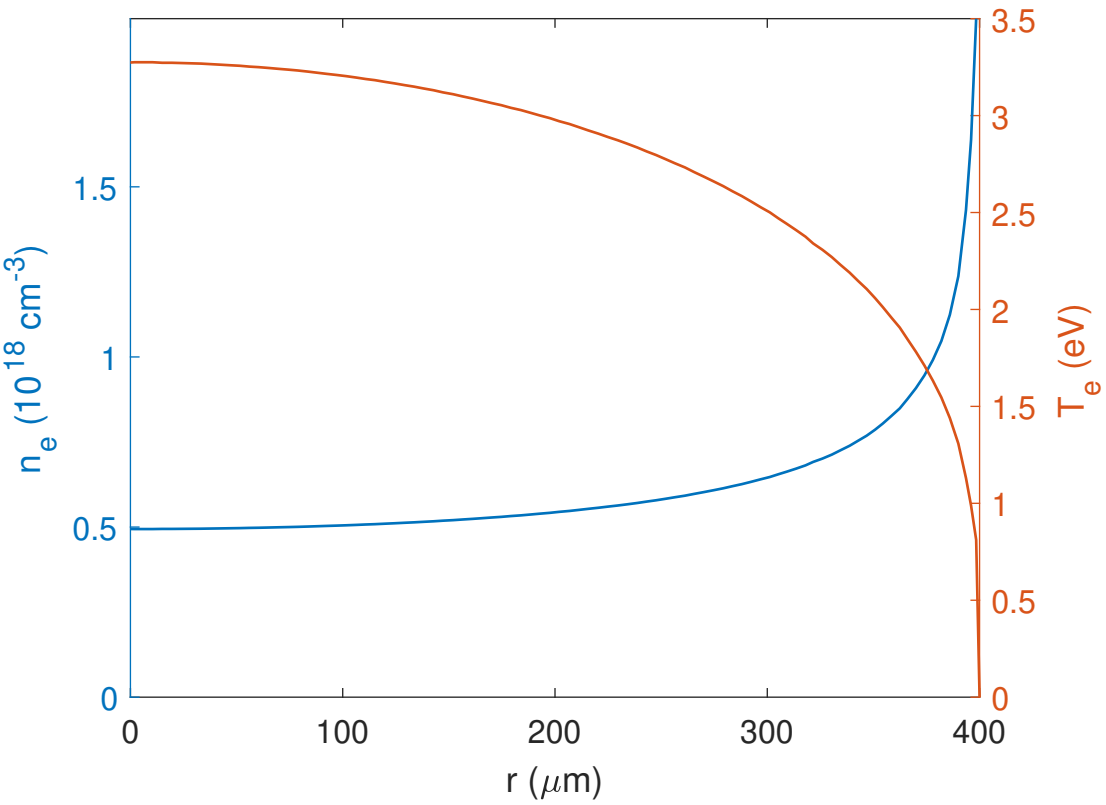

Figure 3.2: Quasi-static model of Ref. [84] solved for a 800 µm diameter capillary with $n_{e0} = 5 \times 10^{17}$ cm^{-3} and discharge current 100 A.

temperature depends on the discharge current according to $T_e \propto I^{2/5}$. Once the quasi-static condition is reached, the plasma channel is very stable, with density and matched spot size repeatable to within $< 1\%$ [93].

The density minimum on axis that enables optical guiding is a consequence of heat conduction from the plasma to the capillary walls combined with nearly uniform pressure across the capillary: $n_e \propto T_e^{-1}$ with T_e decreasing with radius. The semi-analytic "quasi-static model" for the plasma profile in a capillary discharge is presented in Ref. [84]. The model is based on an approximation of the classical plasma transport equations [94, 95] assuming radial symmetry, and requires no special computational techniques beyond the solution of a single ordinary differential equation. The output of this model has been plotted for an 800 µm diameter capillary in Fig. 3.2. The density profile of a capillary discharge waveguide is closely approximated by a parabola near the axis, with the quasi-static model giving the scaling [84]

$$r_m(\mu\text{m}) \simeq 1.37 \times 10^5 r_c(\mu\text{m})^{1/2} n_{e0}(\text{cm}^{-3})^{-1/4} \ , \tag{3.27}$$

with r_c the capillary radius.

Scalings from other computational and experimental studies have been obtained [19,

88–90], however the $r_m \propto r_c^{1/2} n_{e0}^{-1/4}$ scaling remains a common feature. This scaling dictates that the only means of tuning r_m and n_{e0} in a capillary discharge waveguide are the fill gas pressure and the capillary radius, with the latter fixed at the time of fabrication. The matched spot size r_m then becomes a strictly decreasing function of n_{e0}, leaving a capillary discharge waveguide with effectively one degree of freedom.

3.5 On the need for a laser-heated capillary discharge waveguide

The coupling of r_m and n_{e0} inherent to capillary discharge waveguides is problematic for efforts to increase the performance of channel-guided LPAs. First, reducing n_{e0} to increase energy gain requires reducing the capillary radius to avoid increasing r_m and weakening the channel, which in turn exposes the capillary to laser damage from the wings of the driver beam. For example, reducing plasma density from 7.8×10^{17} cm^{-3}, which produced 4.2 GeV with 300 TW of power from the BELLA laser, to 2.7×10^{17} cm^{-3}, which produced 7.8 GeV with 880 TW of laser power, would have required a 40% decrease in capillary radius in order to maintain the same matched spot size. However, the previous experiments on the BELLA laser with 500 μm diameter capillaries operated at $n_{e0} = 7.8 \times 10^{17}$ cm^{-3} observed destruction of the capillary by energy in the wings of the focal spot when laser power was increased above 300 TW [76]. Therefore, capillaries of that size or smaller cannot be used at petawatt-scale laser power, even with state-of-the-art laser modes.

Additionally, independent control of r_m and n_{e0} is useful for tuning of a laser-plasma accelerator: r_m can be optimized for matched guiding and n_{e0} can be optimized for acceleration, e.g. pump depletion and bunch dephasing, or bunch injection. Furthermore, at high laser power, the channel matched spot size, on-axis plasma density, plasma wave phase velocity, and laser intensity are all coupled [69]. Independent control of n_{e0} and r_m adds a degree of freedom that may be useful for optimization under this coupling. For example, an injection scheme may place constraints on laser intensity and plasma density, requiring an independent adjustment of matched spot size to preserve guiding.

In order to meet the requirements on r_m and n_{e0} for high energy electron beam production without exposing the capillary to laser damage, and independently tune r_m and n_{e0} to optimize accelerator performance, greater control of the plasma profile beyond that afforded by a conventional gas-filled capillary discharge is needed. To provide this additional control of the plasma profile independent of the capillary radius, the laser-heated capillary discharge was developed [18, 21, 22]. In this scheme, a joule-level, nanosecond-scale laser pulse is coupled into a capillary discharge waveguide, which heats the center of the plasma through inverse-bremsstrahlung absorption. The expansion of the heated plasma reduces the density on-axis, creating a channel with a smaller matched spot size than the capillary discharge alone [18]. This new structure recently enabled the production of electron beams with energies up to 7.8 GeV [21, 22].

3.6 Plasma response to inverse-bremsstrahlung heating

In a laser-heated capillary discharge, a channel is formed by the expansion of plasma near the discharge axis upon heating by an energetic laser pulse propagating collinearly with the capillary axis. Similarly to other types of laser-formed or laser-enhanced plasma channels, heating and expansion of the plasma on axis enhances the channel by lowering on-axis density and the matched spot size [78, 96]. In the regime under consideration, heating occurs through inverse-bremsstrahlung absorption [97–99], which is described by the imaginary part of the complex permittivity $\epsilon = \epsilon' + i\epsilon''$. For the relatively low laser intensities ($\sim 10^{12}$ W/cm^2) used in the experiments described here, the inverse-bremsstrahlung power density in the Kramers approximation is given by [97]

$$Q_{IB} = k\epsilon'' I = \frac{2^{5/2}\pi^{1/2}}{3} \frac{Z q_e^4 n_e I}{(k_b T_e)^{3/2} m_e^{1/2} c} \frac{\omega_p^2}{\omega^2} \Lambda, \tag{3.28}$$

with ω, k, and I the laser frequency, wavenumber, and intensity, q_e and m_e the electron charge and mass, Z the ionization degree, n_e the electron density, T_e the electron temperature, k_b the Boltzmann constant, and the Coulomb logarithm

$$\Lambda = \max\left\{ \frac{\pi}{\sqrt{3}}, \frac{1}{2} \ln \frac{2^5 (k_b T_e)^3}{\exp(5C_\gamma) \omega^2 Z^2 q_e^4 m_e} \right\}, \tag{3.29}$$

where $C_\gamma = 0.57721...$ is the Euler-Mascheroni constant. Eq. 3.28 is valid when $T_e \ll Z^2 q_e^4 m_e/\hbar^2 \sim 27Z^2$ eV, and $\omega \gg \omega_p$.

Inverse-bremsstrahlung absorption is a collisional process. Using Eq. 3.28, the coupled rate equations describing the evolution of the electron and ion temperatures (neglecting fluid motion) can be written in terms the electron ponderomotive energy $E_p = 2\pi q_e^2 I/mc\omega^2$ and an effective collision frequency $\nu_{e,IB}$ [84, 100]:

$$\frac{\mathrm{d}(k_b T_e)}{\mathrm{d}t} = \nu_{e,IB} E_p - 3\frac{m_e}{m_i} \nu_{ei} k_b (T_e - T_i) \tag{3.30}$$

$$\frac{\mathrm{d}(k_b T_i)}{\mathrm{d}t} = 3Z\frac{m_e}{m_i} \nu_{ei} k_b (T_e - T_i) \tag{3.31}$$

with m_i the ion mass, T_i the ion temperature,

$$\nu_{e,IB} = \frac{2^{7/2}\pi^{1/2}}{3} \frac{Z q_e^4 n_e}{m_e^{1/2} (k_b T_e)^{3/2}} \Lambda \tag{3.32}$$

from rearranging the factors of Eq. 3.28,

$$\nu_{ei} = \frac{4\sqrt{2\pi} q_e^4 Z^2 n_i \lambda_{ei}}{3\sqrt{m_e}(k_b T_e)^{3/2}}, \tag{3.33}$$

$$\lambda_{ei} = \frac{1}{2} \ln \frac{9(k_b T_e)^3}{4\pi Z^2 q_e^6 n_e (1 + Z T_e/T_i)}, \tag{3.34}$$

the thermal electron-ion collision frequency and Coulomb logarithm from Braginskii transport theory [84, 94, 101], and n_i the ion density.

The first term on the RHS of Eqn. 3.30 describes the heating of electrons by the extraction of ponderomotive energy at the effective collision frequency Eqn. 3.32, which is closely analogous to resistive heating and obeys a very similar scaling law:

$$\left[\frac{\mathrm{d}T_e}{\mathrm{d}t}\right]_{IB} \propto \frac{n_e I}{\omega^2 T_e^{3/2}}\Lambda. \tag{3.35}$$

It is apparent from this relation that the heating rate increases with initial plasma density and laser intensity, and decreases with temperature. Typical conditions for the experiments described here involve initial plasma temperatures T_e of a few eV, initial densities n_e of a few 10^{17} cm^{-3}, and peak laser intensities up to 4×10^{11} W/cm^2, yielding a typical heating rate of a few eV/ns.

The other terms on the RHS of Eqs. 3.30 and 3.31 describe inter-species heating of the ions and electrons. The structure of Eqs. 3.30 and 3.31 indicates that laser absorption by the plasma first proceeds through electron heating via inverse-bremsstrahlung, followed by collisional ion heating by the electrons. Therefore, the absorptivity of the plasma is not only dependent on the thermodynamic state of the electron fluid, but also its coupling to the ion fluid. Generally, this implies that $T_e > T_i$ during plasma heating if it occurs on a shorter timescale than the characteristic time for electron-ion heating $\tau_T = m_i/3m_e\nu_{ei}$. For the typical plasma parameters previously stated, the electron collision time $1/\nu_{ei} \lesssim 1$ ps from Eq. 3.33 yields an electron-ion heating timescale τ_T of order 100 ps. Hence, for the plasmas considered here, the approximation $T_e \approx T_i$ can be made for inverse-bremsstrahlung heating with few-ns laser pulse lengths, in which case the absorbed laser energy can be regarded as being equally partitioned between electrons and ions instantaneously and the temperature evolution is given by

$$\frac{\mathrm{d}(k_b T_e)}{\mathrm{d}t} = \frac{\mathrm{d}(k_b T_i)}{\mathrm{d}t} = \frac{1}{2}\nu_{e,IB} E_p \ . \tag{3.36}$$

The effect of plasma motion in response to heating on the propagation of the heater beam is an important consideration in the formation of a channel by laser heating. The effect becomes important if the laser pulse length is similar to the time scale for plasma motion, which can be estimated with the ion acoustic speed $c_s = \sqrt{(k_b T_e + k_b T_i)/m_i}$, with T_i and m_i the ion temperature and mass. For plasma parameters representative of these experiments, and taking the spatial scale length L equal to the heater laser beam waist $r_{0,h} = 82$ μm, the time scale for plasma motion is ~ 3 ns.

The first simulations of laser-heated capillary discharges considered a 1 ns pulse length, which was chosen to be shorter than the plasma motion timescale [18]. In this regime, the heater beam propagation is mostly decoupled from plasma motion because the plasma is nearly stationary during the pulse, and the pulse propagates as in a linear medium. However, this also requires that the heater be matched to the initial discharge channel to avoid oscillations and nonuniform energy deposition. This limits the heater spot size to the matched spot size

of the initial discharge channel, which for the parameters of interest is quite large, and thus limits the matched spot size of the heated channel. In Ref [18]., the heater beam reduced the matched spot size of the channel from 145 μm to 100 μm. This is much larger than the ~ 60 μm focal spot of the BELLA laser, and insufficient for good confinement of driver energy toward the axis, even accounting for self-focusing effects.

It can be advantageous to use heater pulses significantly longer than the few-ns plasma motion time scale. In this regime, plasma expansion during heating forms a channel during the rise of the pulse, and therefore much of the energy is guided with a smaller effective matched spot size than the discharge alone. This "self-channeling" effect relaxes the requirement to match the heater beam spot to the initial discharge channel, enabling the production of smaller matched spot sizes than in the short pulse regime [21, 22]. To take advantage of this effect, an 8 ns heater pulse length was used in the electron beam production experiments in Refs [21, 22]. and the experiments reported here.

From the preceding discussion, it is clear that formation of a plasma channel in a capillary discharge by laser heating is dynamic process. From the ion acoustic speed and the laser pulse length, the characteristic timescales involved are on the order of nanoseconds. Hence, effective implementation of a laser-heated gas-filled capillary discharge as a guiding structure for LWFA requires detailed characterization of the plasma evolution. Diagnostic measurements and simulations of channel formation in laser-heated capillary discharges, including both the on-axis density and the matched spot size, are the subject of Chapters 4 and 5.

Chapter 4

Diagnostic measurements of laser-heated capillary discharges and a parameter study of channel properties

4.1 Introduction

In this chapter, experiments are described in which key properties of laser-heated capillary discharges are measured, specifically the on-axis plasma density and matched spot size. These are critical parameters for accelerator performance, with on-axis plasma density determining the maximum energy gain as discussed in Chapter 2, and matched spot size determining the extent to which the driver laser energy is confined to the channel as discussed in Chapter 3. Magnetohydrodynamic simulations of laser-heated capillary discharges were performed using the MARPLE code[102], and found to be in excellent agreement with measurements. It was found that laser-heating produced plasma channels with considerably smaller matched spot size and lower on-axis plasma density than possible using conventional capillary discharge waveguides of the same radius, and it was found that channel parameters could be tuned over a wide range by adjusting laser and plasma parameters. Additionally, the work described here is the source of the channel parameters reported for the electron acceleration experiments described in Chapter 6 and Refs. [21, 22]. The text and figures of this chapter have been adapted from the author's previously published work, Ref. [20].

The longitudinally-averaged plasma density on the channel axis $\overline{n}_{e0}$ was diagnosed by measuring the average group velocity of the guided probe pulses using spectral interferometry [91, 103]. The group velocity of a plane electromagnetic wave propagating in a homogeneous plasma is $\beta_g = v_g/c \simeq 1 - \beta_{n_{e0}}$, with $\beta_{n_{e0}} = k_p^2/2k^2$, and k_p and k the plasma and laser wavenumbers. The small term $\beta_{n_{e0}}$ is proportional to plasma density and manifests as an additional delay of the probe pulse compared to propagation through vacuum. Neglecting transverse variation of the plasma profile, for a 20 cm capillary with an on-axis density of 3×10^{17} cm^{-3}, this yields an additional group delay $\Delta T \approx 60$ fs relative to vacuum. This

delay is too small to be resolved electronically (e.g. with a photodiode), but it is readily resolved with spectral interferometry.

In practice, the average group velocity is obtained by measuring the additional group delay induced by propagation through the channel as compared to vacuum. The experiment configuration for performing this measurement is shown schematically in Fig. 4.1. The plasma channel is placed in one arm of a Mach-Zehnder interferometer, the "probe line," on a stage that allows it to be moved in and out of the beam path. The other arm of the interferometer, the "reference line" is static. The relative delay between the probe and reference pulses is measured after they are recombined at the output of the interferometer. The delay itself is measured from the spectrum of the combined probe and reference pulses, which produce a frequency-domain interferogram that encodes the delay between the two pulses. The additional delay induced by the plasma channel is determined by measuring the relative pulse delay with the channel out of the probe line T_{vac} (Fig. 4.1(a)), then with the channel inserted in the probe line T (Fig. 4.1(b)), and then taking the difference ΔT. Mathematically:

$$\Delta T \equiv T - T_{vac} = \frac{1}{c}\int_0^L \left(\frac{1}{\beta_g} - 1\right) \mathrm{d}z, \tag{4.1}$$

with L the path length traversed in the channel, which is typically the capillary length. The group velocity β_g of a laser pulse propagating in an longitudinally uniform parabolic channel is given by the following formula [48]

$$\beta_g = \frac{v_g}{c} \simeq 1 - \beta_{g,n_e} - \beta_{g,geo} \tag{4.2}$$

with the component $\beta_{g,n_e} = k_p^2/2k^2$ from the on-axis plasma density n_{e0}, and the geometrical component $\beta_{g,geo} \propto r_m^{-2}$ from the finite matched spot size of the channel. The total contribution of $\beta_{g,n_{e0}}$ and $\beta_{g,geo}$ is typically $\lesssim 10^{-4}$, and so Eq. (4.1) can be simplified to the following expression, substituting in Eq. (4.2):

$$\Delta T \simeq \frac{1}{c}\int_0^L (\beta_{g,n_{e0}} + \beta_{g,geo})\, \mathrm{d}z,$$

yielding

$$\Delta T \simeq \frac{L}{c}(\overline{\beta}_{g,n_e} + \overline{\beta}_{g,geo}) \ . \tag{4.3}$$

Note that in order to obtain the density from $\overline{\beta}_{g,n_{e0}}$, the geometrical component of the group velocity $\overline{\beta}_{g,geo}$, and so r_m, must be known to measure n_{e0}. Therefore, measurements of r_m are required to diagnose n_{e0} accurately. For the experiments described in this chapter, r_m was diagnosed using the properties of laser guiding in plasma channels described in Chapter 3 and Ref. [86].

This chapter is organized as follows. In Section 7.2, the experiment setup is described, including the heater and probe lasers, and the spectral interferometer. In Section 4.3, the

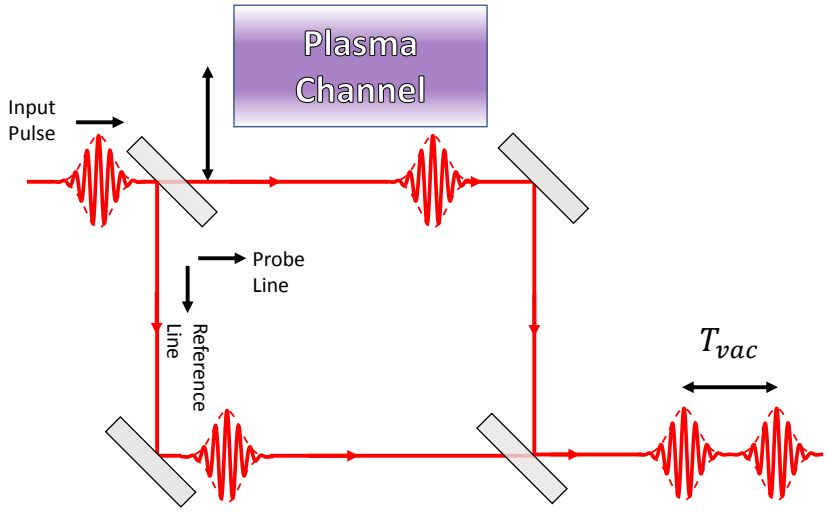

(a) "Vacuum pulse delay" T_{vac} measurement, with the plasma channel (i.e. capillary) removed from the beam path.

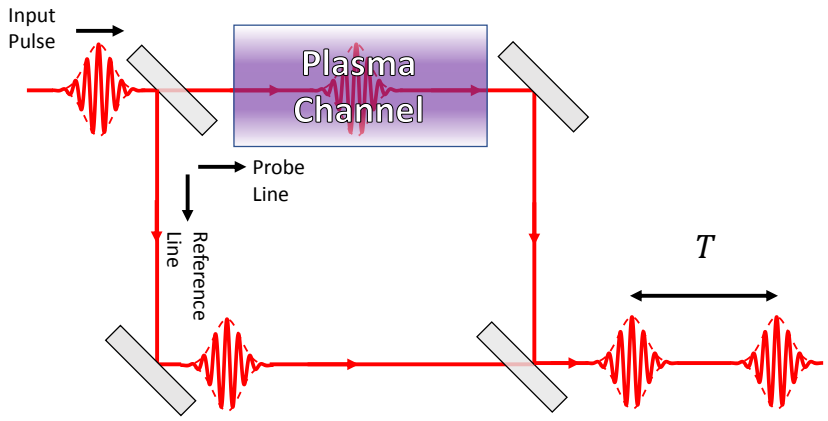

(b) Pulse delay measurement with the plasma channel inserted into the probe beam path.

Figure 4.1: Schematic representation of the group-velocity-based plasma density diagnostic. The delay induced by the plasma channel relative to vacuum, from which the density is can be calculated via Eqn. 4.25, is obtained by taking the difference between to the delay measured for the probe pulse propagating in vacuum (a) and the delay measured for the probe pulse propagating through the plasma channel (b).

analysis algorithm used to analyze the spectral interferograms is described. The matched spot size diagnostic is described in Section 4.4. Systematic errors from geometrical effects, specifically finite matched spot size and asymmetry of the channel formed by laser-heating, are described in Section 4.5. The results of experimental measurements and simulations of the formation of a plasma channel by laser heating are presented in Section 4.6. Tuning of channel properties via laser and plasma parameters is described in Section 4.7. Conclusions are summarized in Section 4.8.

4.2 Experiment setup and methods

The experiments described in this chapter were performed on the Plasma 2 test stand, which is a vacuum chamber independent of the main BELLA laser beam line and is used for LPA target development. The setup used for the experiments described in this chapter is pictured schematically in Fig. 4.2. The capillary and heater laser system were selected to match the parameters of the electron acceleration experiments of Refs [21, 22]. and Chapter 6.

The capillary design is essentially the same as the example shown in Chapter 3. A 800 μm-diameter, 20 cm-long hydrogen-filled capillary was used, driven by a high voltage pulser generating current pulses of the form shown in Fig. 4.3, which peak at 450 A with a FWHM of 500 ns. An electronic pressure controller was used to control gas flow into the capillary, and thus the fill pressure, while a separate set of gas lines and pressure gauges were used to measure the fill pressure. The capillary was mounted on a motorized hexapod stage inside the vacuum chamber, allowing it to be positioned in 6-axes with micron position. The hexapod was used to align the capillary to the laser beams, as well as move it in and out of the beam path for performing delay measurements as described in Section 4.1.

A frequency-doubled Continuum Powerlite Nd:YAG laser system was used for laser heating, which supplied 900 mJ, 8 ns FWHM pulses at 532 nm at 10 Hz, with a 12 mm beam diameter. The repetition rate of the heater laser was cut to 1 Hz to match the repetition rate of the discharge using a mechanical shutter installed after the laser output (not shown). The laser energy was tuned using the combination of a half-wave plate and polarizer. After the polarizer, a 6 mm diameter ceramic iris was installed (not shown), as it was found that excluding the outer portions of the laser beam improved the quality of the focal spot. The beam was expanded using a Keplerian telescope, consisting of a 550 mm plano-convex lens H-TL1 and 1100 mm plano-convex lens HTL-2 165 cm downstream. This particular telescope configuration was chosen to enable the use of a spatial filter at the beam waist, however this capability was not used for these experiments. A vacuum extension is installed between HTL-1,2 to avoid ionization of air at the beam waist. After HTL-2, the beam propagated 185 cm to the final focusing lens FF-1, a 1660 mm plano-convex lens. The slightly divergent heater beam had a diameter of $\sim$ 15 mm at FF-1, and propagates a further 170 cm to focus inside the plasma 2 vacuum chamber, being coupled in through an AR-coated vacuum window. The resulting laser focal spot had $1/e^2$ spot size of 82 μm. The heater laser beam was non-Gaussian and significantly asymmetric in the midfield, which is evident in the beam

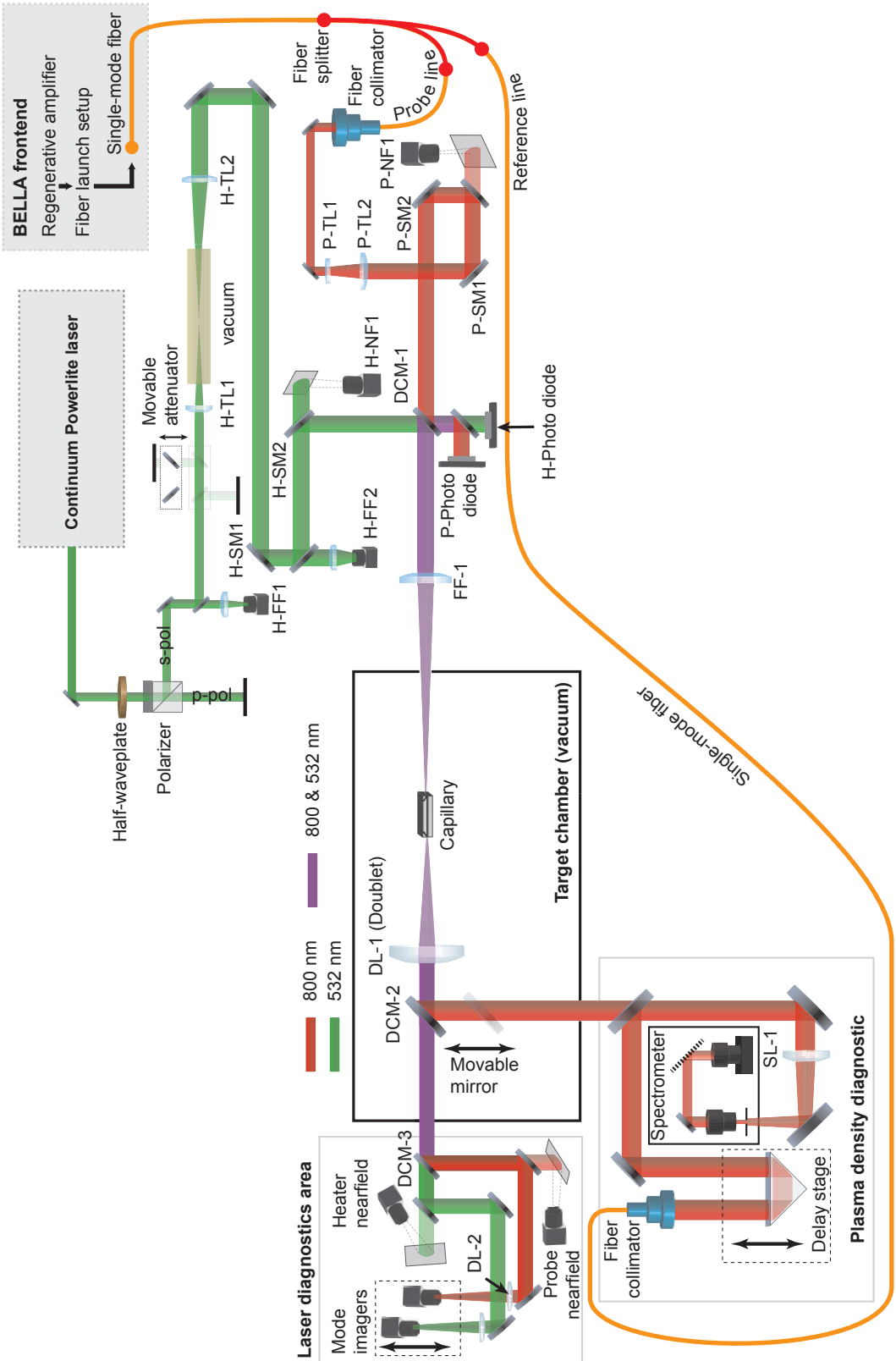

Figure 4.2: Layout of the plasma 2 setup. Heater beam (532 nm) is marked in green, probe beam (800 nm) is marked in red, and areas where the two wavelengths copropagate are marked in purple.

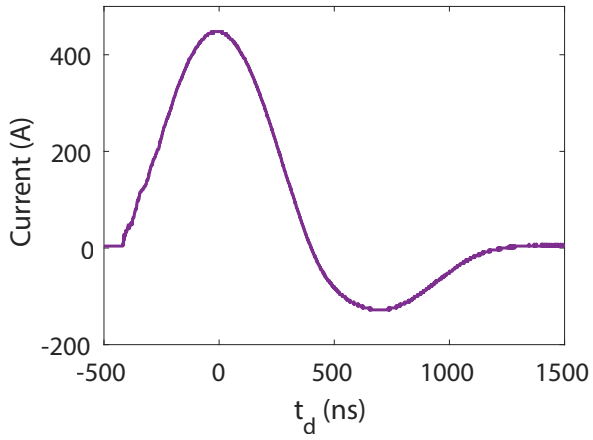

Figure 4.3: Discharge current trace measured with an inductive current monitor on the high voltage lead and a 500 MHz bandwidth oscilloscope.

profiles shown in Fig. 4.4(b). After accounting for transmission through all the optics of the setup, the heater laser system delivered a maximum pulse energy of 300 mJ at the target. The parameters of this heater laser system—namely pulse energy, pulse length, and spot size—closely match those of the heater laser used for the electron acceleration experiments of Refs. [21, 22] and Chapter 6, albeit with greater beam asymmetry.

A separate probe laser was used to diagnose channel properties. It consisted of 4 nJ sub-ns pulses at 780 nm with 30 nm bandwidth carried by a single mode fiber . which were injected collinearly with the heater laser using a fiber collimator and Galilean telescope. The probe pulses originate at the BELLA laser frontend, where they are extracted as rejected light from a polarizer after the regenerative amplifier and then coupled into the single mode fiber through a microscope objective. The pulses are then transported through 30 m of single-mode fiber to the Plasma 2 setup. Pulse lengths are ~ 200 ps at the fiber input. Given the group velocity dispersion GVD $\equiv \mathrm{d}(v_g^{-1})/\mathrm{d}\omega = 36$ fs^2/mm in fused silica [104], the fiber guided probe pulses are stretched an estimated additional ~ 100 ps during their propagation to the test stand.

The probe beam is launched into the Plasma 2 setup using a $f = 12$ mm fiber collimator for an initial beam diameter of 2.5 mm, and expanded with a magnification 5$\times$ Galilean telescope, consisting of a -50 mm plano-concave (P-TL1) lens and 300 mm plano-convex lens (P-TL2) installed 25 cm apart. The probe beam was injected into the system collinearly with the heater beam through the dichroic mirror DCM-1, and focused to the target by the final focus lens FF-1. The probe beam was near Gaussian at focus, as can be seen in Fig. 4.4(a) and Fig. 4.5, with a 73 μm waist. However, the multimode content of the probe beam is evident away from focus in Fig. 4.4(a), and the probe was found to have a beam quality factor $M^2 = \pi\theta_0 r_0/2\lambda \lesssim 1.3$, with θ_0 the divergence angle, and λ the laser wavelength ($M^2 = 1$ for a pure Gaussian TEM$_{00}$ beam) [105, 106].

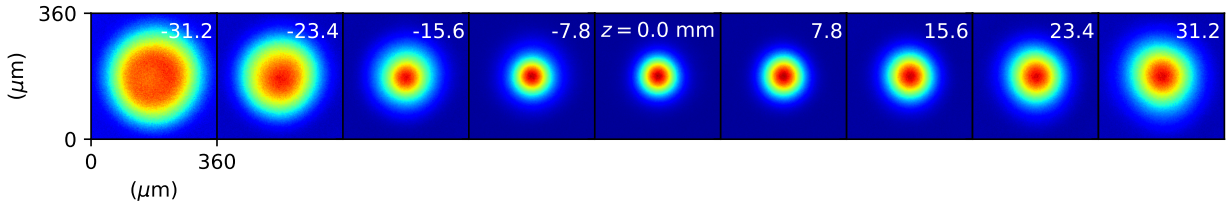

(a) Probe beam. Note the asymmetry about $z = 0$ mm, and the fluence minimum at $z = -31.2$ mm, indicating multimode content.

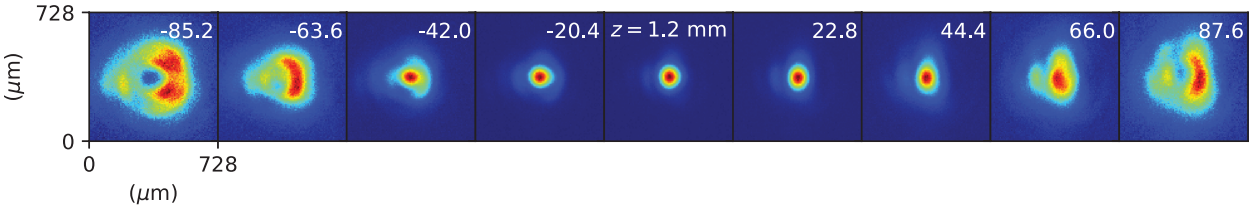

(b) Heater beam.

Figure 4.4: Fluence profiles of the laser beams, plotted for various distances from focus ($z = 0$ mm), defined as the location of maximum peak fluence. Colorscale is normalized for each image.

Separate CCD cameras for each laser wavelength were used for beam tuning and imaging the transmitted laser beam at the capillary exit. For accurate measurements, it is essential to align the probe precisely to the laser-heated channel. This was done by first aligning the probe and heater beams to each other in vacuum, and then aligning the capillary to the heater beam. To facilitate this, the probe imaging line consisted of a 400-700 nm achromatic doublet in the chamber (DL-1) after the capillary and a second 400-700 nm doublet (DL-2) before the stage mounted microscope lens and camera, and was capable of imaging the heater beam with an appropriate change of filtration. This system was used to overlap the probe and heater beam to within ≤ 20 μm in position and ≤ 100 μrad in angle.

The relative delay of the probe and heater pulses, as well as the heater pulse shape, were recorded for every shot with a pair of photodiodes upstream of the target. Leakage light from the dichroic mirror DCM-1 was separated into both wavelengths with a dichroic optic, which were then sent to the photodiodes. The RMS timing jitter between the two pulses was ~ 0.3 ns

A fiber-based spectral interferometer was built for performing the group velocity measurements. A 50-50 fiber splitter upstream of the fiber collimator split the probe pulses, sending one copy through the target and another to the reference arm of the interferometer. A movable dichroic optic was positioned inside the target chamber after the collimating doublet that can be moved into the beam line to send probe pulses to the interferometer for group velocity measurements. Although the spectrometer does not image the capillary exit, the collimating doublet DL-1 and the lens SL-1 before the slit render the delay measurement

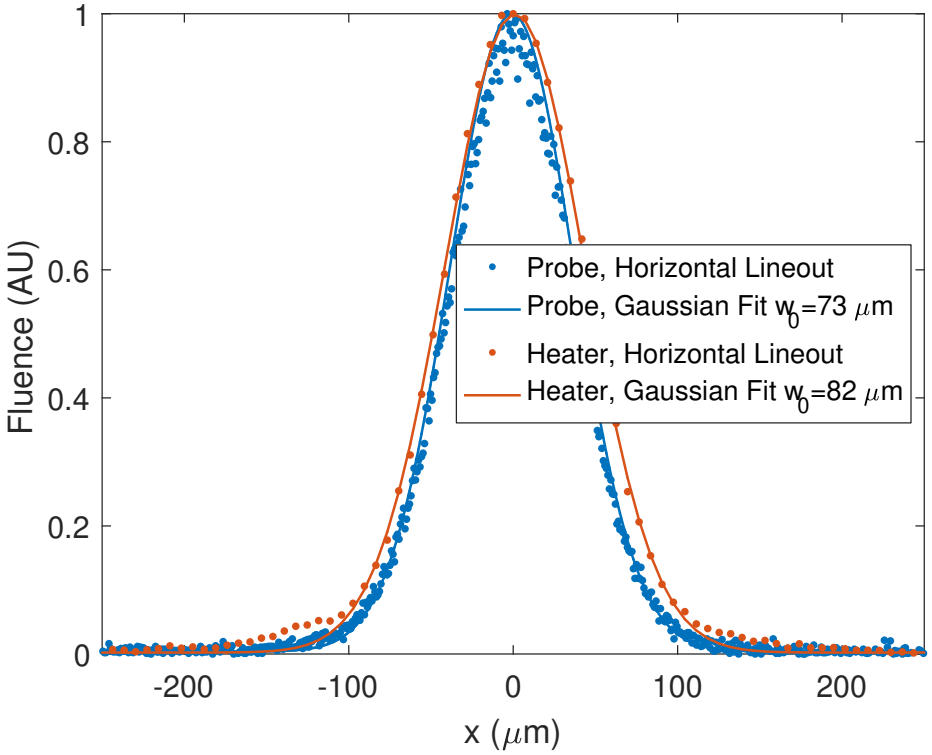

Figure 4.5: Lineouts of the laser modes at focus of Fig. 4.4.

insensitive to displacement and angular deflection of the probe beam in the capillary exit plane. Ray tracing simulations[107] showed that these effects contribute an uncertainty $\lesssim 1$ fs, or $\lesssim 5 \times 10^{15}$ cm^{-3} in these experiments.

4.3 Group velocity measurements and spectral fringe pattern analysis

The most important source of random error in the density measurement is jitter in the relative delay of the probe and reference pulses from the vibration of optics in the setup. Prior experiments using group velocity measurement as a density diagnostic for conventional capillary discharges implemented a standard Mach-Zehnder interferometer configuration, with all optical paths in free space [91, 103]. This was acceptable because optical path lengths in the setup needed only be two or three times the length of the capillary, which was 9 cm at the longest, yielding a total path length around the interferometer ~ 2 m.

To perform the same diagnostic measurement for laser heated capillary discharges requires coupling in the probe pulse collinearly with the heater pulse so as to inject it into the channel formed by plasma heating and expansion, which in turn requires long optical path lengths (1-2 m standoff from the target) to keep the heater fluence at safe levels ($\lesssim 0.5$ J/cm^2) on

the required beam combining optics. Since the additional length of a beam deflected from a straight path between two optics a distance L from one another by angle $\delta\theta$ is $\sim \delta\theta^2 L/2$, the longer path lengths involved in a setup implementing a laser-heater will introduce a proportionately larger delay jitter. The experiments of Refs. [91, 103] observed a 1-2 fs delay jitter, corresponding to a density measurement error of $\lesssim 0.2 \times 10^{17}$ cm^{-3} for a 9 cm capillary, which was acceptable for the plasma densities of interest in the range $5 - 10 \times 10^{17}$ cm^{-3}. Given the ~ 3 m distance between the final focusing lens and the collimating doublet in the setup of Fig. 4.2, at least 6 m of total path length is required in the interferometer, and therefore at least 3 times this delay jitter is to be expected: 3-6 fs, or 0.6×10^{17} cm^{-3} for the same capillary length. For the densities of interest for laser-heater experiments, 2×10^{17} cm^{-3}, this constitutes a $> 25\%$ error and so a means to reduce it was sought.

Optical fibers were used in the interferometer to reduce this delay jitter by eliminating free space path length between optics. However, this in turn introduced a relative spectral chirp between the probe and reference pulses and a slow drift in the vacuum propagation (i.e. with no capillary in the beam path) group delay. These issues necessitated different analysis techniques from the earlier group velocity measurements described in Refs. [91, 103]. Specifically, fast-Fourier-transform (FFT)-based phase mapping [108] and a data acquisition procedure that tracked the group delay drift during measurements. These techniques will now be discussed in detail.

Interferogram analysis

In general, a spectral interferogram formed by the interference of two laser pulses a_1 and a_2 as recorded by the setup of Fig. 4.2 has the mathematical form

$$g(\omega, y) = |a_1(\omega, y) + a_2(\omega, y)|^2 \tag{4.4}$$

$$g(\omega, y) = |a_1(\omega, y)|^2 + |a_2(\omega, y)|^2 + 2|a_1(\omega, y)||a_2(\omega, y)| \cos[\phi(\omega, y)] \tag{4.5}$$

with ω frequency, y the coordinate along the spectrometer slit, and $\phi(\omega, y)$ the relative spectral phase. Measurement of the relative pulse group delay is a matter of extracting the relative phase $\phi(\omega, y)$.

Extracting the relative group delay is straightforward for the simple case of two identical laser pulses separated from each other by a delay τ_0, which corresponds to a spectral phase $\omega\tau$ and the spectral interferogram

$$g_{lin}(\omega, y) = 2|a_0(\omega, y)|^2[1 + \cos(\omega\tau_0)] \tag{4.6}$$

The FFT of Eqn. 4.6 into the τ domain has two narrow sidebands centered at $\pm\tau_0$:

$$\mathrm{FFT}\{g_{lin}(\omega, y)\} \equiv G_{lin}(\tau, y) = 2A_0(\tau, y) + 2A_0(\tau - \tau_0, y) + 2A_0(\tau + \tau_0, y) \ , \tag{4.7}$$

with $A_0 \equiv \mathrm{FFT}\{|a_0(\omega, y)|^2\}$. For such sidebands, the group delay τ_0 is obtained simply by computing the centroid of the sideband $2A_0(\tau - \tau_0, y)$ as in Refs. [91, 103, 108]. Note that by

the convention adopted for this discussion, the FFT transforms the interferogram into the "frequency" domain denoted by the variable τ which has units of s because the interferogram is initially recorded in the "time" domain denoted by ω with units of s^{-1}.

The interferograms generated by the fiber-based spectral interferometer of Fig. 4.2, shown in Fig. 4.6(a), have a more complex structure than Eqn. 4.6. In the ω dimension, there is chirping of the fringes due to the quadratic spectral phase induced by the optical fiber, as well as a prominent phase null. There is a small variation of the phase in the y dimension from the mismatched divergences of the probe and reference beams. The structure in the ω dimension requires a more robust analysis technique than calculation of sideband centroids to extract the relative group delay. The algorithm described in Ref. [108] was adapted for this purpose, which will now be described. For simplicity, the interference pattern Eqn. 4.5 is rewritten

$$g(\omega, y) = a(\omega, y) + b(\omega, y)\cos\phi \ , \tag{4.8}$$

with a and b real. If the relative phase has a rapidly varying component or large central frequency (i.e. a large group delay in this context), then the relative phase can be decomposed as $\phi(\omega, y) = \omega\tau_0 + \phi_{slow}(\omega, y)$ and the interference pattern can be expressed in terms of complex exponentials as

$$g(\omega, y) = a(\omega, y) + c(\omega, y)\exp(i\omega\tau_0) + c^*(\omega, y)\exp(-i\omega\tau_0) \tag{4.9}$$

with

$$c(\omega, y) = (1/2)b(\omega, y)\exp[i\phi_{slow}(\omega, y)] \tag{4.10}$$

The FFT of Eqn. 4.9 is then

$$G(\tau, y) = A(\tau, y) + C(\tau - \tau_0, y) + C^*(\tau + \tau_0, y) \tag{4.11}$$

with τ_0 the central frequency of the interference pattern.

If the central frequency τ_0 is sufficiently large in comparison to the width of the sidebands C in Eqn. 4.11, these sidebands will be well separated from one another as well as the zero-frequency peak A. This separation of the sidebands is crucial to the function of the algorithm because it allows geometric isolation of the complex quantities $c(\omega, y)exp(i\omega\tau_0)$ in τ-space that contain the relative spectral phase. To produce such isolated sidebands for analysis of the spectral interferogram, a Gaussian windowing function was applied the fringe pattern as shown in Fig. 4.6 (b) to suppress the phase null visible in Fig. 4.6 (a). The absolute value of the FFT of the windowed fringe pattern of Fig. 4.6 (b) is shown in Fig. 4.6 (c), with the sidebands of Eqn. 4.11 clearly visible. Note that these sidebands are quite wide–on the order of 500 fs. The uncertainty in the true value of the center frequency τ_0 this creates precludes the use of the simple peak fitting method used in the experiments of Refs. [91, 103], where the FFT sidebands had smaller widths ~ 50 fs.

To retrieve $\phi(\omega, y)$ from the interferogram, one of the complex components $c(\omega, y)\exp(i\omega\tau_0)$ must be isolated from Eqn. 4.9. This is accomplished by selecting a region of the fringe pattern FFT containing the corresponding sideband $C(\tau - \tau_0, y)$ as shown by the dotted lines

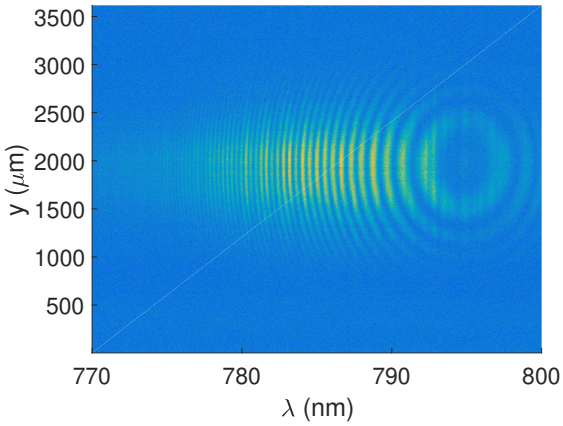

(a) Raw spectral interferogram. Note the chirping of the fringes, and the phase null at ~ 795 nm.

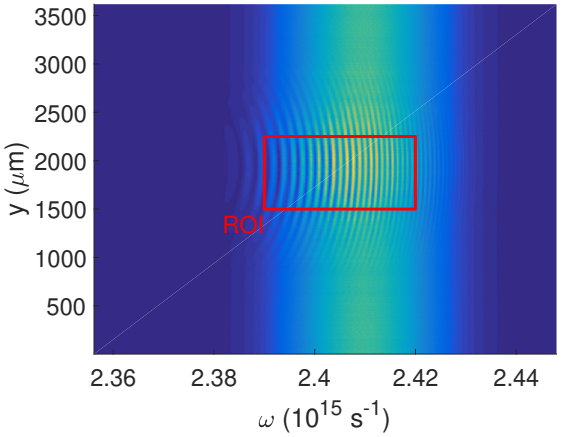

(b) Interferogram of (a), denoised with an SVD reconstruction truncated to 10 eigenvalues, remapped into angular frequency ω, with a Gaussian window applied to suppress the phase null.

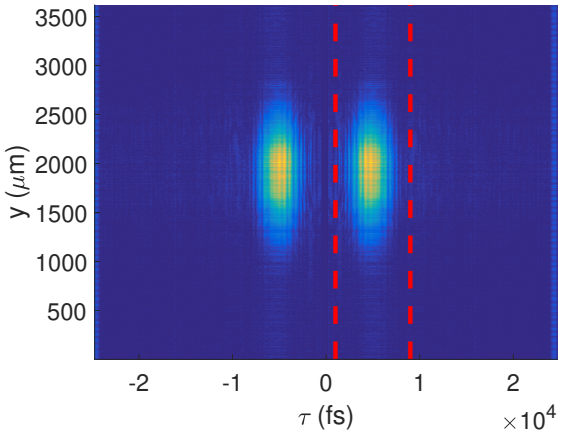

(c) Absolute value of the FFT of (b). Near-zero frequencies have been suppressed to emphasize the sidebands. Dotted lines denote the region used to extract the interferogram phase.

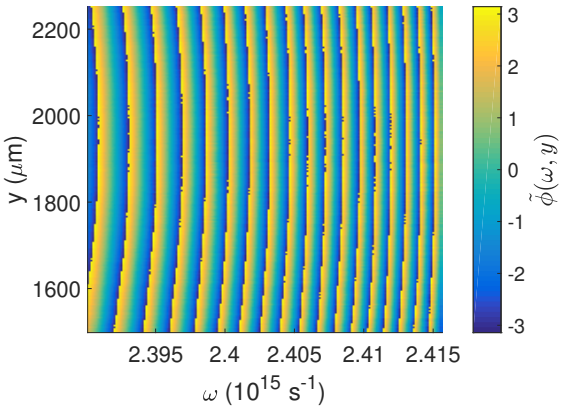

(d) $(-\pi, \pi]$ wrapped phase over the ROI marked in (b) extracted from the FFT sideband of (c).

Figure 4.6: Phase mapping algorithm adapted from Ref. [108]. The underlying phase of the interferogram (a) is extracted from the sideband of the FFT (c) of the interferogram after windowing to suppress the phase null (c). The extracted phase $\tilde{\phi}(\omega, y)$ is wrapped over $(-\pi, \pi]$, requiring the use of a phase unwrapping algorithm.

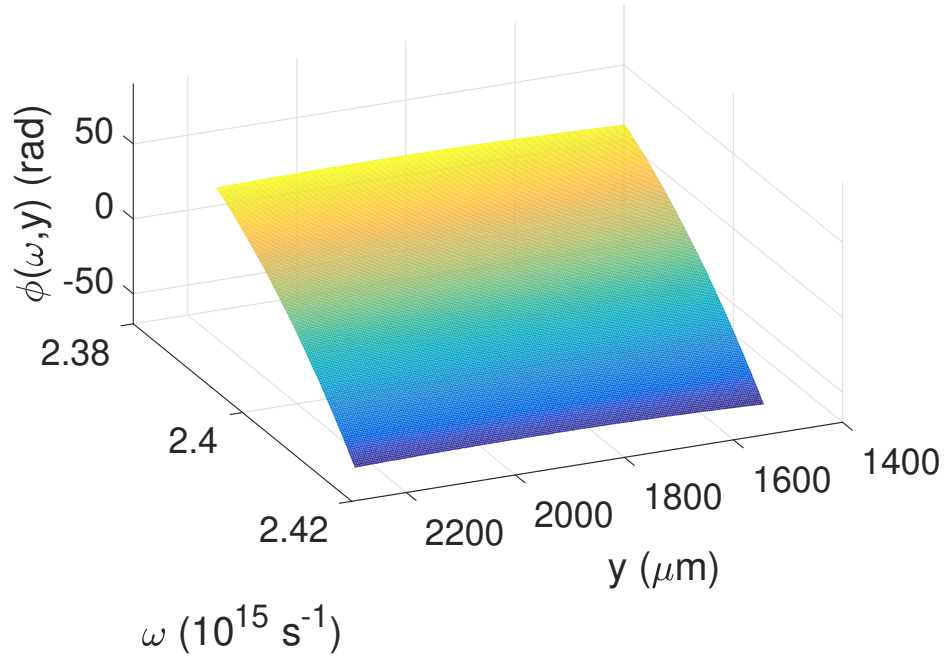

Figure 4.7: Fringe pattern phase surface constructed by unwrapping the phase plotted in 4.6(d).

in Fig. 4.6 (c), setting all data outside this region to zero, and performing an inverse FFT. The resulting complex-valued function

$$\mathrm{FFT}^{-1}\{C(\tau-\tau_0,y)\} = c(\omega,y)\exp(i\omega\tau_0) = (1/2)b(\omega,y)\exp(i\phi(\omega,y)) \tag{4.12}$$

contains the relative spectral phase in the complex angle.

The complex angle $\phi(\omega,y)$ can be readily computed trigonometrically from Eqn. 4.12. However, the angle $\tilde{\phi}(\omega,y)$ obtained by simple trigonometric operations on the real and complex components of Eqn. 4.12 is "wrapped" onto the domain $(-\pi,\pi]$, as shown in Fig. 4.6(d) over the ROI marked in Fig. 4.6(b). Obtaining the continuous phase $\phi(\omega,y)$ requires the use of a phase unwrapping algorithm [109], which for the wrapped phase of Fig. 4.6(d) yields the phase $\phi(\omega,y)$ plotted in Fig. 4.7. It should be noted that the phase unwrapping only permits modulus 2π knowledge of the phase, however this is of no detriment to the analysis. This is because the uncertainty in the absolute phase effectively constitutes an unknown constant offset of the phase and thus has no effect on the group delay $\mathrm{d}\phi/\mathrm{d}\omega$, which is the quantity of interest.

The preceding discussion has described how the relative spectral phase between the probe and reference pulses is obtained from a spectral interferogram of the type shown in Fig. 4.6. However, further analysis of the retrieved spectral phase is required to obtain a measurement of the plasma density. The spectral phase plotted in Fig. 4.6 consists of the components

$$\phi(\omega,y) = \phi_0 + [\phi'_{target}(y) + \phi'_{sys}(y)]\omega + \frac{1}{2}\phi''_{fiber}\omega^2 \ , \tag{4.13}$$

with ϕ_0 a uniform phase offset, $\phi'_{target}(y)$ the relative group delay associated with the target region with or without the target present (e.g. the 20-cm-long region occupied by a 20-cm-long capillary), $\phi'_{sys}(y)$ the relative group delay associated with all other parts of the system excluding the target region, and ϕ''_{fiber} the relative group delay dispersion arising from the different fiber lengths in the probe and reference arms of the interferometer.

The group delay induced by the channel, from which the plasma density is determined, is obtained by a "background subtraction" of the spectral phase measured for propagation in vacuum from the spectral phase measured for propagation through the plasma channel:

$$\Delta\phi(\omega, y) = \phi_p(\omega, y) - \phi_v(\omega, y) \tag{4.14}$$

with $\phi_p(\omega, y)$ the measured phase with the plasma channel in the beam path, and $\phi_v(\omega, y)$ the phase for propagation in vacuum. Because the insertion of the plasma channel does not affect any of the other terms in Eqn. 4.13, this yields the linear spectral phase contributed by the plasma in the target region alone,

$$\Delta\phi(\omega, y) = \Delta\phi_0 + [\phi'_{p,target}(y) - \phi'_{v,target}(y)]\omega = \Delta\phi_0 + \Delta\phi'_p(\omega, y)\omega \tag{4.15}$$

with $\Delta\phi_0$ a uniform phase offset arising from the previously discussed difficulties in determining absolute phase, and $\Delta\phi'_p(y)$ the group delay induced by the plasma channel, which is the quantity required for the plasma density measurement itself. The channel induced group delay itself $\Delta\phi'_p(y)$ is obtained from the "background subtracted" spectral phase through a linear fit of $\Delta\phi(\omega, y)$ with respect to ω, with the first-order coefficient giving the value of $\Delta\phi'_p(y)$.

The implementation of this background subtraction and fitting procedure is shown in Fig. 4.8. In Fig. 4.8(a) and Fig. 4.8(b) are shown the retrieved spectral phase surfaces $\phi_p(\omega, y)$ and $\phi_v(\omega, y)$, for propagation through a 20-cm-long capillary at 20 torr fill pressure at the peak of discharge current ($\sim$ 450 A) and vacuum, respectively. Both of these surfaces possess a noticeable curvature in the ω axis, due to the quadratic spectral phase term in Eqn. 4.13 from the optical fibers. The surface $\Delta\phi(\omega, y) = \phi_p(\omega, y) - \phi_v(\omega, y)$ is shown in Fig. 4.8(c). The common quadratic component has been removed by the background subtraction to yield a purely linear dependence with respect to ω. Moreover, this linear component of the background-subtracted spectral phase is the exclusive contribution of the plasma channel, per Eqn. 4.15. As noted before, the curvature visible in $\Delta\phi(\omega, y)$ in the y direction arises from the differing divergences of the probe and reference beams at the spectrometer slit.

$\Delta\phi'_p(y)$ is obtained by linear fitting of $\Delta\phi(\omega, y)$ with respect to ω at each y index. As an example, the center row of pixels in Fig. 4.8(c) is highlighted in red, and has been plotted in Fig. 4.8(d) with its least-squares fit. The "RMS error" of the fit is defined as the norm of the fit residuals divided by the number of samples $RMS \equiv \sqrt{\sum_i^N (y_{fit} - y_i)^2/N}$. This is used as a rough diagnostic for the quality of the phase fitting, with reliable measurements empirically having $RMS < 10^{-2}$. First order coefficient of the fit shown in Fig. 4.8(d), corresponds to a channel-induced delay of $\Delta\phi'_p = 80.2$ fs at the centroid of the laser beam.

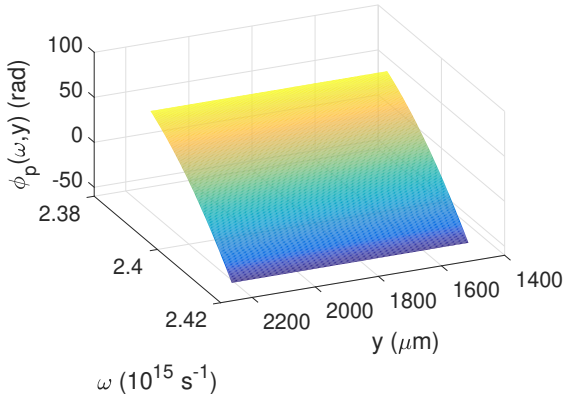

(a) Spectral phase ϕ_p, capillary in beam path.

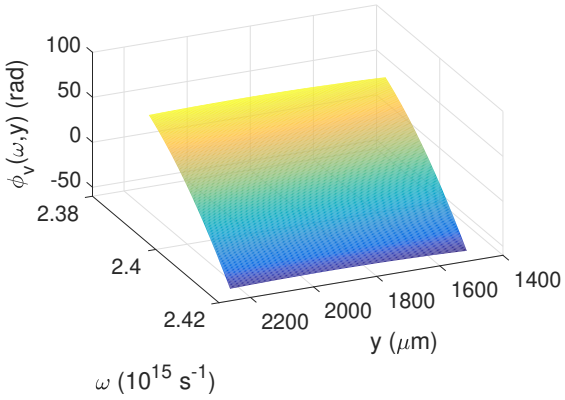

(b) Spectral phase ϕ_v, capillary out of beam path.

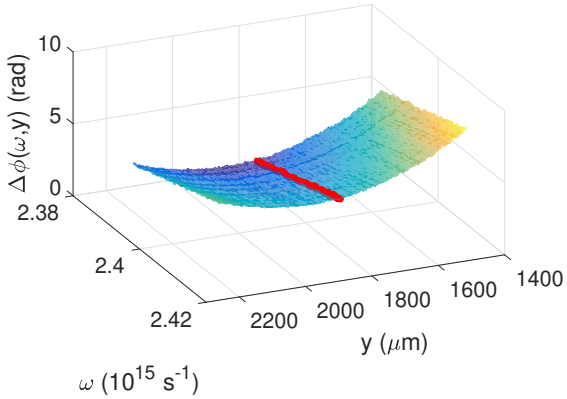

(c) Phase difference $\phi_p - \phi_v$, from (a) and (b). Central phase lineout highlighted in red.

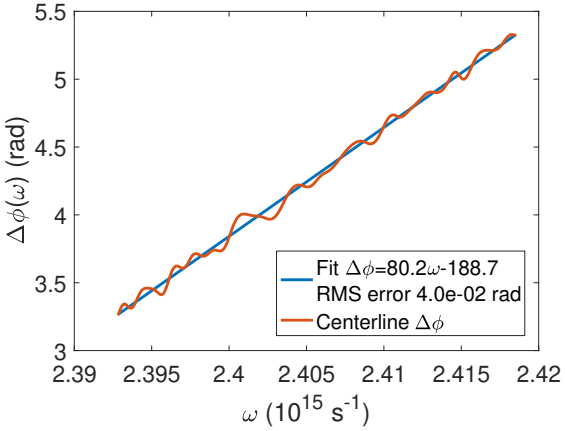

(d) Least-squares linear fit to the central phase lineout marked in (c) for the group delay $\Delta\phi_p^{'}$, with RMS deviation of the phase from the linear fit.

Figure 4.8: Spectral phase background subtraction procedure for determining channel induced group delay. Subtraction of the vacuum spectral phase (b) from the spectral phase for propagation through the plasma channel (a) yields the linear spectral phase contributed by propagation through the plasma channel (c), eliminating the higher order terms of Eqn. 4.13. The channel-induced group delay $\Delta\phi_p^{'}$ is obtained by linear fitting of the background subtracted phase $\Delta\phi$ of (c) as shown in (d).

In general, the retrieved channel-induced delay $\Delta\phi_p^{'}(y)$ will generally vary across the spectrometer slit. This is suggested by the curvature visible in $\Delta\phi(\omega, y)$ as plotted in Fig. 4.8(c), and is shown explicitly in Fig. 4.9, where the fitted channel-induced group delay $\Delta\phi_p(y)$ is plotted across the entire y-domain of Fig. 4.8(c). For the experiments on this setup, the group delay of the probe pulse centroid (corresponding to Eqn. 3.21 from Chapter 3) was used for the plasma density measurement. This was done because this group delay can be reliably measured in the situation where the spectrometer slit is not precisely imaging the capillary exit, as was the case for this experimental setup. The centroid group delay itself was obtained by averaging the fitted group delay $\Delta\phi_p^{'}(y)$ the center 20 y samples, which are plotted in bold in Fig. 4.9.

One might expect to be able to extract information about transverse variation of the plasma profile based on the transverse variation of the channel-induced group delay at the spectrometer slit, however in practice this is extremely difficult. This transverse variation of the group delay results from the divergence of the probe pulse at the slit, which in turn is a function of the imaging optics and the probe's spot size and divergence at the exit of the channel. The latter is due to evolution of the probe pulse during propagation in the channel, where, unless perfectly matched, it will experience oscillations in spot size and beating of channel normal modes [48, 86]. Therefore, the probe laser field at the exit of the channel is best characterized as the interaction of the probe as a whole with the channel as a whole, and so a reductive mapping the properties of the laser field at one axial position on the spectrometer slit to plasma density at a specific radial position in the channel is not practical.

Correction of delay drifts

The fiber based interferometer and associated analysis methods were successful in producing a delay measurement with sufficiently low jitter for useful measurements of plasma density, as will be shown in Section 4.6. However, the long optical fibers introduced a slow, minute-scale drift in the delay between the reference and probe pulses. To obtain accurate density measurements, this drift must be measured and corrected for. The data acquisition procedure used to calibrate the delay drift during measurements is described in this section.

Fig. 4.11(a) shows the measured probe-reference delays for vacuum propagation (i.e. capillary out of the beam path), taken at 1 s intervals over ~ 2 minutes. The fast component of the delay variation is due to vibrations in the setup, which though mitigated through the use of fibers, still contribute random error to the measurement. The slow component, however, is attributed to propagation through through the fibers. As can be seen in Fig. 4.10, this slow drift produces a 12 fs change in pulse delay over the time interval shown, or equivalent to an apparent plasma density change of 0.6×10^{17} cm^{-3}.

The precise mechanism of the slow drift was not determined with certainty. One possible mechanism is frequency drift in the laser frontend: it can be readily shown that shifts in the probe beam center frequency far below the sensitivity of either the spectral interferometer or the spectral diagnostics at the BELLA frontend can produce shifts in the pulse group delay of magnitude similar to the observed drift. Estimating the group velocity dispersion of the

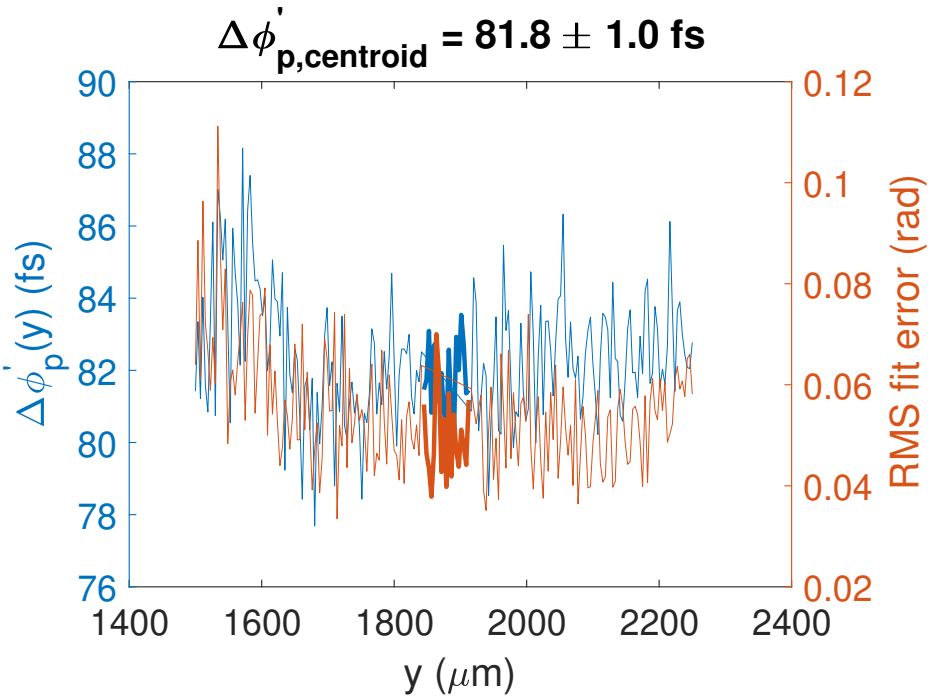

Figure 4.9: Fits of $\Delta\phi'_p$ for the $\Delta\phi$ surface of Fig. 4.8(c), with RMS deviation from the linear fits. Solid lines connect data points used for calculating the probe centroid group delay.

fiber as the literature value for fused quartz $\mathrm{d}(v_g^{-1})/\mathrm{d}\omega \equiv \mathrm{GVD} = 36$ fs^2/mm, the change in group delay induced by a frequency shift $\Delta\omega$ is

$$L_f \frac{\mathrm{d}}{\mathrm{d}\omega}\left(\frac{1}{v_g}\right)\Delta\omega = \Delta t \ , \tag{4.16}$$

with L_f the length of the medium. This can be written in terms of wavelength as

$$\Delta\lambda = \frac{-\lambda^2}{2\pi c}\frac{\Delta t}{\mathrm{GVD}\times L_f} \ , \tag{4.17}$$

with λ the "mean" or "initial" wavelength of the laser pulse. Taking $\lambda = 0.8$ µm, $L_f = 3$ meters (the difference in the fiber lengths in the setup), and $\Delta T = 10$ fs, Eqn. 4.17 yields $\Delta\lambda = -0.03$ nm. No tests were performed that showed with certainty that frequency drift in the laser frontend caused this effect, and 0.03 nm is below the spectral sensitivity of the laser diagnostics. Nevertheless, this mechanism can produce an effect of the correct magnitude under normal operating conditions for the laser system [110].

In these experiments, density measurements are performed while a parameter is varied or "scanned." The delay drift must be measured during these scans in order to correct for it. Parameter scans are performed in a series of bins as the scanned parameter is varied in stepwise fashion, wherein multiple laser shots are taken for a given parameter value, with

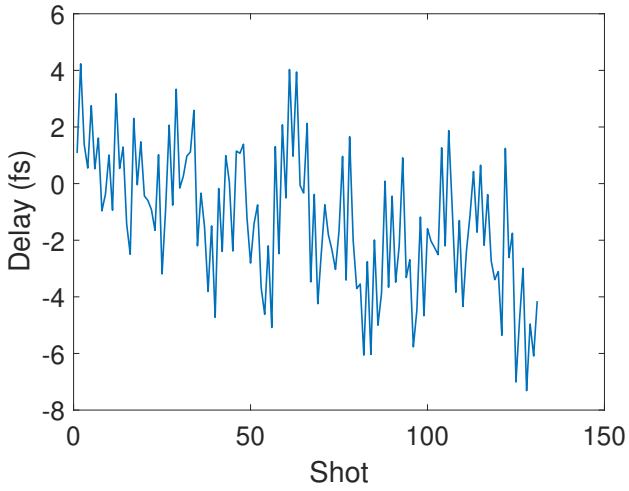

Figure 4.10: Vacuum delay (capillary out of beam path) measurements over ~ 2 minutes. The fast, shot-to-shot fluctuations are due to vibrations. The slow drift of the average delay may be due to small changes in the probe pulse frequency due to alignment drift in the BELLA laser frontend where the probe pulses originate.

typically 50-100 shots per bin. The delay drift is measured by interleaving "reference bins," where delay is measured at a specific set of plasma parameters, with "data bins" taken at the parameter values of interest for the measurement. The discharge density is stable to within 1% between shots [91, 93, 103], and therefore drifts in the delay due to other parts of the setup can be accurately measured with the capillary discharge in the beam path. Measuring the delay drift with the capillary in the beam path is also advantageous because it eliminates the need to move the capillary in and out of the beam path with the hexapod between bins.

This procedure is illustrated in Fig. 4.11, which shows a pressure scan taken in a 800 µm $\times$ 90 mm capillary at $t_d = 300$ ns after the peak of discharge current, without laser heating. The capillary fill pressure for each laser shot during the scan is plotted in Fig. 4.11(a), where reference bins at 15.5 torr fill pressure between successive pressure bins can be seen. The absolute delays $\Delta T^*(t_s)$ as a function of scan time t_s measured for the pressures of Fig. 4.11(a) are plotted in Fig. 4.11(b), as well as the reference delay $\Delta T_{ref}(t_s)$ constructed by interpolating the mean delay of each reference bin. The corrected delay $\Delta T(t_s)$ for the scan is then calculated according to

$$\Delta T(t) = \Delta T^*(t) - \Delta T_{ref}(t) + \Delta T_{ref}(t_{end}) \ . \tag{4.18}$$

The final term of Eqn. 4.18 $\Delta T_{ref}(t_{end})$ exists because the delay associated with the reference bins is calculated from the final reference bin, using a vacuum delay measurement taken immediately after the scan. The density for the data bins is then calculated from the corrected delays, and the uncertainty is calculated as the RMS deviation within each drift-corrected bin, as plotted in Fig. 4.11(d). For scans of probe pulse arrival time t relative to peak heater power, a similar procedure is used, except the reference measurements are taken by setting

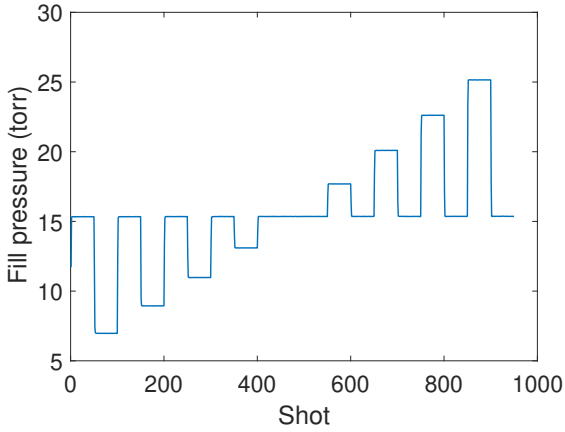

(a) Capillary fill pressure trace. Reference bins taken at 15.5 torr.

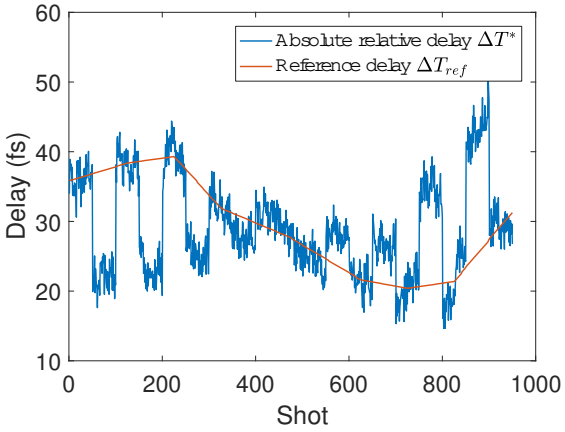

(b) Absolute delays ΔT^* for each shot in the scan, and the reference delay ΔT_{ref} interpolated from mean delay in each reference bin.

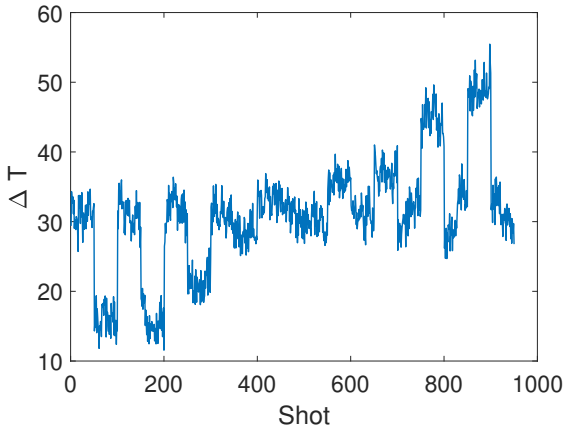

(c) Corrected delay obtained from ΔT^* and ΔT_{ref} from (b).

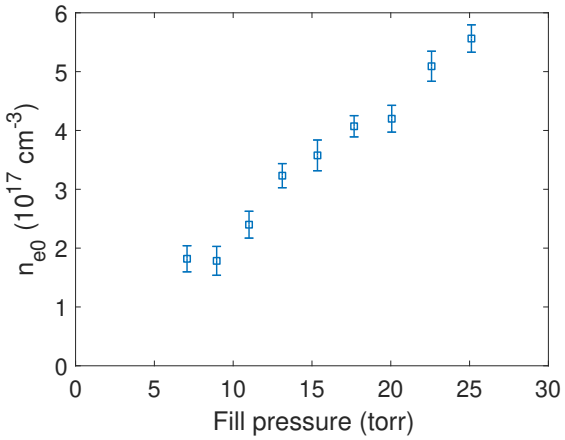

(d) Bin-averaged density as a function of fill pressure, from the corrected delays of (c). Error bars are the RMS deviation of each drift-corrected corrected bin.

Figure 4.11: Correction of delay drifts for density measurement. Measurements taken for a 800 µm × 90 mm capillary, delay $t_d = 300$ ns from the peak of discharge current.

the probe pulse arrival time before the heater, effectively tying delay measurements in the heated plasma channel to the capillary discharge in the absence of heating.

Error in the density measurement using this technique consists of both random and systematic components. The random error arises from the previously discussed delay jitter, which is denoted by the error bars of Fig. 4.11(d) and defined as the RMS deviation within each data bin. The $\sim 0.2 \times 10^{17}$ cm^{-3} error in this case is comparable to prior measurements using the spectral interferometry technique [91], and less than the $\sim 1 \times 10^{17}$ cm^{-3} error of

measurements using transverse spatial interferometry [90]. The uncertainty in the density measurement decreases with capillary length, per Eqn. 4.25. Hence, the error bars for measurements in a 20-cm-long capillary of Fig. 4.12 are less than half those for a 9-cm-long capillary of Fig. 4.11(d).

The drift correction procedure introduces a systematic error into the density measurement. The hexapod moves slowly, taking roughly 20 seconds to move the capillary out of the beam path for the vacuum delay measurement required to obtain $\Delta T_{ref}(t_{end})$. This time, during which the delay drift is not being monitored, introduces error into the delay drift calibration in the form of a small but unknown density offset. For this reason, this setup is best suited to measuring density changes from a known parameter value, or measuring the rate at which density varies with respect to a parameter. The pressure scans plotted in Fig. 4.12, which were performed at three different delays from the peak of discharge current $t_d = 20$ ns, 320 ns, 440 ns, illustrate this point. Notice that the density measured at $t_d = 440$ ns is greater than at $t_d = 320$ ns, the opposite relationship to be expected from either recombination in the cooling discharge plasma on the falling edge of the current pulse[84] or from plasma ejection from the ends of the capillary [100]. This discrepancy is attributed to the error introduced by the drift correction procedure, which is estimated to be $\sim 0.5 \times 10^{17}$ cm^{-3}. In concrete terms, the gradient of plasma density in the capillary discharge with respect to initial molecular density, represented by the first order terms of the fits in Fig. 4.12, is accurately measured, but the offset or zero-order terms have a systematic error from the drift correction procedure. This issue is one factor that motivated the creation of the two-color common path density diagnostic described in Chapter 5, which did not exhibit the delay drift observed in the fiber based setup used for the experiments of this chapter.

4.4 Laser spot size oscillation diagnostic for channel matched spot size

The matched spot size was diagnosed using well-known techniques based on laser propagation in plasma channels as discussed in Chapter 3. In this section, methods employed for these diagnostic measurements are described in detail. In this section, the model used for propagation of the probe beam in the plasma channel is described, as well as its practical implementation in the experiment.

The spot size of a Gaussian laser beam injected into a mismatched parabolic channel will oscillate with wavenumber $4/kr_m^2$ [85, 86]:

$$r_s^2 = \frac{r_i^2}{2}\left[1 + \frac{r_m^4}{r_i^4} + \left(1 - \frac{r_m^4}{r_i^4}\right)\cos\left(2k_{\beta c}z\right)\right]. \tag{4.19}$$

with $k_{\beta c} = 2/kr_m^2$. This oscillation in laser spot size is a diagnostic for r_m, and particularly well suited for laser-heated capillary discharges. If r_m is known for some set of plasma

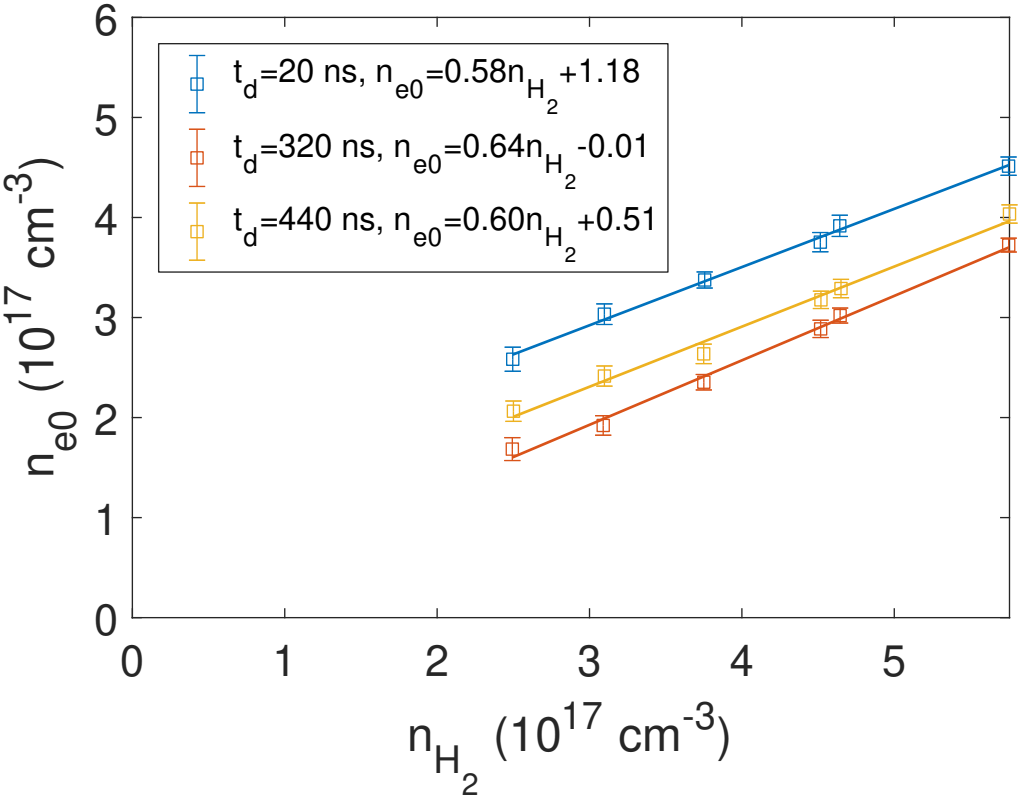

Figure 4.12: On-axis plasma density vs. initial fill gas molecular density for three arrival times t_d of the probe beam relative to the peak of discharge current. The higher measured density at $t_d = 440$ ns than at $t_d = 320$ ns is attributed to a systematic error introduced by delay drifts.

parameter values, oscillations in exit beam size that occur as plasma parameters are slowly varied away from those values can be counted to determine r_m for a different set of parameter values. It should be noted that, for laser heated channels, MARPLE calculations show significant longitudinal variation in the plasma profile. Therefore, in these experiments, spot size oscillation tracking yields the longitudinally averaged matched spot size $\overline{r}_m$.

Similarly to spot-size oscillation, the centroid of a laser beam injected into a plasma channel off-axis will oscillate within the channel with a wavenumber $k_{\beta c} = 2/kr_m^2$ [85, 86]. Laser centroid oscillation is an accurate and easily implemented diagnostic for capillary discharges [86], but it is more difficult to implement for laser-heated capillary discharges because the measurements require precisely displacing the channel from the probe beam. The difficulty arises from pointing jitter of the heater beam, which introduces an uncertainty in the position of the channel and increases the measurement error. Spot size oscillations, however, are relatively insensitive to alignment of the probe beam to the channel. Therefore, $\overline{r}_m$ in laser-heated channels was measured by using centroid oscillations to determine r_m for the capillary discharge in the absence of heating (in which case $r_m = \overline{r}_m$), and then using

spot size oscillations to track the change in $\overline{r}_m$ as heating was gradually increased to the value of interest for measurement.

The probe beam had a nearly Gaussian profile at focus, as can be seen in Fig. 4.5. However, images of the probe beam midfield in Figs. 4.4(a) and 4.13(a) show that the probe beam is in fact non-Gaussian, and contains higher order mode content. Because of this, Eqn. 4.19 does not accurately describe the propagation of the real probe beam in a parabolic plasma channel. Instead, a more detailed model of the probe beam field was constructed using physical optics calculations, and then propagated through idealized parabolic plasma channels for a series of r_m values using the INF&RNO code [111, 112]. Wavefront measurements of the probe beam showed a nearly flat phase, i.e. free of aberrations. Therefore, the phase of the probe beam midfield in Fig. 4.13(a) was modeled as that from an ideal paraxial lens

$$\phi_f(x,y) = -k_0 \frac{x^2+y^2}{2f} \tag{4.20}$$

and propagated using the Fresnel integral

$$E(x,y,z) = \frac{k_0}{2\pi i z} \int\int |E(x',y',0)| e^{i\phi_f(x',y')} \exp\left[ik_0 \frac{(x-x')^2+(y-y')^2}{2z}\right] \mathrm{d}x'\mathrm{d}y' \ , \tag{4.21}$$

with E the complex electric field of the beam x and y the coordinates in the transverse plane of the beam, z the coordinate along the optical axis defined with respect to the plane at which the initial field E(x,y,0) is specified, and f the focal length of the ideal paraxial lens. This model has a single free parameter, f, which needs to be determined by external measurements. Using both the physical optics capabilities of the LightPipes Python package[113] and ZEMAX optical design software [107], the simulated probe beam was propagated through vacuum along z according to Eqn. 4.21 and the simulated peak fluence was compared with measurements of vacuum propagation of the probe beam from the experiment. f was chosen to achieve the best agreement between the simulated and measured peak fluences, as plotted in Fig. 4.14. This procedure yielded a value $f = 65$ mm. Using this model of the laser field, an azimuthally symmetrized laser field was constructed for use with the INF&RNO code and the midfield and focus simulated in INF&RNO using this model of the field plotted in Fig. 4.13(c) and (d) agree well with the measured beam profiles.

This model of the probe beam was used as input to the INF&RNO code [112], where it was propagated through a set of 20 cm-long parabolic channels with r_m ranging from 40 to 120 μm. The INF&RNO simulations were used to calculate the peak fluence at the channel exit as a function of $\overline{r}_m$. These simulated peak fluence values at the capillary exit are plotted in Fig. 4.15(a).

The practical implementation of spot size oscillation measurements in the experiment will now be described for one specific case, using Fig. 4.15 which shows the analysis performed for a heater laser energy of 300 mJ, and the heater pulse timed to arrive 320 ns after the peak of the discharge current pulse. This method of analysis was applied to each set of laser energies and delays from the peak of discharge current investigated.

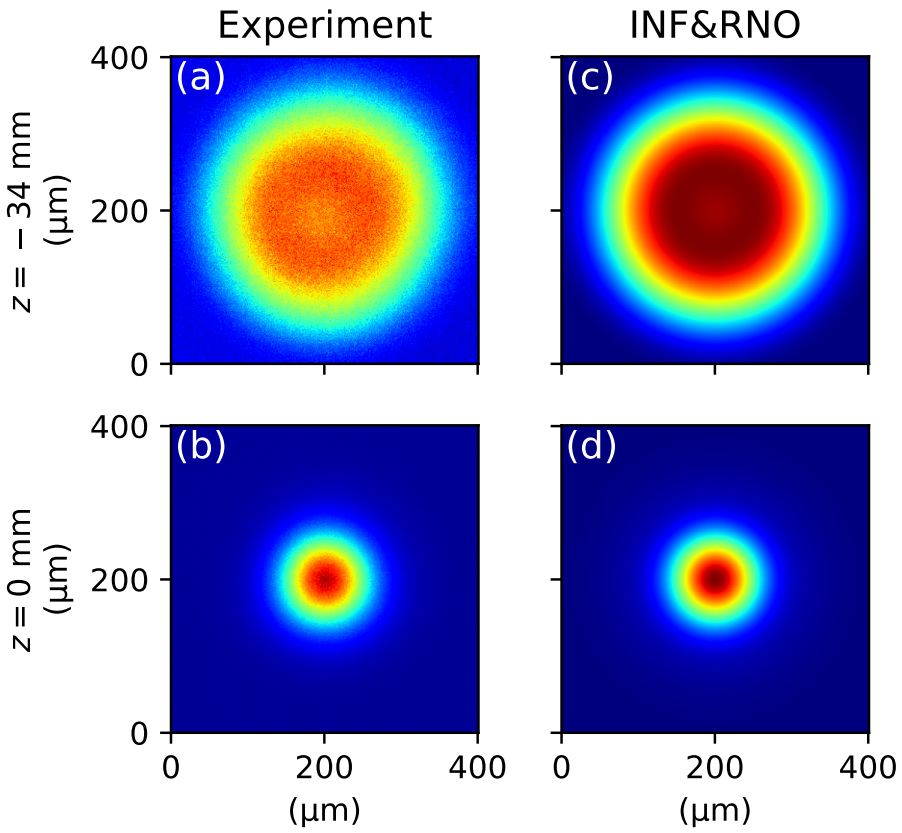

Figure 4.13: (a), (b): Measured fluence profiles at $z = -34$ mm and focus, respectively. (c) Symmetrized model of the field at (a). (d) Symmetrized field of (c) propagated to focus with INF&RNO. Peak fluence for the INF&RNO simulated beam is plotted vs. z in Fig. 4.14.

In the experiment, $\overline{r}_m$ was measured by imaging the beam at the capillary exit as $\overline{r}_m$ is varied. As previously described, the peak fluence of the probe beam at the capillary exit oscillates as $\overline{r}_m$ is varied, and so an oscillating peak fluence "trace" is obtained. A set of such traces for different delays t from the peak of the heater pulse are plotted in Fig. 4.15(b). In the experiments discussed here, $\overline{r}_m$ was varied by adjusting the fill pressure of the capillary, while the probe delay relative to the heater pulse was held constant. Note that there is less contrast between maxima and minima in the experiment data plotted in Fig. 4.15(b) than in the simulated peak fluence of Fig. 4.15(a). This may be due to the fact that the INF&RNO simulations used an idealized parabolic density profile, whereas MARPLE simulations show that the density profile of the laser-heated plasma deviates substantially from a parabolic shape, as will be discussed in Section 4.6. Specifically, early in the heater pulse, the "density well" formed on-axis by heating has a small radial extent, because the hot plasma has not had time to expand. This allows the guided probe beam to overfill the channel and causes energy to leak into the surrounding plasma. The ideal parabolic profile assumed in the simulation

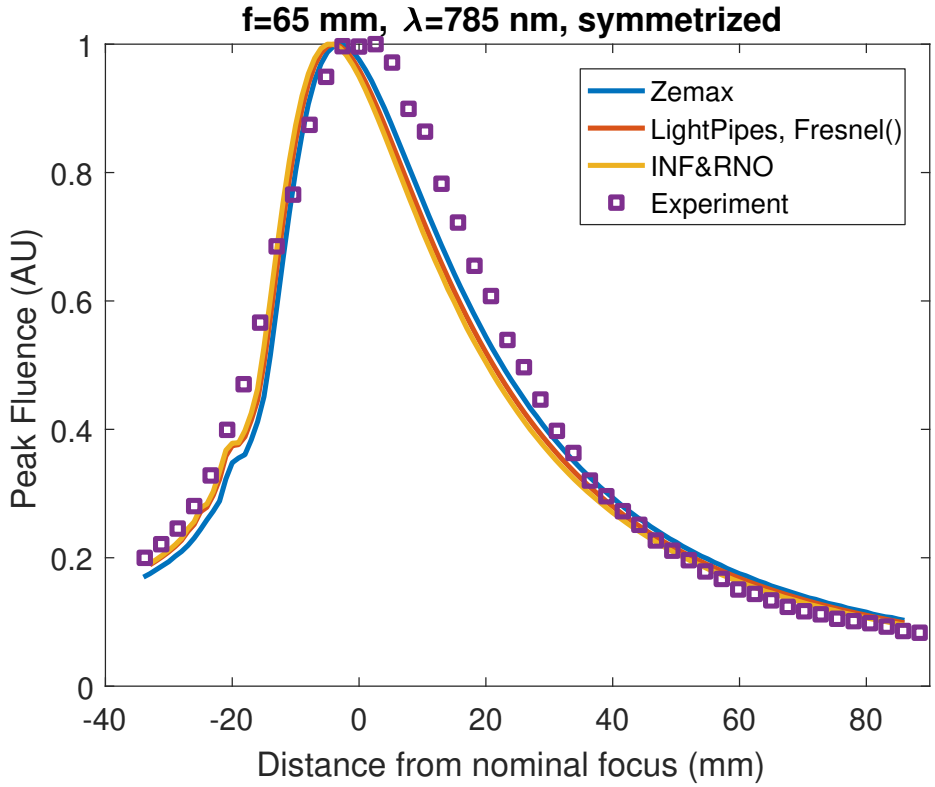

Figure 4.14: Measurements and simulations of the probe beam vs. distance from focus z. Fluctuations in the probe beam fluence were negligible. ZEMAX and LightPipes simulations were used to to select focal length parameter $f = 65$ mm of the initial phase by comparing the simulated peak fluence vs. z to measurements. The symmetrized model of the laser field constructed using this value was then propagated in INF&RNO and compared to measurements, in order to validate the model of the laser beam before simulating propagation in parabolic channels.

suffers from none of these issues.

To identify the $\overline{r}_m$ values for extrema in the peak intensity trace, the peak intensity must include a pressure with known value of $\overline{r}_m$. This was accomplished by beginning each peak intensity trace at very low fill pressure, where the heater has a negligible effect of on the plasma profile and the matched spot size is unchanged from that of the discharge without heating. Therefore, measurements of $\overline{r}_m$ for the discharge alone using probe centroid oscillations were used to determine $\overline{r}_m$ at the low pressure end of the peak intensity trace, and the fact that $\overline{r}_m$ decreases with pressure was used to identify the $\overline{r}_m$ values of the extrema in the trace as pressure was increased. As is shown in Fig. 4.15(b), the three traces all start at a known value of $r_m = 110$ µm, measured for the discharge (without heating) using the centroid oscillation method. With this initial value known, the three maxima that occur in the peak fluence trace for $t = 0$ ns, labeled (i)-(iii), can be identified in simulated fluence

plotted in Fig. 4.15(a). The minima in the measured peak fluence trace are identified in an analogous way.

This diagnostic yields discrete sets of parameter values, in the case of Fig. 4.15, delay from peak heating power t and capillary fill pressure p, known to correspond to values of $\overline{r}_m$ at extrema in the simulated peak intensity of Fig. 4.15(a). These sampled parameter values (t_i, p_i) are plotted in the plane of (t, p) in Fig. 4.15(c). Values of $\overline{r}_m$ for values of (t, p) apart from (t_i, p_i) must be computed by interpolation. Measured values of the matched spot size $\overline{r}_{m,i}$ are treated as discrete values of continuous function $R(t, p)$ such that

$$\overline{r}_{m,i} = R(t_i, p_i) \ , \tag{4.22}$$

with $R(t, p)$ computed via biharmonic spline interpolation of the points (t_i, p_i) [109]. This particular interpolation method was chosen because it produces an interpolating function that intersects all of sample points exactly, i.e. Eqn. 4.22 holds exactly at all points (t_i, p_i). This property matters because the value of $\overline{r}_{m,i}$ is known precisely for each (t_i, p_i), being the location of a maximum or minimum of the peak fluence trace plotted in Fig. 4.15(a). Labeled contours of $\overline{r}_m$ for values of these extrema of the simulated peak fluence are plotted in Fig. 4.15(c), and intersect every sample point (t_i, p_i) except those on the left and bottom edges of the plotted region. The sample points on the left and bottom boundaries of the plot were obtained from centroid oscillation measurements without heating, as these points correspond to times and pressures either before the heater pulse or where heating otherwise has little effect, and thus do not correspond to extrema of the simulated peak fluence.

Uncertainty measurements of $\overline{r}_m$ arises from uncertainty in the locations of exit fluence extrema due to the assumptions made about propagation (i.e. a longitudinally uniform parabolic plasma profile), and the the uncertainty in the values of (t_i, p_i) obtained from the measured peak fluence traces. The former is difficult to quantify, most likely requiring a computational study of propagation in longitudinally nonuniform, nonparabolic plasma channels that lies outside the scope of this dissertation. The latter however is straightforward to estimate, and is the uncertainty used for these measurements. Furthermore, the $\overline{r}_m$ values from MARPLE simulations were found to lie within this uncertainty, as will be shown later.

There is a 0.3 ns uncertainty Δt_i in t_i due to timing jitter in the heater pulse, and a conservatively estimated 2 torr uncertainty Δp_i in p_i from the width of the maxima and minima of the measured peak fluence traces. The upper and lower uncertainties $\Delta\overline{r}_{m,+}$ and $\Delta\overline{r}_{m,-}$ on interpolated values of $\overline{r}_m$ are thus defined

$$\Delta\overline{r}_{m,\pm} = R_\pm(t, p) - R(t, p) \tag{4.23}$$

with the "error functions" $R_\pm(t, p)$

$$R_\pm(t_i, p_i) \equiv R(t_i, p_i) \pm \nabla R(t_i, p_i) \cdot \langle \Delta t_i, \Delta p_i \rangle \ . \tag{4.24}$$

Note that according to the definition Eqn. 4.24, the error functions $R_\pm$ are only precisely computed at the sample points (t_i, p_i). Values of $R_\pm$ elsewhere are computed with the same

biharmonic spline algorithm used to obtain R. Contours of $R_\pm$ are plotted in Fig. 4.15(c) for the same vales of $\overline{r}_m$ as plotted for $R(t,p)$, i.e. $R_\pm = \overline{r}_{m,i}$, in the corresponding colors. Thus, the extrema of the simulated peak fluence can be regarded as lying in bands in (t,p) space determined by the precision to which the location of peaks in the measured fluence can be determined.

4.5 Density measurement uncertainty from geometrical effects

In this section, geometrical contributions to the plasma density measurement from matched spot size and asymmetry of the plasma channel are discussed, including sources of systematic error.

Accurate density measurements using the channel group velocity require knowledge of r_m and the true propagation distance within the channel L. Group velocity in a parabolic channel is lower than in a homogeneous medium, possessing a term $\overline{\beta}_{g,geo} \propto r_m^{-2}$ as described in Ref. [48]. In these experiments, this reduction in group velocity increases the apparent on-axis density by a maximum of 4×10^{16} cm^{-3} at $\overline{r}_m = 60$ μm.

Additionally, it was found that transverse asymmetry of the heater laser mode resulted in the creation of curved plasma channels. As is discussed later, this is evidenced by an intensity dependent deflection of the heater beam as it exits the capillary. It is thus inferred that the center of the heated channel does not remain in the center of the capillary, and in fact follows a curved path through the capillary. This occurs because the tail of the heater pulse is "steered" by the channel created by the head of the pulse in a similar manner to "self-channeling," where the tail of the heater pulse is guided in the channel created by the head as described in Refs [21, 22].. This "channel curvature" causes the probe beam to become misaligned as it propagates and undergo centroid oscillation, introducing additional path length $\delta L \propto \overline{r}_m^{-2}$ and increasing apparent plasma density. The degree of channel curvature is dependent on the properties of the heater beam and the effect was not observed in the experiments of Refs [21, 22]., which used a heater beam with a more symmetric mode. For the experiments in this chapter it is estimated that this effect contributes a maximum of 4×10^{16} cm^{-3} to the apparent on-axis density at $\overline{r}_m = 60$ μm.

Precisely modeling the group velocity reduction from finite matched spot size and the increased path length from channel curvature is difficult, and lies beyond the scope of this dissertation. Therefore, these propagation effects are estimated here using a model of a misaligned probe beam propagating in an longitudinally uniform parabolic channel (per Section 4.5). Because of the limitations of this simplified model, these effects are treated as a systematic error defining the lower uncertainty bound on the plasma density. This systematic error is denoted by wide-cap error bars in the density measurements of Figs. 4.16, 4.19, 4.20, and 4.21. In this section, this model is described in detail.

As discussed previously in Section 4.1, the measured channel-induced delay ΔT consists

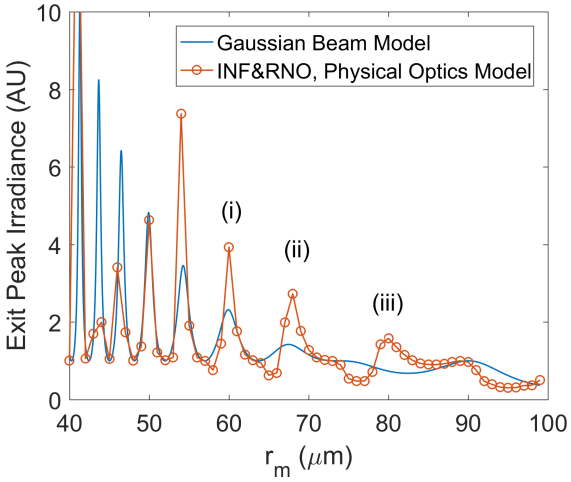

(a) INF&RNO simulation of peak probe irradiance at the exit of a 20-cm-long, ideal parabolic plasma channel for a range of matched spot sizes r_m.

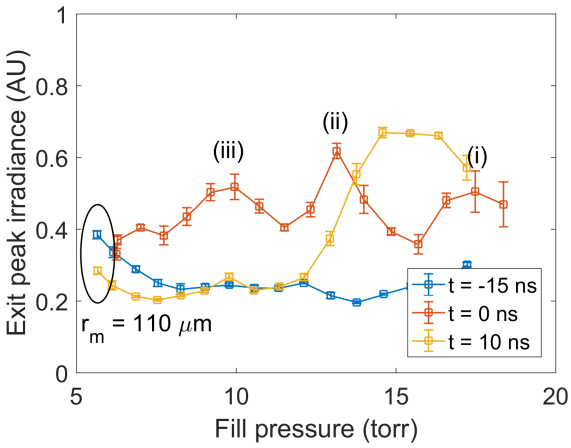

(b) Measured probe beam peak fluence, plotted against capillary fill pressure for probe pulse 3 arrival times t relative to the peak of the heater pulse. Maxima in the peak fluence with respect to fill pressure are labeled in according to their identification in (a). Error contours according to Eqn. 4.23.

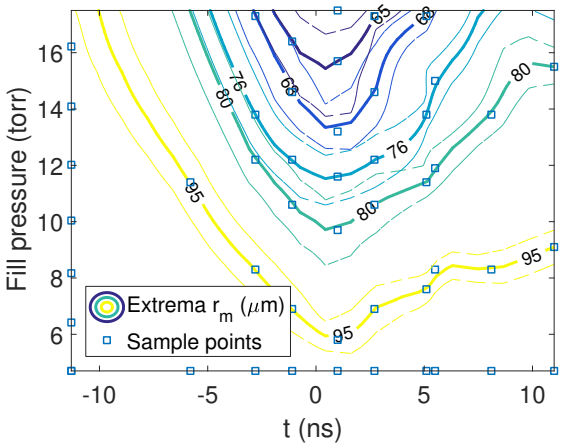

(c) Contours of r_m in pressure and timing space, constructed by identifying extrema in the peak fluence as shown in (a) and (b). Measured fluence extrema locations are plotted as squares. Uncertainty contours are plotted as thin dotted lines.

Figure 4.15: Demonstration of the spot-size oscillation diagnostic for channel matched spot size for a 20-cm-long, 800 µm diameter capillary, with the heater pulse timed to arrive at $t_d = 320$ ns after the peak of discharge current.

of two components, a density component from plasma density on axis, and a geometrical component from the matched spot size:

$$\Delta T \simeq \frac{L}{c}(\overline{\beta}_{g,n_{e0}} + \overline{\beta}_{g,geo}) \tag{4.25}$$

The quantity of interest for n_{e0} is $\overline{\beta}_{g,n_{e0}}$, and so $\overline{\beta}_{g,geo}$ must be determined and its contribution to the group velocity subtracted from Eq. (4.25). This requires an accurate measurement of r_m, and can be readily accomplished for capillary discharges using the methods previously discussed from Ref. [86]. For the experiment configuration here, where the group velocity of the laser centroid is measured (both longitudinally and transversely), the geometrical contribution to the group velocity is given by Eqn. 3.21 [48]

$$\overline{\beta}_{g,geo} = \overline{\beta}_{G,c}(L) = 1 - \frac{k_p^2}{2k_0^2}$$
$$-\frac{2(2m+|p|+1)}{k^2 r_m^2}\frac{r_0^2}{r_m^2}\left\{\frac{2\tan^{-1}[\frac{r_m^2}{r_0^2}\tan(k_{\beta c}L)]}{r_0^2 r_m^2 k_{\beta c}L} + \frac{2}{r_0^4 + r_m^4 + (r_0^4 - r_m^4)\cos(2k_{\beta c}L)}\right\} . \tag{4.26}$$

However, because the channels formed by laser heating can be significantly longitudinally nonuniform, Eq. (4.26) is approximate at best. Because of the lack of diagnostics for the longitudinal variation of r_m, the effects of finite channel matched spot size were treated as a systematic error in the density measurement, estimated with Eq. (4.26) using $\overline{r}_m$ values from spot size oscillations.

As is discussed in section 4.6, asymmetry in the heater beam leads to the creation of curved plasma channels misaligned to the probe beam and the capillary axis. This misalignment increases the path length traveled by the probe beam and thus the apparent plasma density. The channels curvature itself contributes little to the path length of the probe beam through the plasma, but ultimately leads to misalignment of the probe from the channel center, resulting in centroid oscillation of the probe beam. This oscillation contributes significant path length for the probe beam and increases the apparent plasma density by roughly the same amount as finite spot size effects.

The path length contributed by this misalignment was estimated by modeling the channel produced by laser heating as a straight parabolic waveguide, with the probe beam injected at the channel center in the entrance plane but at a nonzero angle θ_i relative to the axis. This geometry does not reflect the curved shape of the channel, which is difficult to diagnose directly and nevertheless contributes negligible path length. However, this model is a useful approximation with which the probe beam path length contributed by centroid oscillations can be estimated analytically while preserving some physical features of the probe beam's coupling into the channel, namely the initial overlap of the probe and heater beams at the capillary entrance plane. In the model, the total path length traveled by the probe beam is then

$$L = L_0 + \delta L = \int_0^{L_0} \sqrt{1 + \left(\frac{dx}{dz}\right)^2}\, \mathrm{dz}, \tag{4.27}$$

with L_0 the capillary length. The trajectory of the probe centroid according to Ref. [85, 86] is

$$x = x_i \sin\left(k_{\beta c} z\right) , \tag{4.28}$$

with $x_i = \theta_i / k_{\beta c}$ and $k_{\beta c} = 2/k{r_m}^2$. Because the additional path length from the centroid oscillation is small compared to the capillary length (at most 10 μm), δL is well approximated by

$$\delta L \simeq \int_0^{L_0} \frac{1}{2} \left(\frac{dx_i}{dz}\right)^2 \mathrm{d}z. \tag{4.29}$$

Using Eq. (4.28) in Eq. (4.29) and integrating,

$$\delta L \simeq \frac{1}{2} L_0 k_{\beta c}^2 x_i^2 \left[\frac{1}{2} - \frac{\cos\left(2k_{\beta c} L_0\right)}{4k_{\beta c} L_0}\right]. \tag{4.30}$$

The model has two free parameters, r_m and x_i, which must be determined by external measurements. The matched spot size r_m is set to $\overline{r}_m$ as measured with the diagnostic techniques described elsewhere. The oscillation amplitude x_i is estimated as half the greatest distance between two probe centroid positions over the course of the plasma evolution. For the case of Fig. 4.16, this distance is 175 μm/2 = 87.5 μm.

The additional path length δL can be incorporated into the model for channel induced delay Eq. (4.25) by expanding around L_0 in Eq. (4.1):

$$\int_0^{L_0+\delta L} \frac{1}{\beta_g} \,\mathrm{dz} \simeq \int_0^{L_0} \frac{1}{\beta_g} \,\mathrm{dz} + \frac{\delta L}{\beta_g} \tag{4.31}$$

Taking $\beta_g \simeq 1$ in the second term on the RHS of Eq. (4.31), substituting through Eq. (4.1) and Eq. (4.25), the following equation for $\overline{\beta}_{g,n_{e0}}$ is obtained:

$$\overline{\beta}_{g,n_{e0}} = \frac{c\Delta T}{L_0} - \overline{\beta}_{g,geo} - \frac{\delta L}{L_0} \tag{4.32}$$

This equation includes both the effects finite matched spot size and channel curvature in the terms $-\overline{\beta}_{g,geo}$ and $-\delta L/L_0$, respectively. These two terms are always negative and therefore define the lower bound on the plasma density for the measured channel induced delay ΔT, and are treated as a systematic error. As discussed in section 4.6, $\overline{r}_m$ measurements are omitted where MARPLE simulations show the channel radius to be less than the probe input spot size. However, these omitted values were used to calculate the wide-cap error bars from the finite matched spot size and channel curvature effects.

4.6 Channel formation and evolution in a laser-heated capillary discharge

Experiments and MARPLE simulations show significant modification of the plasma density by laser heating, with reductions of both $\overline{n}_{e0}$ and $\overline{r}_m$. Fig. 4.16 shows a case for heater pulse

energy 300 mJ, arriving at the capillary entrance at a delay t_d of 440 ns after the peak of discharge current, with initial on-axis plasma density $n_{e0,i} = 3.9 \times 10^{17}$ cm^{-3}. Images of the guided probe beam are shown in Fig. 4.16(a) for a range of delays t relative to the centroid of the heater pulse. In Fig. 4.16(b), $\overline{n}_{e0}$ and $\overline{r}_m$ from measurements and a MARPLE simulation, and the heater power are shown as a function of delay t. The heater power trace shown was obtained by averaging 1000 photodiode traces and smoothing with a lowess fit, and was used to model the heater pulse in the MARPLE simulations.

An average on-axis density of 2.4×10^{17} cm^{-3} and matched spot size of 65 μm is measured at $t = 4.6$ ns, parameters suitable for acceleration to energies approaching 10 GeV [22, 114]. Because of the scaling $r_m \propto r_c^{1/2} n_{e0}^{-1/4}$, realizing these parameters in a capillary discharge would require a 60% reduction in capillary diameter from the initial 800 μm to ~ 300 μm. Capillaries of this size are vulnerable to damage from the BELLA laser and are unsuitable for PW-scale experiments, based on the destruction of 500 μm-diameter capillaries observed above 300 TW of laser power in the experiments of Ref [76]..

Modification of the guided probe beam can be seen in Fig 4.16(a) as early as $t = -6.4$ ns, indicating signicant evolution of the plasma profile ~ 1 ns after the foot of the heater pulse at $t = -7.4$ ns. This is consistent with the 3 ns timescale for plasma motion calculated in section 3.6. The modification of the guided probe beam beginning at $t = -6.4$ ns in Fig. 4.16(a) is also evidence of self-channeling of the heater beam. The evolution of the guided probe beam early in the heater pulse shows that the majority of the pulse energy propagates through a plasma channel with different guiding properties than the discharge before heating at $t = -8.8$ ns. It must be noted that an increase in probe intensity in the exit plane does not necessarily correspond to a reduction in matched spot size. Rather, this indicates that a minimum in the probe spot size oscillation has moved near the exit plane, which can occur during either an increase or decrease in $\overline{r}_m$ depending on the oscillation phase.

The data of Fig. 4.16 show the channel evolves on a nanosecond time scale, and that properly timing the driver pulse relative to the heater pulse is critical for achieving maximum accelerator performance. In typical operation, the driver pulse is timed to arrive during the time interval extending roughly from $t = 0$ ns to 15 ns after the peak of the heater pulse, as density and matched spot size are significantly reduced from the discharge values during this time. This interval is marked in Fig. 4.16, with times lying outside it shaded. For the experiments of Refs [21, 22]., the driver was timed at $t \sim 1$ ns. However, the data of Fig. 4.16 show that ~ 5 ns after the peak of the heater pulse, the plasma density reaches a minimum with $r_m \lesssim 65$ μm, still sufficiently well matched to the ~ 60 μm BELLA beam waist. Hence, it is expected that accelerator performance can be improved over previous experiments by taking full advantage of the plasma evolution to achieve optimal channel properties.

MARPLE simulation

For the simulations in this dissertation, the MARPLE code was augmented with modules from INF&RNO and implemented the inverse-bremsstrahlung power density [Eq. (3.28)]. The heater beam intensity at the capillary entrance was modeled as a function of the form

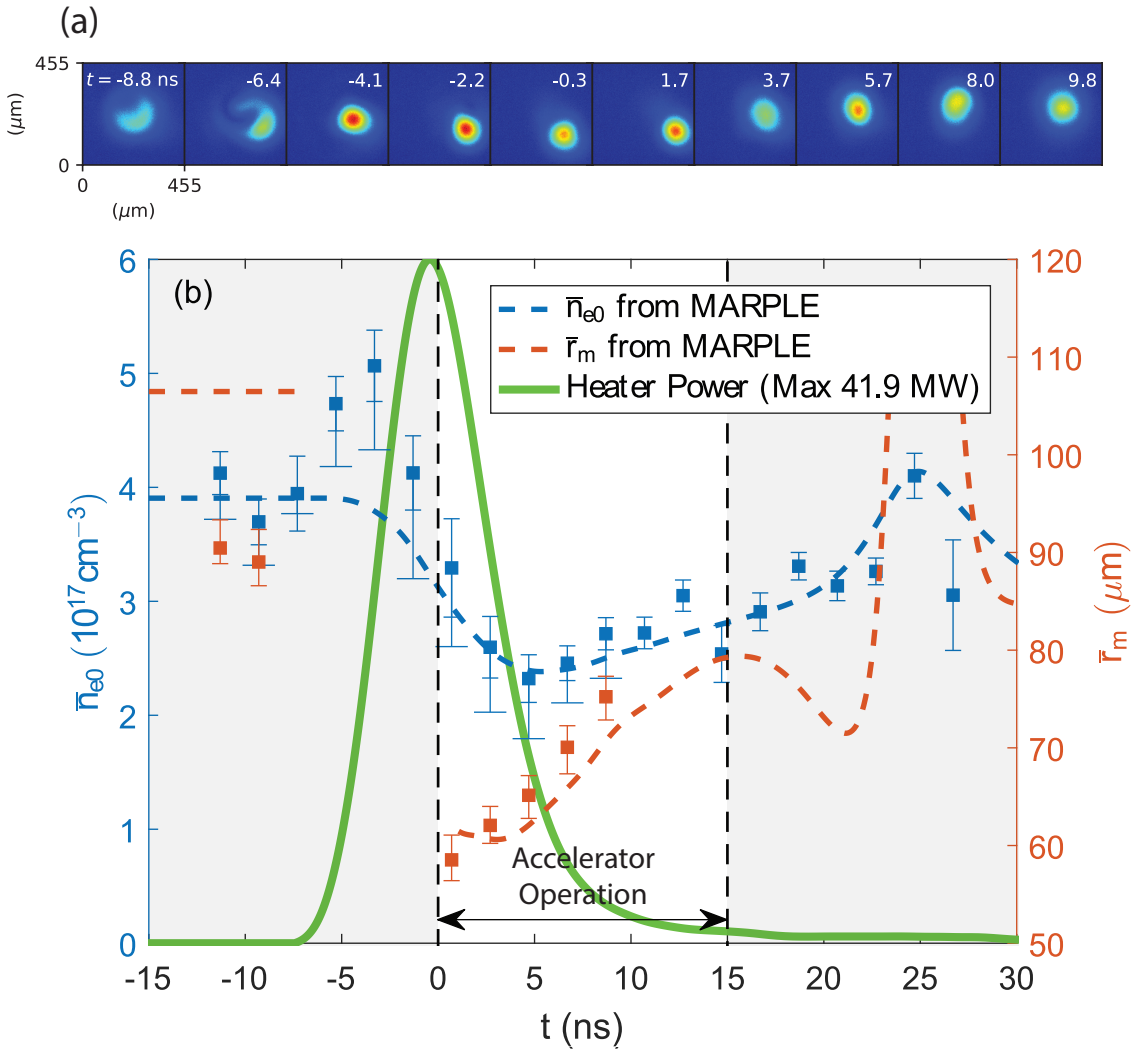

Figure 4.16: Guided laser beam and channel properties for a 20 cm-long, 800 μm-diameter capillary filled with 17.6 torr of H_2, heated with 300 mJ of laser energy. (a) Images of the guided probe beam at the capillary exit vs. delay from the peak of the heater pulse. Jitter in probe beam position at the capillary exit was < 10 μm. (b) Longitudinally averaged on-axis density $\overline{n}_{e0}$ and longitudinally averaged matched spot size $\overline{r}_m$ vs. delay t from the heater pulse centroid from measurements and a MARPLE simulation. The representative heater power trace used in the MARPLE calculations (obtained from averaged photodiode traces) is shown in green. Narrow-cap error bars denote uncertainty from group delay jitter between the probe and reference pulses. Wide-cap error bars denote uncertainty in the density measurement from misalignment of the probe to the channel due to channel curvature. $\overline{n}_{e0}$ and $\overline{r}_m$ values are omitted when the MARPLE simulation shows the channel size is below the input laser spot size of 73 μm. Driver arrival times typical for accelerator operation are marked, with shading applied for times outside this interval.

${J_1}^2(r)/r^2$ with a $1/e^2$ radius of 82 μm, where $J_1(r)$ is a Bessel function of the first kind, and the laser power was modeled using the trace in Fig. 4.16. The simulations were performed on an 800 μm-diameter, 20 cm-long, axisymmetric, uniform (r, z) grid with 50 cells in the radial direction and 200 cells in the longitudinal direction, with a time step of 0.1 ns. Plasma evolution was simulated from the the initiation of the discharge 420 ns before the peak of current, through the arrival of the heater laser pulse, to 1000 ns after the peak of current. The initial neutral hydrogen density was chosen to match the measured density at the arrival time of the heater pulse. The discharge plasma was modeled as initially longitudinally uniform, ignoring the 6 mm density ramp at each end of the capillary arising from gas flow out the ends into the surrounding vacuum. These "end effects" are expected to have little effect on guiding since the 6 mm length of the density ramp is smaller than the 20 and 40 mm Rayleigh lengths of the probe and heater beams, respectively.

The longitudinally-averaged matched spot size $\overline{r}_m$ was calculated from the MARPLE output by computing the quasi-matched Gaussian spot size derived in Ref [87]. for each longitudinal grid point of the calculated electron density $n_e(r, z)$ and then averaging in z. This definition of the matched spot size was used because it is well defined for non-parabolic plasma profiles. MARPLE simulations show that early in the heater pulse, the density well formed by laser heating is small in radial extent because the heated plasma has had little time to expand under its own pressure. In this situation the channel may be smaller than the guided beam, and a large fraction of the beam will not be coupled into the channel formed by heating. Instead, the beam will effectively sample two guiding structures: both the density well on axis from heating and the density well formed by the background plasma profile of the discharge. Another condition that may arise is the formation of a local maximum of the plasma density on the channel axis, due to plasma motion driven by uneven heating in the transverse plane by the mismatched, multimode heater beam.

Both of these conditions constitute a qualitative departure from the model on which the spot size oscillation diagnostic is based, which assumes propagation in a single, parabolic density well, and thus renders the measurement difficult to interpret. Therefore, $\overline{r}_m$ measurements were only retained at times where the MARPLE output shows the average radial extent of the channel as defined by the location of the first radial inflection point of the plasma density (i.e., $\partial^2 n_e/\partial r^2 = 0$) to be greater than the probe input spot size, and the density to be locally minimized in the transverse plane ($\partial^2 n_e/\partial r^2|_{r=0} > 0$) at all points on the channel axis. Overall agreement between experimental measurements of plasma density and MARPLE simulations is excellent.

Due to mismatched guiding and self-channeling of the heater beam, n_{e0} and r_m are not longitudinally uniform in general. This is clear in the MARPLE output shown in Fig. 4.17, which is for select time points of the case in Fig. 4.16. MARPLE simulations show that self-channeling and mismatching of the heater beam produce a channel with complex structure problematic for guiding at early times. Fig. 4.17 shows that during the rise of the heater pulse at $t = -3.0$ ns, the transverse extent of the channel is small, and in some longitudinal positions a local density maximum exists on axis. This can be seen in the transverse density profiles plotted in Fig. 4.17(a). The longitudinal variation of r_m is plotted in Fig. 4.17(e),

with values suppressed at locations with channel extents less than the probe beam waist size or density maxima on-axis. At $t = -3.0$ ns, roughly 25% of the length of the channel meets these criteria, hence the spot size oscillation diagnostic for $\overline{r}_m$ cannot be applied. Near the peak of the heater pulse at $t = 1.6$ ns, a density well has formed at all points on the channel axis, but the channel remains relatively small in transverse extent and highly nonuniform in the longitudinal direction. However, several ns later at $t = 5.6$ ns the channel has expanded radially and become more uniform, with longitudinal variation of n_e and $r_m < 10\%$.

Density measurement uncertainty due to channel curvature

As stated previously in Section 4.5, asymmetry of the heater beam introduces curvature in the heated plasma channel. Evidence of this can be seen in Fig. 4.16(a), which shows considerable deflection of the probe beam as the channel evolves. Moreover, this deflection is very repeatable between shots, with jitter in the probe beam centroid < 10 μm. Overlap of the probe and heater was accurate to within 20 μm and 100 μrad at the capillary entrance, which for the measured values of $\overline{r}_m$ should yield a maximum deflection < 25 μm, and a maximum density error $< 5 \times 10^{15}$ cm^{-3} from probe centroid oscillation [86]. Instead, the maximum deflection observed was 175 μm. This is attributed to "steering" of the heater beam within the discharge channel due to the combined effects of the beam asymmetry visible in Fig. 4.4(b) and self-channeling, which creates a slightly curved plasma channel.

Consistent with the evolution of the guided probe beam during the rise of heater pulse shown in Fig. 4.16(a), the effect of self-channeling on the heater beam itself can be seen directly in Fig. 4.18, which shows the time-integrated downstream nearfield of the heater beam after propagation through a 9 cm-long, 800 μm-diameter capillary operated at a similar initial plasma density to the case plotted in Fig. 4.16 as a function of laser arrival time t_d relative to the discharge peak. The capillary discharge channel axis was aligned to the heater beam such that the paths of the guided and vacuum beam centroids overlapped within 20 μm and 200 μrad using the methods of Ref [86]., with a pulse energy of 30 mJ at delay $t_d = 56.8$ ns from the discharge peak.

Fig. 4.18 shows the heater propagation is strongly dependent on pulse energy and arrival time in the discharge pulse. At 30 mJ the nearfield is nearly unchanged as discharge timing is varied. This is consistent with a capillary discharge in the quasi-static regime, a condition reached near the peak of current where the plasma density profile ceases evolving and the electron temperature becomes a function of current alone, varying as $T_e \propto I^{1/2}$ [84]. However, at 420 mJ, reductions of ~ 3 mrad in divergence angle and deflections of ~ 3 mrad are observed when the heater pulse arrives later in the discharge. Similarly to the deflection of the probe beam shown in Fig. 4.16(a), the changes in heater beam divergence and propagation direction are stable between shots, with jitter < 1 mrad. Increased delay relative to the discharge current peak on the falling edge of the current pulse corresponds to lower plasma temperature because of the $T_e \propto I^{1/2}$ scaling in the quasi-static regime.

That the influence of pulse energy on the propagation of the heater beam is greatest at low plasma temperatures, where inverse-bremsstrahlung heating is stronger according to Eq.

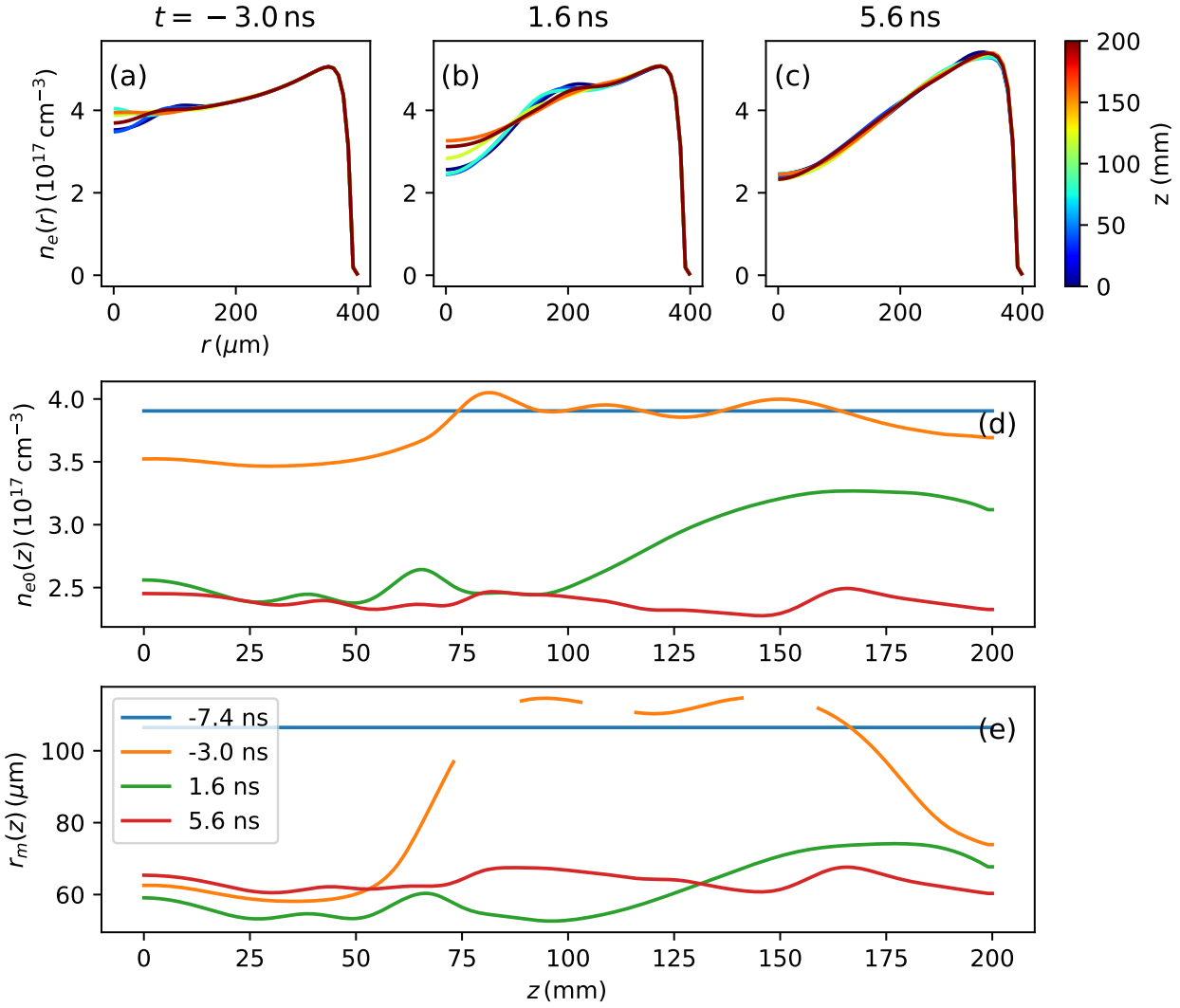

Figure 4.17: MARPLE output for the case of Fig. 4.16. (a),(b) Radial plasma density profile at 6 longitudinal positions z, for two delays from the peak of heating power: $t = -3.0$ ns, $t = 1.6$ ns, and $t = 5.6$ ns. (c),(d) Channel parameters vs. longitudinal position for $t = -7.4,\ -3.0,\ 1.6,\ 5.6$ ns, with $t = -7.4$ ns corresponding to the unmodified discharge plasma density. r_m values are omitted at locations where the channel extent is less than the probe beam spot size or a density maximum exists on axis as described in Section 4.6.

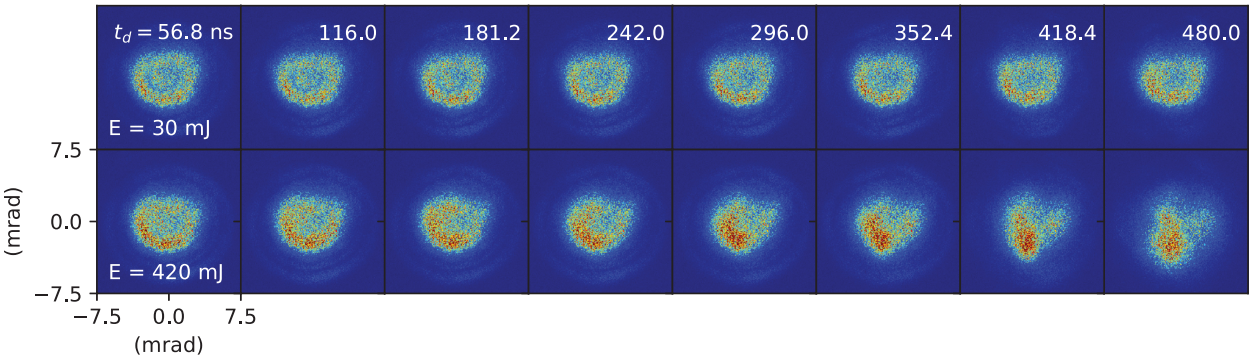

Figure 4.18: Images of the heater beam downstream nearfield (imaging infinity) after interacting with a 9 cm-long, 800 μm-diameter capillary filled with 17.2 torr H_2, vs. delay t_d of the heater pulse relative to the peak of discharge current. Images are shown for 30 mJ and 420 mJ pulse energies. Shot-to-shot variation of propagation direction and divergence angle are both < 1 mrad.

(3.35), is consistent with guiding of the heater beam within a channel created by plasma motion driven by the heater beam itself. Furthermore, deflection of the heater beam from the vacuum beam path and capillary axis at the later discharge times at 420 mJ in Fig. 4.18 implies that this channel is curved under these conditions.

This "self-steering" of the beam is attributed to asymmetric plasma heating, which is in turn due to the asymmetry in the heater beam shown in Fig. 4.4(b). This effect will complicate the alignment of an electron beam to the axis of an accelerator system. Thus, it is beneficial to suppress self-steering to the greatest extent possible, which requires maximizing symmetry of the heater beam. The experiments of Refs [21, 22]. used a different laser system for heating, which produced a more symmetric beam, and self-steering was not observed.

Diagnosing the path of the curved channels formed by self-steering is quite difficult, as discussed in Section 4.5. However, assuming that guided probe beam oscillates about center of the channel as it evolves, the maximum deflection of the probe beam in the exit plane can be used to roughly estimate a characteristic displacement of the channel from the capillary axis. For the case of Fig. 4.16, taking the maximum probe deflection of $\Delta x_f = 175$ μm as the peak-to-peak oscillation amplitude about the channel center yields the estimate $\Delta x_f/2 \approx 90$ μm for the displacement of the channel center from the capillary axis at the exit plane. This value is merely representative, however. The position of the channel center varies with longitudinal position along the capillary, and in fact coincides with the capillary axis at the entrance plane to within the alignment precision of 20 μm previously quoted.

The main difficulty introduced in this experiment by self-steering of the heater beam is a systematic error in the density measurement, caused by the increased path length traversed by the probe pulse in a curved channel. The wide-cap error bars of Fig. 4.16(b) denote the uncertainty in plasma density due to channel curvature and finite matched spot size effects. Uncertainty from jitter in relative group delay of the probe and reference pulses is denoted by the narrow-cap error bars. The wide-cap error bars were calculated using measurements of

$\overline{r}_m$ in combination with the observed maximum deflection of the probe beam, $\Delta x_f = 175$ μm (see Section 4.5). Because these propagation effects scale roughly as r_m^{-2}, they are most pronounced close to the peak of the heater pulse, where $\overline{r}_m$ is smallest.

The peak in $\overline{n}_{e0}$ visible in the experimental data plotted in Fig. 4.16(b) at $t \sim -4$ ns is a diagnostic artifact rather than a physical increase in the plasma density. Measurements on the BELLA main beamline [21, 22] using a different diagnostic technique which will be described in Chapter 5, common-path two-color spectral interferometry [115, 116], agreed well with the simulations and measurements reported in this chapter but did not observe this feature. Moreover, ionization by the heater laser cannot account for the observed effect, as MARPLE shows the fraction of neutral hydrogen on axis to be $< 2\%$ [22], leaving insufficient neutral hydrogen to produce the observed $\sim 25\%$ increase in apparent electron density (see Chapter 6).

In Fig. 4.16(b), the simulated density lies within the systematic uncertainty from propagation effects, with the exceptions of the points at $t = -6$ ns and -4 ns. The discrepancy at these times may arise from the assumption of an ideal, longitudinally uniform parabolic channel in the model of the decreased group velocity and increased path length due to finite matched spot size and channel curvature (see Appendix B). As previously discussed, the MARPLE simulations show that early in the heater pulse, the channel is both longitudinally nonuniform and has a complex, non-parabolic transverse profile. In addition to having these properties, the physical channel is non-axisymmetric. The group velocity of the probe pulse in such a structure will be less than in the idealized parabolic density profile used in the model, in which case the apparent density contribution from propagation effects will be underestimated.

Nevertheless, the group delay plasma density measurements agree well with simulation in the interval most useful for laser-plasma acceleration $0 < t < 15$ ns, when the channel is fully formed and on-axis density and matched spot size are low. Fig. 4.17 shows that plasma expansion produces a transverse density profile with a wide, on-axis minimum by $t \approx 2$ ns, which further evolves into a longitudinally uniform, nearly parabolic shape on-axis by $t \approx 6$ ns. Additionally, the effects of matched spot size and channel curvature are greatly reduced at later times due to increasing $\overline{r}_m$ after $t \approx 0$ ns and the r_m^{-2} scaling of these effects. Therefore, the diagnostic artifacts and nonidealities of the plasma profile previously discussed pose little difficulty for measurements in the interval relevant to accelerator operation.

The measurements and simulation output of Figs. 4.16 and 4.17 show that, for a given capillary radius, laser heating of a capillary discharge can create a channel with lower matched spot size for a given density than the discharge alone. Equivalently, channels can be created with matched spot size and density that would otherwise require a significantly smaller capillary radius without laser heating: 60% smaller in the case of Figs. 4.16 and 4.17. The properties of the channel, including $\overline{n}_{e0}$, $\overline{r}_m$, and the longitudinal variation of the plasma profile, evolve on a nanosecond timescale due to plasma motion. This requires precise timing of the driver pulse to achieve optimal channel properties, with a minimum in on-axis density occurring ~ 5 ns after the peak of the heater pulse. Furthermore, MARPLE simulations

showing $\sim 10\%$ longitudinal variation in $\overline{r}_m$ and $\overline{n}_{e0} \sim 6$ ns after the peak demonstrate that, despite mismatch of the heater spot size to the channel and the complex coupling between plasma motion and heater beam propagation, channels with a high degree of longitudinal uniformity can be created.

4.7 Tuning channel properties via plasma and laser parameters

The primary difficulty addressed by laser-heated capillary discharges is the lack of independent control of r_m and n_{e0} in a conventional capillary discharge. For a capillary discharge, the scaling $r_m \propto r_c^{1/2} n_{e0}^{-1/4}$ restricts a capillary of fixed radius to a one-dimensional curve in (n_{e0}, r_m) space. Independent control of n_{e0} and r_m enables matched guiding of petawatt-scale laser pulses at low plasma densities required for ~ 10 GeV energy gain without reducing capillary diameter to a size at which the structure is subject to laser damage. This additional freedom is also useful for optimization of a channel-guided laser-plasma accelerator, where matched spot size, plasma density, laser intensity, and plasma wave phase velocity are all coupled to one another.

It was demonstrated in Ref [21]. that a laser-heated capillary discharge can be tuned over a two-dimensional region of $(\overline{n}_{e0}, \overline{r}_m)$ by varying the initial discharge plasma density and temperature. In the experiments of Ref [21]., the driver arrived at the peak of the heater pulse, and channel parameters were reported for that delay relative to the heater pulse. Here, the full time evolution of the plasma upon heating is presented for the parameter space discussed in Ref [21]., as well as additional measurements demonstrating the effect of the total heater pulse energy. In agreement with the data of Fig. 4.16, the data presented here show that a minimum in the on-axis density consistently occurs 4-7 ns after the peak of the heater pulse, indicating that for a wide range of parameters, channel properties are optimal for high energy gain at that time. Tunability of channel properties over a wide range via heater laser energy, driver timing, and initial plasma parameters is shown, and strategies for channel optimization are identified.

Initial plasma density

Experiments and MARPLE simulations show that the reduction of $\overline{n}_{e0}$ and $\overline{r}_m$ increases with initial plasma density. Fig. 4.19 shows $\overline{n}_{e0}$ and $\overline{r}_m$ plotted for a heater laser arrival time $t_d = 320$ ns after the discharge peak for four initial plasma densities $\overline{n}_{e0,i}$. Reduction of $\overline{n}_{e0}$ and $\overline{r}_m$ from their initial values is found to increase with $\overline{n}_{e0,i}$. This relationship is to be expected from the n_e scaling of the heating rate [Eq. (3.35)]. Low densities and matched spot sizes cannot be achieved by simply lowering the initial plasma density, because the modification of $\overline{r}_m$ decreases rapidly with density. Instead, there exists an optimal initial density for guiding and acceleration that produces the required reduction in both $\overline{r}_m$ and $\overline{n}_{e0}$.

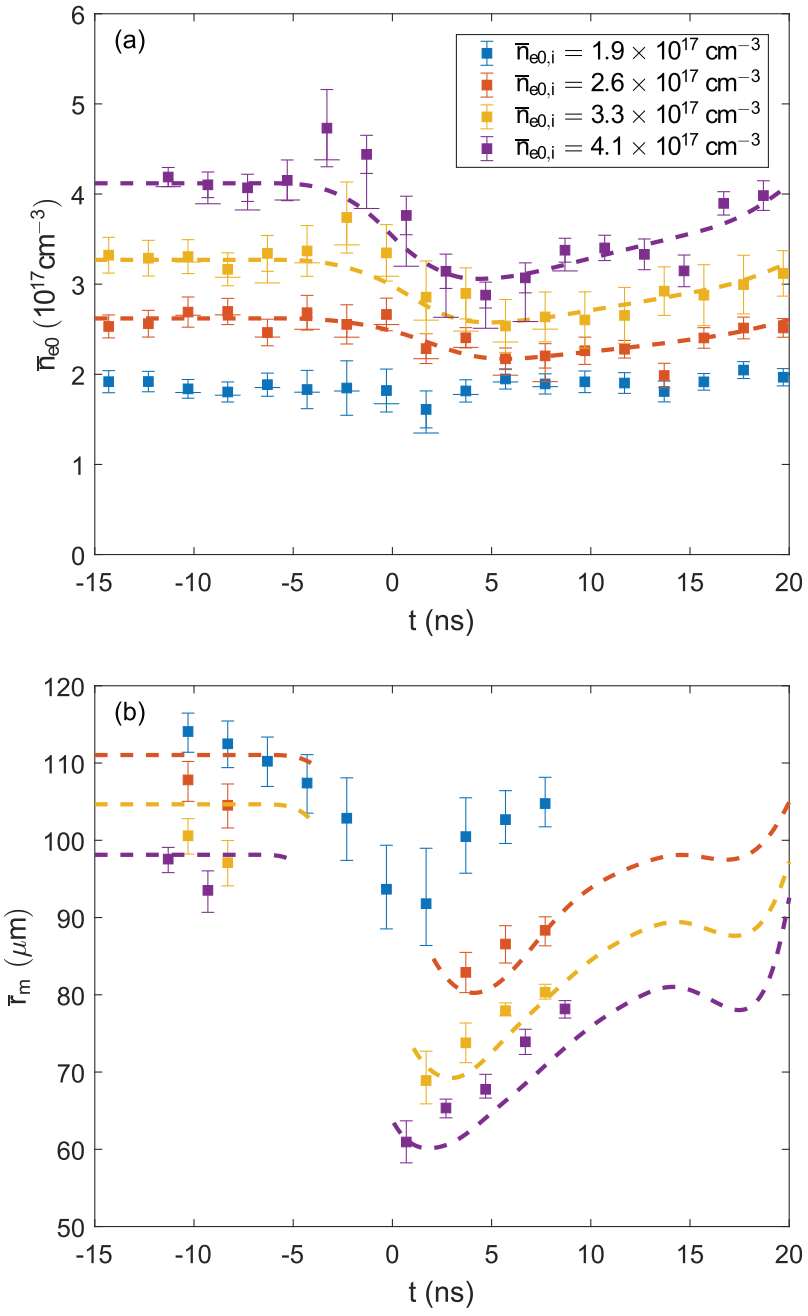

Figure 4.19: (a) $\overline{n}_{e0}$ for 4 initial densities, with arrival time of the heater pulse relative to peak discharge current $t_d = 320$ ns. Error bars as in Fig. 4.16. Values from MARPLE as dotted lines. (b) Measured $\overline{r}_m$ and MARPLE calculated values for the cases of (a).

Initial plasma temperature

Initial plasma temperature $T_{e,i}$ has a strong effect on plasma profile modification. Fig. 4.20 shows $\overline{n}_{e0}$ and $\overline{r}_m$ for three different arrival times of the heater pulse relative to the discharge peak, which correspond to different initial plasma temperatures $T_{e,i}$. As previously discussed, plasma temperature decreases with delay from the peak of discharge current because of the $T_e \propto I^{1/2}$ scaling in the quasi-static regime [84]. Lower $T_{e,i}$ at later times yields larger reductions in both $\overline{n}_{e0}$ and $\overline{r}_m$, due to the $T_e^{-3/2}$ scaling of the heating rate [Eq. (3.35)].

Initial plasma temperature is the most readily exploited parameter for optimization of the heated channel because it can be easily tuned while minimally altering other discharge channel properties. Once the quasi-static regime is reached near the peak of the current pulse, the shape of the plasma profile does not evolve significantly. Centroid oscillation measurements show the matched spot size r_m of the capillary discharge channel (without heating) varied < 2 μm between the three delays shown in Fig. 4.20, which cover an interval of 420 ns.

However, the requirement of near-total ionization on-axis for acceleration imposes a minimum allowable initial temperature, and therefore maximum allowable laser delay from the peak of discharge current. If the neutral fraction becomes too great, ionization defocusing of the driver can overwhelm the effect of the channel. Laser heating can ionize a partially recombined plasma at late times in the discharge current pulse, and therefore the plasma is not necessarily required to be initially fully ionized. The maximum allowable delay from the peak of current is therefore dependent on the parameters of the capillary discharge and the heater laser. For these experiments, ionization blueshifting measurements and MARPLE simulations indicate that up to 420 ns after the peak of discharge current, the plasma on the channel axis is fully ionized ~ 5 ns after the peak of a 300 mJ heater pulse [22].

Heater pulse energy

It might be expected that increasing the energy of the heater pulse would be a straightforward means of decreasing on-axis density and matched spot size. However, the plasma response was observed to saturate with increasing pulse energy. Fig. 4.21 shows $\overline{n}_{e0}$ and $\overline{r}_m$ measurements at four heater pulse energies for $\overline{n}_{e0,i} = 3.8 \times 10^{17}$ cm^{-3} and laser timing $t_d = 440$ ns after the peak of discharge current. Measurable modification of the plasma occurs with as few as 30 mJ of laser energy, 10% of the pulse energy that was used in the LPA experiments of Refs [21, 22].. The plasma modification observed at 30 mJ is strong evidence for the influence of self-channeling on the propagation of the heater pulse at higher energies: based on the effect observed at 30 mJ, the rising edge of a joule-level pulse contains sufficient energy to significantly modify the plasma profile before the majority of the pulse energy has been deposited.

The effect of laser-heating begins to saturate above energies of 100 mJ. Measurements of $\overline{n}_{e0}$ and $\overline{r}_m$ cannot distinguish between channel properties for the cases of 200 mJ and 300 mJ of laser energy, although the MARPLE simulations show a slightly lower density for

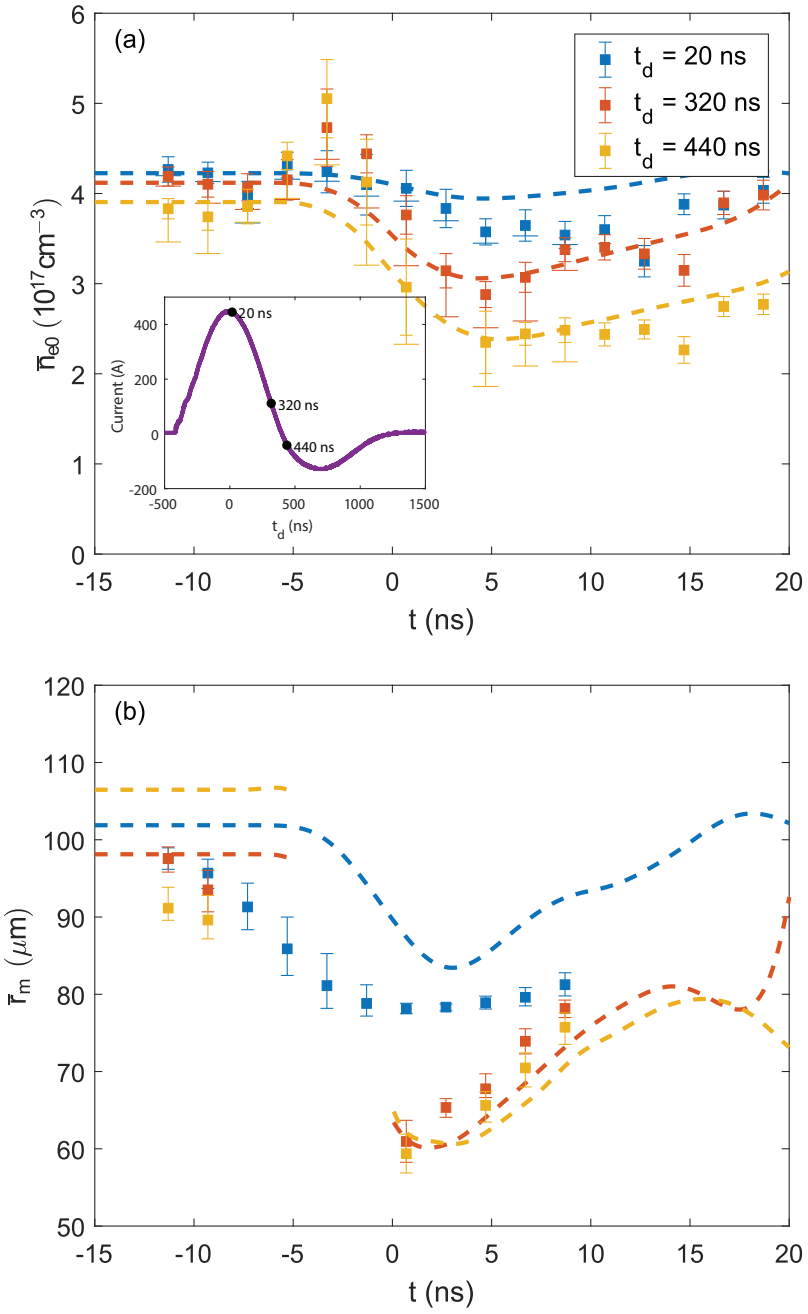

Figure 4.20: (a) $\overline{n}_{e0}$ for 3 arrival times of the heater pulse relative to the discharge current pulse. Heater pulse arrival times t_d are marked on the discharge current trace in the inset. Later times and lower currents correspond to lower initial plasma temperature. Error bars as in Fig. 4.16. Values from MARPLE as dotted lines. (b) Measured $\overline{r}_m$ and MARPLE calculated values for the cases of (a).

300 mJ. This saturation with heater pulse energy is a consequence of the $T_e^{-3/2}$ scaling of the heating rate [Eq. (3.35)]. As the plasma absorbs energy from the heater pulse and T_e increases, it becomes more transparent.

Saturation of the plasma response with respect to pulse energy is predicted by a simplified model of heating as function of the fluence $\Phi \equiv \int_{-\infty}^{t} I \, \mathrm{d}t'$ derived from Eq. (3.36). Taking the factors Λ and n_e constant in Eq. (3.36) and ignoring heat conduction, solving the resulting differential equation yields

$$T_e = (K n_e \Phi \Lambda / \omega^2 + T_{e,i}^{5/2})^{2/5}, \tag{4.33}$$

with $T_{e,i}$ the initial plasma temperature and

$$K = \frac{2^{7/2}\pi^{3/2}}{3} \frac{Z q_e^6}{k_b^{5/2} m_e^{3/2} c} \tag{4.34}$$

a proportionality constant composed of dimensionless factors and physical constants from Eqs. (3.36) and (3.32). Note that as a consequence of neglecting plasma motion and heat conduction, the expression for T_e is independent of the temporal structure of the laser intensity I, depending only on the fluence Φ. This follows from the linearity of the heating rate in the intensity. The saturation behavior is evident from the fact $\mathrm{d}^2 T_e / \mathrm{d}\Phi^2 < 0$. In reality, this simplified model overestimates heating for the experiments reported in this dissertation, as plasma motion will reduce n_e during heating and heat conduction will allow energy to migrate out of the heated region of the plasma. Therefore, plasma temperature will saturate more rapidly than the $\sim \Phi^{2/5}$ scaling of Eq. (4.33).

It is also evident from Eq. (4.33) and its derivation from Eq. (3.36) that sensitivity of the plasma response to the temporal structure of the heater pulse arises through plasma motion and heat conduction, provided the laser intensity remains low enough that the inverse-bremsstrahlung heating rate remains linear in the intensity. Although not directly applicable to the experiments in this dissertation, this may be an important consideration in situations where the heater pulse length is shorter than the characteristic timescales of these processes.

However, the heating rate [Eq. (3.36)] will become nonlinear in the intensity if the electron ponderomotive energy becomes comparable to the plasma temperature, because the collision frequency $\nu_{e,IB}$ will begin to decrease with laser intensity [98, 99]. In this regime, Eq. (4.33) will no longer hold and T_e will become dependent on the heater pulse shape. For the laser and plasma parameters considered in this dissertation, this occurs at a laser intensity and pulse energy of order 10^{14} W/cm^2 and 100 J, respectively. Moreover, Eq. (4.33) does not hold for heater pulse lengths shorter than the electron-ion energy exchange timescale regardless of intensity, as the approximation $T_e \approx T_i$ from which Eqn. (3.36) is derived is no longer valid. Therefore, per the discussion in section 3.6, Eq. (4.33) is not valid for heater pulse lengths of order 100 ps and shorter for the plasmas considered here.

Measurements and simulations show that for laser-heated capillary discharges, channel properties are sensitive to initial plasma density and temperature, delay from the heater pulse, and heater pulse energy. This enables independent tuning of $\overline{n}_{e0}$ and $\overline{r}_m$, and enables

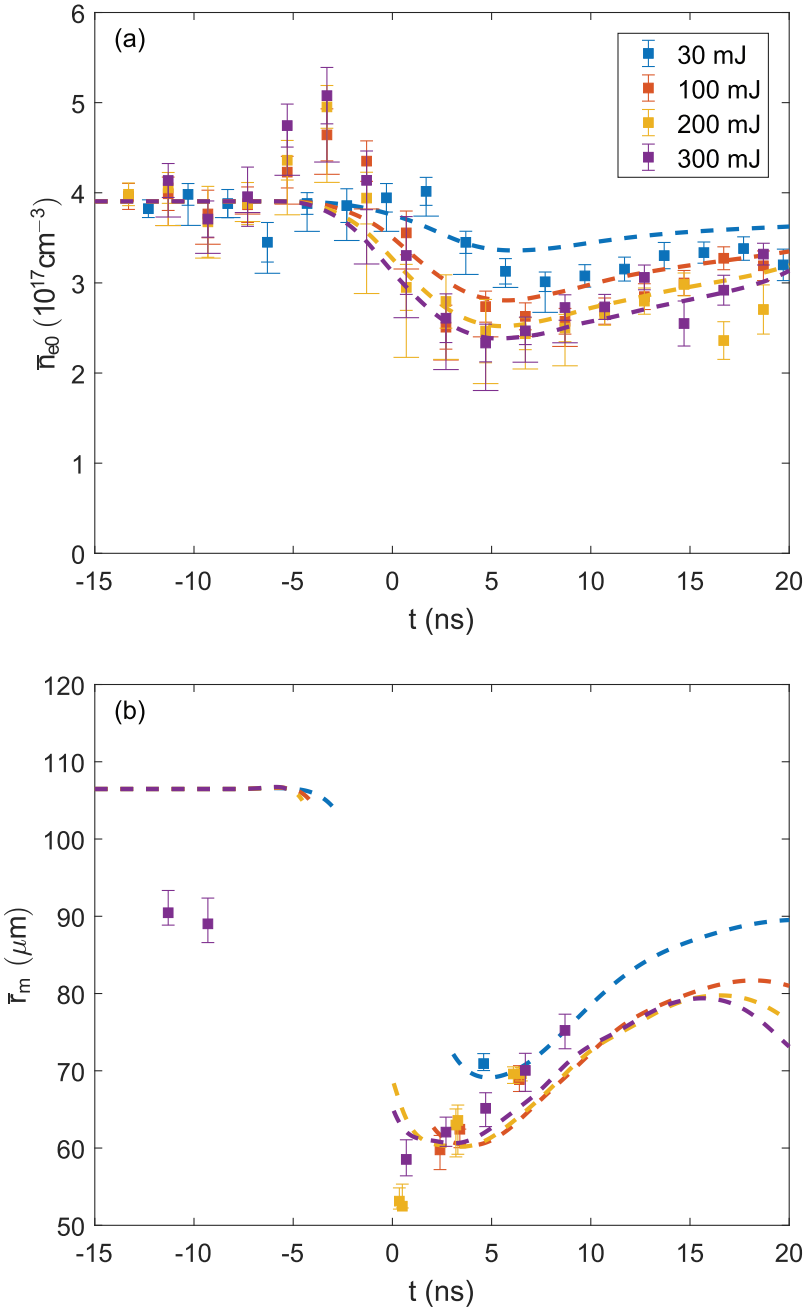

Figure 4.21: (a) $\overline{n}_{e0}$ for 4 heater pulse energies, with identical initial plasma temperature and density. Initial plasma density is 3.8×10^{17} cm^{-3}, arrival time of the heater relative to peak discharge current $t_d = 440$ ns. Error bars as in Fig. 4.16. Values from MARPLE as dotted lines. (b) Measured $\overline{r}_m$ and MARPLE calculated values for the cases of (a).

optimization of guiding with a fixed capillary radius. For example, MARPLE simulations show matched spot sizes of 75 μm and 65 μm at a density of 2.4×10^{17} cm^{-3}: 75 μm at discharge timing and initial density $t_d = 320$ ns and $\overline{n}_{e0,i} = 3.3 \times 10^{17}$ cm^{-3} (Fig. 4.19), and 65 μm at $t_d = 440$ ns and $\overline{n}_{e0,i} = 3.8 \times 10^{17}$ cm^{-3} (Fig. 4.19). To vary matched spot size over the same interval with a capillary discharge, the scaling $r_m \propto {r_c}^{1/2} {n_e}^{-1/4}$ would require a 50% increase in density for fixed capillary radius, or a 25% decrease in capillary diameter for fixed density.

Density can be tuned while matched spot is kept fixed as well. The MARPLE simulations of Fig. 4.21 show that density can be tuned between 3.4×10^{17} cm^{-3} and 2.5×10^{17} cm^{-3} at a constant matched spot size of 69 μm by varying laser energy between 30 mJ and 300 mJ and delay from the heater pulse peak between 5 and 8 ns. Simulations show that single-stage acceleration to energies approaching 10 GeV is possible within this space of accessible spot sizes and densities [114], and tunability of these parameters independent of the capillary radius adds useful flexibility over a conventional capillary discharge, especially when capillary radius is restricted by other factors such as laser damage.

4.8 Conclusion

Laser-heated capillary discharge waveguides have been characterized as novel, tunable guiding structures for LPAs. The independent control of matched spot size and plasma density afforded by these structures has enabled guiding of petawatt-scale pulses focused to a beam waist of ~ 60 μm at low plasma densities required for the production of multi-GeV electron beams within capillaries of large enough diameter to avoid laser damage [21, 22]. This independent tunability of matched spot and density is also useful for the optimization of channel-guided LPAs, where one of these parameters may be constrained by such considerations as required beam energy or control of bunch injection. In this chapter, important trends in the properties of laser-heated capillary discharge waveguides have been identified. Guiding and acceleration can be tuned via initial plasma density and temperature, heater laser pulse energy, and arrival time of the driver relative to the heater pulse. Trends observed in these experiments are consistent with the theoretical models of low power inverse-bremsstrahlung described in Chapter 3, and specific experimental measurements are well reproduced by the MARPLE MHD code. Importantly, the measurements of the time evolution of the plasma channel reported here indicate a path toward improved accelerator performance over prior experiments [21, 22] through optimizing the arrival time of the driver relative to the heater pulse.

Future experiments and simulations with MARPLE will investigate additional strategies for optimizing channel performance through tuning of the heater beam focal spot size, pulse length, and wavelength, which are known to be important parameters for laser-heated capillary discharge waveguides.

Though successful in characterizing laser-heated capillary discharges as just described, the diagnostic techniques for measuring plasma density in laser-heated capillary discharges could be improved upon. Specific issues warranting further development of diagnostics include

the anomalous density peak described in Section 4.6, as well as the complicated spectral fringe patterns and delay drift arising from the use of fiber optics in the interferometer. Motivated by these considerations, as well as the desire to implement a density diagnostic on the main BELLA beamline for in-situ diagnostic measurements of the plasma channels used in electron acceleration experiments, a two-color common-path interferometer[115, 116] density diagnostic was commissioned on the BELLA beamline, which will be the subject of Chapter 5.

Chapter 5

In-situ plasma channel diagnostics on the BELLA laser using two-color common-path interferometry

5.1 Introduction

In this chapter, an interferometric density diagnostic for laser-heated capillary discharge waveguides installed on the BELLA beamline is described, and the results of measurements with this diagnostic are presented. The approach used on the Plasma 2 test stand described in Chapter 4 was not practical for use on the BELLA laser system. For the sake of simplicity, it is desirable to use the BELLA laser itself, in a low power mode of operation, as a probe beam. However, the existing focusing optics are ~ 10 m from the target to reduce the fluence to safe levels at PW-scale laser power, which will introduce unacceptable delay jitter into the measurement as discussed in Section 4.3.

To overcome these difficulties, a two-color common path interferometer was built, which is pictured schematically in Fig. 5.1. Instead of measuring the time delay between two pulses of the same frequency propagating on different optical paths, this scheme relies on measuring the time delay between two pulses of different frequencies propagating on the same optical path. Because the pulses propagate along a common optical path, with a temporal separation < 1 ps, the influence of vibrations on the inter-pulse delay is effectively eliminated.

The diagnostic functions as follows. An 800 nm–"red"–probe pulse is propagated through a nonlinear crystal to produce its second harmonic at 400 nm–"blue". These two pulses, the second harmonic and the residual fundamental, then propagate collinearly through the plasma channel, and acquire a relative delay due to the frequency dependence of the group velocity. Downstream of the plasma channel, a second nonlinear crystal converts the residual fundamental to the second harmonic, resulting in two pulses at the second harmonic with a temporal separation proportional to the plasma density. The delay between these pulses is then measured via spectral interferometry.

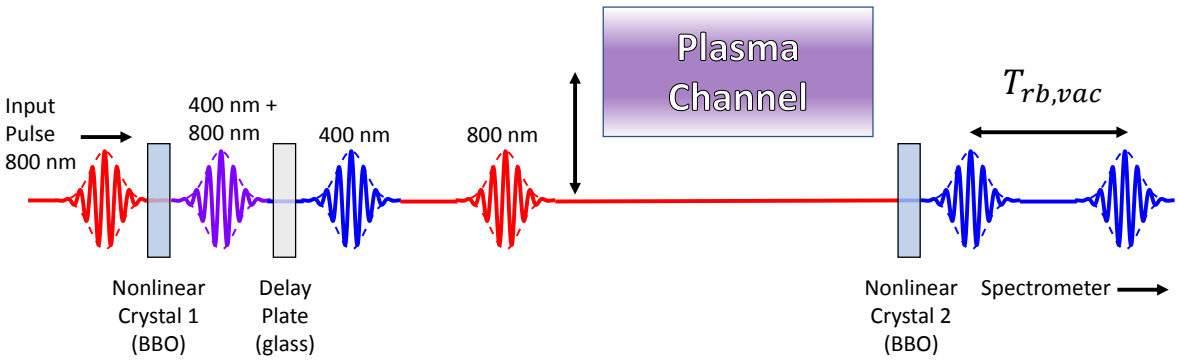

(a) "Vacuum pulse delay" $T_{rb,vac}$ measurement, with the plasma channel (i.e. capillary) removed from the beam path.

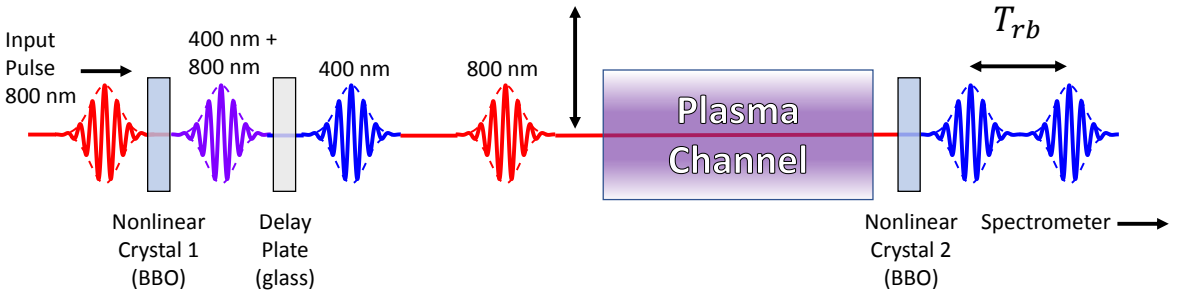

(b) Pulse delay T_{rb} measurement with the plasma channel inserted into the probe beam path.

Figure 5.1: Schematic representation of the two-color common-path interferometer plasma density diagnostic. The delay induced by the plasma channel relative to vacuum, from which the density is can be calculated via Eqn. 4.25, is obtained by taking the difference between to the delay measured for the probe pulse propagating in vacuum (a) and the delay measured for the probe pulse propagating through the plasma channel (b).

The red and blue pulses are initially overlapped after the first nonlinear crystal as shown in Fig. 5.1, being separated by < 100 fs. This is too small a group delay to resolve within the 20 nm bandwidth of the second harmonic pulses, i.e. there are too few spectral fringes for the phase mapping algorithm. Therefore, a delay plate between the two nonlinear crystals (also shown in Fig. 5.1) is used to increase delay between the pulses sufficiently for an interferometric delay measurement. Therefore, a density measurement requires two delay measurements, a vacuum delay $T_{rb,vac}$ measurement with the capillary out of the beam path (Fig. 5.1(a)) and channel delay T_{rb} measurement with the capillary in the beam path (Fig. 5.1(b)), to isolate the effect of the plasma channel on the delay. Note that the delay between the two pulses decreases with the cap in (i.e. $T_{rb} < T_{rb,vac}$), because the red pulse leads the blue pulse after the delay plate, but the blue pulse has a higher group velocity in the plasma.

The plasma density is obtained from the delay measurements in a similar manner to that described in Chapter 4. The channel-induced delay is given by:

$$\Delta T_{rb} = T_{rb} - T_{rb,vac} = \frac{1}{c}\int_0^L \left(\frac{1}{\beta_{g,r}} - \frac{1}{\beta_{g,b}}\right) \mathrm{d}z \ . \tag{5.1}$$

The contribution from the delay plate is canceled out in the difference between the channel and vacuum delay measurements $T_{rb} - T_{rb,vac}$. The group velocity for each wavelength $\beta_{g,\lambda}$ has the familiar form

$$\beta_{g,\lambda} = \frac{v_{g,\lambda}}{c} = 1 - \beta_{g,n_e,\lambda} - \beta_{g,geo,\lambda} \ . \tag{5.2}$$

Once again, $\beta_{g,n_e,\lambda}$ and $\beta_{g,geo,\lambda}$ are $\lesssim 10^{-4}$, and so Eqn. 5.1 can be simplified to

$$\Delta T_{rb} = \frac{L}{c}(\Delta\overline{\beta}_{g,n_{e0}} + \Delta\overline{\beta}_{g,geo}) \tag{5.3}$$

with $\Delta\overline{\beta}_{g,n_{e0}} = \overline{\beta}_{g,n_{e0},r} - \overline{\beta}_{g,n_{e0},b}$ and $\Delta\overline{\beta}_{g,geo} = \overline{\beta}_{g,geo,r} - \overline{\beta}_{g,geo,b}$. Note that the the group velocities are expressed as longitudinal averages as in Chapter 4, since the considerations of longitudinal nonuniformity in laser-heated capillary discharges discussed there still apply.

The density contribution $\Delta\overline{\beta}_{g,n_{e0}}$ is given by

$$\Delta\overline{\beta}_{g,n_{e0}} = -\frac{3}{8}\frac{k_p^2}{k_0^2} \ , \tag{5.4}$$

which results in a relative blue-red delay of 14.5 fs for a plasma density of 1×10^{17} cm^{-3} in a 20-cm-long capillary. Similarly to Chapter 4, these delays are measured using spectral interferometry, which can easily resolve them. The calculation of the geometrical contribution to the group velocity $\Delta\beta_{g,geo}$ which goes as r_m^{-4}, will be addressed in detail in Section 5.4.

This chapter is organized as follows. The experiment setup is described in Section 5.2. The fringe pattern analysis algorithm, which is very similar to that used in Chapter 5, is outlined in Section 5.3. Calculation of the geometrical contribution to the group velocity density measurement is described in detail in Section 5.4. Density measurements in capillary discharges without laser heating are presented in Section 5.5, and measurements in laser-heated capillary discharges are presented in Section 5.6. Findings are summarized in Section 5.8

5.2 Experiment setup

The two-color common-path interferometer described in this chapter is shown schematically in Fig. 5.2. For clarity, only those parts of the laser system directly relevant to the experiments of this chapter are shown. The interferometer setup was installed in the "Plasma 1" target chamber used for electron acceleration experiments on the main BELLA beam line, to obtain in-situ density measurements of laser-heated capillary discharges. However, as the diagnostic involves propagation of laser pulses through solid materials, these measurements can only be performed when the BELLA laser is operated at low power. For high power operation of the laser (above the millijoule level), the nonlinear crystals and delay plate assembly must be removed from the beam path. Nevertheless, the advantage of measuring the same plasma channels used for LWFA experiments, generated by the same discharge capillary and heater system, remain. Details of the BELLA laser system are largely beyond the scope of this dissertation. Key features of note to the operator and experimenter are summarized in Chapter 6.

The capillary and discharge system are identical to those used for the experiments of Chapter 4. Specifically, an 800 µm diameter, 20-cm-long hydrogen-filled capillary with discharge current pulse as in Fig. 4.3 was investigated.

The heater laser used an identical 532 nm q-switched, frequency-doubled, Nd:YAG laser system to that used for the experiments of Chapter 4. The 12 mm diameter beam was expanded using a Galilean telescope consisting of a -200 mm plano-concave lens L1 and a 2123 mm plano-convex lens L2, separated by 1930 mm. A 75 mm diameter iris was placed 28.5 cm upstream of L2 to spatially filter the heater beam in a similar manner to that described in Chapter 4. The position of the iris in the telescope was selected to maximize the peak fluence of the heater beam at focus. The resulting 87 mm diameter collimated beam is focused to the target by a 12.96 meter plano-convex lens L3, for a system F/# of 150. The beam enters the evacuated beamline through an anti-reflective-coated window, and is coupled in collinearly with the 800 nm BELLA laser through a dichroic mirror, as is shown in Fig. 5.2. At the target, the system delivers up to 300 mJ of laser energy in an 8 ns pulse, with a focal spot of 81 µm. Beam profiles for the heater laser near focus are shown in Fig. 5.3.

The "probe beam" used for these experiments was the 800 nm BELLA Ti:Sapphire laser itself, albeit operated in a low power configuration that only generated 9 mJ pulses. The grating compressor was set to its "zero point," where pulse length is minimized, to produce $\sim$ 40 fs pulses. As designed, the BELLA laser produces a $\sim$ 200 mm diameter nearfield, which is focused to a $\sim$ 60 µm focal spot with a 13.5 m focal length off-axis paraboloid (OAP). However, to spatially filter the probe beam and improve the precision of the density measurements (see Section 5.5), for these experiments a 70 mm iris was inserted upstream of the grating compressor to increase the focal spot to 134 µm, which also reduced the total pulse energy to 2 mJ on target. In this configuration, the probe system had an $F/\#$ of 193. Profiles for the "red" (800 nm) probe beam near focus are shown in Fig. 5.4(a).

Even with the laser operating in this low power configuration, the peak intensity at focus is $\sim 2 \times 10^{14}$ W/cm^2, above the 1.4×10^{14} W/cm^2 threshold for barrier-suppression

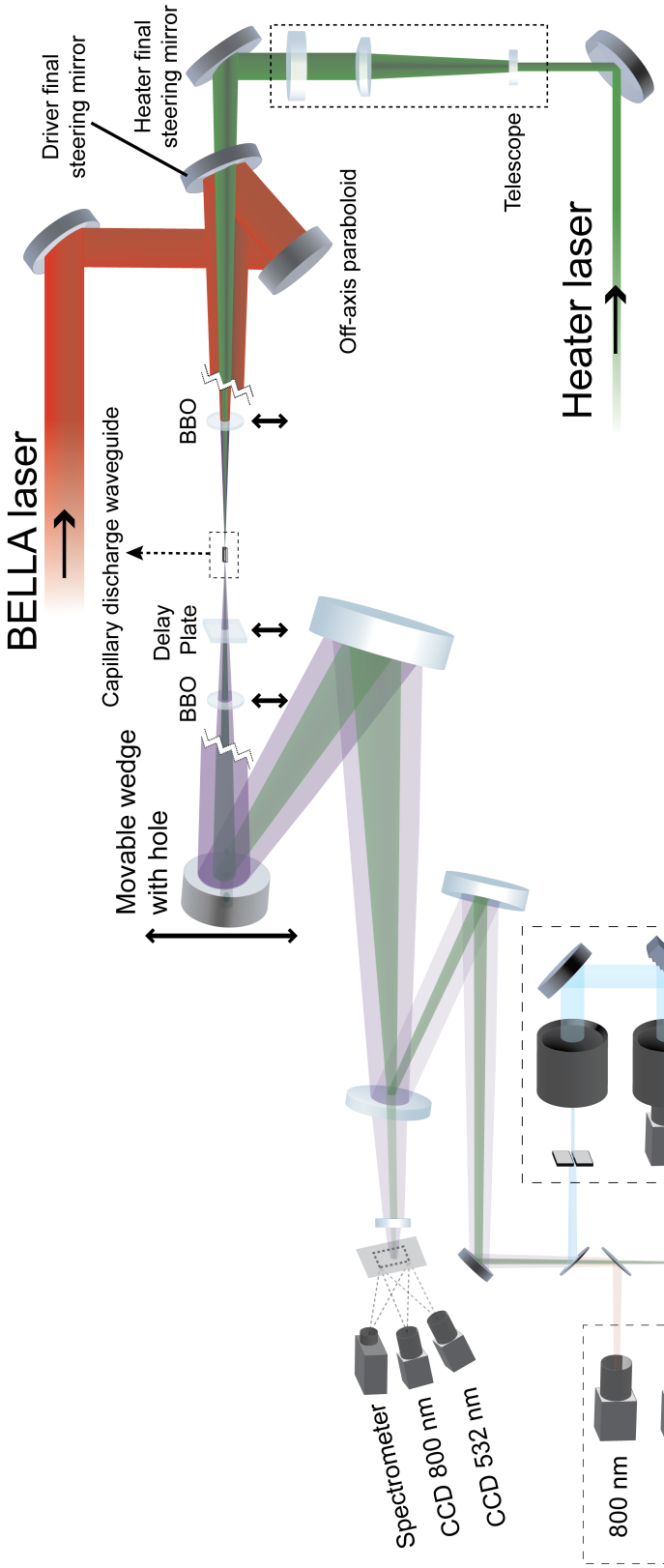

Figure 5.2: Layout of the two-color common-path interferometer setup. Heater beam (532 nm) is marked in green, probe beam (800 nm) is marked in red, and areas where the two wavelengths copropagate are marked in purple.

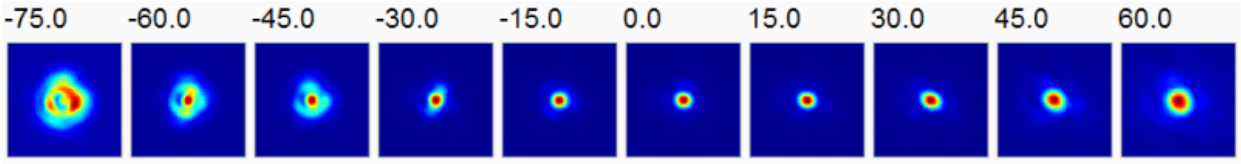

Figure 5.3: Image size 886 µm. Fluence profiles of the heater beam as a function of distance z from focus, in mm.

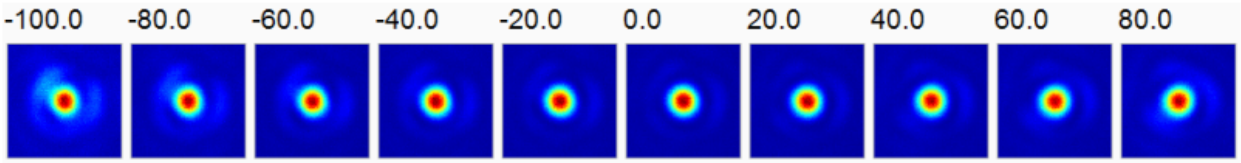

(a) Image size 886 µm. 800 nm "red" probe beam fluence.

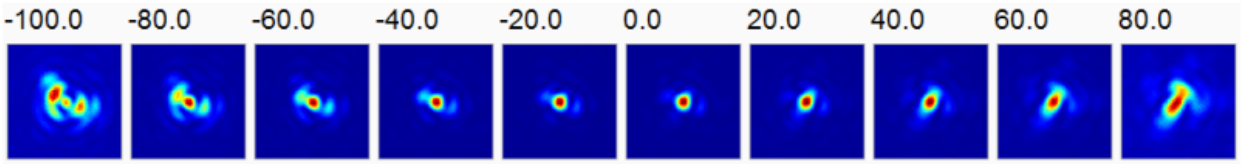

(b) Image size 886 µm. 400 nm "blue" probe beam fluence.

Figure 5.4: Fluence profiles of the red and blue beams as a function of distance z from focus, in mm. 70 mm iris installed upstream of the compressor.

ionization of neutral hydrogen [37]. However, MARPLE simulations and spectral blueshifting measurements in Chapter 6 show that the neutral fraction on-axis in the channel is at most $\sim 1\%$, and then only for discharge delays $\gtrsim 420$ ns. A 1% increase in plasma density from ionization is well below the sensitivity of the diagnostic, and hence can be neglected.

however no ionization blueshifting was observed and no dependence of plasma density on the probe pulse length was observed, and hence it was concluded that ionization by the probe laser did not impact the density measurements.

The common-path interferometer setup in the target chamber consisted of two β-Barium Borate (BBO) crystals for second harmonic generation, each 100 µm thick and cut for type-I phase matching, and a pair of delay plates constructed from two 1-mm-thick microscope slides. All three optical elements were installed on motorized stages, allowing them to be moved in and out of the beam path as experiments require. In the setup as constructed, in contrast to the schematic of Fig. 5.1, the delay plates were installed after the capillary, as shown in Fig. 5.2 (in the figure, the two delay plates were merged together for the sake of clarity). This was strictly a matter of mechanical convenience, as long as the delay plate is installed between the two nonlinear crystals, it will produce the temporal separation between the two wavelengths required for the delay measurement. The frequency doubled "blue" (400 nm) beam was focused to an 84 µm spot, and the conversion efficiency at each BBO crystal was

estimated to be $\sim 10\%$. Fluence profiles of the blue beam are plotted in Fig. 5.4(b), showing the the blue beam also appears to have more high order mode content compared to the red beam. This is to be expected from the second harmonic generation process. The production of the second harmonic is a second-order nonlinear process, and so any intensity fluctuations in the fundamental are exaggerated in the second harmonic, and the phase associated with any wavefront error in the fundamental is doubled.

The BBO crystals were installed 980 mm upstream and downstream of the target, with the delay plate assembly roughly 30 mm upstream of the downstream BBO crystal. The large standoff distances of the nonlinear crystals from the target is a departure from the setup described in Ref. [115], however this change was necessary to keep the fluence of the heater beam—which copropagates with the probe—on the optics within safe limits to avoid laser damage. With a heater $F/\#$ of 150 and pulse energy 300 mJ, this results in a fluence of 0.8 J/cm^2 in a ~ 7 mm diameter laser spot on the crystals and delay plates from the heater laser. For the probe, with $F/\#$ of 192 and pulse energy 2 mJ, the beam diameter on the crystal was 5 mm with fluence 0.01 J/cm^2. No damage was observed for these fluences.

The lasers were imaged using a reflective achromatic telescope. Through multiple reflections off uncoated fused silica wedges, the telescope attenuates the laser energy delivered to the laser high power diagnostics table by a factor 5×10^{-5}. The capillary entrance plane is imaged onto the the high power diagnostics table with magnification 1. As shown in Fig. 5.2, two CCD cameras were used to image the "probe" (i.e. the BELLA driver beam) and heater beams, these were installed on a motorized stage to facilitate imaging of the laser beams along the direction of propagation. A 700 nm longpass filter was installed on the probe camera to reject light from the heater laser. The filtration on the heater beam camera, which consisted of a 600 nm shortpass filter, allowed it to also image the 400 nm second harmonic of the probe beam. Hence, the heater mode imager was used to acquire the beam profiles of Fig. 5.4(b).

The same imaging spectrometer used for the experiments on Plasma 1 of Chapter 5 was repurposed for these experiments. The only change made was the exchange of the 1200/mm diffraction grating with a 2400/mm grating to accommodate the halving of the operating wavelength. The spectrometer was positioned on the high power laser diagnostics table such that it images the exit plane of a 20-cm-long capillary. In this configuration, all rays incident on the spectrometer slit are guaranteed to travel the same path length from the capillary exit by Fermat's Principle of Least Time [117]. This minimizes the contribution of pointing jitter (in both position and angle) at the capillary exit to the delay measurement. This was arranged by installing a dichroic mirror in the optical line to the heater and probe mode imagers to separate the second harmonic light and send it to the spectrometer slit.

5.3 Fringe pattern analysis

The spectral interferograms produced by this diagnostic are analyzed using the algorithm described in Section 4.3, however the analysis for the two-color common path diagnostic

differs in some key ways. As there was no quadratic spectral phase introduced between the red and blue pulses (due to the absence of long fibers), the no phase background subtraction was required to calculate the relative pulse delay. Also, the global group delay of the laser pulses was used to define the measured delay between the red and blue pulses, rather than the centroid group delay. The global group delay was used because the shot-to-shot jitter in the positions of the red and blue beams at the capillary exit, as well as the multimode structure of the guided beams, made it difficult to assign a "centroid" to the beams imaged on the spectrometer slit. However, calculating the global group delay requires taking a weighted average of the group delay measured at each row of pixels on the spectrometer.

The analysis procedure used will now be described, with the aid of Fig. 5.5, to the extent that it differs from Section 4.3. The delay between the red and blue pulses is calculated from the interferogram Fig. 5.5(a) according to

$$T_{rb} = \int_0^{y_{CCD}} \phi'_{rb}(y)\overline{C}(y)\mathrm{d}y \tag{5.5}$$

with y_{CCD} the height of the spectrometer camera sensor, $\phi'_{rb}(y)$ the linear group delay between the red and blue pulses across the slit, and the weighting function $\overline{C}$

$$\overline{C}(y) = \frac{\int_{-\infty}^{\infty} C(\tau - \tau_0, y)\mathrm{d}\tau}{\int_0^{y_{CCD}} \int_{-\infty}^{\infty} C(\tau - \tau_0, y)\mathrm{d}\tau\mathrm{d}y} \ , \tag{5.6}$$

defined according to Eqn. 4.11. The sideband C is marked in Fig. 5.5(b), with the integration in τ performed over the marked interval. The fitted group delay $\phi_{b,r}$ and weighting function $\overline{C}$ are plotted in Fig. 5.5(c). As can be seen in Fig. 5.5(c), the weighting function was thresholded at 5% of its peak value, to suppress noise.

Eqn. 5.5 is an intuitive definition of the the delay, as there is not one single group delay measured across the interferogram, but rather a group delay measurement for every row of pixels and thus an average of some kind is required. That said, there is a physical meaning to associated with the choice of weighting function. $\overline{C}$ is proportional to the spectral energy density associated with the interference term in Eqn. 4.5, i.e. $C \propto |a_b(\omega, y)||a_r(\omega, y)|$. Therefore, $\overline{C}$ is essentially the distribution in y of the "spatially overlapping laser energy" that produces the interferogram.

5.4 Correction for finite matched spot size in density measurements

It was necessary to accurately model the contribution of the channel finite matched spot size to the density measurement, as spatial filtering with the iris described in Section 5.2 increased the beam size such that the geometrical contribution to the density measurement cannot be ignored or simply treated as a systematic error. This requires accurately treating the multimode nature of the blue and red beams. The electric field of each laser beam was

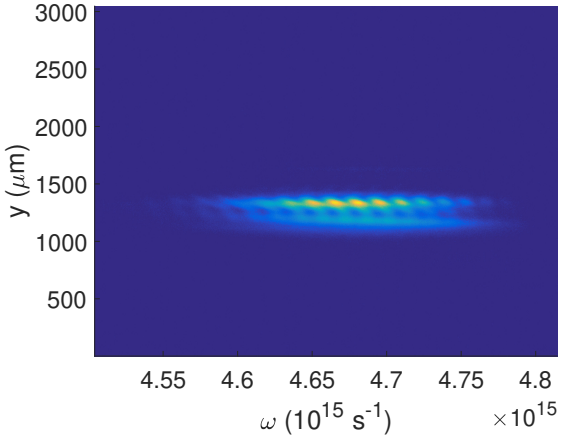

(a) Fringes on the Plasma 1 setup.

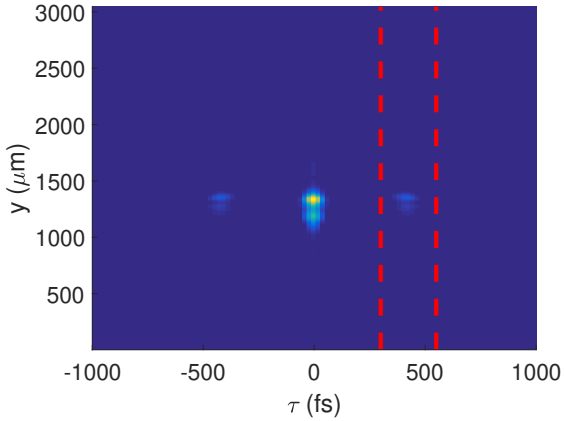

(b) FFT of (a). Weighting function $\overline{C}(y)$ calculated by integrating over the marked area.

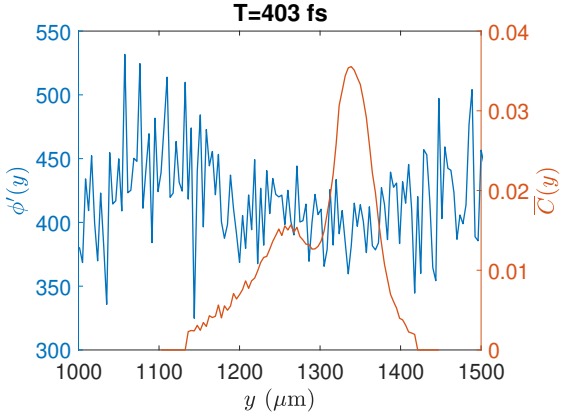

(c) Group delay and weighting function $\overline{C}(y)$

Figure 5.5: Fringe pattern analysis. For the case of a 800 µm, 20-cm-long capillary operated with 17 torr fill pressure, $t_d = 420$ ns after the peak of discharge current.

decomposed into the normal modes of a parabolic channel as described in Section 3.2, from which the global group velocity of the laser pulse in the channel was calculated. A standard phase retrieval procedure [118, 119] was performed to obtain the electric field for each beam.

It must be noted that this technique is approximate: First, as was shown in Chapter 4, the plasma profile is, in general, not parabolic in a laser-heated capillary discharge. Second, the matched spot size and density are not longitudinally uniform. Nevertheless, this simple model effectively captures the influence of the channel radius on the density measurement, as will be shown later.

Modeling the group velocity of a multimode pulse in a parabolic channel is a straightforward application of the material of Section 3.2. The group velocity for a beam with arbitrary mode content is given by a weighted average of Eqn. 3.15:

$$\overline{\beta}_g = 1 - \frac{k_p^2}{2k_0^2} - \frac{2\langle N_{r_m}\rangle}{k_0^2 r_m^2} \ , \tag{5.7}$$

with the mean Laguerre-Gaussian mode number $\langle N_{r_m}\rangle$ for parabolic channel of matched radius r_m

$$\langle N\rangle \equiv \sum_{m=0}^{\infty}\sum_{p=-\infty}^{\infty}(2m+|p|+1)|C_{m,p}|^2 \ , \tag{5.8}$$

and the amplitudes $C_{m,p}$ such that

$$\sum_{m=0}^{\infty}\sum_{p=-\infty}^{\infty}|C_{m,p}|^2 = 1 \ . \tag{5.9}$$

The geometrical component of the group velocity $\overline{\beta}_{geo,\lambda}$ is given by the third term of Eqn. 5.7:

$$\overline{\beta}_{geo,\lambda} = \frac{2\langle N_{r_m}\rangle}{k_0^2 r_m^2} \tag{5.10}$$

Taking the difference $\Delta\overline{\beta}_g = \beta_{g,r} - \beta_{g,b}$, with $k_r = k_0$ and $k_b = 2k_0$,

$$\Delta\overline{\beta}_g = \Delta\overline{\beta}_{g,n_{e0}} + \Delta\overline{\beta}_{g,geo} = -\frac{3}{8}\frac{k_p^2}{k_0^2} - \frac{1}{k_0^2 r_m^2}\left(\langle N_{r_m,b}\rangle - \frac{1}{4}\langle N_{r_m,b}\rangle\right) \ , \tag{5.11}$$

and hence

$$\Delta\overline{\beta}_{g,geo} = -\frac{1}{k_0^2 r_m^2}\left(\langle N_{r_m,b}\rangle - \frac{1}{4}\langle N_{r_m,b}\rangle\right) \ . \tag{5.12}$$

Note that the influence of the mode content $\langle N_{r_m,b}\rangle$ of the blue beam in Eqn. 5.11 is diminished by the k_0^{-2} scaling of Eqn. 5.10. Hence, the geometrical correction to the plasma density will be dominated by the mismatch and mode content of the red beam.

To calculate $\langle N\rangle$, the electric field of the laser beam must be determined, which requires the use of a phase retrieval algorithm. For this purpose, the standard Gerchberg-Saxton

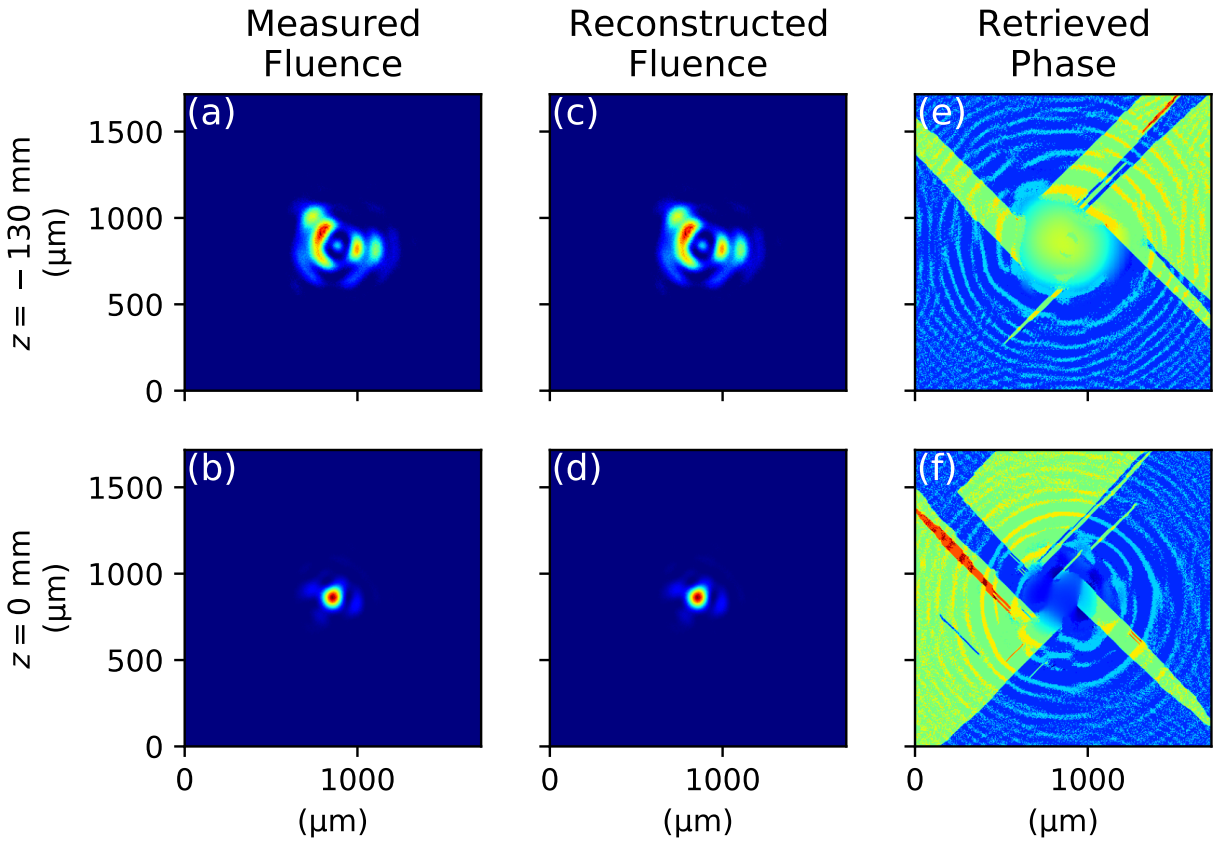

Figure 5.6: Phase retrieval for the blue (400 nm) beam. (a),(b): Measured beam profiles at the "nearfield" $z = -130$ mm and focus $z = 0$ mm, respectively. (c),(d): Reconstructed fluence from the phase retrieval at z positions of (a) and (b). (e),(f): Retrieved phase for (a) and (b). Discontinuities in the phase, i.e. the large "patches," are a numerical artifact of the $[-\pi, \pi]$ branch cut in the complex plane that can occur where the image signal is low.

algorithm was used [118, 119]. Phase retrieval was performed on both the red and blue beams, and the results of this phase retrieval for the blue beam are shown in Fig. 5.6.

From the electric field $|E|e^{i\phi(x,y)}$ at focus, with $|E|$ from the laser fluence and $\phi(x, y)$ from Fig. 5.6(f), the laser field can be decomposed into the Laguerre-Gaussian modes of Eqn. 3.10 according to Eqn. 3.11. Note that this decomposition must be performed for each value of the matched spot size r_m. The energy in each mode $|C_{m,p}|$ is plotted for both beams in Fig. 5.7, for the "best fit" value of r_m for each, where r_m is approximately equal to the beam waist defined by the second moment of the fluence $\sigma^2_{r,0}$. The range of mode numbers for the decomposition was chosen to encompass $> 95\%$ of the total laser energy. Unsurprisingly, the blue beam, which is generated by nonlinear frequency conversion in the upstream BBO crystal, contains significantly more higher-order mode content than the red beam.

To verify the accuracy of the modal decomposition, the beams were reconstructed according

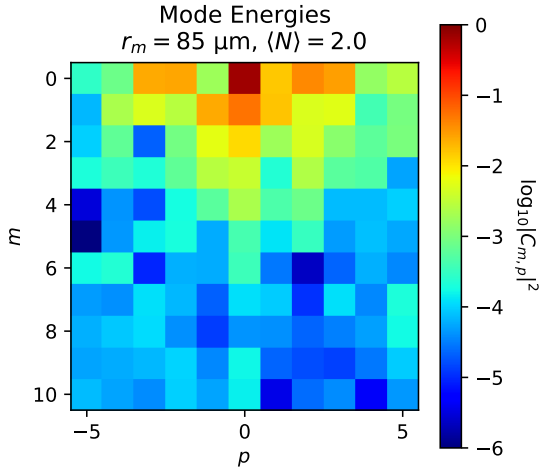

(a) Laguerre-Gaussian mode energies for the blue beam, for matched radius $r_m = 85$ µm.

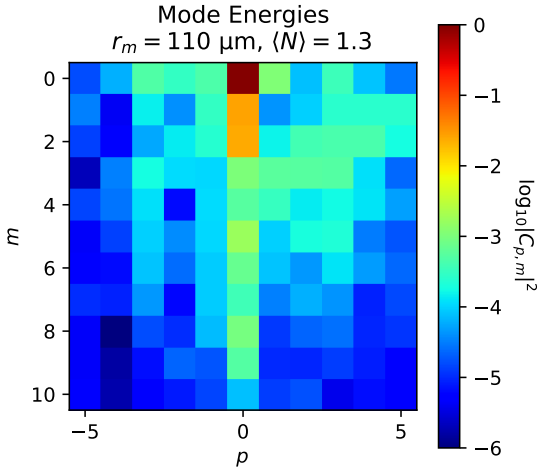

(b) Laguerre-Gaussian mode energies for the red beam, for matched radius $r_m = 110$ µm.

Figure 5.7: Distribution of beam energy in the Laguerre-Gaussian basis for each beam, calculated from the reconstructed electric field (as shown in Fig. 5.6). The matched radius r_m for each beam was chosen for the "best fit," i.e. lowest effective mode number $\langle N_{r_m} \rangle$ according to Fig. 5.9. Scale is logarithmic, total energy normalized to 1.

to the mode amplitudes of Fig. 5.7. This reconstruction is shown for the blue beam in Fig. 5.8, and it is clear that the model decomposition and faithfully reproduces the measured laser field. Note that for both the phase retrieval and the modal decomposition, the laser profile images were thresholded (i.e. pixels below noise level of the sensor value were set to zero) to suppress noise, as can be seen in Fig. 5.8(b).

The effective mode number $\langle N_{r_m} \rangle$ and geometrical contribution to the group velocity $\overline{\beta}_{g,geo,\lambda}$ as a function of matched spot size r_m for each wavelength is plotted in Fig. 5.9. Despite having a larger effective mode number, the blue beam has a smaller geometrical correction to the group velocity due to the k_0^{-2} scaling of Eqn. 5.7, as can be seen in Fig. 5.9.

The geometrical correction to the group velocity can then be used to calculate a correction to the measured density according to Eqn. 5.3.

$$\overline{n}_{e0} = -\frac{8}{3}\frac{k_0^2}{4\pi r_e}\left(\frac{c\Delta T_{rb}}{L} - \Delta\overline{\beta}_{g,geo}\right) \tag{5.13}$$

This can be rewritten

$$\overline{n}_{e0} = n_{e,raw} - \Delta n_{e,geo} \ , \tag{5.14}$$

with $n_{e,raw}$ the density from treating propagation in terms of plane waves, and $\Delta n_{e,geo}$ the geometrical correction for the finite matched spot size. The calibration curve for $\Delta n_{e0,geo}$ obtained from the eigenmode model is plotted in Fig. 5.10, as well as an analytical fit

$$\Delta n_{e0,geo}[10^{17}\ \mathrm{cm}^{-3}] = 0.032[1 + (128/r_m[\mu\mathrm{m}])^4] \ , \tag{5.15}$$

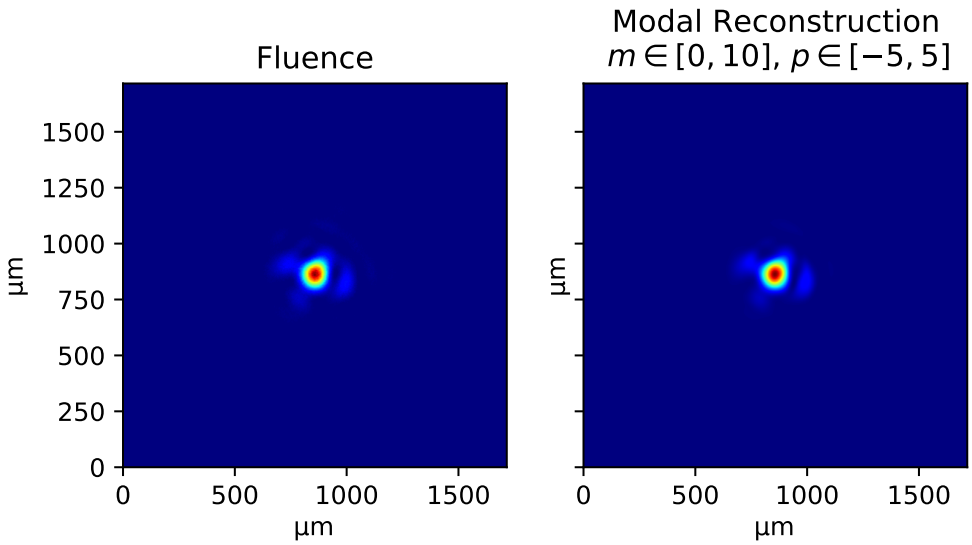

(a) Left: Measured fluence profile of the blue beam. Right: Reconstructed fluence profile in the Laguerre-Gaussian basis, using the mode weights of Fig. 5.7(a).

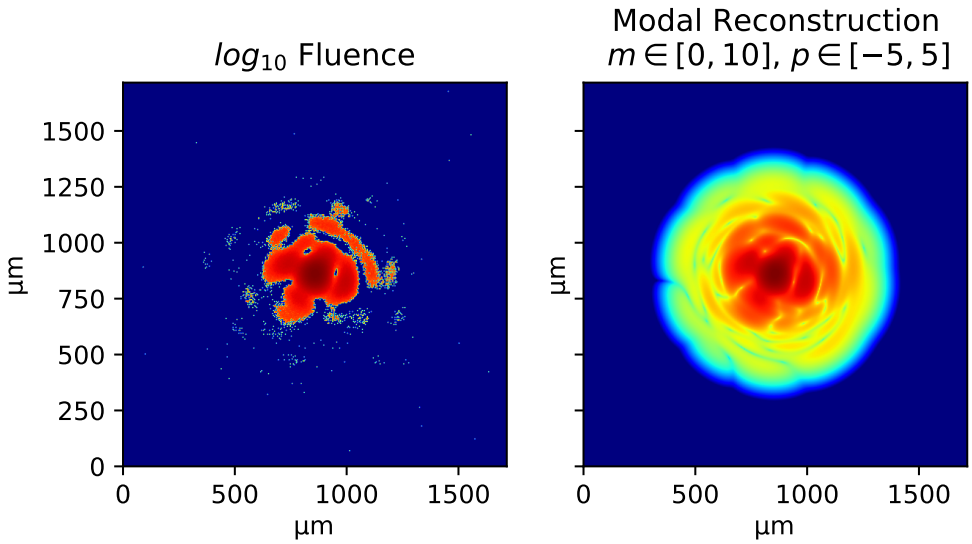

(b) Log scale plots of the fluence of (a). Measured beam profile (left) was thresholded to suppress noise.

Figure 5.8: Reconstruction of the blue beam in the Laguerre-Gaussian basis according to the mode weights of Fig. 5.7(a).

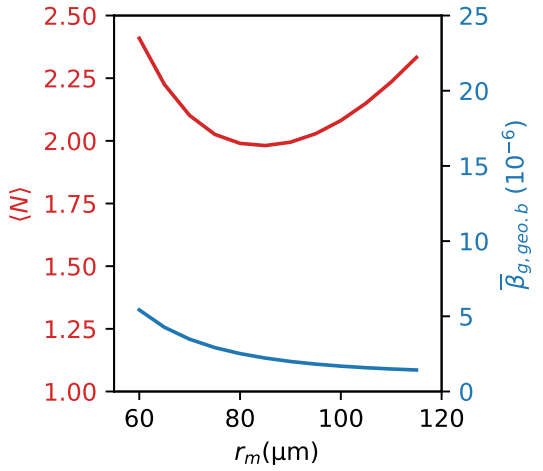

(a) Effective mode number and group velocity correction for the blue beam.

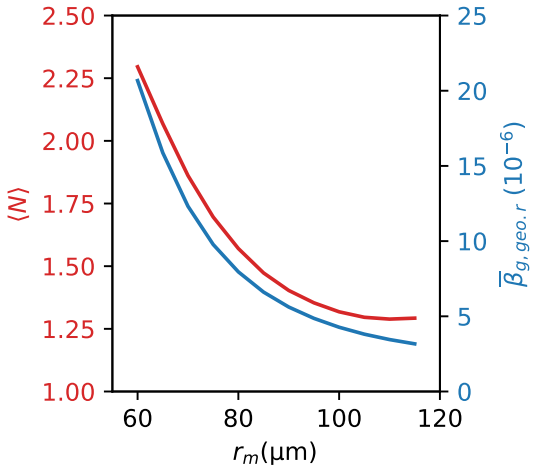

(b) Effective mode number and group velocity correction for the red beam.

Figure 5.9: Effective mode numbers and group velocity correction as function of matched radius r_m for the red and blue beams.

which was used to correct the measurements presented in the following sections of this chapter. This yields a correction of 0.7×10^{17} cm^{-3} at $r_m = 60$ µm, $\sim 25\%$ of the 2-3 $\times 10^{17}$ cm^{-3} plasma densities relevant for LWFA.

An alternative method for calculating the geometrical group velocity contribution for multimode beams

It is possible to measure the mode content of a laser beam using only beam profile measurements in a series of axial slices along the propagation direction, without performing a phase retrieval. This potentially enables a more convenient method to correct for the geometrical contribution to the laser group velocity for the plasma density measurements described in this section, provided sufficiently accurate beam profile measurements can be performed. Though it was not implemented for the work described here, it may be useful technique for future experiments. The proposed method relies on measurements of the beam quality factor M^2 [105, 106]:

$$W_r(z) = W_{r0}\sqrt{1 + M^4\left(\frac{z}{\tilde{Z}_R}\right)^2}\,, \tag{5.16}$$

with $W_{r0}^2 = 2(\sigma_{x0}^2 + \sigma_{y0}^2)$ the vacuum beam waist, σ_{x0} and σ_{y0} the transverse second moments of the laser fluence at focus, and the effective Rayleigh length $\tilde{Z}_R = kW_{r0}^2/2$. For a Gaussian laser beam $W_{r0} = r_0$, with r_0 the Gaussian spot radius. The mean mode number defined for

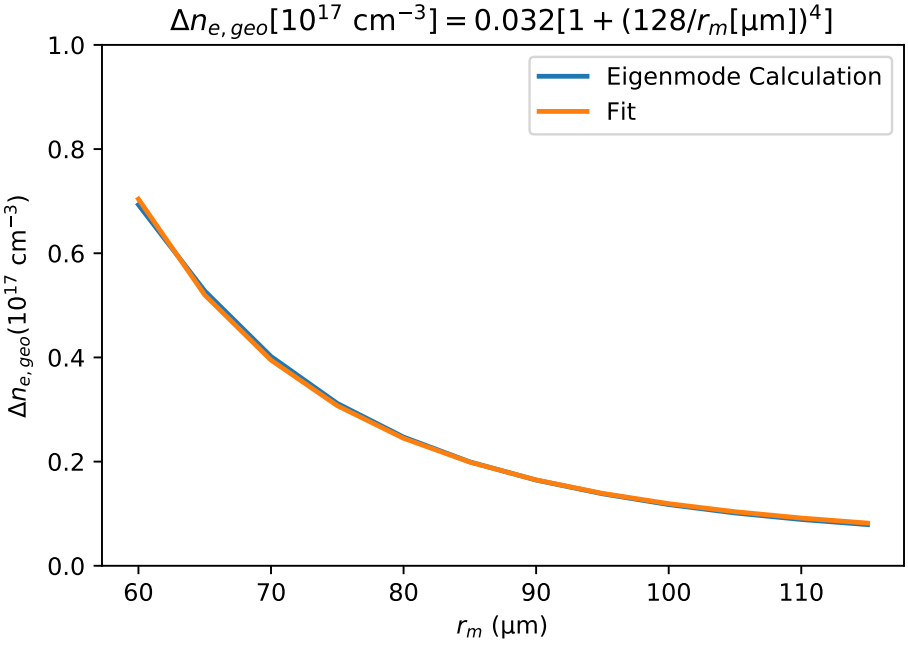

Figure 5.10: Correction for the geometrical contribution to the density measurement vs. r_m for the red and blue beams of Figs. 5.4(a) and 5.4(b), using the eigenmode model of Eqn. 5.12 with the effective mode numbers of Figs. 5.9(a) and 5.9(b). An analytical fit to the output of the eigenmode model is also shown.

the Laguerre-Gaussian basis with vacuum waist W_{r0} is given by

$$\langle N_{r0} \rangle = M^2 \ . \tag{5.17}$$

The quantity M^2 can be combined with Eqn. 3.18 [48] to obtain the global group velocity for a multimode Laguerre-Gaussian beam:

$$\langle \beta_G \rangle = 1 - \frac{k_p^2}{2k_0^2} - \frac{M^2}{k_0^2 r_m^2}\left(1 + \frac{W_{r0}^4}{r_m^4}\right) \tag{5.18}$$

It should be noted that the average over the modes in Eqn. 5.18 relies on the orthogonality of the constituent eigenmodes of the beam. In a parabolic channel, this condition holds throughout the propagation even for mismatched beams, as the spot size evolution for the individual Laguerre-Gaussian modes [48]

$$\frac{\partial^2 r_s}{\partial z^2} = \frac{4}{k^2 r_s^2}\left(1 + \frac{r_s^4}{r_m^4}\right) \ , \tag{5.19}$$

is independent of the mode number. Therefore, the spot sizes r_s of all the constituent modes oscillate together as the beam propagates in the channel, and the orthogonality condition [Eqn. 3.11] (with $r_m \to r_s$) holds.

The geometrical correction using Eqns. 5.17 and 5.18 is then written

$$\Delta\overline{\beta}_{M^2,geo} = -\frac{1}{k_0^2 r_m^2}\left[M_r^2\left(1+\frac{W_{r0,r}^2}{r_m^4}\right) - \frac{M_b^2}{4}\left(1+\frac{W_{r0,b}^2}{r_m^4}\right)\right] , \tag{5.20}$$

with the r and b subscripts denoting the quantities for the red and blue beams, respectively. This can be written as a correction to the density using Eqn. 5.13

$$\Delta n_{e0} = \frac{8}{3}\frac{1}{4\pi r_e r_m^2}\left[M_r^2\left(1+\frac{W_{r0,r}^2}{r_m^4}\right) - \frac{M_b^2}{4}\left(1+\frac{W_{r0,b}^2}{r_m^4}\right)\right] . \tag{5.21}$$

As stated previously noted, this technique was not implemented for the experiments described here. However, correction of the geometric group velocity contribution using beam profile measurements with Eqn. 5.21 would be a useful further development of the diagnostic.

5.5 Density measurements in capillary discharges, without laser-heating

Density vs. pressure

In Fig. 5.11, plasma density is plotted as a function of fill pressure for delays $t_d = 300$ ns, 360 ns, and 420 ns relative to the peak of discharge current. The interferometer is very stable due to the common-path configuration, with random error in the density measurement $< 0.2 \times 10^{17}$ cm^{-3}. The absence of long optical fibers also eliminated the slow delay drift described in Chapter 4, and the absolute plasma density can therefore be accurately measured. The measured density gradients (slope of the fits) agree well with the slopes measured on plasma 2, and because of the lack of delay drift, the zero-pressure offset can be accurately determined. This zero pressure offset exists because of the contribution to the plasma density from hydrogen adsorbed to the capillary walls [89, 120] that vaporizes when the discharge is fired.

Some interesting comparisons of the data plotted in Fig. 5.11 with prior studies of capillary discharge waveguides can be made [17, 84, 88–91, 120–122]. The Quasi-Static Model developed by Bobrova et al [84]. referred to in Chapter 3 gives the scaling

$$n_{e0,QSM}[\text{cm}^{-3}] = 1.473 \times n_{H_2}[\text{cm}^{-3}] \tag{5.22}$$

Measurements in square capillaries with side lengths 125, 210, and 465 µm by Gonsalves et al [90]. yielded the empirical scaling law

$$n_{e0,Gonsalves}[\text{cm}^{-3}] = 0.87 \times n_{H_2}[\text{cm}^{-3}] + 0.11 \times 10^{18} , \tag{5.23}$$

which agreed well with a scaling deduced by Broks et al [89]. for 250 µm side-length square capillaries using a non-local thermal equilibrium ("non-LTE") magnetohydrodynamics code

$$n_{e0,Broks}[\text{cm}^{-3}] = 0.74 \times n_{H_2}[\text{cm}^{-3}] + 0.28 \times 10^{18} . \tag{5.24}$$

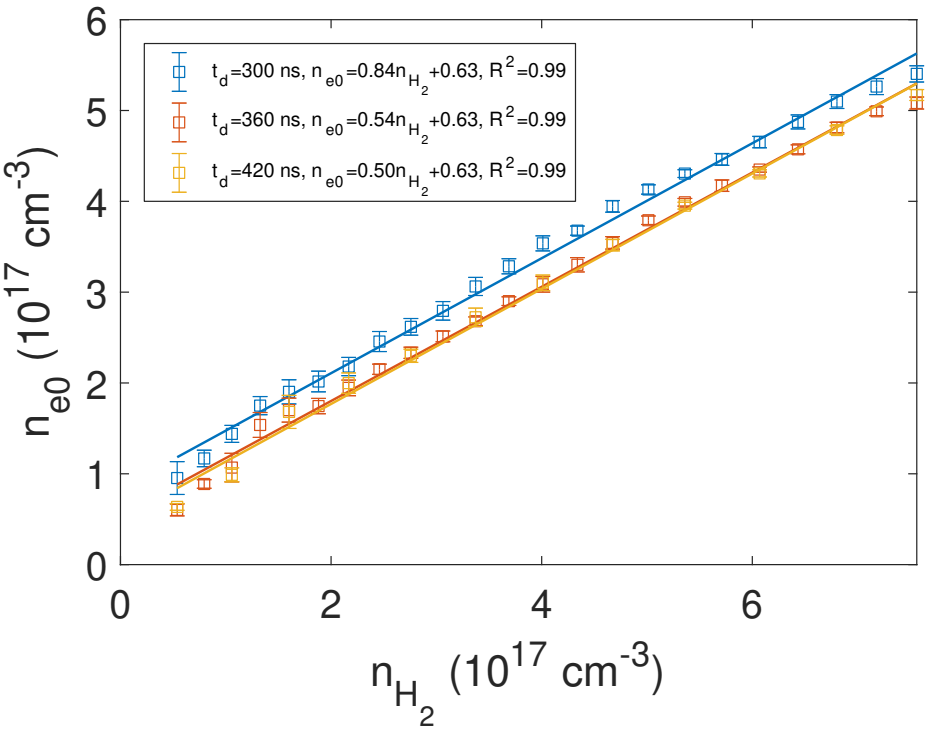

Figure 5.11: Plasma density vs. initial neutral H_2 density for three delays t_d relative to the peak of discharge current in a 800 µm diameter, 20-cm-long laser-heated capillary discharge. Least-squares fits to the density measurements are shown in corresponding colors.

Later density measurements by Daniels et al. in 500 µm diameter capillaries obtained the scaling

$$n_{e0,Daniels}[\mathrm{cm}^{-3}] = 0.57 \times n_{H_2}[\mathrm{cm}^{-3}] + 0.17 \times 10^{18} \ . \tag{5.25}$$

Finally, taking the $t_d = 300$ ns case from Fig. 5.11 because it most closely matches the experiments of [91], these measurements yield the scaling

$$n_{e0}[\mathrm{cm}^{-3}] = 0.63 \times n_{H_2}[\mathrm{cm}^{-3}] + 0.084 \times 10^{18} \ . \tag{5.26}$$

$R^2 = 0.99$ for all the fits in Fig. 5.11. However, a perfectly linear fit of plasma density to neutral gas density at a given delay from the peak of discharge current is not necessarily expected, due to evolution of the plasma during the discharge current pulse. However, this was not investigated in detail.

First, it should be stated that it is not straightforward to compare the foregoing results with one another. The discharge current and timing of the density measurement relative to peak discharge currents varies widely between the models and data sets from which Eqns. 5.22-5.26 were deduced. Therefore, only very broad conclusions can be drawn. However, there does appear to be a trend towards lower values of the gradient (the slope with respect to initial H_2 molecular density) as the capillary radius is increased. This difference may be

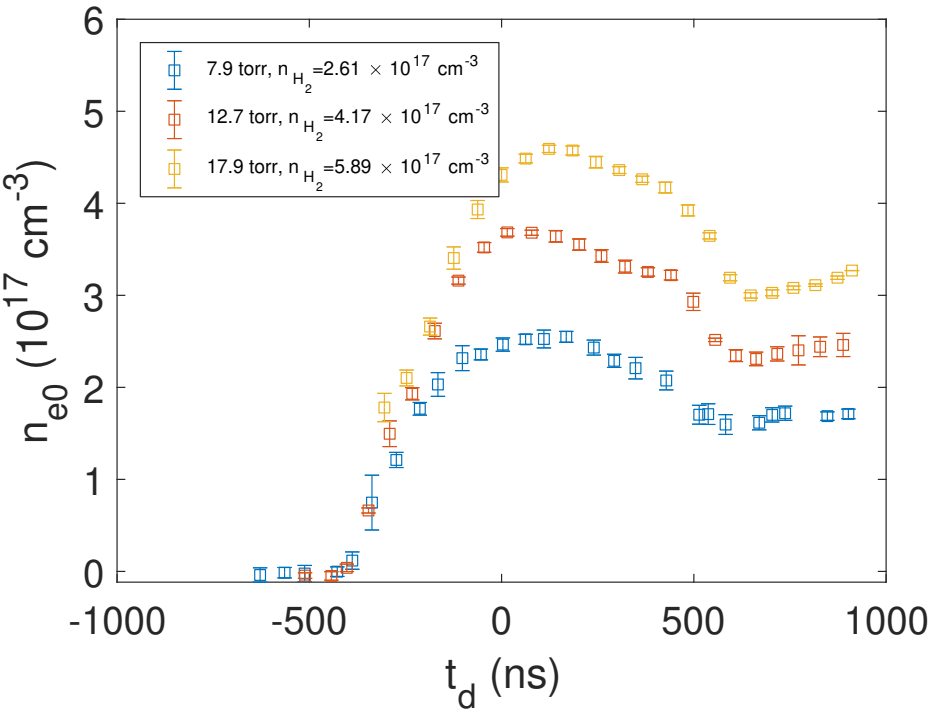

Figure 5.12: Plasma density vs. delay from peak discharge current t_d in a 800 µm diameter, 20-cm-long laser-heated capillary discharge, for three different initial fill pressures of H_2.

due to less complete ionization of the fill gas because the overall current density is lower in a larger diameter capillary. Nonetheless, laser blueshifting measurements described in Chapter 6 show complete ionization on axis. This reduced volume averaged ionization degree may be due to a layer of neutral or weakly ionized gas near the capillary wall, where the temperature is lowest and density is highest. A detailed investigation of this issue may be a fruitful avenue for future research, however, it lies beyond the scope of this dissertation.

Density vs. discharge timing

Discharge plasma densities as a function of delay relative to the peak of discharge current for three fill pressures are plotted Fig. 5.12. Density peaks near the peak of discharge current, as would be intuitively expected and is consistent with prior measurements of plasma density evolution in capillary discharges [91]. The density decrease on the falling edge of the current pulse is attributable to recombination as the plasma cools, rather than ejection of plasma from the capillary ends, as this latter process is too slow to have a significant effect on the plasma density in the capillary for $t_d < 1$ µs [84, 100].

5.6 Density measurements in laser-heated capillary discharges

Measurements of the longitudinally averaged on-axis plasma density $\overline{n}_{e0}$ and matched spot size $\overline{r}_m$ for laser-heated capillary discharges are plotted in Fig. 5.13, for two sets of initial discharge parameters. The matched spot size was measured the laser spot size oscillation method described in Section 4.4. However, because matched spot size measurements for the experiments on Plasma 1 were taken over a restricted space of fill pressures and laser delays, a simple analytical fit was used to compute the plotted $\overline{r}_m$ values, instead of a biharmonic spline fit. The error bars for the matched spot size were calculated as the mean residual of the fit, which was 5 µm.

Because the input spot size for these measurements is so large, correcting for the finite matched spot size of the channel is essential to obtain an accurate density measurement, as to be expected from the $(r_0/r_m)^4$ scaling of Eqn. 3.18. The corrected density values were computed using Eqn. 5.15, with $\overline{r}_m$ taken from the MARPLE simulation. As can be seen in Fig. 5.13, the uncorrected density measurement (i.e. the value of n_{e0} calculated without accounting for the matched spot-size term in Eqn. 5.7) differs by up to 0.7×10^{17} cm^{-3} from the corrected value. However, agreement with MARPLE is quite good for the corrected density measurements.

Finally, no anomalous density peak is observed near the peak of heating power, in contrast to the measurements shown in Chapter 4. This fact is further evidence that the density peak feature was an artifact of that particular diagnostic setup, rather than a physical feature of the plasma evolution.

5.7 Effect of input spot size on density measurements

Small input spot sizes were found to result in large errors in the density measurement, hence the use of a large input spot size requiring correction for the geometrical component of the group velocity. This was determined during an experiment where the size of the iris before the compressor was varied to determine the optimal spot size for measurement accuracy, defined as the variance of the density measurement for fixed discharge parameters. The laser beam profiles at focus for the red beam are compared in Fig. 5.14 for a 125 mm iris and the 70 mm iris in the experiments described in this chapter, which yielded spot sizes of 70 µm and 134 µm, respectively. It is preferable to match the laser spot size to the channel, considering the $(r_0/r_m)^4$ scaling of the geometrical component of the group velocity, and as such the 70 µm spot would be expected to yield more accurate measurements. However, as is shown in Fig. 5.15, a much larger variance in the measured density was observed for the smaller focal spot of Fig. 5.14(a). For this reason, the 70 mm iris producing the larger spot of Fig. 5.14(b) was used for the experiments of this chapter. Density in capillary discharges is known to be stable to within a few percent [116], so this effect must be an artifact of the diagnostic.

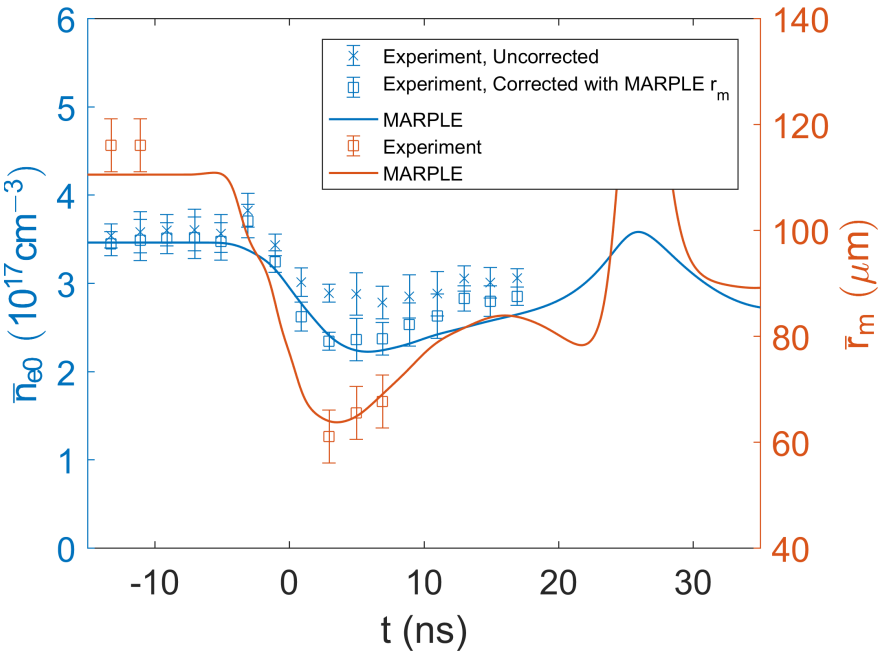

(a) 15.2 torr fill H_2, delay from peak discharge current $t_d = 460$ ns, heater pulse energy 240 mJ.

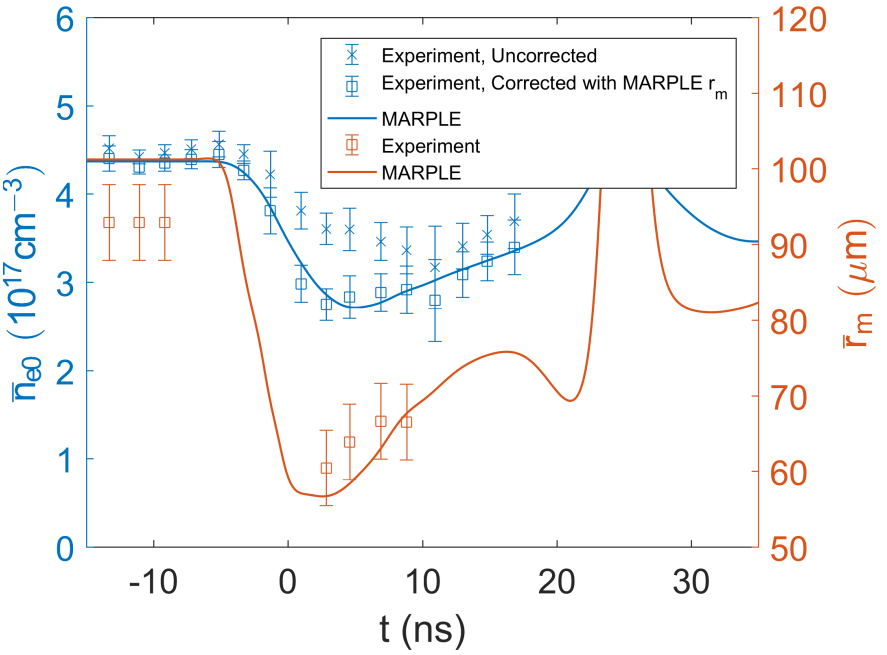

(b) 19.1 torr fill H_2, delay from peak discharge current $t_d = 420$ ns, heater pulse energy 240 mJ.

Figure 5.13: Density and matched spot size in 800 µm diameter, 20-cm-long laser-heated capillary discharges, from measurements with the two-color common-path interferometer and simulations with the MARPLE MHD code. Simulation setup and analysis as in Chapter 4.

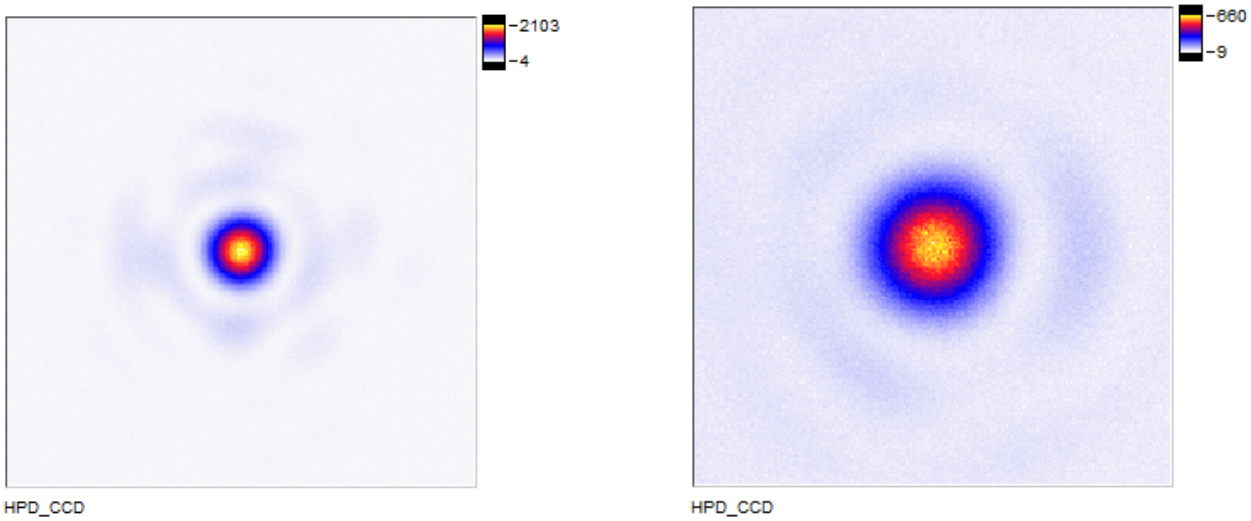

(a) Image size 886 µm. 125 mm iris. **(b)** Image size 886 µm. 70 mm iris.

Figure 5.14: Red beam focal spots for (a) 125 mm and (a) 70 mm irises. Color scale chosen to emphasize regions of low fluence.

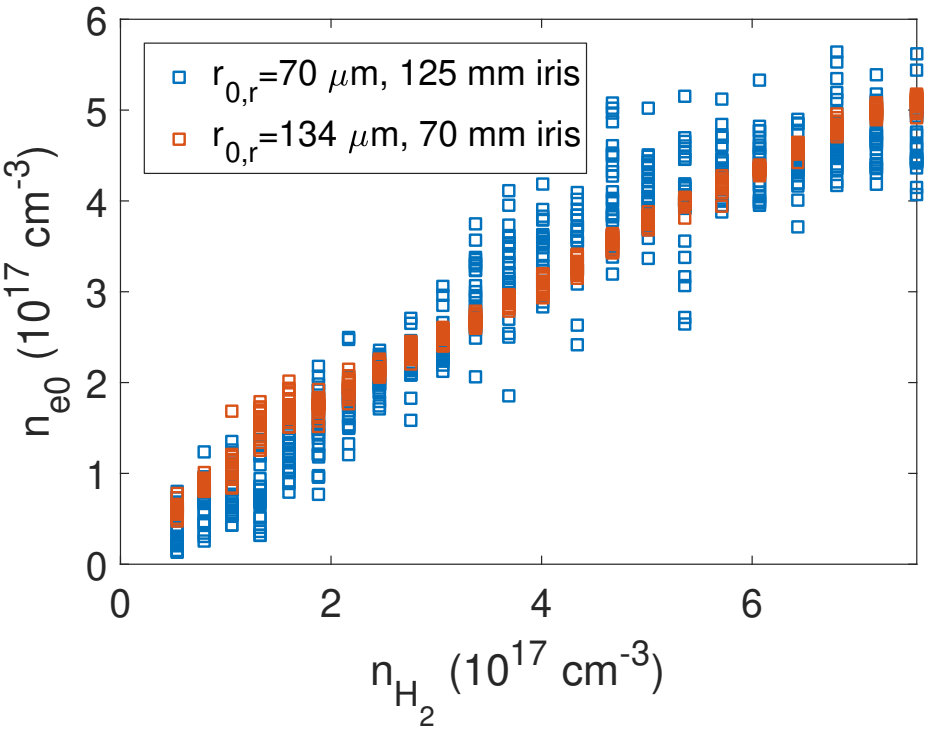

Figure 5.15: Plasma density vs. neutral H_2 density $t_d = 360$ ns in a 800 µm diameter, 20-cm-long capillary, for the 125 mm and 70 mm irises of Figs. 5.14(a) and 5.14(b). Density measurements for individual laser shots have been plotted (squares), instead of mean and standard deviation for each neutral pressure bin.

(a) Image size 1019 µm. Red beam at capillary exit, 125 mm iris. Fluences are for values of n_{H_2} in units of 1×10^{17} cm^{-3}. Saturation in some images is due to color scale bounds set to emphasize low signal regions.

(b) Image size 1019 µm. Red beam at capillary exit, 70 mm iris. Fluences are for values of n_{H_2} in units of 1×10^{17} cm^{-3}.

Figure 5.16: Sample red beam fluence profiles at the capillary exit plane for the two data sets of Fig. 5.15. Color scale chosen to emphasize regions of low fluence.

The cause of this increased variance in the measured density is not clear, and a detailed investigation of this behavior lies beyond the scope of this dissertation. However, some possible causes will be discussed here which may inform further development of the diagnostic.

Although the higher intensity in the smaller focal spot produced with a larger iris will in principle result in more ionization, this is cannot account for the observed effect. As was stated in Section 5.2, the experiments and MARPLE simulations of Chapter 6 show the neutral fraction on axis to be $< 1\%$, far smaller than the variance in Fig. 5.15.

The spatial asymmetry of the beam with the 125 mm iris visible in Fig. 5.14 may lead to excitation of high-order modes of the plasma channel. Some evidence of high-order mode content can be seen in the asymmetry of the diffraction rings in Fig. 5.14(a). Furthermore, the images of the red beam at the capillary exit plane shown in Fig. 5.16 for the pressure scans plotted in Fig. 5.15 indicate that high mode numbers of the waveguide are excited to a much greater extent with the 125 mm iris. The differences in propagation with fill pressure are due to variation of the capillary discharge matched radius with plasma density according to $r_m \propto n_{e0}^{-1/4}$, as discussed in Chapter 3, which in the case of Fig. 5.16 approximately spans the range 120 - 90 µm (decreasing with pressure).

In Fig. 5.16(a), mode numbers $m \sim 2$ and $|p| \sim 2$ are clearly visible in the range 2.2 - 4.7 $\times 10^{17}$ cm^{-3}, in contrast to Fig. 5.16(b) where relatively little high order structure is visible above 3 torr. Images of the blue beam were not available for that data set of Figs. 5.15 and 5.16, however, given that the frequency doubling process effectively doubles the size of wavefront aberrations for the blue beam, the higher order mode content of the blue beam can be reasonably expected to be even higher than the red beam.

High order mode content may increase the variance in the density measurement by two

mechanisms. First, if the mode content is not stable, but varies from shot-to-shot, random fluctuations in the group velocity will will result through the effective mode number $\langle N \rangle$ in Eqn. 5.7. Second, overlap of the blue and red beams at the slit will become less reliable if the two beams have a complex mode structure, more so if that mode structure is different for each frequency.

Determining the cause of the increased error in the density measurement observed with a larger laser nearfield and smaller spot size warrants a dedicated experimental effort well beyond the scope of this dissertation. However, such further development of the two-color common-path interferometer is worthwhile. Specifically, if the diagnostic can be operated with smaller focal spot sizes, this will reduce the geometrical correction to the density per Section 5.4 and Chapter 3. This in turn reduces the diagnostic's reliance on assumptions about the longitudinal channel structure, which for laser-heated capillary discharges was shown to be quite complicated in Chapter 4, and the propagation of the probe pulses within this structure.

5.8 Conclusion

In this chapter, a two-color common-path interferometer plasma density diagnostic on the BELLA laser system has been described. The diagnostic setup has been successfully commissioned and has produced measurements of plasma density in capillary discharge targets with and without laser-heating. Agreement between density measurements in laser-heated capillary discharges and simulations with the MARPLE MHD code is excellent. Additionally, this diagnostic eliminates two important technical challenges present in the Mach-Zehnder fiber interferometer of Chapter 4, namely the slow delay drift attributed to the combined effects of temperature drifts in the laser oscillator center frequency and group delay dispersion in the fibers, and the anomalous "density peak" measured early in the heater pulse. Future development of the diagnostic may perhaps focus on improving the measurement precision with smaller laser spots so as to reduce the size of the geometrical density correction. Nevertheless, this setup represents the addition of a powerful new diagnostic capability to the BELLA laser system, and the objective of performing in-situ density measurements on plasma channel LWFA targets has been unambiguously achieved. Moreover, this diagnostic setup enabled precise characterization of the laser-heated capillary discharge targets used in the controlled injection experiments of Chapter 7.

Chapter 6

Petawatt guiding experiments

6.1 Introduction

In this chapter, acceleration of electrons to 7.8 GeV with petawatt laser pulses from the BELLA laser system in a laser-heated capillary discharge waveguide is demonstrated. Moreover, during the experiments in question, thousands of petawatt-scale pulses were guided through a 20-cm-long capillary without damage. As of writing, this represents the highest energy gain from a laser-plasma accelerator.

These results were enabled by the use of a laser-heated capillary discharge waveguide as a guiding structure. The combination of low on-axis density and low matched spot size mitigated bunch dephasing and kept the driver pulse confined such that high amplitude plasma waves were excited, per Chapter 2 and Chapter 3. Additionally, the decoupling of channel matched spot size from capillary diameter discussed in Chapter 4 enabled the use of large diameter capillaries less vulnerable to damage from the driver.

This chapter is organized as follows. Section 6.2 gives an overview of the BELLA laser system and beamline. In Section 6.3, diagnostic measurements of laser-heated capillary discharges using femtosecond pulses are presented which further validate the results of Chapter 4 and Chapter 5. Section 6.4 presents the results of petawatt guiding experiments, including the production of 7.8 GeV electron beams in the self-trapping regime and computational studies of laser and channel parameters for electron acceleration to $\sim$ 10 GeV. Conclusions and directions for further experiments with these guiding structures are presented in Section 6.5.

6.2 BELLA laser system parameters and diagnostics

The BELLA laser system is a Ti:Sapphire chirped-pulse-amplified (CPA) laser [8]. As discussed in Chapter 2, resonant excitation of plasma waves requires both high peak intensities and short pulse lengths $\Delta t_0 \sim \omega_p^{-1}$, hence the need for a high power broadband laser source. Ti:Sapphire CPA lasers are a mature a technology capable of supplying pulses with the required properties for LWFA, and are commonly used as drivers for not only LWFA but a

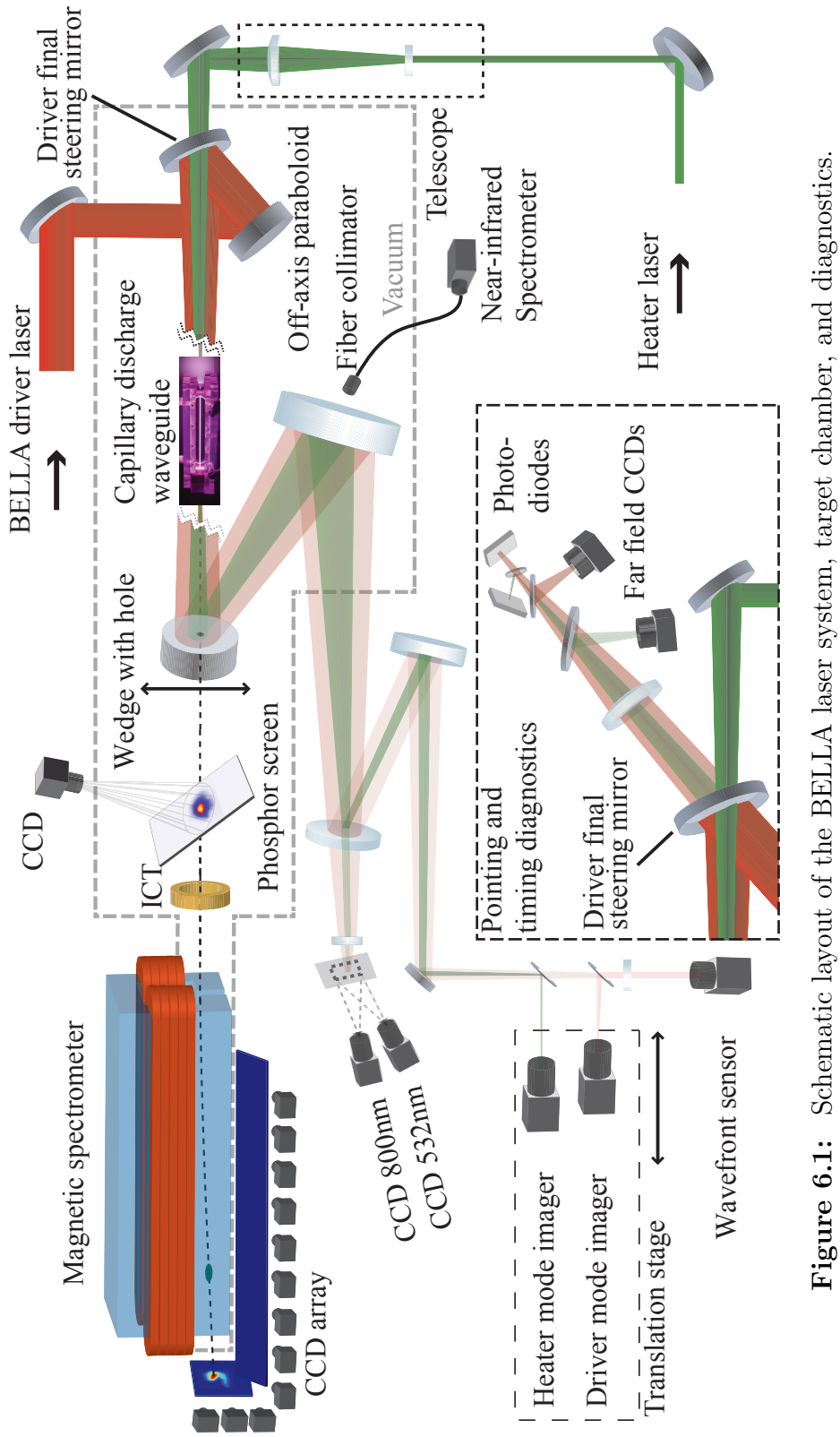

Figure 6.1: Schematic layout of the BELLA laser system, target chamber, and diagnostics.

wide variety of other relativistically-intense laser-plasma processes: commercially available systems can supply femtosecond-scale scale pulses at the $\gtrsim 100$ TW level. Ultrafast laser engineering is a complex discipline and an exhaustive treatment of the BELLA laser and its various subsystems lies well beyond the scope of this dissertation. In this section, an overview is given of aspects of the laser system and diagnostics of immediate relevance to experiment design, with key parameters of the BELLA laser summarized in Table 6.1.

The BELLA beam transport system, target chamber, and laser and electron beam diagnostics are pictured schematically in Fig. 6.1. The BELLA laser employs 6 amplifier stages and a reflective grating compressor (not pictured) to amplify µJ femtosecond pulses from a mode-locked oscillator to 40 J and petawatt peak power. Because the peak intensity developed after compression is sufficient to ionize air, the grating compressor is held under high vacuum with the rest of the beam transport line and target chamber, with stretched laser pulses coupled in through a coated vacuum window after the final amplifier stage. The heater laser system, pictured schematically in relation to the BELLA beamline in Fig. 6.1 is as described in Chapter 5.

Stretched pulses are compressed to the femtosecond scale with a reflective 4-grating compressor. The laser pulse shape can be modeled (very approximately) as a Gaussian such that the electric field takes the form $E(t) \sim (E_0/2)e^{-2\ln 2\left(\frac{t}{\tau}\right)^2}$. To lowest order, dispersive optical elements, including grating compressors, contribute a quadratic spectral phase or group delay dispersion (GDD) that modifies the pulse length Δt (defined as the intensity FWHM) according to[123]

$$\Delta t = \Delta t_0 \sqrt{1 + \left(4\ln 2 \frac{\mathrm{GDD}}{\Delta t_0^2}\right)^2}\,. \tag{6.1}$$

The quantity t_0 is the minimum pulse length, which is set by the laser bandwidth through the time bandwidth product, which in turn has the form $c\lambda^{-2}\Delta\lambda\Delta t_0 \geq 2\ln 2/\pi$ for Gaussian pulses. In the case of the grating compressor, GDD is controlled by the translating the gratings relative to each other with a motorized stage. The BELLA laser compressor has an effective $\mathrm{GVD}_{eff} = -4812$ fs^2/mm such that $\mathrm{GDD} = \mathrm{GVD}_{eff} L_c$, with L_c the translation of the gratings from the "zero-point" where $\Delta t = \Delta t_0$.

The laser pulse shape was measured via frequency resolved optical gating (FROG), a standard technique for the measurement of femtosecond laser pulses [124], which are too short to measure with electro-optical methods. A number of important departures from the simple Gaussian model of the pulse shape exist in a real laser system. High order spectral phase (i.e. beyond quadratic) will increase pulse length for a given bandwidth, in close analogy with the effect of wavefront errors on the laser focal spot. Femtosecond pulses frequently feature a nanosecond-scale "pre-pulse" or "pedestal" that leads the main pulse that arises from amplified spontaneous emission within the laser system. This pre-pulse can contain sufficient energy to ionize and heat the target, modifying the plasma profile encountered by the main pulse, and so reduction of pre-pulse energy is an important aspect of optimizing pulse shape. Spatiotemporal coupling, where the intensity profile varies within the laser

pulse beyond a simple time-dependent scale factor, can occur because of alignment errors in dispersive elements of the laser system as well as gain depletion effects in the amplifiers [125–127].

Generally speaking, characterizing and optimizing the laser pulse shape requires a wide array of techniques and diagnostics [110, 128–133]. Moreover, the simple Gaussian pulse model fails to accurately capture many important features of real ultrashort laser pulses as has just been discussed. Hence, the values pertaining to the temporal structure, including the peak intensity, listed in Table 6.1 were obtained experimentally as is described in detail in Ref. [110], rather than calculated from first principles.

The 200 mm nearfield of the laser is focused to a $\sim$ 53 µm beam waist (according to a Gaussian fit of the focused laser fluence profile) in the target chamber with a 13.5 m off-axis-paraboloid (OAP). After the final amplifier and upstream of the grating compressor, a mechanically actuated deformable mirror (DM) is used to correct wavefront errors and optimize the laser focus [134]. Wavefront correction is further assisted by the use of Shack-Hartmann wavefront sensors[134] that directly measure the optical wavefront at multiple locations in the laser system, which include the DM plane and the high power diagnostics are after the target. The DM and wavefront sensors can be used for either manual ("open-loop") or feedback controlled ("closed-loop") wavefront correction. The Strehl ratio, defined as the ratio of peak intensity at focus of an aberrated beam to that of a beam with flat phase $S \equiv I_0/I_{0,F} \leq 1$, is a widely used measure of laser focus quality [123, 135, 136]. The Strehl ratio can be related to the RMS wavefront error σ_w by $S \simeq \exp(-\sigma_w^2)$ [137]. Wavefront correction with the DM and wavefront-sensor on the BELLA laser system can reduce wavefront error to $\sigma_w \sim 0.3$, and hence produce a Strehl ratio $S \sim 0.9$.

The capillary setup used in these experiments, including the capillary design (800 µm diameter, 20-cm-long), gas fill and pressure measurement system, and multi-axis hexapod stage, was identical to that used for the diagnostic experiments of Chapter 5. The high voltage pulser used was identical as well, producing the same current waveform pictured in Fig. 4.3.

The Plasma 1 target chamber that housed the capillary included additional transverse diagnostics. Visible light cameras viewing the target area through vacuum windows monitored the state of the capillary during experiments, primarily for the purposes of quickly identifying laser damage. Additionally, a simple transverse optical spectrometer, imaging the full length of the capillary, was used to diagnose the capillary plasma. The acquired spectra were time-integrated, and so of limited use for measuring plasma density and temperature using atomic emission lines. However, the time-integrated spectrally dispersed images of the capillary were used to diagnose the location of various ion species in the plasma, which is of greater relevance to the ionization injection experiments of Chapter 7.

As discussed in Chapter 5, CCD cameras on motorized translation stages were used to measure fluence profiles of the driver and heater beams. In addition to laser mode images, two spectrometers were used to measure the laser spectrum after interaction with the target, a UV-NIR spectrometer covering the range 300 nm - 1050 nm, and a NIR spectrometer covering the range $\geq$ 1000 nm. The NIR spectrometer is required to capture the low frequency end

Parameter	Symbol	Scaling	Value
Wavelength	λ		815 nm
Bandwidth	$\Delta\lambda$		40 nm
Pulse Length (Intensity FWHM)	Δt_0	$\lambda^{-2}\Delta\lambda$	35 fs[a]
Energy	U		46 J
Repetition Rate			1 Hz
Nearfield Diameter	D		200 mm
OAP Focal Length	f		13.5 m
1st wedge, from focus			10.4 m
Beam Waist (Focus)	r_0	$\lambda f D^{-1}$	53 µm[b]
Peak intensity	I_0	$\Delta t_0^{-1} r_0^{-2} U$	2×10^{19} W/cm^2
Normalized vector potential	a_0	$\lambda I_0^{1/2}$	3[c]
Electric Field	E_0	$I_0^{1/2}$	1×10^{13} V/m[d]

[a] Minimum measured value. Subject to spectral phase error.
[b] Minimum measured value. Subject to wavefront error.
[c] $a_0^2 = 7.3 \times 10^{-19}[\lambda(\mu\text{m})]^2 I_0(\text{W/cm}^2)$
[d] $E_0(\text{TV/m}) = 3.21 a_0/\lambda(\mu\text{m})$

Table 6.1: Key parameters of the BELLA laser system.

of highly depleted laser spectra. The UV-NIR spectrometer (not shown) samples the beam on the high power diagnostics table from the location where the mode imagers are installed. The NIR spectrometer collects light though a fiber collimator from the backside of the second wedge after the target, as shown in Fig. 6.1.

Electron bunch diagnostics, for charge, transverse bunch profile, and energy spectrum, are shown downstream of the first wedge in Fig. 6.1, which is located 10.4 m downstream of the laser focus. This wedge has a 25.4 mm diameter hole to allow electron beams to enter the electron spectrometer, and is mounted on a motorized stage that allows the hole to be translated out of the beam path to improve imaging of the laser mode for the beam profile cameras previously discussed. Transverse electron beam profiles were measured with a fluorescent LANEX screen imaged by a CCD camera. Bunch charge is measured with an integrating current transformer (ICT)[138] as pictured in Fig. 6.1, which had a charge resolution < 1 pC. Fig. 6.1 shows the magnetic spectrometer, which consists of a ≤ 1.2T magnet and 2.5-m-long LANEX screen imaged by an array of CCD cameras. The magnetic spectrometer has an acceptance of 0.5-1 mrad about the beam axis, depending on electron energy and field strength. The acceptance of the spectrometer is large enough for the electron bunch energy spectrum to vary measurably with pointing into the spectrometer. The bunch profiles measured with the phosphor screen are used to correct the energy spectrum for this effect on each shot. Resolution and energy range of the magetic spectrometer both depend

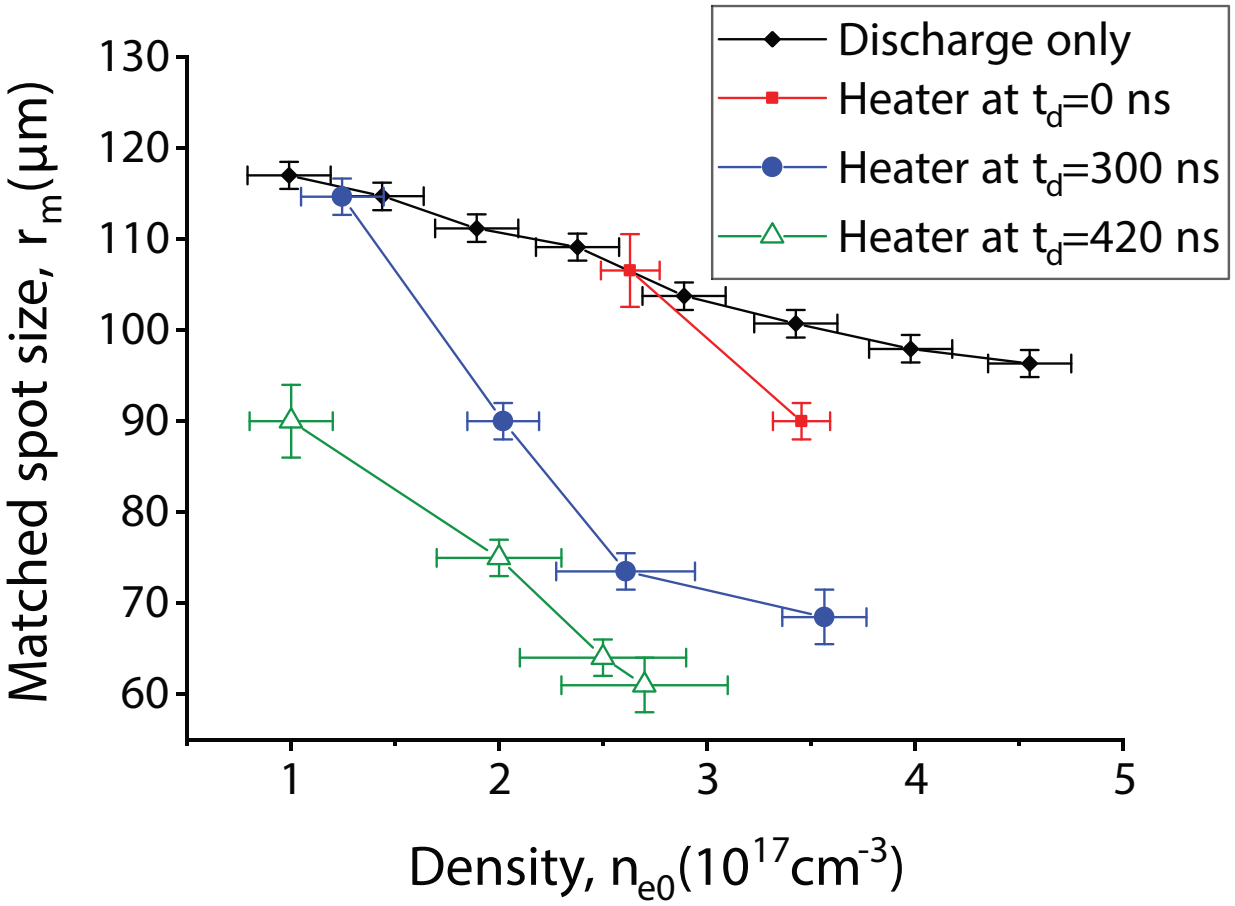

Figure 6.2: Longitudinally averaged on-axis density and matched spot size for the laser-heated capillary discharge used for the experiments of this chapter. Capillary is 20 cm long, 800 μm diameter. Values are taken from the measurements of Chapter 4 at the peak of heater power $t = 0$ ns, when the driver arrived at the target for these experiments.

on the field, the former increasing with field and the latter decreasing. For a field of 1.2 T and maximum resolvable energy of 10 GeV, energy resolution of the magnetic spectrometer was ~ 0.2 GeV.

6.3 High power diagnostic measurements of laser-heated capillary discharges

Diagnostic measurements of channel parameters for the experiments of this chapter were taken from the experiments on the Plasma 2 test stand described in Chapter 4. These parameters are summarized in Fig. 6.2, for the case where the driver pulse arrives $t < 1$ ns from the peak of heater power, as was the case for the experiments of this chapter. However,

the high power laser pulses supplied by the BELLA laser offer opportunities for additional diagnostic measurements of the channel. Specifically, spectral redshifting from the excitation of plasma waves can be used as a diagnostic for on-axis plasma density and to a lesser extent matched spot size. Spectral blueshifting from field ionization of neutral atoms by the driver can be used to diagnose ionization degree.

After driving a plasma wave, a laser pulse will be spectrally redshifted as described in Section 2.4. Redshifting in general increases with laser pulse energy and plasma density, and some examples of redshifted laser spectra measured with a near-infrared (NIR) spectrometer for pulses of various energies guided in a laser-heated capillary discharge are shown in Fig. 6.3(a).

The density and matched spot size measurements described in Chapter 4 and summarized in Fig. 6.2 were verified by comparing measurements of redshifted spectra with PIC simulations using INF&RNO for a range of on-axis densities and matched spot sizes. The results of this procedure are shown in Fig. 6.3(b) for the case of $\overline{n}_{e0} = 3.2 \times 10^{17}$ cm^{-3} and $\overline{r}_m = 68$ µm, with these values obtained from the measurements of Chapter 4. In Fig. 6.3(b), the spectral redshift, defined as the wavelength above which $1/e^2$ of the pulse energy resides, is plotted as a function of pulse energy for measurements at the aforementioned channel parameters and a series of INF&RNO simulations at multiple values of $\overline{n}_{e0}$ and $\overline{r}_m$. Best agreement between the measured and simulated redshift is obtained for the quoted parameters obtained with the methods of Chapter 4. This provides further evidence of the reliability of the diagnostics described in Chapter 4 and Chapter 5, and suggests the plasma density can be reliably measured to within 10%.

Spectral blueshifting measurements were performed to diagnose ionization degree in the capillary discharge channel [2, 122, 125], with and without laser heating. Ionization degree is a particularly salient in situations where the heater pulse arrives late in the discharge current pulse, where the low plasma temperature enhances the inverse-bremsstrahlung heating but also allows recombination. A large concentration of neutrals in the plasma channel is best avoided as this will cause ionization defocusing [37] and degrade the guiding. Pulses with sufficient peak intensity for spectral blueshifting (33 mJ energy and 35 fs duration) were guided through plasma channels to diagnose the ionization degree of the plasma. The results of the spectral blueshifting measurements are shown in Fig. 6.4. The spectral blueshift is defined as the wavelength below which $1/e^2$ of the laser pulse energy resides. Spectral blueshift as a function of driver arrival time t_d relative to the peak of discharge current (without laser heating) is plotted in Fig. 6.4(a). There is a long plateau from $t_d \sim 0$ ns to $t_d \sim 300$ ns where the spectral blueshift is constant and does not differ significantly from the vacuum spectrum (dashed line). However, outside this interval, on the rising edge of the current pulse and late on the falling edge, the blueshift wavelength shifts low, indicating ionization of neutrals by the laser pulse. Notably, blueshifting is observed for $t_d \gtrsim 400$ ns, where the strongest channels were formed with the heater laser.

Blueshifting at late times in the discharge relevant for high-performance operation of laser-heated capillary discharges (according to the parameter studies of Chapter 4) indicates the presence of neutral hydrogen in the discharge plasma for these conditions. However,

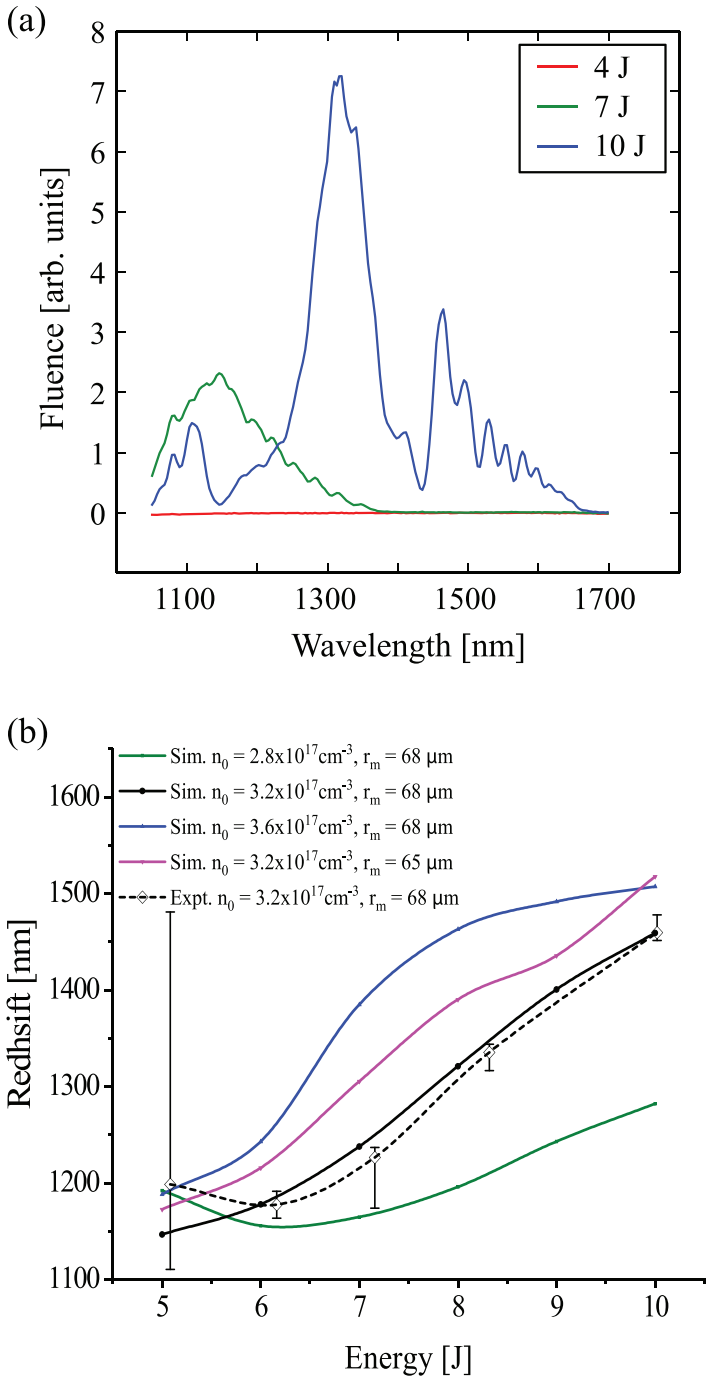

Figure 6.3: (a) Redshifted NIR spectra for 3 driver energies, pulse length ~ 40 fs. $\overline{n}_{e0} = 3.2 \times 10^{17}$ cm^{-3} and $\overline{r}_m = 68$ µm. (b) Driver redshift vs. energy from experiment and simulation. Agreement is best for $\overline{n}_{e0} = 3.2 \times 10^{17}$ cm^{-3}, $\overline{r}_m = 68$ µm, corresponding to the parameters measured in the diagnostic experiments of Chapter 4.

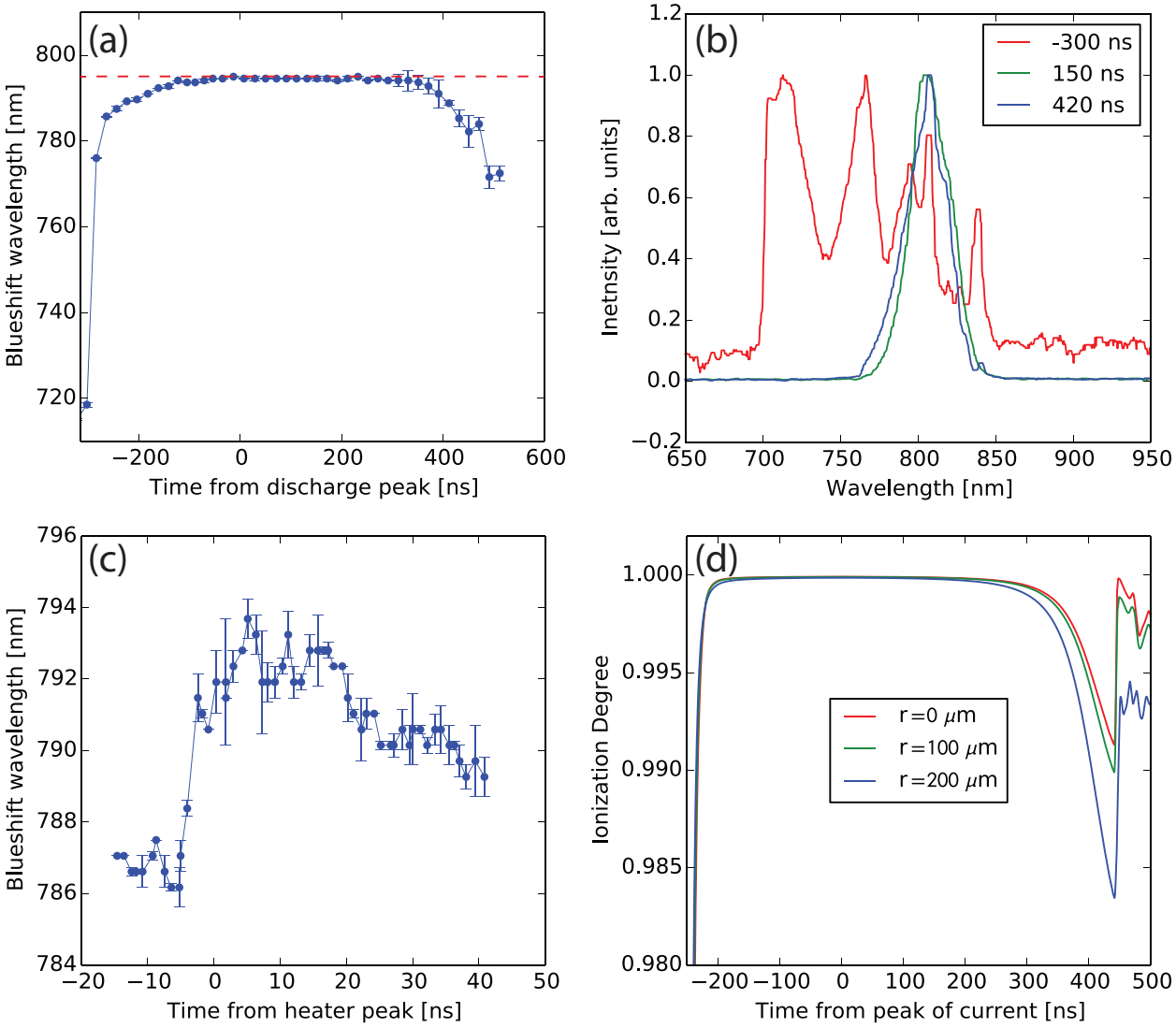

Figure 6.4: Spectral blueshifting measurements for a 33 mJ, 35 fs pulse guided in a 20-cm-long capillary with initial density $\overline{n}_{e0} = 3.8 \times 10^{17}$ cm^{-3} at full ionization without laser-heating. (a) $1/e^2$ blueshift wavelength vs. discharge delay. (b) Example spectra for 3 time points of (a). (c) Blueshift wavelength vs. delay from peak heater power. 300 mJ heater pulse, arriving 420 ns afte the peak of discharge current. (d) Ionization degree at 3 radial locations from a MARPLE simulation for the conditions of (c). The drop in ionization degree at $t_d \sim 300$ ns is consistent with the onset of decreasing blueshift wavelength observed in (a). The rapid increase in ionization degree corresponds with the arrival of the heater pulse, and is consistent with the increased blueshift wavelength in (c).

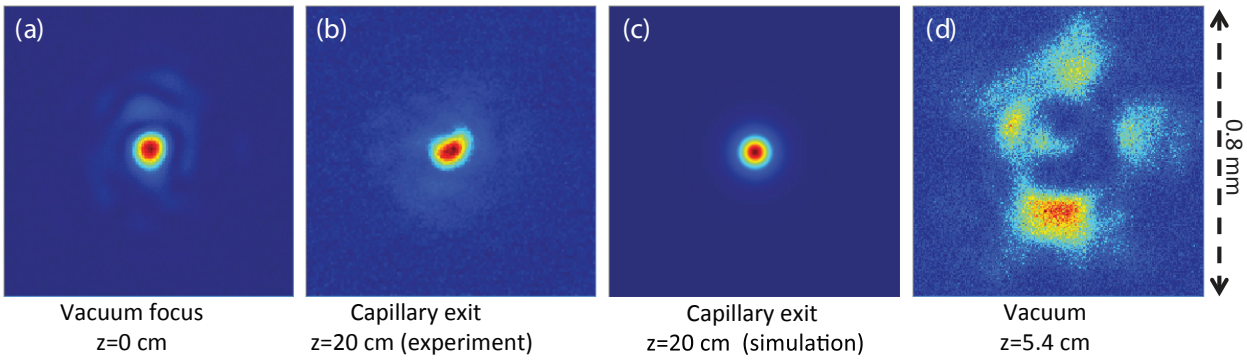

Figure 6.5: Guiding of 850 TW laser pulses in laser-heated capillary discharge with $\overline{n}_{e0} = 3.4 \times 10^{17}$ cm^{-3} and $\overline{r}_m = 69$ µm. (a) Vacuum driver focus. Beam waist is ~ 53 µm. (b) Guided driver mode at the capillary exit. (c) Guided driver mode at the capillary exit from an INF&RNO simulation for the conditions of (b). (d) Beam profile 5.4 cm downstream of the laser focus, in vacuum. The importance of plasma guiding is illustrated by the fact that the laser fluence overfills a 400 µm radius about the beam axis, corresponding to the capillary wall location.

Fig. 6.4(c) shows that for a heater arrival time $t_d = 420$ ns, the blueshift wavelength returns to the vacuum value ~ 5 ns after the peak of heater power.

Ionization degree from a MARPLE simulation for the conditions of Fig. 6.4(a) and Fig. 6.4(c) is plotted in Fig. 6.4(d). The trends observed in the experiment are reproduced in the simulation, with ionization fraction plateauing for roughly 500 ns before falling as the current decreases on the falling edge of the discharge pulse. Upon arrival of the heater pulse at 440 ns, the plasma becomes once more fully ionized on axis. Note that off-axis, the plasma ionization fraction rises upon laser heating but remains < 1, as the influence of laser heating is reduced far from the laser axis. However, a well matched driver pulse, being confined near the axis of the channel, will not interact with this region of the plasma, and thus the reduced ionization fraction off-axis is not expected to degrade the guiding.

6.4 Electron acceleration to 7.8 GeV in a laser-heated capillary discharge

Driver pulses with 850 TW peak power were successfully guided over distances of $\sim 15 Z_R$ in 800 µm diameter, 20-cm-long laser heated capillary discharges, resulting in the acceleration of electrons to a maximum energy of 7.8 GeV [21, 22]. Driver energy was sufficiently well confined that thousands of shots at this power level were guided through the capillary without damage. As of writing, this represents the highest energy gain ever demonstrated in a laser-wakefield accelerator, and was enabled by a combination of the long channel and the low on-axis density and matched spot size created by laser-heating.

Shot	n_0 ($\times 10^{17}$ cm^{-3})	r_m (μm)	Charge (pC)	
			Total	1.5 GeV Window
(a)	3.4	68	190	24
(b)			320	21
(c)			270	40
(d)			210	62
(e)	2.7	61	420	5

Table 6.2: Channel parameters and captured bunch charges for the measured electron spectra of Fig. 6.6.

High-quality laser guiding of 850 TW (pulse energy 31 J and intensity FWHM $\sim$ 35 fs) laser pulses is shown in Fig. 6.5. The heater arrived 300 ns after the peak of discharge current for channel parameters $n_0 = 3.4 \times 10^{17}$ cm^{-3} and $r_m = 69$ μm at the peak of heater power. The vacuum fluence profile at focus is shown in Fig. 6.5(a), and the fluence profile at the exit of the 20 cm capillary is shown in Fig. 6.5(b). The guided driver beam has roughly the same transverse size as the vacuum beam waist, which is consistent with the exit fluence profile calculated from an INF&RNO simulation for the conditions of the experiment shown in Fig. 6.5(c).

The importance of plasma guiding for confinement of laser energy near the axis is evident in Fig. 6.5(d), which shows a vacuum fluence profile taken 5.4 cm downstream of the vacuum focus where $\sim$ 10% of the laser energy falls outside the 400 μm capillary radius. The vacuum beam size at the capillary exit plane was found to be 2.4 mm. Hence the requirement for a plasma guiding structure to sustain laser intensities required for acceleration over the length of the plasma.

Electron beam spectra measured with the magnetic spectrometer for the conditions of Fig. 6.5 are shown in Fig. 6.6. The spectrum over the full energy range of the diagnostic is plotted, as well as a 1.5 GeV window denoted by the white dotted lines in the full range plots. The beams shown constitute a subset well aligned to the spectrometer, which comprises 10-20% of all laser shots due to fluctuations in alignment and the 1 milliradian angular acceptance of the magnetic spectrometer.

For Fig. 6.6(a-d), the heater pulse arrived 300 ns after the peak of discharge current to produce channel parameters $n_0 = 3.4 \times 10^{17}$ cm^{-3} and $r_m = 68$ μm. For Fig. 6.6(e), the heater pulse arrived 300 ns after the peak of discharge current to produce channel parameters $n_0 = 2.8 \times 10^{17}$ cm^{-3} and $r_m = 61$ μm. Bunch charge for the laser shots of Fig. 6.6 is listed in Table 6.2.

A maximum electron energy was observed for the 420 ns heater pulse arrival time of Fig. 6.6. This increased performance over the 300 ns case is to be expected from simple physical considerations. First, the initial plasma temperature is lower, enhancing inverse-bremsstrahlung heating as discussed in Chapter 3 and Chapter 4. This increased heating

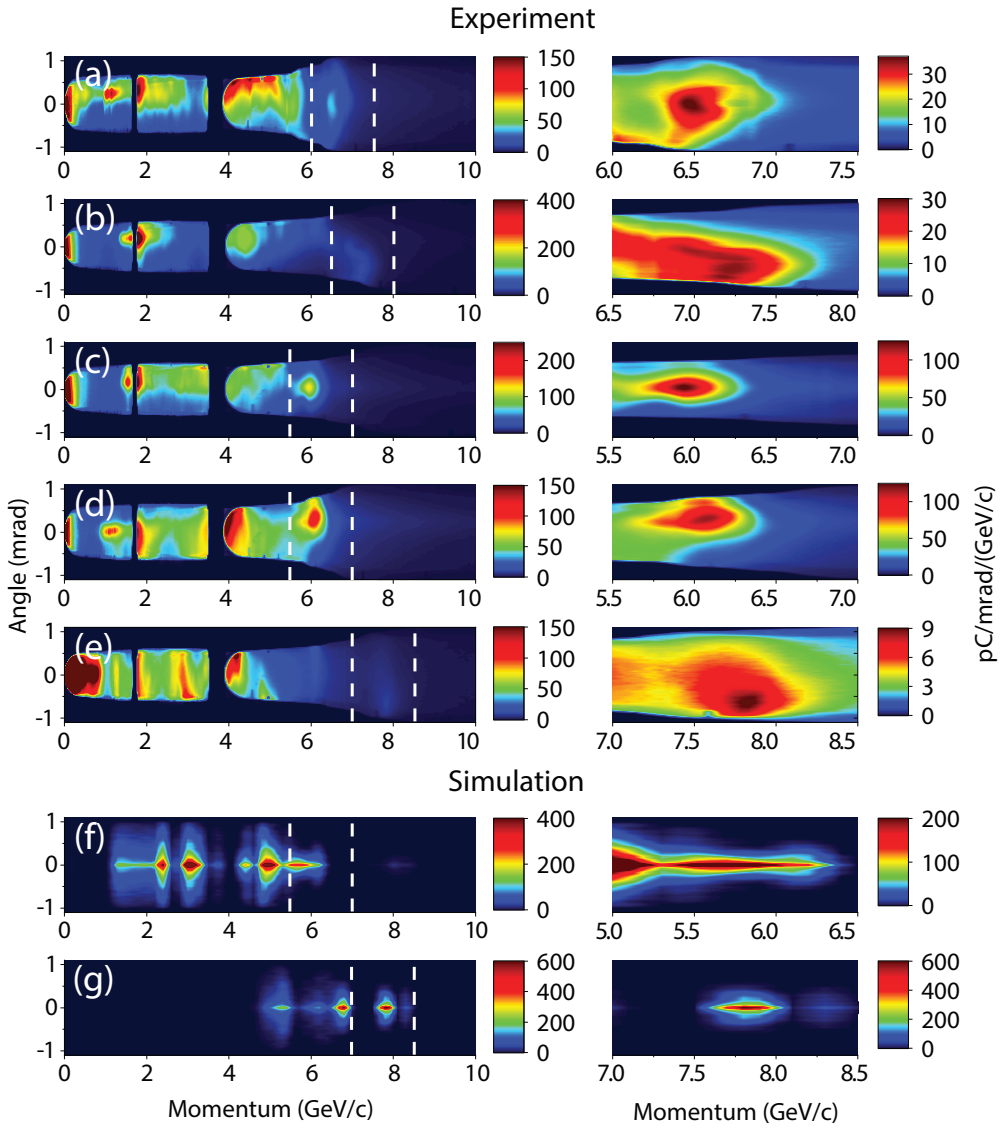

Figure 6.6: Measured and simulated electron bunch spectra for laser power 850 TW and two sets of channel parameters. The full energy range of the spectrum is shown in the left column, and a 1.5-GeV-wide high-energy window on the right. The location of the high energy window is denoted with white dotted lines in the full range spectra. Measured bunch charges are listed in Table 6.2. (a-d)$\overline{n}_{e0} = 3.4 \times 10^{17}$ cm^{-3} and $\overline{r}_m = 69$ µm, with a 300 mJ heater pulse arriving 300 ns after the peak of discharge current. (e) $\overline{n}_{e0} = 2.7 \times 10^{17}$ cm^{-3} and $\overline{r}_m = 61$ µm, with a 300 mJ heater pulse arriving 420 ns after the peak of discharge current. (f) INF&RNO simulations for the conditions of (a-d). Plasma profile was taken from a MARPLE simulation of a laser-heated capillary discharge matching the discharge and laser parameters in the experiment. (g) INF&RNO simulations for the conditions of (e). Plasma profile was modeled as longitudinally uniform and transversely parabolic.

results in lower on-axis density, which increases the energy gain in accordance with the n_{e0}^{-1} scaling derived in Chapter 2.

Simulations were performed with INF&RNO for both sets of parameters in Fig. 6.6 and Table 6.2. For these simulations, the complex laser envelope was modeled as jinc function in the transverse plane, with temporal evolution from measurements of the laser pulse discussed in Section 6.2 as was done in Ref. [76, 77]. Mathematically,

$$\hat{a}(\zeta, r, t = 0) = a_0 \mathrm{jinc}\left(\frac{r}{R_{\mathrm{jinc}}}\right) f_{\parallel}(\zeta) \ , \tag{6.2}$$

with $\mathrm{jinc}(u) \equiv 2J_1(u)/u$, J_1 the first-order Bessel function of the first kind, $R_{\mathrm{jinc}} \simeq 0.364 r_0$, and $f_{\parallel}(\zeta)$ a complex-valued function describing the measured temporal profile of the laser envelope. The resulting simulated electron spectra at the capillary exit, windowed in solid angle to account for the acceptance of the magnetic spectrometer, are plotted in Fig. 6.6(f) and (g) for heater arrival times 300 ns and 420 ns, respectively. For the case of Fig. 6.6(a-d), the plasma density distribution from a MARPLE simulation matching the conditions of the experiment was used. The heater was modeled with a 84 µm Gaussian beam waist and 8 ns FWHM pulse length, in agreement with the parameters of the BELLA laser heater system for these experiments. As in Chapter 4, the channel was longitudinally nonuniform in both density and matched radius. On-axis density varied between 3.35 and 3.41 $\times 10^{17}$ cm^{-3}, and matched radius varied between 68 µm and 72 µm. For Fig. 6.6(e), the plasma density was modeled as transversely parabolic and longitudinally uniform, with density and matched spot size from the measurements of Fig. 6.2.

INF&RNO simulations show the production of electron beams with multiple quasi-energetic peaks, as observed in the experiment. In the simulation of Fig. 6.6(f), self-injection of electrons begins after ~ 5 cm into the capillary, after self-focusing and self-steepening has increased the laser strength parameter a_0 above its initial value. Evolution of the driver pulse is complex, with self-steepening and spot-size oscillation within the channel causing injection to start and stop multiple times along the length of the capillary. This delocalized injection process traps multiple populations of electrons with different energies within the first plasma wave period (or wake "bucket"), resulting in broad energy spread electron beams. The beam divergence (energy integrated) measured on the transverse phosphor screen was 0.2 ± 0.05 mrad FWHM and 0.6 ± 0.15 mrad RMS, larger than the simulated results of 0.19 mrad FWHM and 0.35 mrad RMS. This discrepancy may be due to the axisymmetry of the simulation, which does not capture the effect of nonsymmetric features in the laser mode.

For the case of Fig. 6.6(e) and (g), the peak at 7.8 GeV is reproduced. However, there is less low energy charge in the simulated beam for the conditions of Fig. 6.6(e), perhaps due to the axisymmetry of the INF&RNO simulation failing to capture the effects of nonsymmetrical features in the laser mode, or differences in the real transverse plasma profile from the assumed parabolic shape. Note that although self-trapping in this nonlinear regime tends to produce broad energy spreads, the process is very sensitive to laser and plasma parameters, and so departures from the conditions of the experiment in the simulation setup will produce discrepancies in the resultant electron energy spectrum.

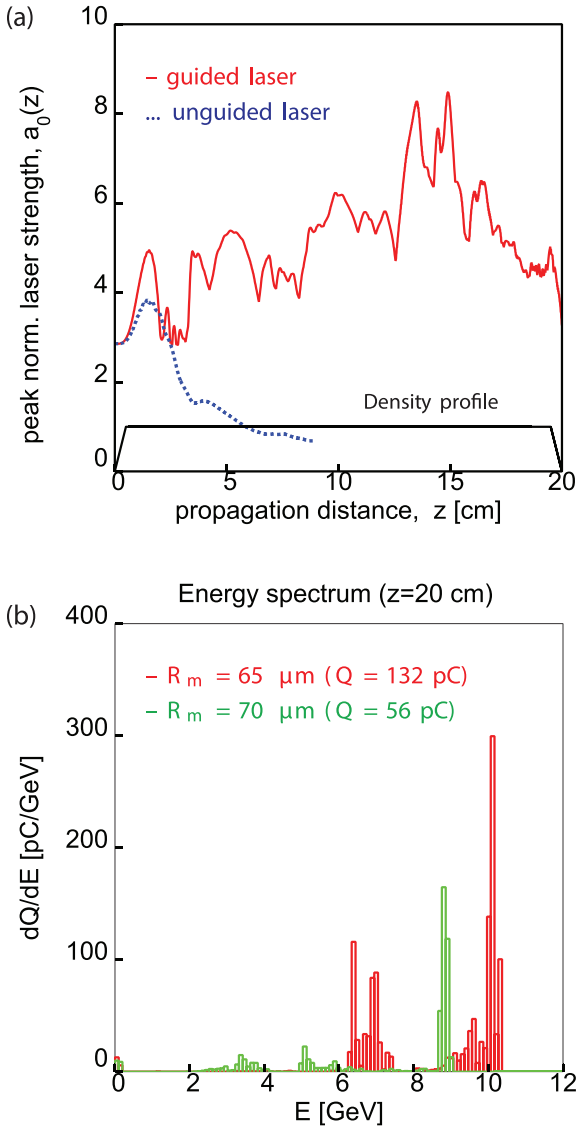

Figure 6.7: INF&RNO simulations of LWFA in an optimized laser-heated capillary discharge, for a longitudinally uniform, parabolic channel with $\overline{n}_{e0} = 2.2 \times 10^{17}$ cm^{-3} and $\overline{r}_m = 65$ µm. Parameters of the driver pulse are $U = 39$ J, $r_0 = 64$ µm, and $\Delta t_0 = 30$ fs. (a) Longitudinal evolution of the peak normalized vector potential a_0 (red) in the channel. The unguided case for the same plasma density (i.e. a plasma slab with no pre-formed transverse density gradient to confine the driver) is plotted as well (blue). On-axis density profile, including gradients to account for capillary end effects, is plotted in black. (b) Electron bunch spectrum and charge Q at the capillary exit for the guided case of (a), as well as for a case with the same on-axis density but $r_m = 70$ µm.

Options for optimizing acceleration in laser-heated capillary discharges and reaching 10 GeV were investigated using INF&RNO. Channel parameters were chosen to be just above the threshold for self-injection. The channel was additionally constrained by the requirement that the driver pulse remain well guided, which in practice requires a matched radius ~ 60 µm and in turn sets a minimum on-axis density as the matched radius decreases with density according to the results of Chapter 4. Finally, the on-axis density was constrained such that the dephasing and depletion lengths were roughly equal, which ensures efficient conversion of laser energy to electron bunch energy.

Fig. 6.7 shows a simulation in which a bunch with quasi-monoenergetic peaks $\gtrsim 10$ GeV was produced for laser energy $U = 39$ J on target with pulse length $T_0 = 30$ fs FWHM and beam waist $r_0 = 64$ µm, for a peak laser power of 1.3 petawatts (PW) and $a_0 = 2.86$. The channel was uniform and parabolic, with $n_{e0} = 2.2 \times 10^{17}$ cm^{-3} and $r_m = 65$ µm, which is similar to the channel parameters demonstrated in the experiments of Chapter 4 and Chapter 5.

In Fig. 6.7(a), evolution of the maximum normalized vector potential $a_0(z)$ is plotted for the guided driver pulse. The laser intensity is increased above the initial value at focus by the combined effects of self-focusing and self-steepening (per Chapter 2). Effective laser guiding is provided by the plasma channel, maintaining the laser intensity at or above the vacuum focus value for over the length of the channel.

Although $a_0 > 1$ and hence the accelerator operates in the nonlinear regime, it does not operate in the bubble regime [53, 54], i.e. resonant ponderomotive self-guiding of the laser pulse does not occur. For the same laser parameters and on-axis plasma density, but with no channel (i.e. a transversely infinite plasma slab), an INF&RNO simulation showed self-focusing was insufficient to confine the pulse and hence a pre-formed guiding structure was required. The result of this simulation is plotted alongside the guided case in Fig. 6.7(a), and after an initial increase from self-focusing, the normalized vector potential decreases monotonically as the pulse diffracts.

The electron bunch spectrum for the channel guided case of Fig. 6.7(a) is plotted in Fig. 6.7(b) (red). Total bunch charge is 132 pC, with 80 pC in a quasi-monoenergetic peak at 9.9 GeV with 5% RMS energy spread and 0.26 mrad RMS divergence. Most of the charge is injected via self trapping while $z \lesssim 10$ cm. Electron bunch properties were found to sensitive to channel parameters. For the same on-axis density but with a 5 µm increase in matched spot size to 70 µm, an electron bunch with maximum energy $\lesssim 9$ GeV and 56 pC charge, as plotted in Fig. 6.7(b) (green). Simulations at 75 and 80 µm showed rapid decrease in charge and maximum energy with matched spot size, with no bunch produced for a matched spot size of 80 µm.

These simulations show that with an increase in laser power to 1.3 PW and channel parameters $n_{e0} = 2.2 \times 10^{17}$ cm^{-3} and $r_m = 65$ µm, 10 GeV single-stage energy gain is attainable, motivating further work to optimize the laser-heated capillary discharge scheme.

6.5 Conclusion and directions for future research

In this chapter, guiding of petawatt scale pulses in a laser-heated capillary discharge resulting in electron bunch acceleration to a maximum energy of 7.8 GeV was demonstrated. Moreover, good agreement was observed between electron bunch spectra, particle-in-cell simulations with the INF&RNO code, MARPLE simulations, and the diagnostic measurements of Chapter 4. Further simulations with the INF&RNO code show that acceleration to 10 GeV is possible for parameters that may be accessible with further optimization of the laser-heated capillary discharge channel. With the experiments described here, laser-heated capillary discharge waveguides have been characterized and demonstrated to be suitable high-performance guiding structures according to the physical criteria laid out in Chapter 2 and Chapter 3.

The results reported in this chapter represent a substantial increase in the realized capabilities of laser-wakefield accelerators. Nevertheless, important work remains to be done. The accelerator described here was operated in the nonlinear self-trapping regime, which lead to the production of electron bunches with $\sim 100\%$ energy spread. Improved electron bunch quality, including reduction of energy spread and transverse emittance, is necessary for practical applications, including particle colliders and free-electron-lasers.

The most straightforward means to reduce energy spread is to operate in a regime where self-trapping is suppressed, and inject an electron bunch in a controlled manner through a different mechanism, such as ionization injection. To access this regime for 40 J pulses requires lowering the on-axis density to $\sim 1 \times 10^{17}$ cm^{-3} according to Ref. [64], assuming a_0 self-evolves in a similar manner to that shown in Fig. 6.7. Based on the measurements and simulations of Chapter 4, producing the required 60 µm matched spot size at his density is well outside the capabilities of the current laser-heater setup.

For this reason, experiments were undertaken at 16 J driver energy to demonstrate both suppression of self-trapping and ionization injection in laser heated capillary discharges, for channel parameters demonstrated in Chapter 4 and Chapter 5. Such pulse energies are insufficient for acceleration to 10 GeV, but are relevant for staging at the multi-GeV level, which requires narrow energy spreads [74, 139].. These experiments are the subject of Chapter 7 and the author's working paper, Ref. [23].

Chapter 7

Ionization injection in a 20-cm-long laser-heated capillary discharge

7.1 Introduction

Laser wakefield accelerators (LWFAs) have been the focus of intense research activity as a potential new class of compact sources of ultrashort relativistic electron bunches for applications including high energy physics and free electron lasers [2].

For a given laser pulse energy, the highest electron beam energies from LWFAs have been attained through the use of pre-formed plasma channels [10, 13, 21]. The laser-heated capillary discharges, a novel class of plasma channel, offer greater tunability of density and matched spot size [18, 20, 140] over conventional gas-filled capillary discharges [17, 141]. As a specific example of the capabilities afforded by such a guiding structure, electron acceleration to 7.8 GeV was achieved using a laser-heated capillary discharge with matched spot size 61 μm and on-axis density 2.7×10^{17} cm^{-3} [21, 22].

In Ref. [21] the accelerator was operated in a highly nonlinear regime. Electrons were injected at multiple locations along the plasma channel via self-trapping, resulting in $\sim 100\%$ energy spread. In general, practical applications for LWFAs require much lower energy spreads, of order $\lesssim 1\%$ [2]. Moreover, multi-stage acceleration, essential to achieving high energy gain without sacrificing acceleration gradient or efficiency [40], also requires narrow energy spread for efficient bunch transfer between stages [74, 139]. Various schemes have been proposed that may enable the production of very high quality electron bunches via laser-wakefield acceleration [67, 68]. However, these techniques require that self-trapping be suppressed.

In this chapter, ionization injection in laser-heated capillary discharges with 16 J laser pulses is studied via experiment and simulation. This is less than half the pulse energy available to each beamline of the BELLA laser system when operated in the two-beamline configuration. Prospective experiments in the two-beamline configuration include demonstration of staged acceleration in using two 5 GeV stages [24], and strong-field quantum electrodynamics

experiments [25].

In experiments, ionization injection in the absence of self-trapping was demonstrated in 20-cm-long structures with resonant laser pulses ($\sim$ 80 fs FWHM) at a plasma density of 2.5×10^{17} cm^{-3}. Additionally, ionization injection in laser-heated capillary discharges with shorter pulse lengths ($\sim$ 40 fs FWHM) produced electron bunches with quasi-monoenergetic peaks at 3.9 GeV with tails > 5 GeV.

Finally, strategies for high quality bunch production were investigated with simulations. Due to limitations of the channel, the matched spot size r_m was greater than the input laser spot size r_0 for the experiments reported here. Contributions from self-guiding were expected to be sufficient to achieve quasi-matched guiding despite $r_m > r_0$, however simulations with INF&RNO show that $r_m < r_0$ is optimal at laser intensities where self-trapping was suppressed. These simulation results indicate an approach for future staging experiments. As a specific example, one simulation with INF&RNO shows that with on-axis density 2.5×10^{17} cm^{-3} and matched spot size 45 µm, 4.8 GeV bunches with 70.5 pC charge and 6 % energy spread can be produced.

The chapter is organized as follows. The experiment setup is described in Section 7.2. Ionization injection with suppressed self-trapping is demonstrated in Section 7.4. High charge, high energy bunch production with short driver pulses is described in Section 7.3. Channel parameter optimization for bunch quality using the INF&RNO code is presented in Section 7.5. Conclusions are summarized in Section 7.6.

7.2 Experiment setup

These experiments were performed using BELLA, a 815 nm, 40 nm bandwidth Ti:Sapphire laser system capable of delivering 40 J pulses on target with minimum pulse length 35 fs FWHM [76, 110]. The pulse energy was reduced to 16 J for these experiments. The spot size of the driver $r_0 = 53$ µm, which is defined as the waist of a Gaussian beam with the same FWHM.

The heater laser system was as described in Ref. [21]. This consisted of a 532 nm frequency-doubled q-switched Nd:YAG laser system delivering 300 mJ, 8 ns FWHM pulses to the target in a focal spot with e^{-2} radius 81 µm.

A 800 µm diameter, 20-cm-long sapphire capillary and high voltage pulser system similar to that of Ref. [21] were used for these experiments. To facilitate ionization injection using a high-Z "donor" gas, a gas slot was added to the front of the capillary, as pictured in Fig. 7.1(a). This allows a short region of donor gas to be created for ionization injection at the front of the capillary by flowing donor gas into the front slot, while a uniform region of hydrogen plasma can be created by flowing hydrogen into the fill gas slots.

In a capillary discharge, ionization injection can be implemented by localizing a high-Z "donor" gas at the front of the capillary, while a while a uniform region of hydrogen plasma is created by flowing hydrogen into one or both of the fill gas slots [22]. Localization of the donor gas in the front of the structure requires that a higher pressure be created between

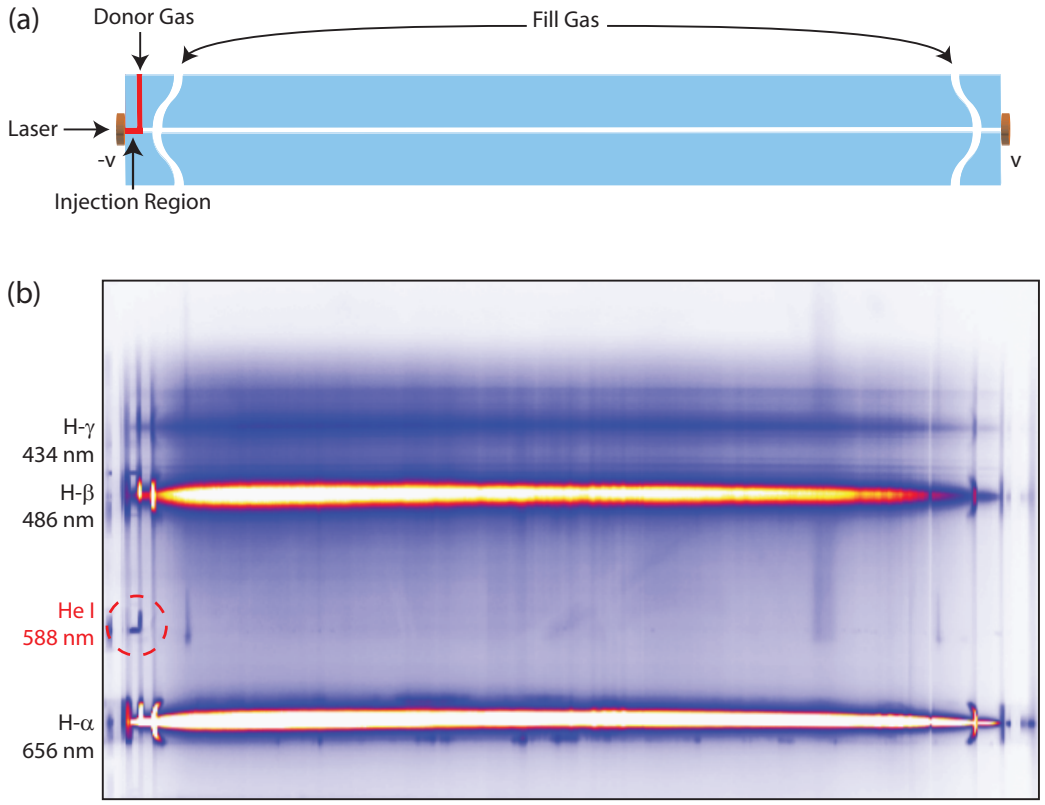

Figure 7.1: (a) Schematic of the 3-slot 800 μm $\times$ 20 cm capillary. (b) Spectrally dispersed image of the capillary discharge, showing the emission lines. Localization of the mixed gas at the entrance of the capillary can be seen through the presence of the 588 nm He I line exclusively at the entrance of the capillary.

the main body of the capillary between the fill gas slots. This can be done with a two-slot capillary by flowing low pressure donor gas into the front slot, and H_2 at higher pressure into the second slot. This arrangement results in a pressure gradient between the two slots. For short capillaries, this pressure gradient is negligible and two slots are sufficient to localize the donor gas at the front of the structure, as was the case for the 3-cm-long capillaries used in the ionization injection experiments of Ref. [22]. However, for long structures this pressure gradient becomes significant. Thus, additional control is required to maintain longitudinally uniform pressure (or a specific profile) throughout the structure while localizing a donor gas for ionization injection.

The addition of a third gas slot, as pictured in Fig. 7.1(a), provides this additional control over the pressure profile of the structure [142]. Specifically, with three slots, flow pressures can be adjusted such that the donor gas is localized at the front of the capillary without a pressure gradient between the two fill gas slots. A mixture of 5% N_2 with balance He (He-5%N_2) was used as a donor gas and flowed into the front slot, and pure H_2 flowed into both downstream fill gas slots. The use of (He-5%N_2) enables the location of the donor gas

to be diagnosed with a simple imaging spectrometer using He emission lines. A dispersed image of the capillary discharge plasma is shown in Fig. 7.1(b), with localization of the donor gas at the front of the capillary visible via the 588 nm He I line.

The laser and electron beam diagnostics are as described in [21, 22, 76, 77, 110]. Electron bunch spectra were measured using a magnetic spectrometer, which consisted of a 2.5-m-long LANEX phosphor screen imaged by a CCD array, with field $\leq$ 1.2 T. Electron bunches enter the magnetic spectrometer through a 25.4 mm diameter hole in the first optic after the target, an uncoated fused silica wedge. Depending on energy and applied magnetic field, the magnetic spectrometer has an angular acceptance of 0.5-1 mrad. Bunch charge was measured using an integrating current transformer (ICT) with aperture 10 cm installed 11 m downstream of the capillary, with angular acceptance $\sim$ 5 mrad [138]..

Laser spectra were measured by a pair of spectrometers, a UV-NIR spectrometer covering the range 250-1050 nm, and a NIR spectrometer covering the range 1000-2200 nm. The wide spectral range is required to capture spectra of highly depleted laser spectra, and in general electro-optical devices sensitive to light over this entire frequency range are not readily available. Complete laser spectra are constructed by scaling and merging the spectra acquired on both spectrometers to match the energy spectral density in the region of overlapping spectral sensitivity 1000-1050 nm.

7.3 High-energy bunch production via ionization injection in the nonlinear regime

In Ref. [21], electron bunches with maximum energy 7.8 GeV were produced in a 20-cm-long, 800 µm diameter laser-heated capillary discharge with 31 J, 35 fs FWHM driver pulses focused to a 53 µm. The capillary discharge was operated with initial fill pressure 17.6 torr H_2, with a peak current of 450 A and 400 ns rise time. The laser heater pulse had energy 300 mJ, FWHM 8 ns, and arrived 420 ns after the peak of discharge current. The driver pulse arrived within 1 ns of the peak of the heater pulse, when the channel was measured to have on-axis density $\overline{n}_{e0} = 2.7 \pm 0.4 \times 10^{17}$ cm^{-3} and matched spot size $\overline{r}_m = 61 \pm 3$ µm. The resulting acceleration was highly nonlinear, with self-trapping occurring at multiple locations along the guiding structure.

For the experiments here, the driver energy was lowered to 16 J, corresponding to the energy available to a single beamline with the BELLA laser system operated in the two-beamline configuration, with FWHM 40 fs. The parameters of the laser-heated capillary discharge were similar, with a 300 mJ heater pulse arriving 360 ns after the peak of discharge current, and capillary fill pressure 17.6 torr. The driver pulse arrived $t = 2.2 \pm 0.5$ ns after the peak of heating power. Spot size oscillation measurements[20] and group velocity measurements with a two-color common path interferometer[115] determined that $\overline{n}_{e0} = 3.1 \pm 0.2 \times 10^{17}$ cm^{-3} and $\overline{r}_m = 63 \pm 5$µm respectively. A He-5%$N_2$ donor gas mixture was localized in the front of the capillary using the front gas slot, to facilitate ionization injection. Electron bunches with

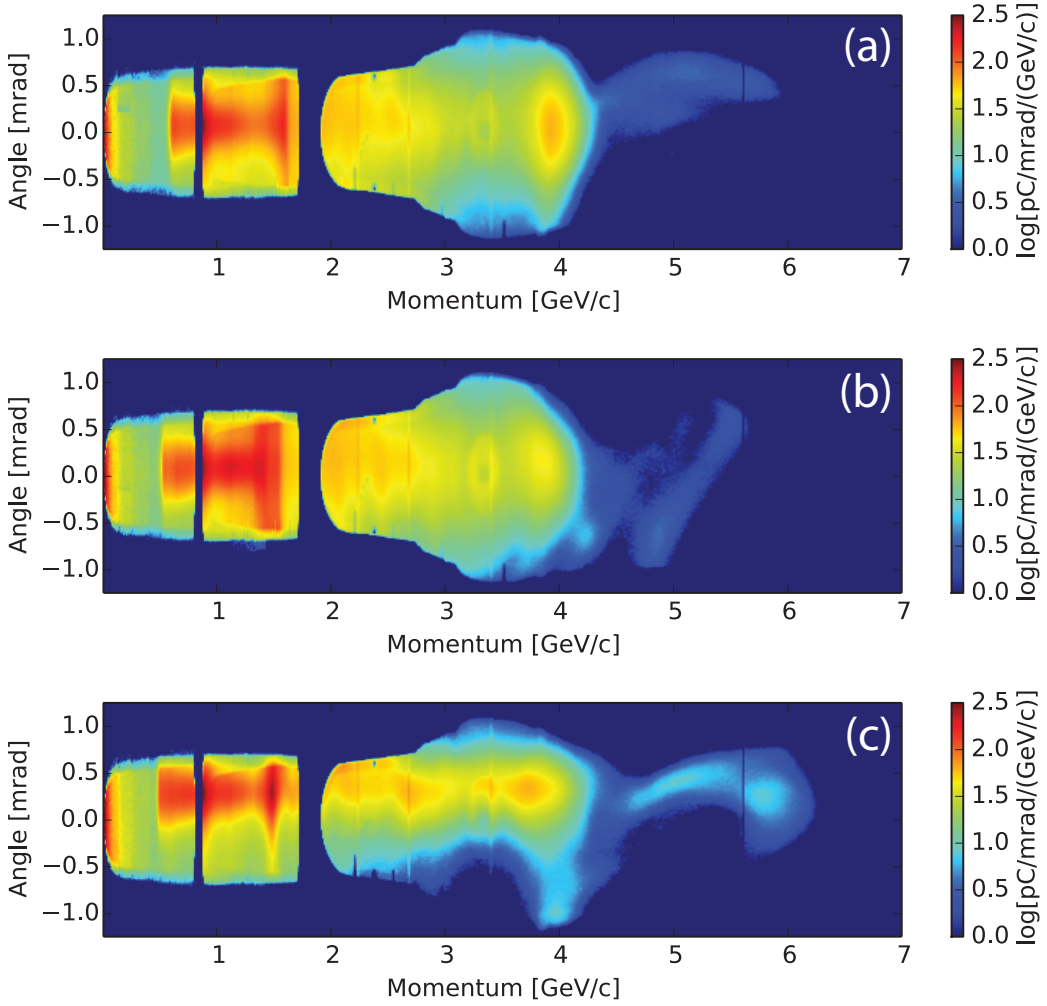

Figure 7.2: Measured electron bunch spectra for 16 J pulse energy, 40 fs intensity FWHM arriving at $t = 2.2 \pm 0.5$ns after the peak of heating power, and channel parameters $\overline{n}_{e0} = 3.1 \pm 0.2 \times 10^{17}$ cm^{-3} and $\overline{r}_m = 63 \pm 5$µm. Total charge registered on the magnetic spectrometer and (charge in the tail $\gtrsim 4.5$ GeV) is listed for each shot. (a) 214 pC (2 pC) (b) 247 pC (2 pC) (c) 194 pC (5 pC)

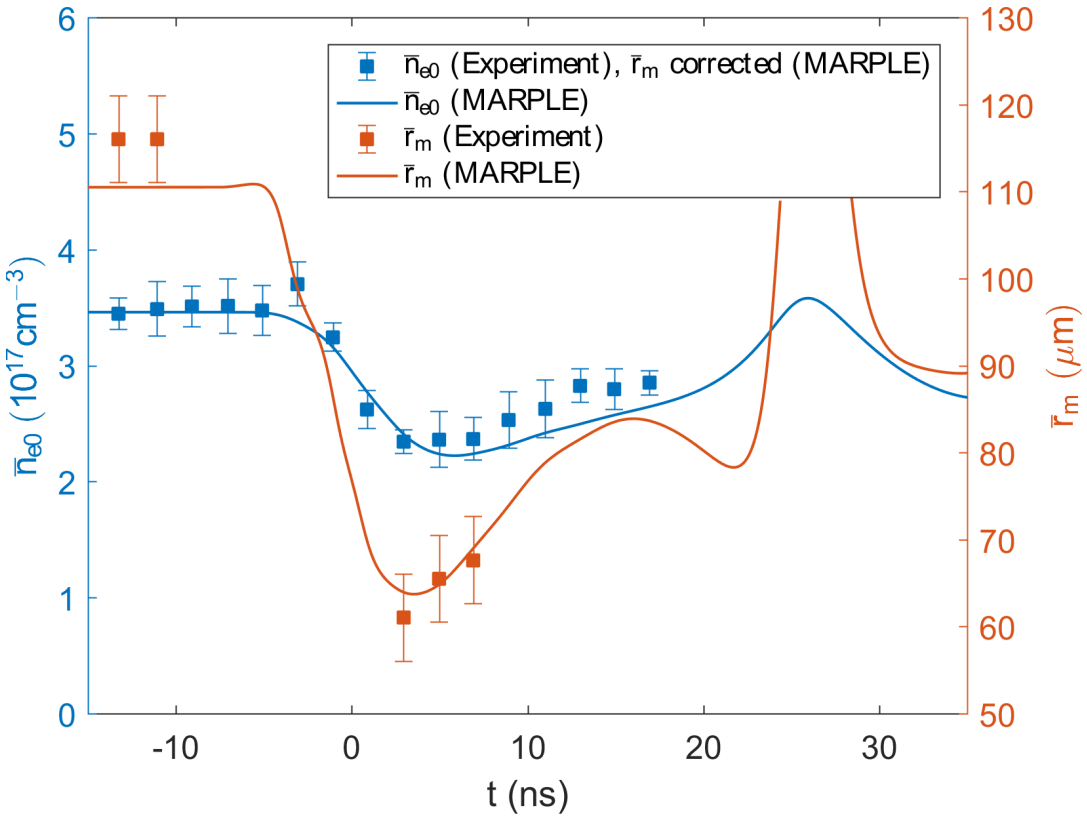

Figure 7.3: Measured longitudinally-averaged on-axis density $\overline{n}_{e0}$ and matched spot size $\overline{r}_m$ in the heated channel as a function of delay from peak heater power, for capillary fill pressure 15.5 torr H_2 and heater pulse energy 240 mJ arriving 460 ns after the peak of discharge current. Plotted as solid traces is are longitudinally averaged on-axis density and matched spot size from a MARPLE simulation for the conditions of the experiment.

peaks at 3.9 GeV and tails > 5 GeV were produced. Electron spectra for three bunches that were well aligned to the spectrometer are plotted in Fig. 7.2.

In contrast to the bunch spectra shown in Fig. 7.2, efficient transfer of electron bunches between acceleration stages requires narrow energy spread. One approach to achieving this is to tune the driver and plasma parameters to suppress self-trapping, and then trigger injection through another mechanism. This is the subject of the next section.

7.4 Guiding of stretched pulses without self-trapping in a laser-heated capillary discharge waveguide

The threshold for self-trapping is dependent on both the laser normalized vector potential a_0 and plasma wave phase velocity [64]. In this section, ionization injection without self-trapping in a laser heated capillary discharge with 16 J pulses is shown. Reduction of a_0 was achieved

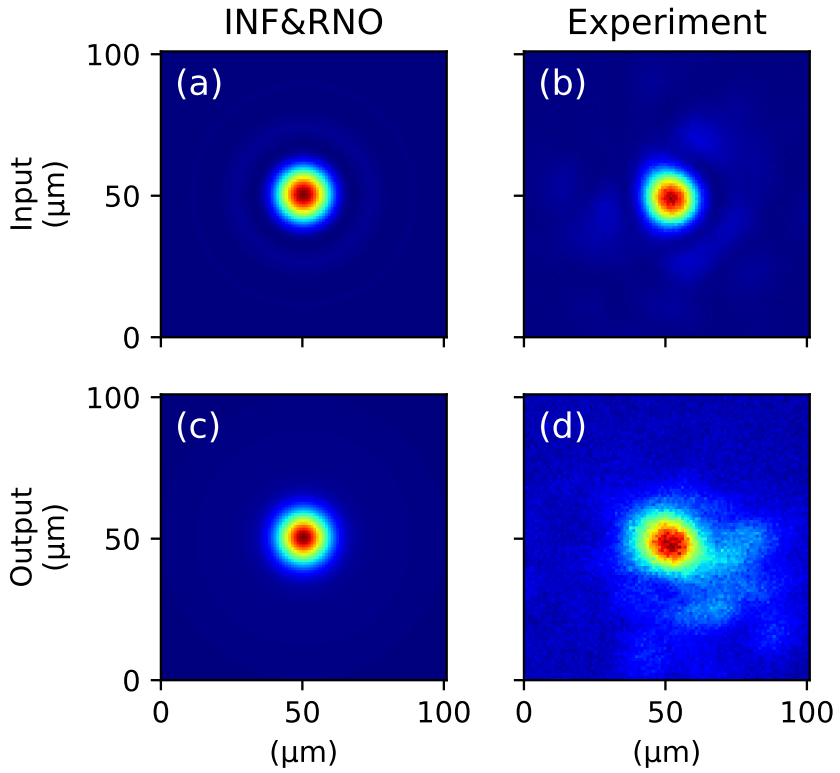

Figure 7.4: Input and output laser modes for the plasma channel of Fig. 7.3 at $t = 2.6$ ns. (a),(b): Input modes from INF&RNO simulation and experiment, respectively. (c),(d) Output modes from INF&RNO simulation and experiment, respectively. The fluence from INF&RNO simulations has been scaled according to the known spectral response of the CCD sensor.

by increasing the pulse length to 80 fs FWHM. The density and matched spot size evolution of the channel are plotted in Fig. 7.3. Capillary fill pressure was 15.5 torr, and the heater pulse energy was 240 mJ with the pulse arriving 460 ns after the peak of discharge current.

The longitudinally averaged on-axis plasma density $\overline{n}_{e0}$ and matched spot size $\overline{r}_m$, from both measurements and simulations with the MARPLE MHD code [102, 140], are plotted in Fig. 7.3. The longitudinally averaged on-axis plasma density $\overline{n}_{e0}$ of the channel was measured via two-color common-path spectral interferometry [115]. The longitudinally-averaged matched spot size $\overline{r}_m$ was measured by tracking oscillation of the probe beam spot-size at the capillary exit as plasma and laser parameters were varied as described in Ref. [20]. Matched spot size from the simulations is calculated according to the quasi-matched spot size derived in Ref. [87]. The geometrical contribution to the group velocity[48] for the density measurements was compensated using the matched spot size from the MARPLE simulations.

With pure H_2 flowing into the front gas slot (i.e. no donor gas for ionization injection), no electron beams were observed for channel parameters $\overline{n}_{e0} = 2.5 \pm 0.2 \times 10^{17}$ cm^{-3} and

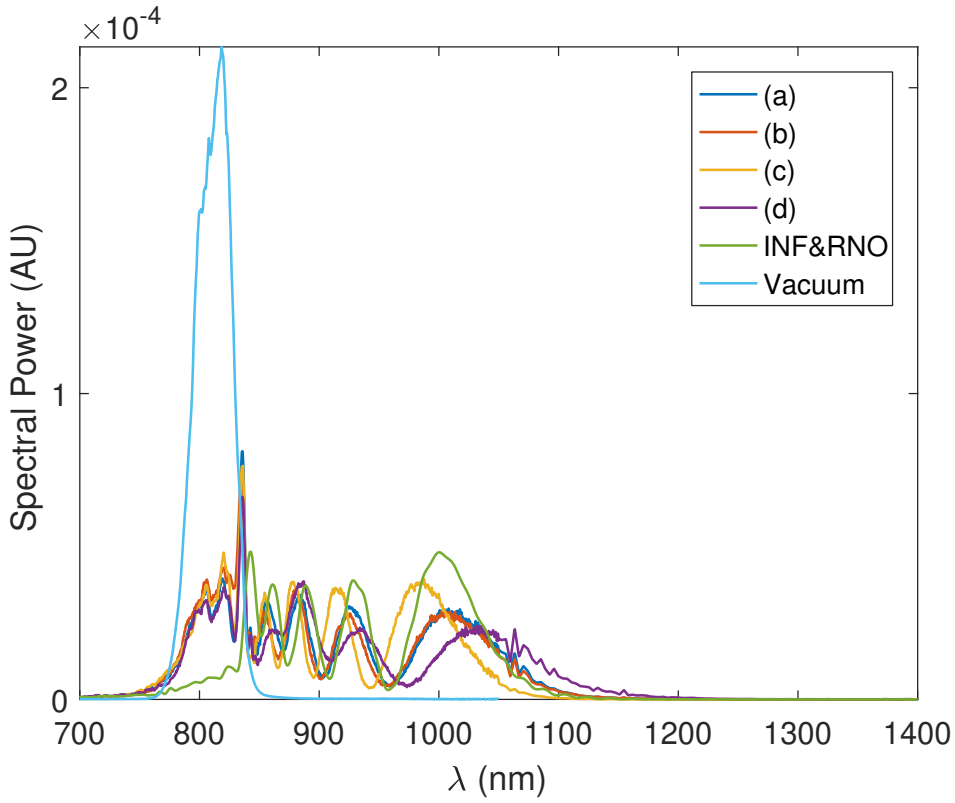

Figure 7.5: Post-interaction driver spectra for the conditions of Fig. 7.4, labeled with the corresponding shots of Fig. 7.7, simulated spectrum from INF&RNO (using the density profile from the MARPLE simulation of Fig. 7.3 at $t = 2.6$ ns), and vacuum driver spectrum.

$\overline{r}_m = 60 \pm 5$ µm, corresponding to $t = 2.6$ ns in Fig. 7.3. The driver pulse had energy 16 J and intensity FWHM pulse length 80 fs.

Measurements and simulations indicate that driver pulse is well confined in the channel, while the plasma wave amplitude is maintained below the threshold for self-trapping. Fig. 7.4 shows the driver vacuum focus and guided fluence profile at the exit of the channel, from both the experiment and an INF&RNO simulation. The driver was modeled in INF&RNO as in Refs. [21, 22, 76], with the transverse fluence given by a jinc(r) function and the temporal profile from the diagnostic measurements described in Ref. [110]. Specifically, the spatiotemporal driver pulse structure is defined

$$\hat{a}(\zeta, r, t = 0) = a_0 \mathrm{jinc}\left(\frac{r}{R_{\mathrm{jinc}}}\right) f_{\parallel}(\zeta) \ , \tag{7.1}$$

with $\zeta = z - ct$ the longitudinal co-moving coordinate, r the radial coordinate, the function $\mathrm{jinc}(u) \equiv 2J_1(u)/u$ with $J_1(u)$ the Bessel function of the first kind, $R_{\mathrm{jinc}} \simeq 0.364 r_0$, and the complex function $f_{\parallel}(\zeta)$ describing the temporal structure of the laser pulse.

The INF&RNO simulation was performed using the plasma density profile at $t = 2.5$ ns from the MARPLE simulation of Fig. 7.3, the on-axis density and matched spot size of which are plotted in Fig. 7.6. The spot size at the channel exit is roughly the same size as the vacuum focus, consistent with effective guiding of the driver by the channel. However, the laser spot can oscillate in the channel such that the spot size at the exit is equal to the vacuum focal spot size. The guided laser spectrum after propagation through the channel, combined with INF&RNO simulations, can be used to gain insight into the laser guiding.

Measured and simulated post-interaction laser spectra corresponding to Fig. 7.4 are plotted in Fig. 7.5. The plotted energy spectral densities have all been normalized to the same (arbitrary) value of the wave action, which is an adiabatic invariant of the laser-plasma interaction [46–48]. The measured and simulated spectra agree well with each other, and simulations for range of on-axis densities in Fig. 7.8 show that the tail and fringe features of the spectrum are sensitive to fluctuations of scale 0.1×10^{17} cm^{-3}. Agreement in the long-wavelength tail, which corresponds laser energy redshifted deep in the plasma wave[44, 45, 143, 144], suggests the simulation is faithfully modeling the plasma wave structure. Additionally, reproduction of the spectral "fringes" in the simulation indicates that granular features of the evolution of the guided laser pulse are being captured.

However, measured spectra show excess energy at short wavelengths $\lambda \lesssim 825$ nm compared to the simulation. This is may be due to imperfections in the driver focus in the experiment, which featured more energy in the halo than the perfect jinc function used in the simulation, which can be seen by comparing Fig. 7.4(a) and (b). The additional energy in the focus halo will experience less self-focusing and may not be guided as effectively in the channel, and hence may experience less redshifting. Quantitatively, for the laser fluence profile measured in the experiment, $\sim 40\%$ of the total energy lies outside the first airy minimum at $r \sim 75$ µm, versus $\sim 20\%$ for the ideal jinc profile used in the simulation. This is comparable to the discrepancy in energy spectral density in the short wavelength region. Nevertheless, as previously stated, simulation results agree well in the long wavelength region of the spectrum associated with laser energy propagating deep in the plasma wave, which is in turn most closely associated with wake amplitude and structure relevant to particle trapping.

The simulated driver evolution inside the channel is plotted in Fig. 7.6(a), with the MARPLE simulated on-axis density $n_{e0}(z)$ and $r_m(z)$ plotted in Fig. 7.6(b) and (c), respectively. Density and matched spot size in the channel are nonuniform due to hydrodynamic self-evolution of heater beam in the capillary plasma [20, 21, 140]. The matched spot size $r_m(z)$ for each longitudinal slice was calculated using the quasi-matched guiding condition for a Gaussian pulse derived in Ref. [87].

The INF&RNO simulation shows significant evolution of the guided driver pulse, in both a_0 and the e^{-2} radius of the fluence r_{-2}. Due to a combination of mismatch to the channel, high order mode content of the jinc(r) focal spot [114], and self-focusing, 20 µm excursion in beam size occur during propagation [58].

For the conditions of Figs. 7.4-7.6 with pure H_2 in the front gas slot, no electron bunches were observed on the electron bunch diagnostics [76, 110], specifically the integrating current transformer (ICT) or electron spectrometer. However, flowing a He-5%N_2 mixture into the

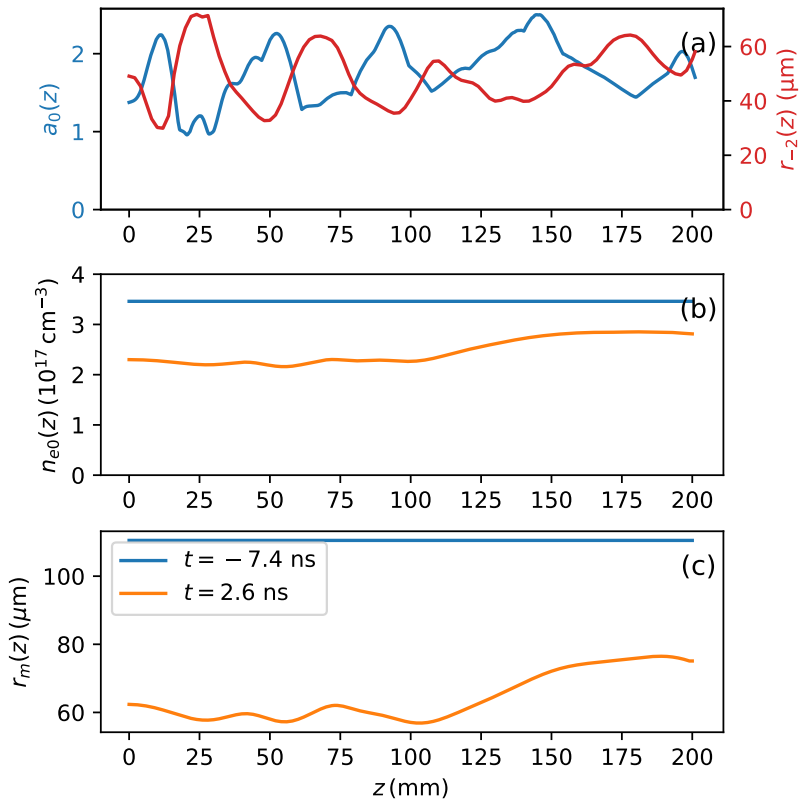

Figure 7.6: (a) Peak driver normalized vector potential a_0 and e^{-2} fluence radius $r_{e^{-2}}$ as a function of longitudinal position from the INF&RNO simulation of Figs. 7.4 and 7.5, using the density profile from the MARPLE simulation at $t = 2.6$ ns. (b) On-axis density as a function of longitudinal position for the density profile from the MARPLE simulation, for both the initial discharge plasma (without heating), and $t = 2.6$ ns after the peak of heater power. (c) Matched spot size as a function of longitudinal position for the density profile from the MARPLE simulation.

front gas slot resulted in the production of electron bunches. Together with the foregoing discussion, this indicates the trapping of electron bunches via ionization injection in an acceleration regime where self-trapping is suppressed.

Electron spectra of four electron bunches are plotted in Fig. 7.7, with (a)-(d) corresponding to the laser spectra (a)-(d) plotted in Fig. 7.5. Depending on electron energy and magnetic field, the acceptance of the magnetic spectrometer is $\pm 0.5 - 1$ mrad [21, 76, 77]. The ICT has an angular acceptance, of ~ 4 mrad, and can measure bunch charge for electron bunches not captured by the electron spectrometer. The shots plotted in Fig. 7.7 were chosen as those best aligned to the magnetic spectrometer, with $> 50\%$ of the charge measured by the ICT observed on the spectrometer for all of them.

There is a large difference in bunch charge between the shots of Fig. 7.7(a),(b) and (c),(d). Formation of the heated channel is a dynamic process, and sensitive to a number

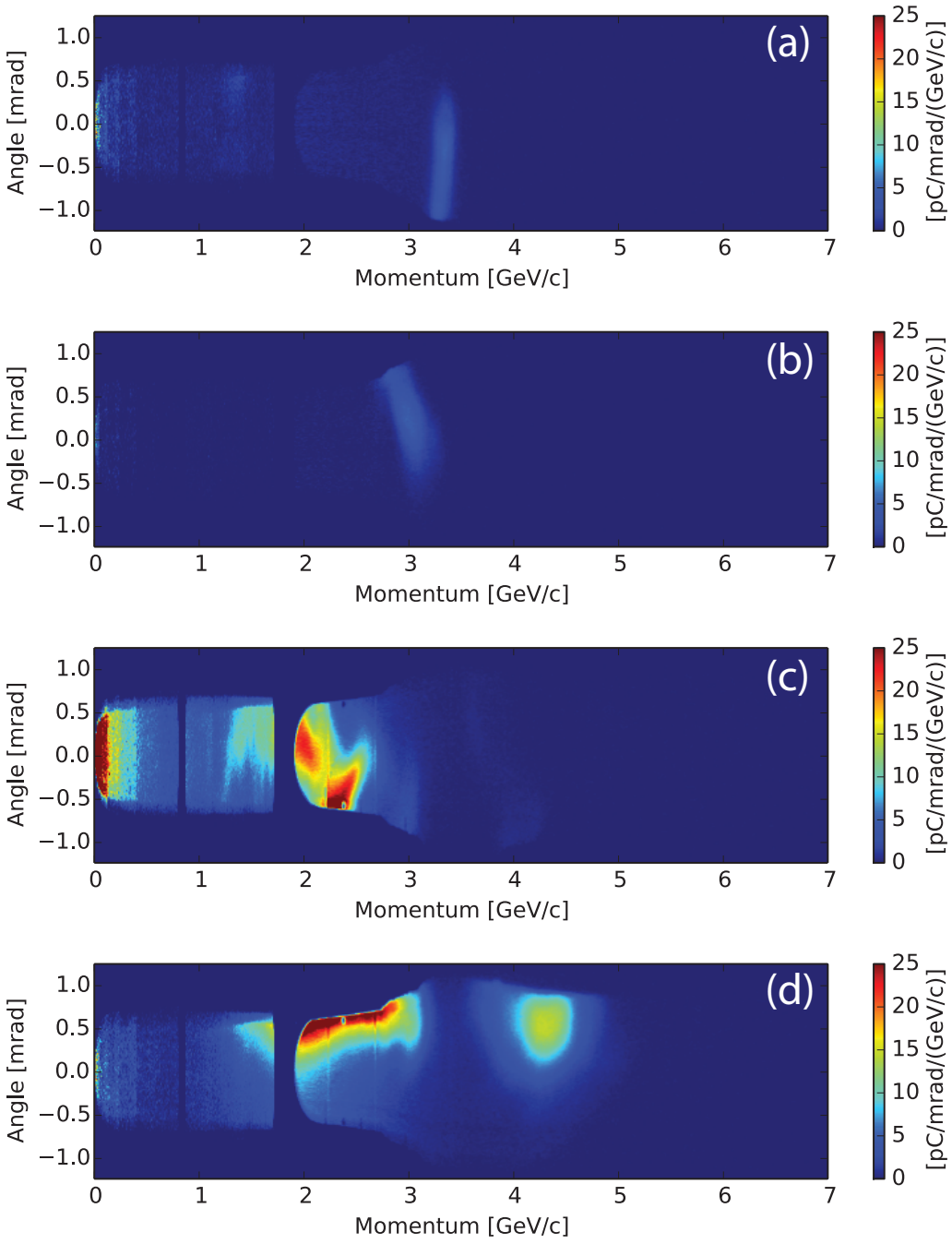

Figure 7.7: Measured electron bunch spectra for the conditions of Fig. 7.4, selected for best alignment to the magnetic spectrometer. 16 J pulse energy, 80 fs intensity FWHM arriving at $t = 2.6$ ns per Fig. 7.3. Total charge registered on the magnetic spectrometer is listed for each shot. (a) 3 pC (b) 2 pC (c) 29 pC (d) 26 pC

of variables that vary from shot to shot, heater alignment to the discharge plasma channel, delay of the heater pulse relative to the driver, and the shape of the heater pulse itself [20]. Therefore, channel parameters $\overline{n}_{e0}$ and $\overline{r}_m$ will fluctuate from shot to shot. Measurements have shown capillary discharges to be stable to within $< 1\%$ [93, 116]. RMS deviation in density measurements of capillaries without laser heating with the two-color common-path interferometer is $\sim 0.1 \times 10^{17}$ cm^{-3}, whereas uncertainty in measurements of heated channels are as $\sim 0.3 \times 10^{17}$ cm^{-3} RMS with this diagnostic. This increased variance in density measurements in laser-heated capillary discharges is attributed to these previously mentioned effects.

Shot-to-shot density fluctuations were modeled by applying a uniform offset to the density profile of Figs. 7.4-7.6. The simulated post-interaction driver spectra and electron bunch spectra are plotted in Fig. 7.8, with the laser redshift $\Delta R = 1 - \langle k/k_0 \rangle$[43] evaluated for each case. The 0.25×10^{17} cm^{-3} density interval over which the accelerated charge increases from 0.3 to 36.5 pC in the simulations is comparable to the uncertainty in the density measurements of Fig. 7.3. Moreover, the variance in driver redshifting over this range of simulated densities is comparable to the variance in driver redshifting observed in the laser spectra corresponding to Fig. 7.7 plotted in Fig. 7.5.

Oscillation of the driver intensity during the first few centimeters of propagation in the channel is the primary process responsible for the retention or loss of injected bunches, and hence the primary cause of charge fluctuations. Specifically, INF&RNO simulations show that bunches are lost at the first minimum of the laser spot size oscillation at $z \approx 25$ mm. At this point, reduction of the nonlinear plasma wavelength moves bunches into the defocusing phase of the wakefield, causing them to be lost.

This can be seen in Fig. 7.8(e), where the bunch charge, defined as accelerated particles within 15 µm of the axis, is plotted as a function of z. The traces all show loss of charge after the first minimum in a_0, with the relative amount of charge loss decreasing with density due to the correspondingly higher values of a_0 and a longer nonlinear plasma wavelength at the first minimum in the oscillation. Note that because it takes time for unfocused particles to exit the defined bunch volume, bunch charge loss as plotted in Fig. 7.7(e) does not precisely coincide with the a_0 minimum. The evolution of the driver responsible for charge loss is naturally a function of the matched spot size r_m, but also a function of n_e through self-focusing, which is responsible for the first maximum in the laser intensity upon coupling into the channel.

In the experiment described in this section, no clear correlation between redshifting and bunch charge was found. This can be attributed to the fact that redshifting yields information about laser propagation averaged over the whole channel, whereas the simulations of retention of bunch charge is extremely sensitive to the laser evolution at the first minimum in the driver a_0 at $z \approx 25$ mm. Redshifting is only correlated with charge in the simulations of Fig. 7.8 because a single parameter is being varied, namely the average on-axis density, to study the effect of small perturbations of channel parameters. In the experiment, however, multiple parameters fluctuate simultaneously shot-to-shot. As stated previously, this includes both density and matched spot size. Furthermore, pointing jitter of the heater and driver with respect to the capillary is of order 20 µm, which in turn perturbs the alignment of the

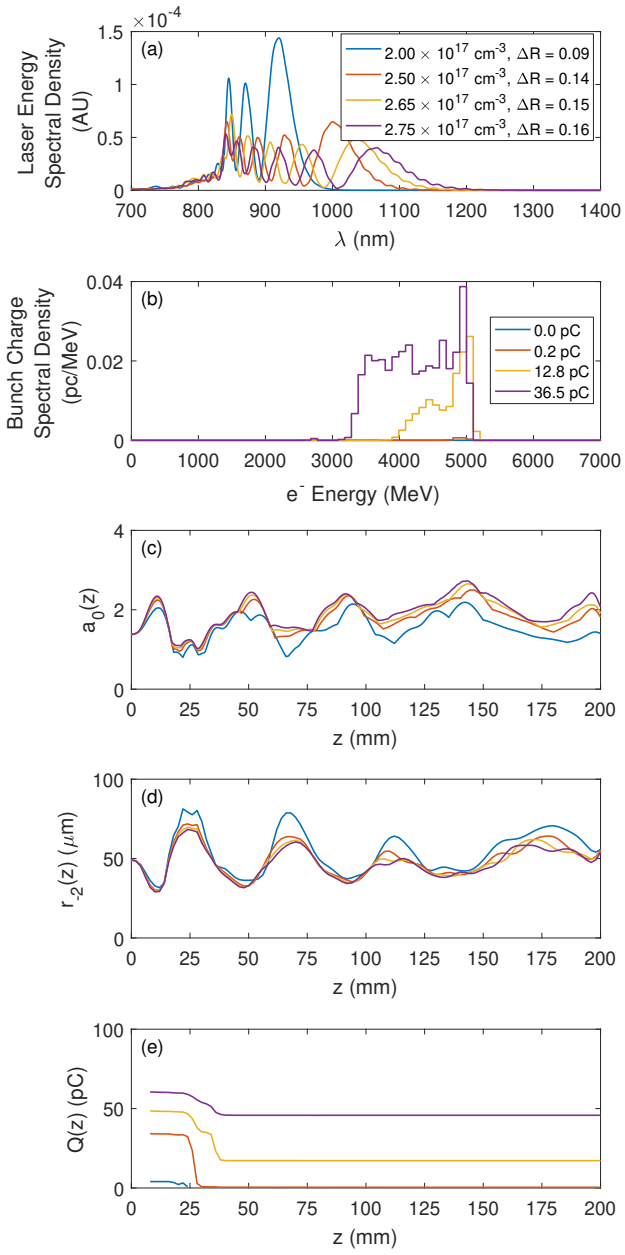

Figure 7.8: Output from INF&RNO simulations using the MARPLE profile of Fig. 7.6 with density offsets to simulate the effect of channel fluctuations. Longitudinally averaged density $\overline{n}_{e0}$ and the laser spectrum redshift ΔR are listed for each simulation case, with the zero-offset case $\overline{n}_{e0} = 2.5 \times 10^{17}$ cm^{-3} corresponding to the original profile. Laser redshift ΔR and bunch charge are plotted with the optical and electron bunch spectra, respectively. (a) Post-interaction driver spectra. (b) Electron bunch energy spectra, windowed for the $pm0.5$ mrad acceptance of the magnetic spectrometer. (c) Peak normalized vector potential evolution $a_0(z)$. (d) e^{-2} fluence radius r_{-2} vs. z. (e) Total bunch charge vs. z. Bunch charge Q defined as accelerated particles within 15 µm of the axis.

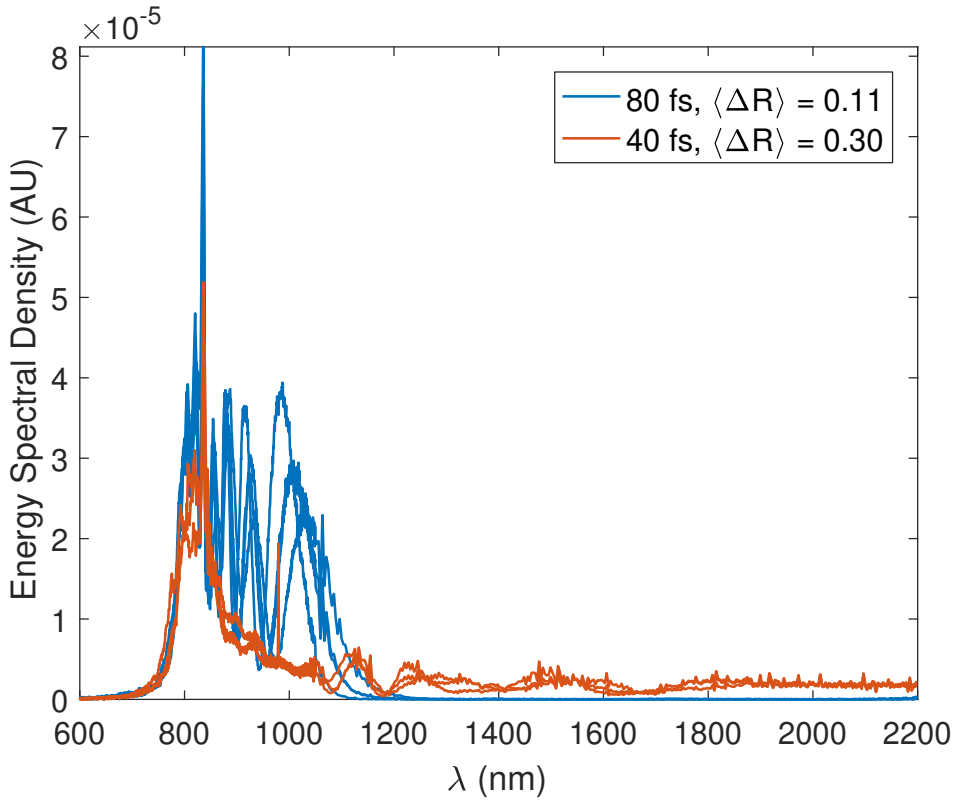

Figure 7.9: Measured post-interaction driver spectra for Fig. 7.7 (blue) and Fig. 7.2 (red). Spectra have been normalized to the same value of the wave action. Average redshift for each group of spectral traces $\langle \Delta R \rangle$ is listed in the plot legend.

driver to the plasma channel. Hence, for this experiment, a longitudinally averaged laser redshifting measurement is not sufficiently sensitive to the laser evolution in the small region where bunch loss occurs to correlate with accelerated charge.

Post-interaction driver spectra are plotted in Fig. 7.9 for the beams of Figs. 7.7 and 7.2. Driver redshift for 40 fs pulses is a factor 3 greater than for 80 fs pulses of Section 7.4, although redshift for the 40 fs case may be underestimated, as the spectral range of the NIR spectrometer appears to be exceeded at the long wavelength limit in Fig. 7.9. In the nonlinear regime, redshift scales approximately according to $\Delta R \sim a_0^2 n_{e0}^{3/2}$ [43], and so a factor $\sim 3^{1/2}$ increase in the normalized laser vector potential in the channel between the 80 fs and 40 fs cases can be deduced. Comparing with the peak value $a_0 = 2.5$ for the case of Fig. 7.6, this implies a peak value $a_0 \sim 4$ and strongly nonlinear laser propagation in the 40 fs case.

In Ref. [64], the empirical threshold for self-trapping $a_0 \gtrsim 2.75[1 + (\gamma_p/22)^2]^{1/2}$, with γ_p the plasma wave phase velocity Lorentz factor, was obtained via INF&RNO simulations. The empirical scaling for the minimum value of γ_p accounting for self-evolution of the driver $\gamma_{p,\mathrm{min}} \simeq 2.4(\omega/\omega_p)^{1/2}$ was also obtained in Ref. [64]. For the conditions of the experiments of this chapter $\gamma_p \gtrsim 20$ with corresponding injection threshold $a_0 \gtrsim 3.5$. Hence, the redshifting

measurements showing $a_0 \sim 4$ within the channel for the 40 fs (Fig. 7.2), as well as the broad energy spectra, are consistent with self-trapping.

By contrast, for the 80 fs case (Fig. 7.7), the INF&RNO simulation output plotted in Fig. 7.8(c) shows that the driver a_0 remains below the threshold for self-trapping over the length of the plasma channel. The maximum value of the normalized vector potential a_0 in the highest density case is 2.7, below the threshold of $a_0 \gtrsim 3.5$. This is consistent with high-resolution simulations with INF&RNO (i.e. sufficient spatiotemporal resolution to model self-trapping) that showed no self trapping for the simulation cases of Fig. 7.7.

In this section, guiding of a LWFA driver pulse without self-trapping in a 20-cm-long structure has been demonstrated. This conclusion is supported by diagnostic measurements of the channel properties, experimentally obtained laser spectra, demonstration of ionization injection of electron bunches, and INF&RNO simulations. However, staging experiments require improved guiding and narrower electron bunch energy spread. Hence, refinements to the plasma channel and driver laser were investigated with simulations, the results of which are presented in the following section.

7.5 Optimizing a 20-cm-long plasma channel for bunch quality

Staged acceleration requires a bunch with few-percent energy spread for efficient capture into successive accelerating stages due to the chromatic focusing of electron beam optics [74]. Simulations were performed with INF&RNO to identify parameters relevant to producing ~ 10 pC bunches with low energy spread at the 5 GeV level. The accelerator parameters used in the experiment where suppression of self-trapping was observed, i.e. the INF&RNO simulation of Figs. 7.4-7.6, were taken as a baseline. Parameters were then evolved away from this baseline to obtain three cases with increased bunch charge. Electron bunch spectra and normalized vector potential evolution for these three modified cases (i-iii), as well as the baseline case (iv), are plotted in Fig. 7.10. For all cases, driver pulse width and peak normalized vector potential a_0 at the channel entrance were fixed at the values of Fig. 7.6, 80 fs and 1.37 respectively. For all cases, the plasma profile from MARPLE of Fig. 7.6 was used, with the exception of case (iii), which considers a longitudinally uniform channel with optimized matched spot size.

Accelerator performance can be improved by matching the driver focal spot to the channel. For case (i) of Fig. 7.10, a jinc(r) profile was assumed for the focus as in Section 7.4, and the spot radius r_0 was tuned to maximize the bunch charge spectral density while the peak fluence (i.e. a_0) at the entrance was held constant (necessitating commensurate variation of the laser pulse energy). Optimal matching of a jinc(r) focus to a parabolic channel requires $r_0 > r_m$ due to the presence of higher order modes [114].

Plotted in Fig. 7.10 is the result of this procedure, a case (i) with $r_0 = 59$ µm and pulse energy 20.6 J. This case has the simplest practical implementation of those investigated,

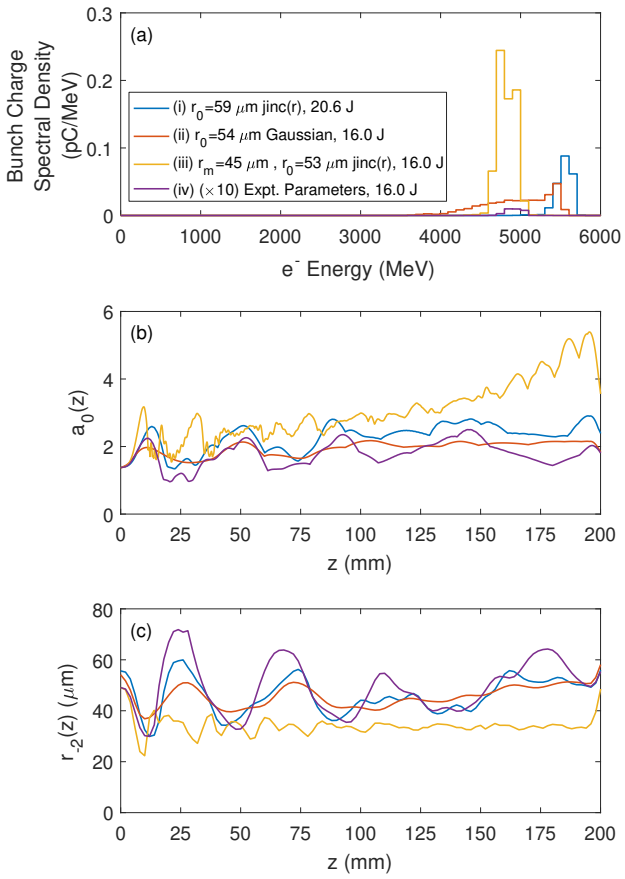

Figure 7.10: Electron bunch spectra windowed for the ±0.5 mrad acceptance of the magnetic spectrometer (a), peak normalized vector potential evolution (b), and e^{-2} laser fluence radius (c) for three accelerator configurations (i-iv) simulated with INF&RNO. (i) Plasma profile of Fig. 7.6, with a jinc(r) fluence profile at focus, with $r_0 = 59$ µm (as defined in Section 7.2), chosen for optimal matching to the channel according to Refs. [87, 114]. Bunch charge 21.4 pC. (ii) Plasma profile of Fig. 7.6, Gaussian fluence profile at focus with $r_0 = 53$ µm. Bunch charge 30.3 pC. (iii) Longitudinally uniform channel with $n_{e0} = 2.5 \times 10^{17}$ cm^{-3} and $r_m = 45$ µm, matched to the jinc(r) fluence profile of Section 7.4. Bunch charge 70.5 pC. Self-injection in the density downramp at the channel exit contributed 25 pC of charge $\lesssim 200$ MeV, shown as the dotted line. (iv) Simulation of Fig. 7.6, corresponding to the conditions of the experiment of Section 7.4. Bunch charge spectral density multiplied ×10 for visibility on the plot scale. Bunch charge 0.2 pC.

requiring only an decrease in the driver laser nearfield size.

The jinc function used to model the laser focus in the simulation (i) and (iv), as well as the real laser focus in the experiment, contains high-order Laguerre-Gaussian modes. Hence, a_0 and $r_{e^{-2}}$ oscillate as the driver propagates in the channel due to not only self focusing, but also beating of these higher mode orders. Suppressing this oscillation further requires better matching of the laser focus and the transverse shape of the plasma channel to one another, not merely a reduction of the channel matched spot size. This can be accomplished through use of a purely Gaussian focus. A case (ii) with $r_0 = 54$ µm and driver pulse energy 16 J, yielding the same peak normalized vector potential at the capillary entrance as case (iv), is plotted in Fig. 7.10.

In both cases (i) and (ii), improved matching of the driver yielded higher bunch charge than the case corresponding to the experiment parameters, case (iv). The first minimum in a_0 is increased for both the matched jinc and the Gaussian profile which reduces the wake-phase-shift associated with the nonlinear plasma wavelength sufficiently to retain the bunch in the focusing region of the wake. Furthermore, in the case of a Gaussian focus, oscillations in a_0 are significantly decreased in amplitude as compared to a jinc(r) focus, due to the elimination of high-order modes.

Finally, because modifying the laser nearfield without significant energy loss is technically challenging, a 20-cm longitudinally uniform channel optimized for the existing jinc(r) laser focus was investigated. INF&RNO simulations for r_m and n_{e0} varied over the intervals 35-60 µm and 2.0-2.5 $\times 10^{17}$ cm^{-3} respectively. Of these simulations, case (iii) in Fig. 7.10 yielded the highest charge spectral density, with $r_m = 45$ µm and $n_{e0} = 2.5 \times 10^{17}$ cm^{-3}. 70.5 pC of charge was trapped via ionization and accelerated to 4.5-5.1 GeV, and 25 pC of charge was injected by self-trapping in the density downramp at the exit of the channel and accelerated to low energies $\lesssim 200$ MeV. These components of the accelerated charge are denoted by the solid and dotted lines in Fig. 7.10(a) respectively. As in case (i), oscillations are present due to high order mode content. Additionally, a_0 grows significantly over the length of the channel due to redshift and self-steepening. The small matched radius obtained from the optimization procedure warrants discussion. Indeed, for a Gaussian laser focus, self-focusing increases the required channel matched spot size [87]. However, the high-order mode content of a jinc profile also reduces the effective channel matched spot size for the laser focus. Specifically, in the linear limit the fraction of energy in the fundamental Laguerre-Gaussian mode is maximized for $r_m = r_{-2}/1.22$ [114]. Confinement of driver energy near the axis of the channel requires these effects be balanced against each other, in this particular case requiring $r_m < r_{-2}$.

Finally, case (iv) yielded the highest bunch charge and spectral density of all those summarized in Fig. 7.10. However, the parameters of this channel are not accessible with the current heater laser system, motivating the use of alternative guiding structures and methods, e.g. hydrodynamically-formed optical field-ionized channels [82, 83, 145].

The results of this section show that multiple paths exist for optimizing ionization-injected bunches. All approaches investigated require improvement of the laser guiding, however this can be accomplished via modification of either the driver focal spot or the plasma channel.

Moreover, all approaches considered yielded substantially higher bunch charge.

7.6 Conclusion

In this chapter, ionization injection of electron bunches in 20-cm-long laser-heated capillary discharge waveguides was studied. Ionization injection with suppressed self-trapping was demonstrated with 80 fs driver pulses, a prerequisite for high quality bunch production. Additionally, high charge, high energy bunches were produced with 40 fs pulses at 16 J. Finally, simulations identified driver and channel parameters that can be optimized to produce high charge, narrow energy spread bunches via ionization injection. The results presented here motivate further development of channel-guided LWFAs as compact sources of multi-GeV electron bunches for applications requiring narrow energy spreads.

Chapter 8

Conclusion

In this dissertation, laser-heated gas-filled capillary discharges have been characterized and demonstrated as novel guiding structures for laser-wakefield acceleration. Density and matched spot size were measured and found to be tunable over a wide parameter space, far in excess of that accessible with a conventional capillary discharge. Moreover, good agreement was observed between measurements and MHD simulations with the MARPLE code.

Acceleration of electrons to 7.8 GeV with 16 J, 850 TW peak power laser pulses from the BELLA laser in a laser-heated capillary discharge was demonstrated, a record for single-stage energy gain in a LWFA as of the time of writing. Additionally, acceleration of electrons to 3.9 GeV with 16 J pulses was demonstrated. Moreover, bunches were successfully injected at 16 J pulse energy using ionization injection with suppressed self-trapping. The results with 16 J demonstrate a capability for production of multi-GeV electron beams with half the BELLA laser's maximum pulse energy, a key technical capability for future staged acceleration experiments. Finally, good agreement was observed between measured post-interaction driver laser spectra and electron spectra, and particle-in-cell simulations with the INF&RNO code based on channel diagnostic measurements and MHD simulations with the MARPLE code.

Future experiments on the BELLA laser are planned for production of 10 GeV electron beams, as well as demonstration of staged acceleration with two 5 GeV stages [24]. As was discussed in Chapter 7, this may require new types of guiding structures capable of supporting lower matched spot sizes, such as optical field-ionized channels [82, 83, 145]. In addition to improved guiding, staged acceleration requires the production of narrow energy-spread electron bunches for efficient charge capture between stages. One means to achieve this is to inject a bunch by ionization injection with a laser pulse at a higher frequency that trails behind the driver pulse [67, 68]. Development of this scheme is the subject of future work at BELLA center. To that end, appendix A presents a numerical model of third harmonic generation for femtosecond laser pulses. As a demonstration of its capabilities, the model is used to simulate a possible configuration for an injector beamline producing a 267 nm injector pulse intrinsically synchronized to a 800 nm driver pulse from a standard Ti:Sapphire CPA laser system.

Bibliography

[1] S. D. Bass, A. De Roeck, and M. Kado, "The Higgs boson implications and prospects for future discoveries", Nature Reviews Physics **3**, 608–624 (2021).

[2] E. Esarey, C. B. Schroeder, and W. P. Leemans, "Physics of laser-driven plasma-based electron accelerators", Reviews of Modern Physics **81**, 1229–1285 (2009).

[3] W. K. H. Panofsky, "The Evolution of Particle Accelerators", Beam Line, 36–44 (1997).

[4] M. Tigner, "Does Accelerator-Based Particle Physics Have a Future?", Physics Today **54**, 36–40 (2001).

[5] S. Hossenfelder, "The World Doesn't Need a New Gigantic Particle Collider", Scientific American (2020).

[6] P. Muggli, "Beam-driven, Plasma-based Particle Accelerators", CERN Yellow Reports **1**, 119 (2016).

[7] T. Tajima and J. M. Dawson, "Laser electron accelerator", Physical Review Letters **43**, 267–270 (1979).

[8] D. Strickland and G. Mourou, "Compression of amplified chirped optical pulses", Optics Communications **55**, 447–449 (1985).

[9] M. D. Perry and G. Mourou, "Terawatt to Petawatt Subpicosecond Lasers", Science **264**, 917–924 (1994).

[10] C. G. R. Geddes, C. Toth, J. van Tilborg, E. Esarey, C. B. Schroeder, D. Bruhwiler, C. Nieter, J. Cary, and W. P. Leemans, "High-quality electron beams from a laser wakefield accelerator using plasma-channel guiding", Nature **431**, 538–541 (2004).

[11] J. Faure, Y. Glinec, A. Pukhov, S. Kiselev, S. Gordienko, E. Lefebvre, J.-P. Rousseau, F. Burgy, and V. Malka, "A laser–plasma accelerator producing monoenergetic electron beams", Nature **431**, 541–544 (2004).

[12] S. P. D. Mangles, C. D. Murphy, Z. Najmudin, A. G. R. Thomas, J. L. Collier, A. E. Dangor, E. J. Divall, P. S. Foster, J. G. Gallacher, C. J. Hooker, D. A. Jaroszynski, A. J. Langley, W. B. Mori, P. A. Norreys, F. S. Tsung, R. Viskup, B. R. Walton, and K. Krushelnick, "Monoenergetic beams of relativistic electrons from intense laser–plasma interactions", Nature **431**, 535–538 (2004).

[13] W. P. Leemans, B. Nagler, A. J. Gonsalves, C. Tóth, K. Nakamura, C. G. R. Geddes, E. Esarey, C. B. Schroeder, and S. M. Hooker, "GeV electron beams from a centimetre-scale accelerator", Nature Physics **2**, 696–699 (2006).

[14] S. Karsch, J. Osterhoff, A. Popp, T. P. Rowlands-Rees, Z. Major, M. Fuchs, B. Marx, R. Hörlein, K. Schmid, L. Veisz, S. Becker, U. Schramm, B. Hidding, G. Pretzler, D. Habs, F. Grüner, F. Krausz, and S. M. Hooker, "GeV-scale electron acceleration in a gas-filled capillary discharge waveguide", New Journal of Physics **9**, 10.1088/1367-2630/9/11/415 (2007).

[15] X. Wang, R. Zgadzaj, N. Fazel, Z. Li, S. A. Yi, X. Zhang, W. Henderson, Y. Y. Chang, R. Korzekwa, H. E. Tsai, C. H. Pai, H. Quevedo, G. Dyer, E. Gaul, M. Martinez, A. C. Bernstein, T. Borger, M. Spinks, M. Donovan, V. Khudik, G. Shvets, T. Ditmire, and M. C. Downer, "Quasi-monoenergetic laser-plasma acceleration of electrons to 2 GeV", Nature Communications **4**, 10.1038/ncomms2988 (2013).

[16] H. T. Kim, K. H. Pae, H. J. Cha, I. J. Kim, T. J. Yu, J. H. Sung, S. K. Lee, T. M. Jeong, and J. Lee, "Enhancement of electron energy to the multi-gev regime by a dual-stage laser-wakefield accelerator pumped by petawatt laser pulses", Physical Review Letters **111**, 1–5 (2013).

[17] D. J. Spence and S. M. Hooker, "Investigation of a hydrogen plasma waveguide", Physical Review E **63**, 015401 (2000).

[18] N. A. Bobrova, P. V. Sasorov, C. Benedetti, S. S. Bulanov, C. G. R. Geddes, C. B. Schroeder, E. Esarey, and W. P. Leemans, "Laser-heater assisted plasma channel formation in capillary discharge waveguides", Physics of Plasmas **20**, 020703 (2013).

[19] J. Daniels, "Measuring and modifying plasma density profiles to confine high power lasers", (2017).

[20] C. V. Pieronek, A. J. Gonsalves, C. Benedetti, S. S. Bulanov, J. van Tilborg, J. H. Bin, K. K. Swanson, J. Daniels, G. A. Bagdasarov, N. A. Bobrova, V. A. Gasilov, G. Korn, P. V. Sasorov, C. G. R. Geddes, C. B. Schroeder, W. P. Leemans, and E. Esarey, "Laser-heated capillary discharge waveguides as tunable structures for laser-plasma acceleration", Physics of Plasmas **27**, 093101 (2020).

[21] A. J. Gonsalves, K. Nakamura, J. Daniels, C. Benedetti, C. Pieronek, T. C. H. de Raadt, S. Steinke, J. H. Bin, S. S. Bulanov, J. van Tilborg, C. G. R. Geddes, C. B. Schroeder, C. Tóth, E. Esarey, K. Swanson, L. Fan-Chiang, G. Bagdasarov, N. Bobrova, V. Gasilov, G. Korn, P. Sasorov, and W. P. Leemans, "Petawatt Laser Guiding and Electron Beam Acceleration to 8 GeV in a Laser-Heated Capillary Discharge Waveguide", Physical Review Letters **122**, 084801 (2019).

[22] A. J. Gonsalves, K. Nakamura, C. Benedetti, C. V. Pieronek, S. Steinke, J. H. Bin, S. S. Bulanov, J. van Tilborg, C. G. R. Geddes, C. B. Schroeder, J. Daniels, C. Tóth, L. Obst-Huebl, R. G. W. van den Berg, G. Bagdasarov, N. Bobrova, V. Gasilov, G. Korn, P. Sasorov, W. P. Leemans, and E. Esarey, "Laser-heated capillary discharge plasma waveguides for electron acceleration to 8 GeV", Physics of Plasmas **27**, 053102 (2020).

[23] C. V. Pieronek, A. J. Gonsalves, K. Nakamura, C. Benedetti, L. Obst-Huebl, M. Turner, R. G. W. van den Berg, S. S. Bulanov, J. Van Tilborg, G. A. Bagdasarov, N. A. Bobrova, V. A. Gasilov, G. Korn, P. V. Sasorov, C. G. R. Geddes, C. B. Schroeder, and E. H. Esarey, "Ionization injection and dark-current suppression in a 20-cm-long channel-guided laser-plasma accelerator".

[24] *Advanced Accelerator Development Strategy Report: DOE Advanced Accelerator Concepts Research Roadmap Workshop*, tech. rep. (USDOE Office of Science (SC) (United States), Feb. 2016).

[25] J. M. Cole, K. T. Behm, E. Gerstmayr, T. G. Blackburn, J. C. Wood, C. D. Baird, M. J. Duff, C. Harvey, A. Ilderton, A. S. Joglekar, K. Krushelnick, S. Kuschel, M. Marklund, P. McKenna, C. D. Murphy, K. Poder, C. P. Ridgers, G. M. Samarin, G. Sarri, D. R. Symes, A. G. R. Thomas, J. Warwick, M. Zepf, Z. Najmudin, and S. P. D. Mangles, "Experimental Evidence of Radiation Reaction in the Collision of a High-Intensity Laser Pulse with a Laser-Wakefield Accelerated Electron Beam", Physical Review X **8**, 011020 (2018).

[26] P. M. Woodward, "A method of calculating the field over a plane aperture required to produce a given polar diagram", J. Inst. Electric. Eng. **93**, 1554–1558 (1947).

[27] J. D. Lawson, "Lasers and accelerators", IEEE Transactions on Nuclear Science **26**, 4217–4219 (1979).

[28] J. M. Dawson, "Nonlinear Electron Oscillations in a Cold Plasma", Physical Review **113**, 383–387 (1959).

[29] A. I. Akhiezer and R. V. Polovin, "Theory of Wave Motion of an Electron Plasma", Soviet Physics, JETP **3**, 696–705 (1956).

[30] E. Esarey and M. Pilloff, "Trapping and acceleration in nonlinear plasma waves", Physics of Plasmas **2**, 1432–1436 (1995).

[31] W. Kruer, *The Physics of Laser Plasma Interactions* (CRC Press, an imprint of Taylor and Francis, Boca Raton, FL, 2018).

[32] J. D. Jackson, *Classical electrodynamics*, 2nd ed. (Wiley, New York, 1975).

[33] P. Sprangle, E. Esarey, J. Krall, and G. Joyce, "Propagation and guiding of intense laser pulses in plasmas", Physical Review Letters **69**, 2200–2203 (1992).

[34] P. Maine, D. Strickland, P. Bado, M. Pessot, and G. Mourou, "Generation of Ultrahigh Peak Power Pulses by Chirped Pulse Amplification", IEEE Journal of Quantum Electronics **24**, 398–403 (1988).

[35] G. Mourou and D. Umstadter, "Development and applications of compact high-intensity lasers", Physics of Fluids B **4**, 2315–2325 (1992).

[36] W. P. Leemans, C. E. Clayton, W. B. Mori, K. A. Marsh, P. K. Kaw, A. Dyson, C. Joshi, and J. M. Wallace, "Experiments and simulations of tunnel-ionized plasmas", Physical Review A **46**, 1091–1105 (1992).

[37] P. Gibbon, *Short Pulse Laser Interactions with Matter* (Imperial College Press, London, Sept. 2005).

[38] P. Sprangle, E. Esarey, and A. Ting, "Nonlinear theory of intense laser-plasma interactions", Physical Review Letters **64**, 2011–2014 (1990).

[39] P. Sprangle, E. Esarey, and A. Ting, "Nonlinear interaction of intense laser pulses in plasmas", Physical Review A **41**, 4463–4469 (1990).

[40] C. B. Schroeder, E. Esarey, C. G. R. Geddes, C. Benedetti, and W. P. Leemans, "Physics considerations for laser-plasma linear colliders", Physical Review Special Topics - Accelerators and Beams **13**, 101301 (2010).

[41] S. V. Bulanov, V. I. Kirsanov, and A. S. Sakharov, "Excitation of ultrarelativistic Langmuir waves by a pulse of electromagnetic radiation", JETP Lett. **50**, 176–178 (1989).

[42] V. Berezhiani and I. Murusidze, "Relativistic wake-field generation by an intense laser pulse in a plasma", Physics Letters A **148**, 338–340 (1990).

[43] S. Shiraishi, C. Benedetti, A. J. Gonsalves, K. Nakamura, B. H. Shaw, T. Sokollik, J. van Tilborg, C. G. R. Geddes, C. B. Schroeder, C. Tóth, E. Esarey, and W. P. Leemans, "Laser red shifting based characterization of wakefield excitation in a laser-plasma accelerator", Physics of Plasmas **20**, 063103 (2013).

[44] E. Esarey, A. Ting, and P. Sprangle, "Frequency shifts induced in laser pulses by plasma waves", Physical Review A **42**, 3526–3531 (1990).

[45] B. A. Shadwick, C. B. Schroeder, and E. Esarey, "Nonlinear laser energy depletion in laser-plasma accelerators", Physics of Plasmas **16**, 056704 (2009).

[46] S. V. Bulanov, I. N. Inovenkov, V. I. Kirsanov, N. M. Naumova, and A. S. Sakharov, "Nonlinear depletion of ultrashort and relativistically strong laser pulses in an underdense plasma", Physics of Fluids B **4**, 1935–1942 (1992).

[47] A. J. Brizard, "A new Lagrangian formulation for laser-plasma interactions", Physics of Plasmas **5**, 1110–1117 (1998).

[48] C. B. Schroeder, C. Benedetti, E. Esarey, J. van Tilborg, and W. P. Leemans, "Group velocity and pulse lengthening of mismatched laser pulses in plasma channels", Physics of Plasmas **18**, 83103 (2011).

[49] V. S. Popov, "Tunnel and multiphoton ionization of atoms and ions in a strong laser field (Keldysh theory)", Physics-Uspekhi **47**, 855–885 (2004).

[50] P. Sprangle, A. Ting, and C. M. Tang, "Analysis of radiation focusing and steering in the free-electron laser by use of a source-dependent expansion technique", Physical Review A **36**, 2773–2781 (1987).

[51] P. Sprangle, C.-M. Tang, and E. Esarey, "Relativistic Self-Focusing of Short-Pulse Radiation Beams in Plasmas", IEEE Transactions on Plasma Science **15**, 145–153 (1987).

[52] B. Hafizi, A. Ting, P. Sprangle, and R. F. Hubbard, "Relativistic focusing and ponderomotive channeling of intense laser beams", Physical Review E **62**, 4120–4125 (2000).

[53] I. Kostyukov, A. Pukhov, and S. Kiselev, "Phenomenological theory of laser-plasma interaction in "bubble" regime", Physics of Plasmas **11**, 5256–5264 (2004).

[54] W. Lu, M. Tzoufras, C. Joshi, F. S. Tsung, W. B. Mori, J. Vieira, R. A. Fonseca, and L. O. Silva, "Generating multi-GeV electron bunches using single stage laser wakefield acceleration in a 3D nonlinear regime", Physical Review Special Topics - Accelerators and Beams **10**, 1–12 (2007).

[55] W. Lu, C. Huang, M. Zhou, W. B. Mori, and T. Katsouleas, "Nonlinear theory for relativistic plasma wakefields in the blowout regime", Physical Review Letters **96**, 1–4 (2006).

[56] W. Lu, C. Huang, M. Zhou, M. Tzoufras, F. S. Tsung, W. B. Mori, and T. Katsouleas, "A nonlinear theory for multidimensional relativistic plasma wave wakefields", Physics of Plasmas **13**, 10.1063/1.2203364 (2006).

[57] S. Y. Kalmykov, S. A. Yi, A. Beck, A. F. Lifschitz, X. Davoine, E. Lefebvre, A. Pukhov, V. Khudik, G. Shvets, S. A. Reed, P. Dong, X. Wang, D. Du, S. Bedacht, R. Zgadzaj, W. Henderson, A. Bernstein, G. Dyer, M. Martinez, E. Gaul, T. Ditmire, and M. C. Downer, "Numerical modelling of a 10-cm-long multi-GeV laser wakefield accelerator driven by a self-guided petawatt pulse", New Journal of Physics **12**, 10.1088/1367-2630/12/4/045019 (2010).

[58] E. Esarey, P. Sprangle, J. Krall, and A. Ting, "Self-focusing and guiding of short laser pulses in ionizing gases and plasmas", IEEE Journal of Quantum Electronics **33**, 1879–1914 (1997).

[59] S. Bulanov, N. Naumova, F. Pegoraro, and J. Sakai, "Particle injection into the wave acceleration phase due to nonlinear wake wave breaking", Physical Review E **58**, 5257–5260 (1998).

[60] C. B. Schroeder, E. Esarey, B. A. Shadwick, and W. P. Leemans, "Trapping, dark current, and wave breaking in nonlinear plasma waves", Physics of Plasmas **13**, 10.1063/1.2173960 (2006).

[61] A. G. Thomas, "Scalings for radiation from plasma bubbles", Physics of Plasmas **17**, 10.1063/1.3368678 (2010).

[62] S. Kalmykov, S. A. Yi, V. Khudik, and G. Shvets, "Electron self-injection and trapping into an evolving plasma bubble", Physical Review Letters **103**, 1–4 (2009).

[63] F. S. Tsung, R. Narang, W. B. Mori, C. Joshi, R. A. Fonseca, and L. O. Silva, "Near-GeV-energy laser-wakefield acceleration of self-injected electrons in a centimeter-scale plasma channel", Physical Review Letters **93**, 1–4 (2004).

[64] C. Benedetti, C. B. Schroeder, E. Esarey, F. Rossi, and W. P. Leemans, "Numerical investigation of electron self-injection in the nonlinear bubble regime", Physics of Plasmas **20**, 103108 (2013).

[65] C. McGuffey, A. G. Thomas, W. Schumaker, T. Matsuoka, V. Chvykov, F. J. Dollar, G. Kalintchenko, V. Yanovsky, A. Maksimchuk, K. Krushelnick, V. Y. Bychenkov, I. V. Glazyrin, and A. V. Karpeev, "Ionization induced trapping in a laser wakefield accelerator", Physical Review Letters **104**, 1–4 (2010).

[66] M. Chen, E. Esarey, C. B. Schroeder, C. G. Geddes, and W. P. Leemans, "Theory of ionization-induced trapping in laser-plasma accelerators", Physics of Plasmas **19**, 033101 (2012).

[67] L.-L. Yu, E. Esarey, C. B. Schroeder, J.-L. Vay, C. Benedetti, C. G. R. Geddes, M. Chen, and W. P. Leemans, "Two-Color Laser-Ionization Injection", Physical Review Letters **112**, 125001 (2014).

[68] C. B. Schroeder, J.-L. Vay, E. Esarey, S. S. Bulanov, C. Benedetti, L.-L. Yu, M. Chen, C. G. R. Geddes, and W. P. Leemans, "Thermal emittance from ionization-induced trapping in plasma accelerators", Physical Review Special Topics - Accelerators and Beams **17**, 101301 (2014).

[69] C. Benedetti, F. Rossi, C. B. Schroeder, E. Esarey, and W. P. Leemans, "Pulse evolution and plasma-wave phase velocity in channel-guided laser-plasma accelerators", Physical Review E **92**, 023109 (2015).

[70] E. Esarey, C. B. Schroeder, B. A. Shadwick, J. S. Wurtele, and W. P. Leemans, "Nonlinear theory of nonparaxial laser pulse propagation in plasma channels", Physical Review Letters **84**, 3081–3084 (2000).

[71] E. Esarey, B. A. Shadwick, C. B. Schroeder, and W. P. Leemans, "Nonlinear Pump Depletion and Electron Dephasing in Laser Wakefield Accelerators", in Aip conference proceedings, Vol. 737, 2004 (2004), pp. 578–584.

[72] B. Dromey, S. Kar, M. Zepf, and P. Foster, "The plasma mirror - A subpicosecond optical switch for ultrahigh power lasers", Review of Scientific Instruments **75**, 645–649 (2004).

[73] C. Thaury, F. Quéré, J. P. Geindre, A. Levy, T. Ceccotti, P. Monot, M. Bougeard, F. Réau, P. D'Oliveira, P. Audebert, R. Marjoribanks, and P. Martin, "Plasma mirrors for ultrahigh-intensity optics", Nature Physics **3**, 424–429 (2007).

[74] S. Steinke, J. van Tilborg, C. Benedetti, C. G. R. Geddes, J. Daniels, K. K. Swanson, A. J. Gonsalves, K. Nakamura, B. H. Shaw, C. B. Schroeder, E. Esarey, and W. P. Leemans, "Staging of laser-plasma accelerators", Physics of Plasmas **23**, 056705 (2016).

[75] J. van Tilborg, S. Steinke, C. G. R. Geddes, N. H. Matlis, B. H. Shaw, A. J. Gonsalves, J. V. Huijts, K. Nakamura, J. Daniels, C. B. Schroeder, C. Benedetti, E. Esarey, S. S. Bulanov, N. A. Bobrova, P. V. Sasorov, and W. P. Leemans, "Active Plasma Lensing for Relativistic Laser-Plasma-Accelerated Electron Beams", Physical Review Letters **115**, 184802 (2015).

[76] W. P. Leemans, A. J. Gonsalves, H.-S. S. Mao, K. Nakamura, C. Benedetti, C. B. Schroeder, C. Tóth, J. Daniels, D. E. Mittelberger, S. S. Bulanov, J.-L. L. Vay, C. G. R. Geddes, and E. Esarey, "Multi-GeV Electron Beams from Capillary-Discharge-Guided Subpetawatt Laser Pulses in the Self-Trapping Regime", Phys. Rev. Lett. **113**, 245002 (2014).

[77] A. J. Gonsalves, K. Nakamura, J. Daniels, H. S. Mao, C. Benedetti, C. B. Schroeder, C. Tóth, J. Van Tilborg, D. E. Mittelberger, S. S. Bulanov, J. L. Vay, C. G. Geddes, E. Esarey, and W. P. Leemans, "Generation and pointing stabilization of multi-GeV electron beams from a laser plasma accelerator driven in a pre-formed plasma waveguide", Physics of Plasmas **22**, 10.1063/1.4919278 (2015).

[78] C. G. Durfee and H. M. Milchberg, "Light pipe for high intensity laser pulses", Physical Review Letters **71**, 2409–2412 (1993).

[79] Y. Ehrlich, C. Cohen, A. Zigler, J. Krall, P. Sprangle, and E. Esarey, "Guiding of high intensity laser pulses in straight and curved plasma channel experiments", Physical Review Letters **77**, 4186–4189 (1996).

[80] D. Kaganovich, A. Ting, C. I. Moore, A. Zigler, H. R. Burris, Y. Ehrlich, R. Hubbard, and P. Sprangle, "High efficiency guiding of terawatt subpicosecond laser pulses in a capillary discharge plasma channel", Physical Review E - Statistical Physics, Plasmas, Fluids, and Related Interdisciplinary Topics **59**, R4769–R4772 (1999).

[81] P. Volfbeyn, E. Esarey, and W. P. Leemans, "Guiding of laser pulses in plasma channels created by the ignitor-heater technique", Physics of Plasmas **6**, 2269–2277 (1999).

[82] R. J. Shalloo, C. Arran, A. Picksley, A. Von Boetticher, L. Corner, J. Holloway, G. Hine, Ô. Jonnerby, H. M. Milchberg, C. Thornton, R. Walczak, S. M. Hooker, J. Jonnerby, H. M. Milchberg, C. Thornton, R. Walczak, and S. M. Hooker, "Low-density hydrodynamic optical-field-ionized plasma channels generated with an axicon lens", Physical Review Accelerators and Beams **22**, 41302 (2019).

[83] A. Picksley, A. Alejo, R. J. Shalloo, C. Arran, A. von Boetticher, L. Corner, J. A. Holloway, J. Jonnerby, O. Jakobsson, C. Thornton, R. Walczak, and S. M. Hooker, "Meter-Scale, Conditioned Hydrodynamic Optical-Field-Ionized Plasma Channels", Physical Review E **102**, 53201 (2020).

[84] N. A. Bobrova, A. A. Esaulov, J.-I. Sakai, P. V. Sasorov, D. J. Spence, A. Butler, S. M. Hooker, and S. V. Bulanov, "Simulations of a hydrogen-filled capillary discharge waveguide", Physical Review E **65**, 016407 (2001).

[85] P. Sprangle, J. Krall, and E. Esarey, "Hose-Modulation Instability of Laser Pulses in Plasmas", Physical Review Letters **73**, 3544–3547 (1994).

[86] A. J. Gonsalves, K. Nakamura, C. Lin, J. Osterhoff, S. Shiraishi, C. B. Schroeder, C. G. R. Geddes, C. Tóth, E. Esarey, and W. P. Leemans, "Plasma channel diagnostic based on laser centroid oscillations", Physics of Plasmas **17**, 056706 (2010).

[87] C. Benedetti, C. B. Schroeder, E. Esarey, and W. P. Leemans, "Quasi-matched propagation of ultra-short, intense laser pulses in plasma channels", Physics of Plasmas **19**, 053101 (2012).

[88] A. J. Gonsalves, "Investigation of a Hydrogen-filled Capillary Discharge Waveguide for Laser-driven Plasma Accelerators", PhD thesis (University of Oxford, 2006), p. 180.

[89] B. H. Broks, W. Van Dijk, and J. J. Van Der Mullen, "Parameter study of a pulsed capillary discharge waveguide", Journal of Physics D: Applied Physics **39**, 2377–2383 (2006).

[90] A. J. Gonsalves, T. P. Rowlands-Rees, B. H. Broks, J. J. Van Der Mullen, and S. M. Hooker, "Transverse interferometry of a hydrogen-filled capillary discharge waveguide", Physical Review Letters **98**, 1–4 (2007).

[91] J. Daniels, J. Van Tilborg, A. J. Gonsalves, C. B. Schroeder, C. Benedetti, E. Esarey, and W. P. Leemans, "Plasma density diagnostic for capillary-discharge based plasma channels", Physics of Plasmas **22**, 073112 (2015).

[92] A. J. Gonsalves, F. Liu, N. A. Bobrova, P. V. Sasorov, C. Pieronek, J. Daniels, S. Antipov, J. E. Butler, S. S. Bulanov, W. L. Waldron, D. E. Mittelberger, and W. P. Leemans, "Demonstration of a high repetition rate capillary discharge waveguide", Journal of Applied Physics **119**, 10.1063/1.4940121 (2016).

[93] M. Turner, A. J. Gonsalves, S. S. Bulanov, C. Benedetti, N. A. Bobrova, V. A. Gasilov, P. V. Sasorov, G. Korn, K. Nakamura, J. Van Tilborg, C. G. Geddes, C. B. Schroeder, and E. Esarey, "Radial density profile and stability of capillary discharge plasma waveguides of lengths up to 40 cm", High Power Laser Science and Engineering **9**, 1–10 (2021).

[94] S. I. Braginskii, "Transport processes in a plasma", in *Reviews of plasma physics*, Vol. 1 (Consultants Bureau, New York, 1965), p. 205.

[95] J. D. Huba, *NRL Plasma Formulary*, tech. rep. (Naval Research Laboratory, Washington, DC, 2009).

[96] P. Volfbeyn, E. Esarey, and W. P. Leemans, "Guiding of laser pulses in plasma channels created by the ignitor-heater technique", Physics of Plasmas **6**, 2269–2277 (1999).

[97] E. M. Lifshitz and L. P. Pitaevski, *Chapter IV - Collisions in Plasmas* (Butterworth-Heinemann, Oxford, 1981), p. 199.

[98] A. Y. Polishchuk and J. Meyer-Ter-Vehn, "Electron-ion relaxation in a plasma interacting with an intense laser field", Physical Review E **49**, 663–666 (1994).

[99] N. David, D. J. Spence, and S. M. Hooker, "Molecular-dynamic calculation of the inverse-bremsstrahlung heating of non-weakly-coupled plasmas", Physical Review E **70**, 056411 (2004).

[100] G. A. Bagdasarov, P. V. Sasorov, V. A. Gasilov, A. S. Boldarev, O. G. Olkhovskaya, C. Benedetti, S. S. Bulanov, A. Gonsalves, H.-S. S. Mao, C. B. Schroeder, J. Van Tilborg, E. Esarey, W. P. Leemans, T. Levato, D. Margarone, and G. Korn, "Laser beam coupling with capillary discharge plasma for laser wakefield acceleration applications", Physics of Plasmas **24**, 83109 (2017).

[101] N. A. Bobrova and P. V. Sasorov, "MHD equations for a fully ionized plasma of complex composition", Plasma Physics Reports **19**, 409 (1993).

[102] V. Gasilov, A. Boldarev, S. Dyachenko, O. Olkhovskaya, E. Kartasheva, G. Bagdasarov, S. Boldyrev, I. Gasilova, V. Shmyrov, S. Tkachenko, J. Grunenwald, and T. Maillard, "Towards an Application of High-Performance Computer Systems to 3D Simulations of High Energy Density Plasmas in Z-Pinches", Advances in Parallel Computing **22**, 235–242 (2012).

[103] J. van Tilborg, J. Daniels, A. J. Gonsalves, C. B. Schroeder, E. Esarey, and W. P. Leemans, "Measurement of the laser-pulse group velocity in plasma waveguides", Physical Review E **89**, 063103 (2014).

[104] I. H. Malitson, "Interspecimen Comparison of the Refractive Index of Fused Silica*,†", Journal of the Optical Society of America **55**, 1205 (1965).

[105] A. E. Siegman, *Lasers* (University Science Books, Sausalito, 1986).

[106] A. E. Siegman, "New developments in laser resonators", Optical Resonators **1224**, 2 (1990).

[107] *Zemax OpticStudio*, 2016.

[108] M. Takeda, H. Ina, and S. Kobayashi, "Fourier-transform method of fringe-pattern analysis for computer-based topography and interferometry", Journal of the Optical Society of America **72**, 156 (1982).

[109] MATLAB, *Version 7.1.0* (The Mathworks Inc., Natick, MA, 2016).

[110] K. Nakamura, H. S. Mao, A. J. Gonsalves, H. Vincenti, D. E. Mittelberger, J. Daniels, A. Magana, C. Toth, and W. P. Leemans, "Diagnostics, Control and Performance Parameters for the BELLA High Repetition Rate Petawatt Class Laser", IEEE Journal of Quantum Electronics **53**, 10.1109/JQE.2017.2708601 (2017).

[111] C. Benedetti, C. B. Schroeder, C. G. R. Geddes, E. Esarey, and W. P. Leemans, "An accurate and efficient laser-envelope solver for the modeling of laser-plasma accelerators", Plasma Physics and Controlled Fusion **60**, 14002 (2017).

[112] C. Benedetti, C. B. Schroeder, E. Esarey, C. G. R. Geddes, and W. P. Leemans, "Efficient Modeling of Laser-Plasma Accelerators with INF&RNO", AIP Conference Proceedings **1299**, 250–255 (2010).

[113] G. Vdovin, F. van Goor, Guyskk, and L. Doyle, *LightPipes for Python*, 2019.

[114] C. Benedetti, C. Schroeder, T. Mehrling, B. Djordjevic, S. Bulanov, C. Geddes, E. Esarey, and W. Leemans, "INF&RNO Modeling of 10 GeV-Class Electron Beams from a Laser-Plasma Accelerator Driven by the BELLA Laser", in 2018 ieee advanced accelerator concepts workshop (aac) (Aug. 2018), pp. 1–5.

[115] J. van Tilborg, A. J. Gonsalves, E. H. Esarey, C. B. Schroeder, and W. P. Leemans, "Density characterization of discharged gas-filled capillaries through common-path two-color spectral-domain interferometry", Optics Letters **43**, 2776 (2018).

[116] J. van Tilborg, A. J. Gonsalves, E. Esarey, C. B. Schroeder, and W. P. Leemans, "High-sensitivity plasma density retrieval in a common-path second-harmonic interferometer through simultaneous group and phase velocity measurement", Physics of Plasmas **26**, 023106 (2019).

[117] E. Hecht, *Optics*, 5th (Pearson, 2016).

[118] R. W. Gerchberg and W. O. Saxton, "A Practical Algorithm for the Determination of Phase from Image and Diffraction Plane Pictures", Optik **35**, 237–246 (1972).

[119] J. R. Fienup, "Phase retrieval algorithms: a comparison", Applied Optics **21**, 2758 (1982).

[120] B. H. P. Broks, K. Garloff, and J. J. A. M. van der Mullen, "Nonlocal-thermal-equilibrium model of a pulsed capillary discharge waveguide", Physical Review E **71**, 016401 (2005).

[121] B. H. P. Broks, W. Van Dijk, J. J. A. W. van der Mullen, A. J. Gonsalves, T. P. Rowlands-Rees, and S. M. Hooker, "Modeling of a square pulsed capillary discharge waveguide for interferometry measurements", Physics of Plasmas **14**, 023501 (2007).

[122] T. P. Rowlands-Rees, C. Kamperidis, S. Kneip, A. J. Gonsalves, S. P. Mangles, J. G. Gallacher, E. Brunetti, T. Ibbotson, C. D. Murphy, P. S. Foster, M. J. Streeter, F. Budde, P. A. Norreys, D. A. Jaroszynski, K. Krushelnick, Z. Najmudin, and S. M. Hooker, "Laser-driven acceleration of electrons in a partially ionized plasma channel", Physical Review Letters **100**, 1–4 (2008).

[123] F. Träger, ed., *Springer Handbook of Lasers and Optics* (Springer New York, New York, NY, 2007).

[124] R. Trebino, K. W. DeLong, D. N. Fittinghoff, J. N. Sweetser, M. A. Krumbügel, B. A. Richman, and D. J. Kane, "Measuring ultrashort laser pulses in the time-frequency domain using frequency-resolved optical gating", Review of Scientific Instruments **68**, 3277–3295 (1997).

[125] D. E. Mittelberger, "Optimization of a Laser Plasma Accelerator through Pulse Characterization and Controlled Spatiotemporal Coupling", PhD thesis (University of California, Berkeley, 2017).

[126] D. E. Mittelberger, M. Thévenet, K. Nakamura, A. J. Gonsalves, C. Benedetti, J. Daniels, S. Steinke, R. Lehe, J. L. Vay, C. B. Schroeder, E. Esarey, and W. P. Leemans, "Laser and electron deflection from transverse asymmetries in laser-plasma accelerators", Physical Review E **100**, 1–9 (2019).

[127] A. Jeandet, A. Borot, K. Nakamura, S. W. Jolly, A. J. Gonsalves, C. Tóth, H. S. Mao, W. P. Leemans, and F. Quéré, "Spatio-temporal structure of a petawatt femtosecond laser beam", JPhys Photonics **1**, 10.1088/2515-7647/ab250d (2019).

[128] F. Verluise, V. Laude, Z. Cheng, C. Spielmann, and P. Tournois, "Amplitude and phase control of ultrashort pulses by use of an acousto-optic programmable dispersive filter: pulse compression and shaping", Optics Letters **25**, 575 (2000).

[129] P. Tournois, "Acousto-optic programmable dispersive filter for adaptive compensation of group delay time dispersion in laser systems", Optics Communications **140**, 245–249 (1997).

[130] T. Oksenhendler, S. Coudreau, N. Forget, V. Crozatier, S. Grabielle, R. Herzog, O. Gobert, and D. Kaplan, "Self-referenced spectral interferometry", Applied Physics B: Lasers and Optics **99**, 7–12 (2010).

[131] P. O'Shea, M. Kimmel, X. Gu, and R. Trebino, "Highly simplified device for ultrashort-pulse measurement", Optics Letters **26**, 932 (2001).

[132] G. Pariente, V. Gallet, A. Borot, O. Gobert, and F. Quéré, "Space–time characterization of ultra-intense femtosecond laser beams", Nature Photonics **10**, 547–553 (2016).

[133] D. E. Mittelberger, K. Nakamura, R. Lehe, A. J. Gonsalves, C. Benedetti, H.-S. Mao, J. Daniels, N. Dale, S. V. Venkatakrishnan, K. K. Swanson, E. Esarey, and W. P. Leemans, "Characterization of the spectral phase of an intense laser at focus via ionization blueshift", Journal of the Optical Society of America B **33**, 1978 (2016).

[134] N. Lefaudeux, X. Levecq, G. Dovillaire, S. Theis, and L. Escolano, "New deformable mirror technology and associated control strategies for ultrahigh intensity laser beam corrections and optimizations", Laser Resonators, Microresonators, and Beam Control XIV **8236**, 82360K (2012).

[135] T. S. Ross and W. P. Latham, "Appropriate Measures and Consistent Standard for High-Energy Laser Beam Quality", Journal of Directed Energy **2**, 22–58 (2006).

[136] E. Perevezentsev, A. Poteomkin, and E. Khazanov, "Comparison of laser beam quality criteria", in Laser beam control and applications, Vol. 6101, edited by A. V. Kudryashov, A. H. Paxton, V. S. Ilchenko, A. Giesen, D. Nickel, S. J. Davis, M. C. Heaven, and J. T. Schriempf, February 2006 (Feb. 2006), p. 610119.

[137] V. N. Mahajan, "Strehl Ratio for Primary Aberrations in Terms of Their Aberration Variance.", Journal of the Optical Society of America **73**, 860–861 (1983).

[138] K. Nakamura, D. E. Mittelberger, A. J. Gonsalves, J. Daniels, H. S. Mao, F. Stulle, J. Bergoz, and W. P. Leemans, "Non-destructive sub-picocoulomb charge measurement for laser-plasma accelerators", AIP Conference Proceedings **1812**, 10.1063/1.4975893 (2017).

[139] S. Steinke, J. V. Tilborg, C. Benedetti, C. G. R. Geddes, C. B. Schroeder, J. Daniels, K. K. Swanson, A. J. Gonsalves, K. Nakamura, N. H. Matlis, B. H. Shaw, E. Esarey, and W. P. Leemans, "Multistage coupling of independent laser-plasma accelerators", Nature **530**, 190–193 (2016).

[140] G. A. Bagdasarov, N. A. Bobrova, O. G. Olkhovskaya, V. A. Gasilov, C. Benedetti, S. S. Bulanov, A. J. Gonsalves, C. V. Pieronek, J. Van Tilborg, C. G. Geddes, C. B. Schroeder, P. V. Sasorov, S. V. Bulanov, G. Korn, and E. Esarey, "Creation of an axially uniform plasma channel in a laser-assisted capillary discharge", Physics of Plasmas **28**, 1–9 (2021).

[141] T. P. A. Ibbotson, N. Bourgeois, T. P. Rowlands-Rees, L. S. Caballero, S. I. Bajlekov, P. A. Walker, S. Kneip, S. P. D. Mangles, S. R. Nagel, C. A. J. Palmer, N. Delerue, G. Doucas, D. Urner, O. Chekhlov, R. J. Clarke, E. Divall, K. Ertel, P. S. Foster, S. J. Hawkes, C. J. Hooker, B. Parry, P. P. Rajeev, M. J. V. Streeter, and S. M. Hooker, "Laser-wakefield acceleration of electron beams in a low density plasma channel", Physical Review Special Topics - Accelerators and Beams **13**, 031301 (2010).

[142] M. Kirchen, S. Jalas, P. Messner, P. Winkler, T. Eichner, L. Hübner, T. Hülsenbusch, L. Jeppe, T. Parikh, M. Schnepp, and A. R. Maier, "Optimal Beam Loading in a Laser-Plasma Accelerator", Physical Review Letters **126**, 174801 (2021).

[143] L. Oliveira e Silva and J. T. Mendonça, "Kinetic theory of photon acceleration: Time-dependent spectral evolution of ultrashort laser pulses", Physical Review E - Statistical Physics, Plasmas, Fluids, and Related Interdisciplinary Topics **57**, 3423–3431 (1998).

[144] D. F. Gordon, B. Hafizi, R. F. Hubbard, J. R. Peñano, P. Sprangle, and A. Ting, "Asymmetric Self-Phase Modulation and Compression of Short Laser Pulses in Plasma Channels", Physical Review Letters **90**, 4 (2003).

[145] B. Miao, L. Feder, J. E. Shrock, A. Goffin, and H. M. Milchberg, "Optical Guiding in Meter-Scale Plasma Waveguides", Physical Review Letters **125**, 10.1103/PhysRevLett.125.074801 (2020).

[146] R. W. Boyd, *Nonlinear optics*, 3rd ed (Academic Press, Burlington, MA, 2008).

[147] R. A. Fisher and W. K. Bischel, "Numerical studies of the interplay between self-phase modulation and dispersion for intense plane-wave laser pulses", Journal of Applied Physics **46**, 4921–4934 (1975).

[148] E. Sidick, A. Knoesen, and A. Dienes, "Ultrashort-pulse second-harmonic generation I Transform-limited fundamental pulses", Journal of the Optical Society of America B **12**, 1704 (1995).

[149] G. G. Gurzadyan, V. G. Dmitriev, and D. N. Nikogosyan, *Handbook of nonlinear optical crystals* (Springer-Verlag Berlin Heidelberg, 1997), p. 413.

[150] A. V. Smith, *SNLO* (AS-Photonics, Albuquerque, NM, 2015).

[151] M. Divall, K. Osvay, G. Kurdi, E. Divall, J. Klebniczki, J. Bohus, Á. Péter, and K. Polgár, "Two-photon-absorption of frequency converter crystals at 248 nm", Applied Physics B **81**, 1123–1126 (2005).

[152] C. Rullière, ed., *Femtosecond Laser Pulses: Principles and Experiments*, 2nd ed., Advanced Texts in Physics (Springer New York, New York, NY, 2005).

[153] O. Sinkin, R. Holzlohner, J. Zweck, and C. Menyuk, "Optimization of the split-step fourier method in modeling optical-fiber communications systems", Journal of Lightwave Technology **21**, 61–68 (2003).

[154] Y. Wang, S. Wang, A. Rockwood, B. M. Luther, R. Hollinger, A. Curtis, C. Calvi, C. S. Menoni, and J. J. Rocca, "085 PW laser operation at 33 Hz and high-contrast ultrahigh-intensity $\lambda = 400$ nm second-harmonic beamline", Optics Letters **42**, 3828 (2017).

[155] G. Duchateau, G. Geoffroy, A. Belsky, N. Fedorov, P. Martin, and S. Guizard, "Interaction of intense femtosecond laser pulses with KDP and DKDP crystals in the short wavelength regime", Journal of Physics Condensed Matter **25**, `10.1088/0953-8984/25/43/435501` (2013).

[156] G. P. Agrawal, *Nonlinear Fiber Optics*, 5th ed., Optics and Photonics (Academic Press, Amsterdam, 2013).

[157] T. Ditmire, A. M. Rubenchik, D. Eimerl, and M. D. Perry, "Effects of cubic nonlinearity on frequency doubling of high-power laser pulses", Journal of the Optical Society of America B **13**, 649–655 (1996).

[158] S. Y. Mironov, V. V. Lozhkarev, V. N. Ginzburg, I. V. Yakovlev, G. Luchinin, A. Shaykin, E. A. Khazanov, A. Babin, E. Novikov, S. Fadeev, A. M. Sergeev, and G. A. Mourou, "Second-Harmonic Generation of Super Powerful Femtosecond Pulses Under Strong Influence of Cubic Nonlinearity", IEEE Journal of Selected Topics in Quantum Electronics **18**, 7–13 (2012).

Appendix A

A numerical model of third harmonic generation for femtosecond laser pulses

A.1 Two-color ionization injection

Two-color ionization injection is a proposed method for the production of low emittance electron beams in a LWFA that relies on ionization injection by a high frequency laser pulse that trails the driver. The high frequency of the injector pulse minimizes distortion of the wake through reduction of the ponderomotive force which scales as ω^{-2}, and minimizes the initial transverse momentum of the ionized electrons through the $a_0 \sim \omega^{-1}$ scaling of the normalized vector potential [68]. Simulations have shown that beams with nanometer scale emittances can be produced with this method [67, 68].

The electrons of the trapped bunch are tunnel-ionized from background ions in the plasma, which requires very high laser intensities, especially for the highly charged ions remaining after the passage of a LWFA driver. The "single cycle" ionization intensity I_t defined according to $\omega^{-1}D = 1$, with D the tunneling ionization rate of Eqn. 2.75, can be regarded as the threshold for ionization of a given species. Tunnel ionization is a nonlinear process, and hence the total charge ionized does not scale with the pulse energy, but rather the total volume over which the threshold intensity I_t is reached.

The scaling of bunch charge with peak power in the injector pulse can be estimated assuming a Gaussian beam profile for the injector laser. Assuming the threshold intensity is reached at the beam waist r_0, the volume over which ionization occurs is roughly $V_{\rm foc} \sim 2\pi r_0^2 z_R$, with $z_R = \pi r_0^2/\lambda_i$ the Rayleigh range and λ_i the wavelength of the injector pulse. The total charge is then

$$Q \sim q_e n_i V_{\rm foc} \sim q_e n_i \frac{2\pi^2 r_0^4}{\lambda} \ , \tag{A.1}$$

with n_i the donor ion density in the plasma. The r_0^4 factor implies that the bunch charge scales as P_i^2, with $P_i = \pi r_0^2 I_t$ the peak power in the injector.

A technologically mature approach to producing high intensity, high frequency injector

pulses synchronized to a LWFA driver is to divert a portion of the driver energy through a system of nonlinear crystals to generate pulses at a harmonic of the laser frequency [146]. However, frequency conversion of femtosecond pulses involves both spatial and temporal evolution of the pulse envelope, and the resulting partial differential equations in time and space cannot be solved analytically. In this appendix, a numerical model based on the split-step algorithm [147] is presented for simulating nonlinear frequency conversion of femtosecond laser pulses in one spatial dimension, i.e. for plane waves. Moreover, the model is used to simulate a potential scheme for generating pulses at the third harmonic of a Ti:Sapphire laser via cascaded second-harmonic generation and sum-frequency generation.

As a note to the reader, symbol definitions used in this appendix are independent of the rest of this dissertation. Additionally, SI units are used here instead of the Gaussian-cgs units used elsewhere.

A.2 Sum Frequency Generation and Second Harmonic Generation of Ultrashort Laser Pulses

It is most efficient to generate the third harmonic by cascading two second-order processes rather than relying on a single stage third order process. This is practically implemented by generating the second harmonic in a nonlinear crystal, and then using the second harmonic and residual fundamental to generate the third harmonic in a second crystal via sum-frequency generation. Both of these processes are well understood and extensively documented in the existing literature, the textbook Ref. [146] being just one introductory example.

However, for femtosecond pulses relevant for LWFA, group velocity mismatch in the crystal limits the efficiency of frequency conversion. Such pulses are sufficiently short for the interaction length to be limited by the distance over which the pulses separate from one another due to their differing group velocities, which in turn limits the conversion efficiency. Additionally, mismatch of pulse group velocities can lead to "smearing" or stretching of the harmonic pulses, which reduces the peak power. The latter issue is of particular concern for tunneling ionization, which is a highly nonlinear process and requires very high laser intensities to be efficient.

Because of this group velocity mismatch, and to a lesser extent second-order dispersion, design of a frequency conversion system for femtosecond laser pulses requires modeling of the spatiotemporal pulse envelope evolution. Moreover, in most cases of interest, analytical solution of the governing partial differential equations is not practical and numerical methods must be used. Second harmonic generation of femtosecond pulses was studied numerically in Ref. [148] using the split-step algorithm [147]. In this section, the formalism developed in that work is extended to the closely related process of sum-frequency generation.

Propagation of electromagnetic waves in a nonlinear medium can be described with the macroscopic electromagnetic wave equation, with the nonlinear polarization $\mathbf{P}_{\mathrm{NL}}$ separated

from the linear dielectric displacement $\mathbf{D}_{\mathrm{L}}$ and acting as a source term:

$$\nabla^2\mathbf{E} - \mu_0\frac{\partial^2\mathbf{D}_{\mathrm{L}}}{\partial t^2} = \mu_0\frac{\partial^2\mathbf{P}_{\mathrm{NL}}}{\partial t^2}\ , \tag{A.2}$$

with μ_0 the vacuum magnetic permeability.

Some important simplifications are made when treating the problem of second harmonic generation and sum-frequency generation in a nonlinear crystal. First, the problem is explicitly formulated such that the field is separated into discrete frequency components $\omega_3 = \omega_1 + \omega_2$. Moreover, of principle concern is the laser pulse envelope, rather than the wavelength-scale structure of the field. Hence, the electric fields of the interacting frequencies ω_j are expressed in terms of slowly varying envelopes with a carrier frequency according to

$$\mathbf{E}_j(z,t) = \frac{1}{2}\mathbf{A}_j(z,t)e^{i(\omega_j t - k_j z)} + \text{c.c.}\ . \tag{A.3}$$

In reality, the nonlinear susceptibility of a crystal is a tensor, and the mixing frequencies typically possess different polarizations due to the requirement for phase matching [146]. However, calculation of the nonlinear polarization response using this tensor is tedious and complex, which motivates the second simplification. Specifically, the vectorial nature of the electromagnetic field, as well as the tensorial nature of the nonlinear susceptibility can be accounted for implicitly by appropriate choice of the nonlinear coupling coefficients. For the most common case of propagation in a uniaxial crystal, the only information needed is the polarization state, ordinary (O) or extraordinary (E), of the interacting frequencies, and the direction of the wave vectors relative to the crystal axes. Formulas for the coupling coefficients of commonly used nonlinear crystals can be found in Ref. [149] and other reference works. For the work in this dissertation, coefficients for the nonlinearity as well as linear propagation of the interacting frequencies were calculated with the software package SNLO [150]. Therefore, vector and tensor notation can be dropped and the problem of the laser pulse evolution formally treated in terms of interacting scalar fields. Moreover, parallel wavevectors for the interacting frequencies will be assumed.

Adopting the foregoing simplifications, expanding the material dispersion to second order (up to group velocity dispersion or GVD), and restricting the problem to one spatial dimension as stated previously, the LHS of Eqn. A.2 can be rewritten for the linear propagation of the laser envelope at each frequency ω_j as

$$\begin{aligned}\frac{\partial^2 E_j}{\partial z^2} - \mu_0\frac{\partial^2 D_{\mathrm{L},j}}{\partial t^2} \\ = \frac{1}{2}\left[\frac{\partial^2 A_j}{\partial z^2} - 2ik_j\frac{\partial A_j}{\partial z} - 2ik_j\dot{k}_j\frac{\partial A_j}{\partial t} - (\dot{k}_j^{\,2} + k_j\ddot{k}_j)\frac{\partial^2 A_j}{\partial t^2}\right]e^{i(\omega_j t - k_j z)} + \text{c.c.}\ ,\end{aligned} \tag{A.4}$$

with wavenumber $k_j = \omega n_j/c$, refractive index n_j, $\dot{k}_j = \mathrm{d}k/\mathrm{d}\omega|_{\omega_j}$ the inverse group velocity, and $\ddot{k}_j = \mathrm{d}^2k/\mathrm{d}\omega^2|_{\omega_j}$ the inverse group velocity dispersion GVD^{-1}. Note that in general each polarization state involved in the interaction will have its own dispersion relation.

Following the standard treatment of second-order nonlinear frequency conversion [146], the nonlinear polarization source term for ω_j with $j = 1, 2$

$$\mu_0 \frac{\partial^2 P_{\mathrm{NL},1,2}}{\partial t^2} = -\frac{\omega_{1,2}^2}{2c^2} d_{\mathrm{eff}} A_{2,1}^* A_3 e^{i[\omega_{1,2}t + (k_{2,1} - k_3)z]} + \text{c.c.} \ , \tag{A.5}$$

with d_{eff} the nonlinear coupling coefficient. The polarization source term for the sum-frequency ω_3 is

$$\mu_0 \frac{\partial^2 P_{\mathrm{NL},3}}{\partial t^2} = -\frac{\omega_3^2}{2c^2} d_{\mathrm{eff}} A_1 A_2 e^{i[\omega_3 t - (k_1 + k_2)z]} - \frac{1}{4} n_3 c \epsilon_0 \beta |A_3|^2 A_3 e^{i(\omega_3 t - k_3 z)} + \text{c.c.} \ , \tag{A.6}$$

with β the two-photon absorption coefficient and ϵ_0 the vacuum permittivity.

The first term of Eqn. A.6 is the standard nonlinear source term for sum-frequency generation. The second term accounts for two-photon absorption (TPA), which is a nonlinear absorption process that occurs when two photons interact nonlinearly to excite an electron across the crystal bandgap. This requires that the individual photons possess a minimum of half the gap energy. For crystals commonly used for nonlinear frequency conversion of laser light, TPA becomes important for wavelengths < 300 nm. The TPA coefficient β is defined such that the laser intensity is attenuated according to [151]

$$\left[\frac{\partial I}{\partial z}\right]_{\mathrm{TPA}} = -\beta I^2 \ . \tag{A.7}$$

Combining Eqns. A.4-A.6 according to Eqn. A.2 yields a system of coupled partial differential equations for the evolution of the laser pulse envelopes. The frequencies ω_1 and ω_2, denoted by indices $j = 1, 2$ evolve according to

$$\frac{\partial^2 A_{1,2}}{\partial z^2} - 2ik_{1,2}\frac{\partial A_{1,2}}{\partial z} - 2ik_{1,2}\dot{k}_{1,2}\frac{\partial A_{1,2}}{\partial t} - (\dot{k}_{1,2}^2 + k_{1,2}\ddot{k}_{1,2})\frac{\partial^2 A_{1,2}}{\partial t^2} = -\frac{\omega_{1,2}^2}{c^2} d_{\mathrm{eff}} A_{2,1}^* A_3 e^{-i\Delta k z} \ , \tag{A.8}$$

with $\Delta k = k_1 + k_2 - k_3$ the phase matching parameter. The envelope evolution equation for the sum frequency ω_3 is written

$$\frac{\partial^2 A_3}{\partial z^2} - 2ik_3\frac{\partial A_3}{\partial z} - 2ik_3\dot{k}_3\frac{\partial A_3}{\partial t} - (\dot{k}_3^{\,2} + k_3\ddot{k}_3)\frac{\partial^2 A_3}{\partial t^2} = -\frac{\omega_3^2}{c^2} d_{\mathrm{eff}} A_1 A_2 e^{i\Delta k z} - \frac{1}{2} n_3 c \epsilon_0 \beta |A_3| A_3 \ . \tag{A.9}$$

As in the long-pulse regime, efficient frequency conversion requires phase matching, i.e. $\Delta k = 0$ [146]. Phase matching is commonly achieved by exploiting crystal birefringence, and is often the primary constraint on the frequency range over which a given nonlinear crystal can be used efficiently [146, 149].

Eqns. A.8 and A.9 have the same fundamental structure as the equations for sum-frequency generation with long pulses [146]. The LHS of both equations treats the evolution of the pulse envelope, the only difference in this case being the inclusion of terms beyond $-2ik\partial A/\partial z$ which arise from first and second order dispersion. The RHS contains the nonlinear source terms with the familiar phase matching parameter. The only process added to the model is the two-photon absorption term on the RHS of Eqn. A.9, which becomes important for the high peak intensities of ultrashort pulses [152].

It is convenient to express the pulse envelopes in terms of the comoving coordinates (z, τ), with $\tau = t - \gamma z$ and γ^{-1} the comoving frame velocity. γ is defined as the average of the inverse group velocities of the interacting laser pulses so as to keep them centered on the defined temporal grid. With the transformation to comoving variables such that $A(z,t) \rightarrow A(z,\tau)$, the derivatives in Eqns. A.8 and A.9 become

$$\left(\frac{\partial A}{\partial z}\right)_t = \left(\frac{\partial A}{\partial z}\right)_\tau - \gamma\frac{\partial A}{\partial \tau} \tag{A.10}$$

$$\left(\frac{\partial A}{\partial t}\right)_z = \frac{\partial A}{\partial \tau} \tag{A.11}$$

$$\left(\frac{\partial^2 A}{\partial t^2}\right)_z = \frac{\partial^2 A}{\partial \tau^2} \tag{A.12}$$

$$\left(\frac{\partial^2 A}{\partial z^2}\right)_t = \left(\frac{\partial^2 A}{\partial z^2}\right)_\tau - 2\gamma\frac{\partial^2 A}{\partial z \partial \tau} + \gamma^2\frac{\partial^2 A}{\partial \tau^2} \simeq \gamma^2\frac{\partial^2 A}{\partial \tau^2} \tag{A.13}$$

Eqn. A.13 is a statement of the slowly-varying envelope approximation. That is, the characteristic length for evolution of the pulse envelope is much longer than the pulse envelope itself. Finally, applying the transformation

$$A_3 \rightarrow A_3 e^{i\Delta k z} \tag{A.14}$$

allows phase matching to be treated with an additional linear term in the equation for ω_3. This transformation only alters the envelope of the sum frequency ω_3 by a phase factor, which in many cases can be neglected. However, should the phase of the envelope be required, the "physical" envelope can be recovered by adding the phase factor according to

$$\tilde{A}_3 = A_3 e^{i\Delta k z} \ . \tag{A.15}$$

The set of partial differential equations for modeling sum-frequency generation obtained through the application of Eqns. A.10-A.15 are summarized in Table A.1. The corresponding equations for second harmonic generation, derived in Ref. [148], are summarized in Table A.2.

Low Frequency 1	$\frac{\partial A_1}{\partial z} = \frac{\eta_1}{3}\frac{\partial A_1}{\partial \tau} + i\xi_1\frac{\partial^2 A_1}{\partial \tau^2} - i\rho_1 A_2^* A_3$	(A.16a)
Low Frequency 2	$\frac{\partial A_2}{\partial z} = \frac{\eta_2}{3}\frac{\partial A_2}{\partial \tau} + i\xi_2\frac{\partial^2 A_2}{\partial \tau^2} - i\rho_2 A_1^* A_3$	(A.16b)
Sum Frequency	$\frac{\partial A_3}{\partial z} = \frac{\eta_3}{3}\frac{\partial A_3}{\partial \tau} + i\xi_3\frac{\partial^2 A_3}{\partial \tau^2} - i\Delta k A_3 - i\rho_3 A_1 A_2 - \sigma\lvert A_3\rvert^2 A_3$	(A.16c)
ω_3 physical field	$\tilde{A}_3 = A_3 e^{i\Delta k z}$	(A.16d)
Comoving Coordinates	$z,\ \tau \equiv t - \gamma z$	(A.17a)
Comoving Group Delay	$\gamma \equiv \frac{1}{3}\sum_{i=1}^{3}\dot{k}_i$	(A.17b)
Interpulse Group Delay	$\eta_i \equiv \sum_{j\neq i}\dot{k}_j - 2\dot{k}_i$	(A.18a)
Group Delay Dispersion	$\xi_i \equiv (\dot{k}_i^{\,2} - \gamma^2 + k_i\ddot{k}_i)/2k_i$	(A.18b)
Nonlinear Coupling Coefficient	$\rho_i \equiv \omega_i d_{eff}/2n_i c$	(A.18c)
Two-Photon Absorption Coefficient	$\sigma \equiv n_3 c\epsilon_0\beta/2$	(A.18d)
Characteristic Time	Intensity full-width half-max T_{FWHM}	(A.19a)
Characteristic Length	$L_{\mathrm{SFG}} \equiv \frac{T_{\mathrm{FWHM}}}{(\dot{k}_1 + \dot{k}_2)/2 - \dot{k}_3}$	(A.19b)

Table A.1: Sum-frequency generation equations in SI units

A.3 The split-step algorithm for numerical modeling of nonlinear wave propagation

Equations of the type collected in Tables A.1 and A.2 can be solved numerically using the "split-step" method [147, 153]. This algorithm was first used for modeling self-phase modulation of pulses in optical fibers, but it can also be used to model second harmonic generation, as was done in Ref. [148], as well as sum-frequency generation. The essence of the method is to separate the evolution of the laser envelope in z into a linear operation and a nonlinear operation, and apply these operations separately over each spatial step Δz. This allows the pulse group velocity and dispersion to be treated in the frequency domain, and the nonlinear frequency conversion to be treated with an ordinary differential equation. A split-step code was written in MATLAB [109] to solve the equations of Tables A.1 and A.2.

Fundamental	$\frac{\partial A}{\partial z} = \frac{\eta}{2}\frac{\partial A}{\partial \tau} + i\xi_1 \frac{\partial^2 A}{\partial \tau^2} - i\rho_1 A^* B$	(A.20a)
Second Harmonic	$\frac{\partial B}{\partial z} = -\frac{\eta}{2}\frac{\partial B}{\partial \tau} + i\xi_2 \frac{\partial^2 A}{\partial \tau^2} - i\Delta k B - i\rho_2 A^2$	(A.20b)
ω_2 physical field	$\tilde{B} = Be^{i\Delta kz}$	(A.20c)
Comoving Coordinates	$z,\ \tau \equiv t - \gamma z$	(A.21a)
Comoving Group Delay	$\gamma \equiv (\dot{k}_1 + \dot{k}_2)/2$	(A.21b)
Interpulse Group Delay	$\eta \equiv (\dot{k}_2 - \dot{k}_1)$	(A.22a)
Group Delay Dispersion	$\xi_i \equiv (\dot{k_i}^2 - \gamma^2 + k_i \ddot{k_i})/2k_i$	(A.22b)
Nonlinear Coupling Coefficient	$\rho_i \equiv \omega_0 d_{eff}/2n_i c$	(A.22c)
Characteristic Time	Intensity full-width half-max T_{FWHM}	(A.23a)
Characteristic Length	$L_{\mathrm{SHG}} = \frac{T_{\mathrm{FWHM}}}{\dot{k}_2 - \dot{k}_1}$	(A.23b)

Table A.2: Second harmonic generation equations in SI units

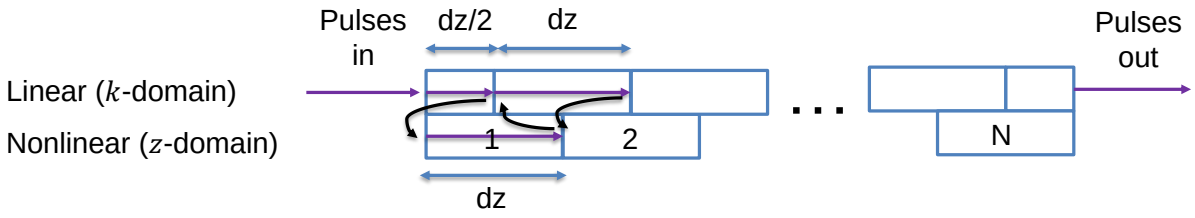

Figure A.1: Schematic representation of the split-step algorithm. The propagation medium is divided into interleaved domains where the laser envelope is alternately evolved according to the linear and nonlinear terms of the envelope equation. The linear component of the evolution equation is solved in the k-domain using a fast Fourier transform. The nonlinear component is solved in the z domain using a fourth-order Runge-Kutta integration.

Linear Component Fourier Transforms		
Low Frequency 1	$\hat{k} = -\frac{\eta_1}{3}\hat{\omega} + \xi_1\hat{\omega}^2$	(A.24a)
Low Frequency 2	$\hat{k} = -\frac{\eta_2}{3}\hat{\omega} + \xi_2\hat{\omega}^2$	(A.24b)
Sum Frequency	$\hat{k} = -\frac{\eta_3}{3}\hat{\omega} + \xi_3\hat{\omega}^2 + \Delta k$	(A.24c)
Nonlinear Component ODEs		
Low Frequency 1	$\frac{\partial A_1}{\partial z} = -i\rho_1 A_2^* A_3$	(A.25a)
Low Frequency 2	$\frac{\partial A_2}{\partial z} = -i\rho_2 A_1^* A_3$	(A.25b)
Sum Frequency	$\frac{\partial A_3}{\partial z} = -i\rho_3 A_1 A_2 - \sigma\lvert A_3\rvert^2 A_3$	(A.25c)

Table A.3: Split-step operations for sum-frequency generation, according to definitions of Table A.1.

In this section, a brief overview of the design of the code will be given.

The operation of the split-step algorithm is shown schematically in Fig. A.1. The interaction medium is discretized into $2N-1$ overlapping steps of thickness $\Delta z = L/N$, with the exception of two steps of $\Delta z/2$ on the ends of the medium, with L the thickness of the medium. The temporal evolution of each pulse at $z = 0$ is specified, i.e. $A_j(0,\tau)$, as a 1-D numerical array of time samples. After being evolved through a linear propagation interval, the resulting pulses are evolved through a nonlinear propagation interval, and the laser pulses are propagated through the entire medium according to alternating application of the linear and nonlinear components of the envelope evolution equations.

The linear component of the equations is solved in the frequency domain via a fast Fourier transform according to

$$A(z+\Delta z,\tau) = \mathrm{FFT}_\tau^{-1}\{\mathrm{FFT}_\tau\{A(z,\tau)\}e^{-i\hat{k}(\hat{\omega})\Delta z}\}\ , \tag{A.28}$$

with $\hat{\omega} = \omega - \omega_0$ the frequency associated with the Fourier transform of the laser envelope (i.e. with the carrier frequency shifted to zero) and $\hat{k}(\omega)$ the wavenumber from the dispersion relation for the laser envelope. These dispersion relations are collected for sum-frequency

Linear Component Fourier Transforms		
Fundamental	$\hat{k} = -\frac{\eta}{2}\hat{\omega} + \xi_1\hat{\omega}^2$	(A.26a)
Second Harmonic	$\hat{k} = \frac{\eta}{2}\hat{\omega} + \xi_2\hat{\omega}^2 + \Delta k$	(A.26b)
Nonlinear Component ODEs		
Fundamental	$\frac{\partial A}{\partial z} = -i\rho_1 A^* B$	(A.27a)
Second Harmonic	$\frac{\partial B}{\partial z} = -i\rho_2 A^2$	(A.27b)

Table A.4: Split-step operations for second-harmonic generation, according to definitions of Table A.2.

generation and second-harmonic generation as Eqns. A.24 and A.26 of Tables A.3 and A.4, respectively.

The nonlinear component of the equations is integrated using the fourth-order Runge-Kutta method, using the coupled ordinary differential equations of Eqns. A.25 and A.27 in Tables A.3 and A.4. The integration is performed independently on each time sample of the pulses, hence the partial derivatives. As implemented, the discretized intervals Δz form the mesh over which the Runge-Kutta integration is performed. Hence, the solver operates essentially as a Runge-Kutta integrator of N steps, with the dispersion operation of Eqn. A.28 performed between each step.

Generally, the step size should be chosen such that $\Delta z \ll L_{\mathrm{SHG,SFG}}$, and the temporal grid for the pulses should be sampled such that $\Delta t \ll T_{\mathrm{FWHM}}$. For the simulations here, $\Delta z / L_{\mathrm{SHG,SFG}} \sim 10^2$ and $\Delta t / T_{\mathrm{FWHM}} \sim 10^3$. Propagation through ~ 1 mm of material with several hundred integration steps can be simulated in a few seconds on a personal computer.

A.4 Numerical investigation of third-harmonic generation for two-color ionization injection

To demonstrate the capabilities of the code, a potential scheme for generating femtosecond deep ultraviolet laser pulses by third harmonic generation from 800 nm Ti:Sapphire laser

pulses was simulated. As previously described, generation of the third harmonic is performed in two stages in two separate crystals, beginning with second harmonic generation followed by sum-frequency generation with the second harmonic and residual fundamental. Potassium dihydrogen phosphate (KH_2PO_4) or "KDP" was chosen as the nonlinear material. KDP is a commonly used crystal for laser frequency conversion: it is phase-matchable to $\lesssim 250$ nm [149] and commercially available as large single crystals required to accommodate high energy laser pulses without damage [154]. Other candidate crystals include β-barium borate (β-$Ba(BO_2)_2$ or "BBO") and Lithium Triborate (LiB_3O_5 or "LBO"). However, BBO is not available in large crystal sizes (as of writing), and LBO possesses a lower nonlinear coupling coefficient for sum-frequency generation at the wavelengths of interest [149, 150].

Between the two nonlinear crystals, two other optical components are required. The first optic is a group velocity compensator to delay the fundamental relative to the second harmonic before the sum-frequency stage. This is to maximize the distance over which the pulses overlap, as the fundamental pulse will "overtake" the second harmonic due to its higher group velocity. The second optic is a half-wave plate, to rotate the polarization of the residual fundamental from the first crystal into the same plane as the second harmonic to achieve type-I phase matching in the second crystal. Neither of these were directly modeled in this case, with their function being being accounted for by the addition of delay between the pulses and selection of type-I coefficients for both processes. However, explicit modeling and design of these components is a requirement for future development of a third harmonic generation system.

For the simulation presented here, the fundamental pulse had a 30 fs intensity FWHM, with 51 $\mathrm{mJ\,cm^{-2}}$ fluence. This fluence value was chosen to be less than the single-shot damage threshold for KDP at 267 nm [155]. Optical parameters for both the second harmonic generation and sum-frequency generation stages are collected in Table A.5, generated with SNLO [150], from which the coefficients of Tables A.1 and A.2 were calculated.

These simulations are directed towards maximizing the peak intensity in the third harmonic, which is the key parameter for efficient tunnel ionization as discussed in Section A.1. The strategy adopted to achieve this is to maximize the source term for the third harmonic in Eqn. A.16. A simple argument shows that 50% conversion efficiency in the second harmonic generation stage is optimal for this purpose. The third harmonic source term scales as $(I_1 I_2)^{1/2}$, with I_1 and I_2 the intensities at the summing frequencies ω_1 and ω_2. These intensities sum approximately to the initial fundamental input intensity I_0 such that $I_0 \approx I_1 + I_2$, in which case the source term scales roughly as $\sim [(I_0 - I_2)I_2]^{1/2}$. Thus, the source term is maximized for $I_2/I_0 = 1/2$.

A simulation of second harmonic generation is shown in Fig. A.2. Pulses are modeled with 8000 time samples over a 300 fs window, and the nonlinear medium is discretized into $N = 200$ steps. Evolution of the peak intensities of the fundamental and second harmonic pulses is plotted in Fig. A.2(b), showing continuous depletion of the peak intensity of the fundamental and saturation of the peak intensity of the second harmonic. This arises from the group velocity mismatch between the two frequencies. Essentially, the peak intensity of the second harmonic pulse can only grow while it overlaps with the fundamental pulse. The

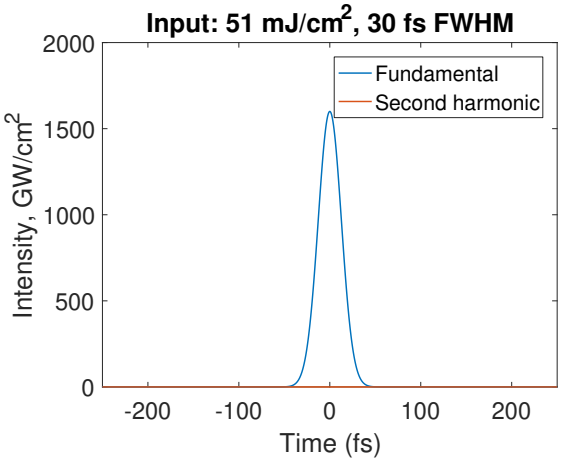

(a) 800 nm input pulse.

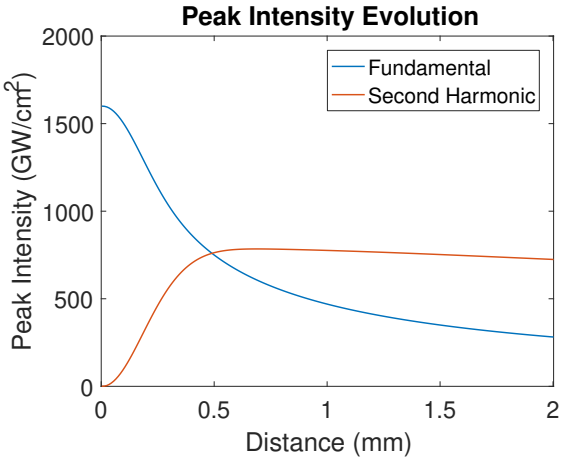

(b) Variation of the peak intensity of fundamental and second harmonic pulses with propagation distance through the crystal.

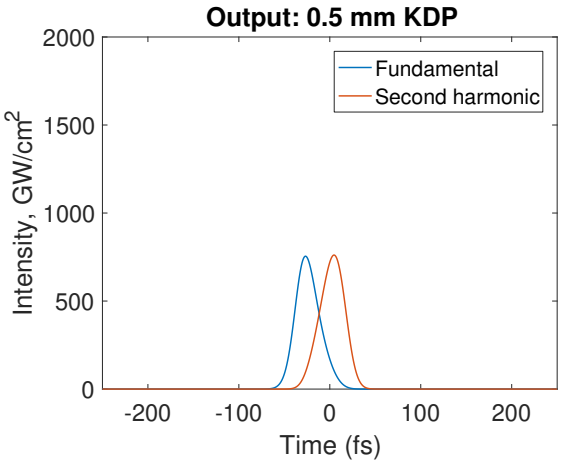

(c) Pulse intensities at the "optimal" propagation distance, where intensity is equally partitioned between the two frequencies.

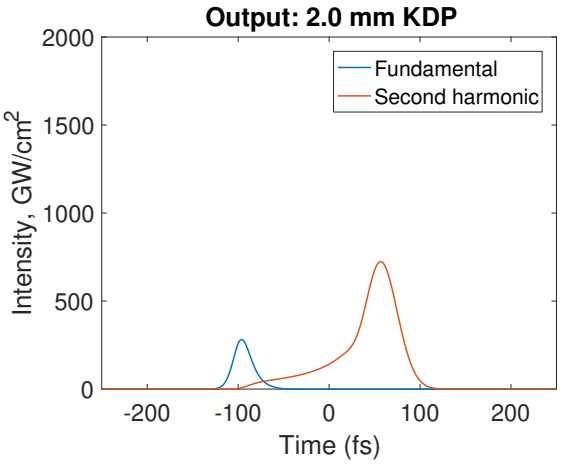

(d) Pulse intensities after 2 mm of propagation. Group velocity mismatch has produced a long tail on the second harmonic pulse.

Figure A.2: Split-step simulation of second harmonic generation, using the parameters of Table A.5.

λ_0 (nm)	Pol.	d_{eff} (pm V^{-1})	β (cm GW^{-1})	n	Δk (μm^{-1})	$c\dot{k}$	$\ddot{k}$ ($\text{fs}^2\,\text{mm}^{-1}$)
Second Harmonic Generation, Type I, $\theta = 44.9°$							
800	O	0.302	0	1.502	0	1.526	27.3
400	E					1.550	106.8
Sum-Frequency Generation, Type I, $\theta = 67.5°$							
800	O	0.442	0	1.502	0	1.526	27.3
400	O		0	1.524		1.577	114.5
267	E		0.27	1.517		1.638	213.2

Table A.5: Optical parameters for phase-matched third harmonic generation in KDP from SNLO [150]. Parameters are listed for each crystal, with the phase matching type and wavevector angle relative to the optical axis.

effective interaction length where this condition holds is estimated as the distance required for the second harmonic to accumulate a delay of one FWHM relative to the fundamental, i.e.

$$L_{\text{SHG}} = \frac{T_{\text{FWHM}}}{\dot{k}_2 - \dot{k}_1} \ , \tag{A.29}$$

with T_{FWHM} the intensity FWHM of the fundamental, and other quantities as defined in Table A.2. For the case of Fig. A.2, $L_{\text{SHG}} \sim 0.5$ mm, and Fig. A.2(b) shows the second harmonic peak intensity saturates after a propagation distance very near this value.

A crystal thickness $\sim L_{\text{SHG}}$ is optimal for sum-frequency generation as it maximizes the peak power in the residual fundamental and thus the source term for sum-frequency generation. This is evident in Figs. A.2(c) and A.2(d), which show the fundamental and second harmonic pulses at the saturation point ($z = 0.5$ mm $\sim L_{\text{SHG}}$) and the end of the simulation ($z = 2.0$ mm $\sim 4L_{\text{SHG}}$), respectively. The peak intensity of the second harmonic is nearly equal in both cases, whereas the the peak intensity in the fundamental has been reduced by more than half between $z = 0.5$ mm and $z = 2.0$ mm. Fig. A.2(d) shows that the energy lost from the fundamental has been deposited into a long tail on the second harmonic pulse by the group velocity mismatch. In the sum-frequency generation stage, the energy in this tail does not contribute to the peak intensity in the third harmonic, and is effectively wasted. Moreover, depletion of the fundamental intensity reduces the source term for sum-frequency generation. Hence, for purposes of generating high peak intensity in the third harmonic, a crystal with thickness $\sim L_{\text{SHG}}$ is preferable for the second harmonic generation stage.

A simulation of the sum-frequency generation stage, which actually produces the third harmonic, is shown in Fig. A.3. The input pulses at the fundamental and second harmonic are shown in Fig. A.3(a), which are taken from Fig. A.2(c) with a delay applied to compensate for the group velocity mismatch. As for second harmonic generation, this group velocity

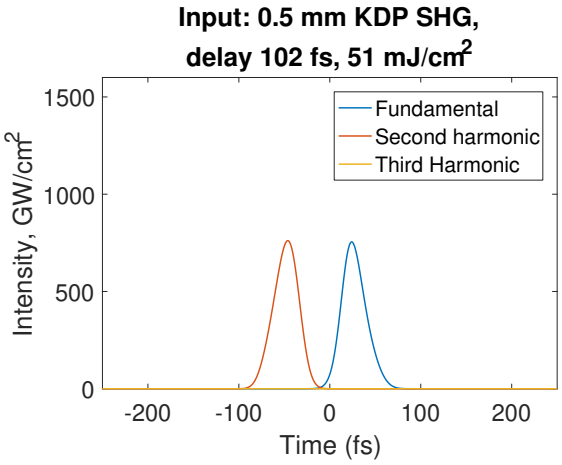

(a) Input to the sum-frequency stage. Pulses of Fig. A.2(c) with 102 fs delay applied to the fundamental.

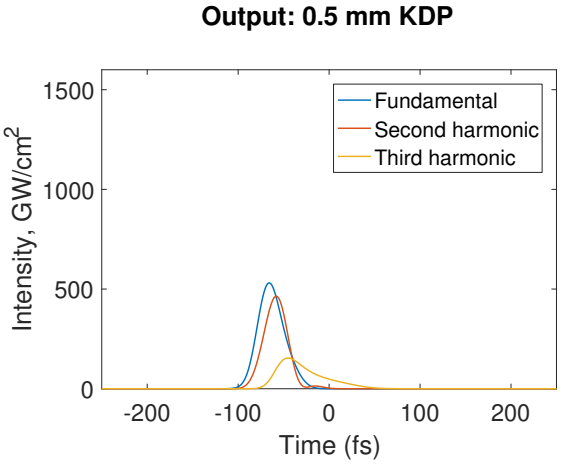

(b) Output at maximum third harmonic intensity.

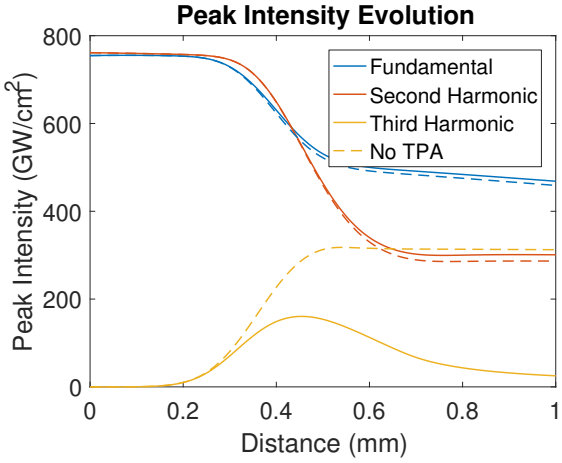

(c) Peak intensity evolution. Solid lines for a simulation with TPA constant β of Table A.5, dotted lines for TPA suppressed.

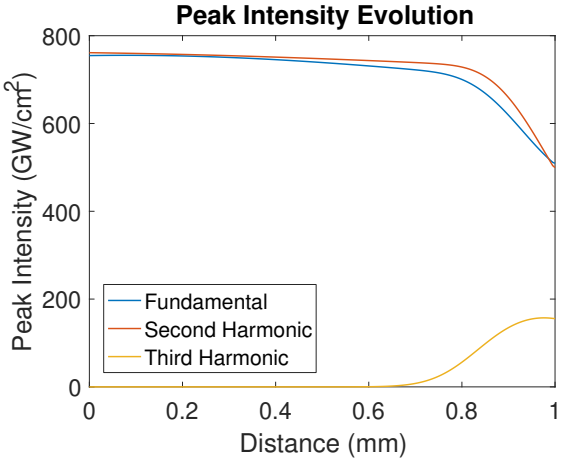

(d) Pulse evolution as in Fig. A.3(c), but with initial fundamental pulse delay 190 fs to delay third harmonic generation and mitigate TPA.

Figure A.3: Split-step simulation of sum-frequency generation, using the parameters of Table A.5.

mismatch limits the interaction length, which is defined in terms of the difference between the source frequencies (fundamental and second harmonic) and the sum-frequency according to

$$L_{\mathrm{SFG}} = \frac{T_{\mathrm{FWHM}}}{\dot{k}_3 - (\dot{k}_1 + \dot{k}_2)/2} \ , \tag{A.30}$$

with T_{FWHM} the intensity FWHM of the fundamental as before, and the other quantities as defined in Table A.1. Note that sum-frequency generation does not occur until the fundamental and second harmonic overlap, and the location in the crystal at which this overlap occurs is dependent on the initial delay between these two pulses. Hence, L_{SFG} does not specify the total propagation distance at which the maximum intensity in the third harmonic is reached, but rather the distance after overlap at which this maximum is reached. Peak intensity evolution for all three frequencies is plotted in Fig. A.3(c). For this case $L_{\mathrm{SFG}} = 0.15$ mm, similar to the 0.2 mm distance over which the third harmonic grows from zero intensity to its maximum in the simulation. The maximum intensity of the third harmonic is roughly 10% the peak intensity of the initial unconverted fundamental pulse, consistent with the literature [152].

Sum-frequency generation consumes more energy from the higher of the two summing frequencies, which can be seen in Fig. A.3(c). This is a consequence of the Manley-Rowe relations, which dictate that every sum-frequency photon produced requires the consumption of one photon from each of the summing frequencies [146]. This enters the field equations used here through the ω_j scaling of the nonlinear coupling coefficients of Table A.1. Since the photon energy $\hbar\omega$ is proportional to frequency, photons lost from the second harmonic consume twice as much energy as those from the fundamental.

Photon balance in sum-frequency generation can be thought of in terms of the "reaction" $\gamma_{\omega_1} + \gamma_{\omega_2} \rightarrow \gamma_{\omega_3}$, which is mediated by the nonlinear medium. This constitutes a "stoichiometric" limit on the total efficiency of the frequency conversion process. That is, the maximum number of ω_3 photons that can be produced is limited to the number of photons in whichever of the summing frequencies ω_1 and ω_2 has the fewest. This suggests that optimal conversion efficiency into the third harmonic is achieved with the second harmonic and fundamental intensities in a 2:1 ratio. This is indeed the case for longer laser pulses where group velocity mismatch is not a concern. However, because the primary mechanisms limiting conversion efficiency in this regime are group velocity mismatch and two-photon absorption ("TPA"), maximizing the source term for the third harmonic over the interaction length L_{SFG} is more important. Hence, equipartition of the initial fundamental intensity into the summing frequencies was chosen, as discussed in the beginning of this section. Only at intensities high enough to deplete one or more of the summing frequencies over an interaction length will photon balance become important for conversion efficiency.

Conversion efficiency into the third harmonic is severely limited by two-photon absorption in the case of Fig. A.3. This can be seen by comparing the peak intensity evolution for a simulation with TPA suppressed, i.e. $\beta = 0$, plotted in Fig. A.3(c). For suppressed TPA, the third harmonic retains its maximum peak intensity through the remainder of the crystal after it is generated, apart from a small decrease due to group delay dispersion. With the

literature value of the TPA constant in KDP $\beta = 0.27$ cm GW^{-1} [151] however, the third harmonic is attenuated by a factor ~ 3 after 0.5 mm. Hence, the third harmonic must be extracted from the crystal immediately upon reaching maximum intensity to suppress TPA losses. This can be done by reducing the crystal thickness for the sum-frequency generation stage, but this generally presents a manufacturing challenge. Alternatively, the delay of the fundamental relative to second harmonic can be tuned such that overlap and sum-frequency generation occur within $\sim L_{\mathrm{SFG}}$ of the downstream end of the crystal, such that the third harmonic pulse is extracted once it reaches maximum intensity. This avoids the attenuation from TPA shown in Fig. A.3(c), at the cost of a few-percent intensity loss in the fundamental and second-harmonic due to dispersion.

A.5 Further work and possible extensions of the model

In this section, a numerical model of frequency conversion of ultrashort pulses in nonlinear crystals based on the split-step algorithm was presented. Using this model, a possible scheme for producing high intensity femtosecond pulses at the third harmonic of 800 nm Ti:Sapphire laser light was simulated. However, more work remains to be done to obtain a practical design for a frequency conversion system. Realistic pulse shapes and spectral phase should be investigated. Transform-limited Gaussian pulses were used as a matter of convenience to model the fundamental pulse here, but pulses from a real laser system will depart from this idealized model. It is straightforward to model arbitrary pulse shapes and spectral phases, only requiring appropriate specification of the complex envelope $A(z, \tau)$.

Moreover, third-order nonlinearities have been neglected, specifically self-phase modulation [146] and cross-phase modulation [156]. These processes will detune phase matching or lead to pulse distortion, which will in turn reduce the conversion efficiency. The effect of third-order nonlinearities on second harmonic generation of high power laser pulses has been investigated numerically in Ref. [157, 158]. Extending that work to the model presented here requires adding nonlinear terms of the form $\sim i|A|^2 A$ to Eqns. A.20 and A.16. The split-step algorithm can accommodate these interaction terms with no substantial modifications, requiring only that they be added to the ODEs for the nonlinear integration step Eqns. A.27 and A.25.